INTERNATIONAL DOCTORAL
SCHOOL OF THE USC

Alicia
Rioboo Vidal

PhD Thesis

New supramolecular concepts for the development of functional systems in cells and protocells

Santiago de Compostela, 2024

Doctoral Programme in Chemical Science and Technology

ESCOLA DE DOUTORAMENTO
INTERNACIONAL DA USC

DOCTORAL THESIS

NEW SUPRAMOLECULAR CONCEPTS FOR THE DEVELOPMENT OF FUNCTIONAL SYSTEMS IN CELLS AND PROTOCELLS

Author

Alicia Rioboo Vidal

Supervisor/s: Javier Montenegro García, Juan Ramón Granja Guillán

Tutor: Juan Ramón Granja Guillán

PHD PROGRAMME IN CHEMICAL SCIENCE AND TECHNOLOGY

SANTIAGO DE COMPOSTELA


USC
UNIVERSIDADE
DE SANTIAGO
DE COMPOSTELA

Agradecementos

Nesta etapa da miña vida marcada pola gran dedicación ao desenvolvemento desta tese de doutoramento, foron partícipes moitas persoas que tiveron nela unha influenza fundamental. Por ilo, gustaríame dedicarlle unhas palabras a todas elas.

En primeiro lugar, grazas aos meus directores de tese, Juan Ramón Granja Guillán e Javier Montenegro García, por abrirme as portas dos vosos laboratorios cando eu era unha xove estudante de segundo de carreira, e permitirme que avanzara no mundo da investigación ao voso carón ata converterme en doutora. Sempre valorarei que forades capaces de ver en min as ganas e a ilusión por aprender e medrar a nivel científico, e que non dubidarades en darme a oportunidade. A Juan, pola túa preocupación, axuda e comprensión en todos os aspectos que englobaron a miña experiencia como estudante no teu grupo. A Javier, por ter sempre valorado o meu criterio científico e personalidade, e ver en min alguén capaz de alcanzar un futuro prometedor no mundo da academia. Gracias por tenderme a túa man e abrirme as portas deste camiño, aínda que ao final a vida me levase por outro.

Grazas a todas as persoas que compoñen e compuxeron o grupo de investigación de Juan e Javier. Cada día de tese, cada experimento fallido ou cada angustia derivada (sabedes que son moi intensa) foron sempre máis levadeiros grazas á vosa presenza. Creo que todos sabemos que o noso grupo ten algo especial a nivel persoal, que o bo ambiente que nos caracteriza non pasa desapercibido. Sabedes tamén que eu son quizais a menos festeira e a que se mantén máis ao marxe dalgunhas das cousas que organizades, pero de verdade que foi sempre un privilexio poder traballar rodeada de xente tan especial. E o mellor de todo é que, a pesar de ver chegar e marchar a moitas persoas ao longo destes anos, sempre se mantivo un grupo onde non so hai compañeiros de laboratorio, se non verdadeiros amigos. Todos sodes especiais e únicos, pero merécenme uns agradecementos especiais:

Marisa, por ser a miña nai científica. O meu primeiro contacto no laboratorio foi contigo, descubrindo que era iso dos péptidos. O teu carácter sempre tan amable e cheo de dozura fixéronme ver dende o primeiro momento que era unha sorte poder terte como guía. E o paso do tempo non so mo confirmou, se non que me deixou claro que non eras unha máis do grupo, se non a peza clave que mantiña ao grupo en conexión e funcionando. Grazas por todo, por cada momento compartido dentro e fóra do laboratorio. Deséxovos o mellor tanto a ti como a Alberto. TraffikGene é so o comezo de todos os éxitos e alegrías que vos deparará o futuro.

Jose J. Reina, por enseñarme todas las bases y trucos de la síntesis orgánica que me han permitido convertirme en la química que hoy en día soy. Tu mente brillante, tu humor, tu alegría y tu buena cara ante las adversidades han sido esenciales para mí en mis primeros años en el laboratorio. Creo que nunca me habría atrevido a adentrarme en el doctorado si no hubiera contado con tu ayuda y apoyo. Sé siempre muy feliz en Málaga, rodeado de tus niños y tu familia.

Nacho, por ser o meu terceiro director, aínda que a USC non nolo queira recoñecer. Moitísimas grazas por toda a axuda durante estes anos, por estar sempre disposto a debater comigo os resultados e os futuros experimentos, aínda que houbera que esperar o que fixera falta a que o meu ordenador decidira acender (Mac, xamais). E, sobre todo, grazas por saber sempre prestarme a túa axuda sen limitar a miña capacidade de opinar e propoñer solucións. Grazas tamén polos largos debates sobre a vida académica, e moitas felicidades por lograr afianzar a túa carreira profesional ligado a ela. Como seguro recordarás, eu xa che dixen que isto ocorrería, pois tiña xa daquela moi claro que non podía existir ningún postdoc que o merecera máis ca ti.

Patri, por ser a miña orgullosa pupila. Recordo perfectamente o primeiro día que nos coñecemos, cando Javier me dixo que iba ser a encargada de ensinarche a traballar co SNARF, nada menos. Eu sentíame moi insegura e tiña medo de non ser quen de conseguir que nos saíra nin unha soa reacción, pero ti sempre mo puxeches todo moi fácil. Pouco a pouco fun descubrindo en ti a alguén moi especial, co equilibrio perfecto entre responsable e festeira, alegre e botada para adiante, e que trouxo ao laboratorio máis galego e máis concienciación sobre numerosos aspectos da sociedade actual que tanta falta nos fan a todos, e dos que ti me convences cada día que non nos poden deixar indiferentes. Grazas por facer de min alguén mellor e grazas por converterte na miña mellor amiga dentro do laboratorio.

Grazas tamén a Irene, pola túa inconmensurable sabedoría e a túa disposición para axudar en todo o que sexa preciso. Grazas a Arcadio por solucionar todas as complicacións técnicas que nos farían imposible facer ciencia se non contaramos contigo. Grazas a Juan, pola túa axuda e amabilidade cos experimentos *in vivo*. Grazas a Rebeca, por todas as facilidades para suplirme cos millóns e millóns de células que moitas veces che pedía con excesiva pouca antelación. Grazas a Xosé, por ser un amor todas as veces que fun a Farmacia a facer ozonólisis ou a dar prácticas de laboratorio. Grazas tamén á Fundación Segundo Gil Dávila, á Xunta de Galicia (ED481A-2019/038) e ao Ministerio de Ciencia (FPU18/03192 e EST21/00485) pola súa financiación durante estes anos de tese.

Durante o meu doutoramento, tamén tiven a oportunidade de facer dúas estancias predoutorais, en Edimburgo e en Groningen, e nelas atopeime con xente marabillosa á que tamén quero mencionar.

Gracias a Marc Vendrell. Creo que nunca habría podido tener ningún tutor de estancia mejor que tú, ni a nivel científico ni personal. Cuando fui a Edimburgo era mi primera vez fuera de Santiago durante meses, y tu amabilidad y ayuda me hicieron sentirme muy segura y confiada desde el primer día. No cualquiera da su número de teléfono personal ni se ofrece a ir a buscar al aeropuerto a una estudiante de estancia en su grupo. Creo que esto habla por sí mismo. Además, siempre has tenido plena disponibilidad para hablar conmigo, para supervisar mi proyecto e incluso para tomarnos un café los días antes de irme. Muchas gracias por esos meses tan enriquecedores en Edimburgo, y gracias también por seguir acordándote de mí varios años después, y no dudar en ofrecerme tu ayuda. Nunca lo olvidaré.

Thanks also to all Marc lab members for be so nice with me, but specially to Emily. You were the best lab supervisor I have never had, full of hapiness and willing to help me. Maybe the time has made that our ways get distanced, but you will always be well received in my house in Santiago.

Thanks also to Anna. It was a pleasure to have you as flatmate. Everything with you was easy and natural. I hope you were able to return to your loved Poland to be closer to your dad.

Thanks to Nathalie Katsonis for your supervision and help during my stay in Groningen. Also, thank you for accepting me in your lab even being necessary to move the dates so many times, and for give me the opportunity to learn about droplets mobility. Moreover, thanks for trust in my scientific validity and offer me future research opportunities.

Thanks to all Nathalie lab students for be also so nice with me and to organize the awesome “Friedays”, but specially to Beatrice, who works with me hand in hand. I wish you the best in the last years of your PhD.

Gracias a Eider, por ser mi gran apoyo durante los meses de la estancia. Me has ayudado muchísimo a no sentirme sola en casa, a saber que podía compartir contigo todas las locuras que nos tocó vivir. Espero seguir siempre en contacto contigo y que nos volvamos a ver en Galicia o en el País Vasco. Mucha suerte en todo. Sé que el trabajo que deseas de química pronto llegará.

E polo seu importante papel neste último ano da tese, quero tamén ter unhas palabras de agradecemento para os integrantes de Smart Vitamins e o laboratorio de María José Alonso. Grazas, en primeiro lugar, a Alfredo e a María José Alonso por darme a oportunidade de empezar a miña carreira profesional na industria química en Santiago. Grazas por confiar na miña valía científica e persoal, mesmo non tendo defendido aínda a miña tese, pois puiden así saber cales iban ser os meus pasos tras esta etapa formativa. Grazas a Patri, por ser unha gran compañeira de traballo. Sinto que traballar día a día contigo faime mellorar como científica. Grazas por compartir comigo todas as nosas dúbidas e decisións, tanto persoais como laborais. Grazas por levarme aos descansos reflexivos tomando infusións de frutos vermellos. Grazas por tantísimas risas cada día. E, sobre todo, grazas por compenetrarte tan ben comigo e que fagamos tan bo equipo. Oxalá sigamos sempre en contacto. Grazas a Belén, por tanta axuda, por tanta terapia psicolóxica e por tantos pases de modelo. Eres a alma do laboratorio e, simplemente, encántasme. Grazas a todos os integrantes do laboratorio de MJ por facerme sentir como en casa dende o primeiro día, pero sobre todo aos meus anteriores compis da planta 6: Germán, Marcos, Cris, Julia, Jorge e Eva.

Grazas tamén á miña familia, polo seu apoio durante estes anos. Grazas a meus pais por terme sempre permitido tomar decisións libremente en todos os aspectos da miña vida, e polo voso apoio incondicional en todas elas. Non sabedes o privilexiada que me sinto por saber que sempre vos terei ao meu lado para todo. Sei tamén o orgullosos que vos sentides de min pola muller na que me convertín, pero vós fuchedes os que me permitíchedes forxarme tal e como son. Grazas a Manuel, por amarme e coidarme tan intensamente como ti o fas. Nunca poderei agradecerche tanto como o mereces o teu apoio en todos os difíciles momentos que a tese trouxo consigo. Apórtasme moita seguridade, paz, sentimento de fogar e plenitude vital. Pequeno spoiler, pero “si, quero” todo contigo sempre e por sempre. Grazas tamén a Sara, a Patri, a Alberto, aos meus avós, e a todas aquelas persoas que son importantes na miña vida.

E, xa por último, quero darme as grazas a min mesma. Grazas á eu de 23 anos, que se atreveu a comezar a tese doutoral chea de ilusión, de ganas de aprender, de medrar cientificamente, de facerse un oco no mundo da investigación. Grazas á eu que foi capaz de superar os seus medos e afrontar experiencias novas fóra da súa zona de confort. E grazas tamén por, ao longo destes anos de tese, non ter cambiado, por seguir fiel ás túas conviccións e forma de entender e vivir a vida. Grazas por tomar as túas propias decisións baixo o teu propio prisma. Grazas, por fin, por ter atopado cal é o teu camiño cara a felicidade.


USC
UNIVERSIDADE
DE SANTIAGO
DE COMPOSTELA

Index

Abbreviations

+eV: positive ion mode
3-DMAP: 3-dimethylaminophenol
a.u.: arbitrary units
AcOEt: ethyl acetate
Ala: alanine
ANTS: 8-aminonaphthalene-1,3,6-trisulfonic acid
Ar: argon
Arg: arginine
Asn: asparagine
Asp: aspartate
BCECF: 2′,7′-Bis-(2-carboxyethyl)-5-(and-6-)carboxyfluorescein
BCPCF: 2′,7′-bis-(2-carboxypropyl)-5-(and-6-)-carboxyfluorescein
Boc: tert-butyloxycarbonyl
C.SNARFs: carboxy-seminaphthorhodafluors
ca.: *circa*
CAC: Critical Aggregation Concentration
CDCl$_3$: deuterated chloroform
CFC: Critical Fibrillar Concentration
CMC: Critical Micellar Concentration
CPP: Cell Penetrating Peptide
Cys: cysteine
DCM: dichloromethane
DIEA: *N*,*N*-diethylisopropylamine
DLS: Dynamic Light Scattering
DMEM: Dulbecco’s Modified Eagle Medium
DMF: dimethylformamide
DMS: dimethyl sulfate
DMSO: dimethyl sulfoxide
DNA: desoxyribonucleic acid
DPX: *p*-xylene-*bis*-pyridinium bromide
DST: Dynamic Surface Tension
EDT: ethane-1,2-dithiol
e.g.: for examples
EMA: European Medicines Agency
eq: equivalents
ESI: electrospray ionization
FBS: Fetal Bovine Serum
FDA: Food and Drug Administration (USA)
FITC: fluorescein isothiocyanate
GFP: Green Fluorescent Protein
Glu: glutamate
Gly: glycine
GOx: glucose oxidase
GUVs: Giant Unilamellar Vesicles
HEPES: 2-[4-(2-hydroxyethyl) piperazin-1-yl]ethanesulfonic acid
His: histidine
HPLC: High-Performance Liquid Chromatography

HRP: horseradish peroxidase
Hz: hertz
i.e.*: id est*
IR: infrared
kcps: kilocounts per second
Lys: lysine
m/z: mass/charge ratio
MasX: mastoparan X
MeOH: methanol
MES: 2-(*N*-morpholino)ethanesulfonic acid
MQ-H_2O: Milli-Q water
MS: Mass Spectrometry
Mtt: 4-methyltrityl
n**BuLi**: n-butyllithium
NFSI: *N*-fluorobenzenesulfonimide
N**-HATU**: 1-[Bis(dimethylamino)methylene]-1H-1,2,3-triazolo[4,5-b]pyridinium 3-oxid hexafluorophosphate
N**-HBTU**: *N,N,N′,N′*-Tetramethyl-O-(1H-benzotriazol-1-yl)uronium hexafluorophosphate
NIR: near infrared
NMR: Nuclear Magnetic Resonance
PBS: Phosphate-Buffered Saline
PMB*: p*-methoxybenzyl
POPC: L-α-phosphatidylcholine (Egg, Chicken)
POPG: 1-palmitoyl-2-oleoyl-sn-glycero-3-phospho-(1'-rac-glycerol) (sodium salt)
ppm: parts per million
QD: quantum dots
RFP: Red Fluorescent Protein
SD: standard deviation
SNAFRs: seminaphthofluoresceins
SNARFLs: seminaphthofluorones
SNARFs: seminaphthorhodafluors
SPPS: solid phase peptide synthesis
STEM: scanning transmission electron microscopy
t: time
TAMRA: 5-(and-6)-carboxytetramethylrhodamine
TFA: trifluoroacetic acid
THF: tetrahydrofuran
ThT: Thioflavin T
TLC: thin layer chromatography
TMA: trimellitic anhydride
TPP: triphenyl phosphine
Trp: tryptophan
Tyr: tyrosine
u: micro
UV: ultraviolet
Val: valine
w/o: water-in-oil
λ_{em}: emission wavelength
λ_{exc}: excitation wavelength

Summary

In this manuscript, we have approached the development of new functional supramolecular systems from a chemical perspective and with the objective to modify or replicate cellular functions. The main driving force and link between the systems developed during this PhD work is the dynamic character of stimuli-responsiveness, which is crucial for their specific functional behaviour.

In the first case, a protofilament mimetic of an artificial cytoskeleton system has been approached by using a supramolecular peptide fibrillar system. Synthetic supramolecular strategies like this, where artificial surrogates can template their own structure and thus physically catalyse their own synthesis, have been studied by the scientific community showing great potential for their application in biomedicine and soft nanofabrication. They are characterized by their biological inspiration and also by their potential to self-assemble into supramolecular hierarchical architectures. Building on bottom-up strategies, the artificial reconstruction of different biomimetic amphiphilic lipid and lipid-like materials have been studied in the context of biomimetic compartmentalization and autopoiesis. However, very little is known about the potential functionality derived from the chemically triggered self-assembly of amphiphilic fibrillar networks inside aqueous compartments. The potential functional consequence of one-dimensional supramolecular polymers in conferment could be of interest to understand, using a simple synthetic system, the importance of early cytoskeletal-like entities in the first cellular entities. Inspired by the importance of the hydrophobic effect, we decided to study the amphiphilic self-assembly of dormant peptide precursors triggered by a chemical reaction (e.g. oxyme connection) inside water droplets. These experiments allow the study of one-dimensional supramolecular networks under confinement, and their potential effects over droplet functional properties and their interactions with the environment. We employed a non-assembling peptide precursor, $\mathbf{P_{C8}}$, consisting in short and anionic peptide fragment (EEAAVV) equipped with a short aliphatic tail (8 carbon atoms) bearing an alkoxyamine reactive group at the *N*-terminus. This peptide precursor readily reacts with a hydrophobic aldehyde tail, $\mathbf{T_8}$ (octanal) to generate *in situ* the self-assembling peptide amphiphile, $\mathbf{P_{C8}T_8}$, through a stable oxime connection. This amphiphile is composed of two anionic glutamic acids, a short β-sheet-inducer sequence (two alanine and two valine residues) and an aliphatic chain at the *N*-terminus, which are crucial to $\mathbf{P_{C8}T_8}$ supramolecular polymerization. Thanks to Thioflavin T fluorimetry assay and CD measurements, we could confirm the co-assembly of $\mathbf{P_{C8}T_8}$ with its precursors, which resulted in a physically autocatalyzed process that accelerates the reaction and thus the microfibres formation. Hierarchical supramolecular polymerization of the individual nanofibres lead to the formation of microfibrillar bundles. The $\mathbf{P_{C8}}$ peptide precursor was then confined inside aqueous droplets of a water-in-oil (w/o) emulsion to test whether the reaction and subsequent self-assembly would tolerate an additional interfacial boundary. $\mathbf{T_8}$ was added outside in the external media, and fibrillation was observed as $\mathbf{T_8}$ diffuse across the oil and partitions into aqueous droplets. The reaction profile under confinement showed the same physically autocatalyzed behaviour. Intriguingly, as the fibrillar networks grew longer and bundled together, fibres reorganized spatially from the core to the cortex of the water droplets. Free-floating $\mathbf{P_{C8}T_8}$ fibres, in random motion due to molecular thrust during self-assembly, tend to accumulate at droplet boundaries with high local concentration of $\mathbf{P_{C8}T_8}$ monomers (*vide* infra surface tension assay), which should drive their elongation and bundling into larger assemblies at droplet edges. Once fibrillation process was confirmed inside droplets, we focused our attention on the potential consequences that these coupled chemical and physical processes could have on the droplets. It was observed that, after fibrillation, droplets in proximity tended to maximize their physical contact with other droplets and showed stochastic

coalescence events that mixed the internal content of the fused droplets, which was assigned to the bundling of $\mathbf{P_{C8}T_8}$ fibrillar networks at the cortex of adjacent droplets. To further explore the interaction of droplets with their environment, the fibrillation process was studied in the presence of exogenous fluorescent probes possessing different physicochemical properties. Pixel intensity analysis allowed the estimation of dye uptake, revealing higher uptake values for more cationic dyes, according to negative nature of the fibres: Hoechst ~ Rhodamine 6G > Rhodamine B > TAMRA (56% ~ 52% > 18% > 5% uptake). Also, cationic dyes (*i.e.*, Rhodamine 6G and Hoechst) induce fusion into larger droplet populations after anionic fibrillation, supporting the electrostatic foundation of fibrillar functionality. Being able to trigger molecular uptake by confined supramolecular fibrillation, the possibility of inducing contact-based exchange of cargoes between droplet populations was envisioned, as the preferential accumulation of fibrillar bundles at the interface between contacting droplets would generate tight contacts between neighbouring droplets to maintain their association and promote content exchange. This hypothesis was confirmed through a two-step enzymatic cascade incorporated into droplets, making substrate and product exchange between droplet populations necessary to generate a fluorogenic reporter at the end of the biocatalytic pathway. These results show that minimalistic 1D supramolecular polymerization could have played a role in the functional mechanisms that individual aqueous entities may have used to interact with their environment and within communities. In general, these findings will aid in advancing the foundational comprehension and structural creation of intricate 1D supramolecular biomimetic assemblies. Furthermore, they will play a pivotal role in shaping the future landscape of novel 1D functional materials, imbued with lifelike attributes and responsive behaviour to external stimuli.

In the second system, new fluorescent probes that change their fluorescence with pH were synthetized. Moreover, their response to the whole cellular pH range was optimized, allowing to precisely identify the pH of even the more acidic compartments, which is not possible with currently existing probes. The main examples of pH fluorescent probes for biological purposes are: fluorescent proteins, quantum dots and organic fluorophores, with widely employed small-molecule fluorescent probe families like coumarins, naphtalimides, xanthenes, BODIPYs and cyanines. However, for the purpose of precise cellular pH tracking in organelles or during endocytic pathway, ratiometric pH sensing fluorophores result the most appropriated. Ratiometric pH sensing fluorophores have two differentiated emission or absorbance bands depending on the pH, which allows to use two wavelengths at the same time to record fluorescence and, consequently, pH. This property makes possible to perform a self-calibration, avoiding potential errors induced by dilution or quenching, giving more accurate results. Apart from ratiometric behaviour, there are other fluorophore functional requirements for biological purposes, like their pK_a value, NIR emission, compatibility with single-molecule localization microscopy, compatibility with two-photon fluorescence and intracellular organelle targeting. In this second chapter, we selected **C.SNARF-1** ratiometric pH sensitive fluorophore for further optimization for cellular pH tracking purposes. **C.SNARF-1** presents a high production cost, being commercially available just as an isomeric mixture of its two positional isomers (**C5.SNARF-1** and **C6.SNARF-1**) and in milligrams scale. Therefore, these synthetic limitations hinder the attachment of these probes to potential drugs or molecular target molecule with biological interest, and the pH tracking of the resulting hybrid inside cells. Moreover, the pK_a of this probe, around 7.5, is too high to precisely report on the pH of the most acidic intracellular regions such as late endosomes, which pH can reach values close to 5.0. Consequently, the precise tracking of the pH along the endocytic pathway can be limited. In order to improve this **C.SNARF-1** limitations, we designed a short synthesis based on previously reported routes towards the SNARF core, consisting in two synthetic steps. First, 3-dimethylaminophenol (3-DMAP) is reacted with trimellitic anhydride (TMA) in toluene to obtain a mixture of the two intermediate positional isomers **5** and **6**. These two compounds are used without further purifications in the second and last synthetic step, the reaction with 1,6-dihydroxynaphtalene to directly obtain the mixture of the two positional isomers of **C.SNARF-1**. Following this route, it was possible to obtain **C.SNARF-1** mixture with an overall yield of 45 % and scaled up to 1 gram scale. Based on this **C.SNARF-1** synthesis, the next step was to optimize chromatographic methods to allow the separation of the two isomers, **C5.SANRF-1** and **C6.SNARF-1**. Thus, from the mixture of intermediate positional isomers **5** and **6**, compound **5** was isolated by precipitation, while compound **6** was isolated after 2 consecutive chromatographic columns. Isolated **5** and **6** were individually employed to give **C5.SNARF-1** and **C6.SNARF-1** with 11 % and 6 % overall yield, respectively. Once **C5.SNARF-1** and **C6.SNARF-1** were obtained, their photophysical characterization was performed. Although both show **C.SNARF-1** characteristic acidic (584 nm) and basic bands (633 nm), **C5.SNARF-1** have shown quenched basic band. Also, regarding their pK_a, differences were not found, showing both a value around 7.5 (7.66 and 7.65, respectively). With **C.SNARF-1** and its isomers already isolated and properly studied, the next step was to try to improve its pK_a, as it should be lower to allow the precise measurement of pH in the most acidic late steps of the endocytic pathway. Thus, we designed the synthesis of new fluorinated derivatives of **C5.SNARF-1** and **C6.SNARF-1** with fluorine in xanthene position 2, which were not previously described. Employed synthetic route is based on **C5.SNARF-1** and **C6.SNARF-1** route, but with additional steps required for the preparation of 7-fluoronaphthalene-1,6-diol, which substitutes 1,6-dihydroxynaphtalene in the last reaction of the previous route. 7-fluoronaphthalene-1,6-diol is prepared carrying out 4 steps that lead to the introduction of a fluorine atom selectively in the position 7 of the naphthalene ring, with a final yield of 18 %. Thus, compounds **C5.SNARF-2F** and **C6.SNARF-2F**, were obtained with overall yields of 2 % and 3 %, respectively. Then, photophysical studies of **C5.SNARF-2F** and **C6.SNARF-2F** were performed. Studied parameters have shown important differences compared to their non-fluorinated versions. First, a shift in the position of acidic and basic band has been observed. Basic band shift was of few nanometers, moving from 633 to 627 nm. However, basic band moves more than 30 nm, from 584 to 550 nm. Moreover, basic band seems quenched compared to non-fluorinated probes, especially in the case of C5 isomer, which could be related with stacking or electronic effects. Same phenomenon was previously described in other fluorinated SNARFs. Regarding their pK_a values, they have shown values of 6.16 and 6.21 for **C5.SNARF-2F** and **C6.SNARF-2F**, respectively. Consequently, **C.SNARF-1** pK_a was optimized, reaching a reduction of close of 1.5 units of pK_a, which was one of the main objectives of this PhD chapter. Thus, **C5.SNARF-2F** has appeared as the **C.SNARF-1** derivative with lower pK_a value reported, which make it very promising as an optimized ratiometric probe for drug tracking during endocytic pathway, among other biological purposes. Finally, a derived structure of **C.SNARF-2F** with 4 fluorine atoms in the lower aromatic ring, **SNARF-F-2F**, has been synthesized for the first time. For the synthesis of **SNARF-F-2F**, a similar route to that employed for **C.SNARF-2F** derivatives synthesis have been employed, but substituting trimellitic anhydride by 4,5,6,7-tetrafluoroisobenzofuran-1,3-dione in the first reaction. The product of this first reaction is 2-(4-(dimethylamino)-2-hydroxybenzoyl)-3,4,5,6-tetrafluorobenzoic acid, which limits the presence of two positional isomers, and just affording, after the second reaction, the desired **SNARF-F-2F**. The overall yield of this synthetic procedure was 5 %. Regarding its photophysical characterization, it has shown less ratiometric behaviour than the other studied probes along this chapter, and not changes in the pK_a value compared to **C.SNARF-2F** isomers. The results obtained during this chapter have allowed to improve **C.SNARF-1** synthesis to 1 gram scale, to obtain and characterize **C5.SNARF-1** and **C6.SNARF-1** isolated isomers, and to synthesize new fluorinated derivatives for the first time, obtaining **C5.SNARF-2F** as a promising optimized ratiometric probe present in the literature for drug tracking during endocytic pathway.

In the third case, Section affected by confidentiality: under the protection of rights.

Resumo

Neste manuscrito abordamos o desenvolvemento de novos sistemas supramoleculares funcionais desde unha perspectiva química e co obxectivo de modificar ou replicar funcións celulares. A principal forza impulsora e vínculo de unión entre os sistemas desenvoltos ao longo desta tese de doutoramento é o carácter dinámico da súa capacidade de resposta a estímulos, o cal é crucial para o seu comportamento funcional específico.

No primeiro caso, abordouse un sistema de protofilamentos artificial mimético dun citoesqueleto, utilizando un sistema fibrilar peptídico supramolecular. A comunidade científica estudou estratexias supramoleculares sintéticas como esta, nas que substitutos artificiais poden moldear a súa propia estrutura e, por tanto, catalizar fisicamente a súa propia síntese, o que demostra un gran potencial para a súa aplicación en biomedicina e nanofabricación branda. Caracterízanse pola súa inspiración biolóxica e tamén polo seu potencial para autoensamblarse en arquitecturas xerárquicas supramoleculares. Baseándose en estratexias ascendentes, estudouse a reconstrución artificial de diferentes lípidos biomiméticos anfifílicos e materiais similares a lípidos no contexto da compartimentación biomimética e a autopoiesis. Con todo, sábese moi pouco sobre a funcionalidade potencial derivada da autoensamblaxe provocada químicamente de redes fibrilares anfifílicas dentro de compartimentos acuosos. A posible consecuencia funcional dos polímeros supramoleculares unidimensionales en confinamento podería ser de interese para comprender, utilizando un sistema sintético simple, a importancia das entidades temperás de tipo citoesquelético nas primeiras entidades celulares. Inspirados pola importancia do efecto hidrofóbico, decidimos estudar a autoensamblaxe anfifílica de precursores de péptidos inactivos desencadeada por unha reacción química (por exemplo, conexión oxima) dentro das pingas de auga. Estes experimentos permiten o estudo de redes supramoleculares unidimensionais baixo confinamento e os seus efectos potenciais sobre as propiedades funcionais das pingas e as súas interaccións co medio ambiente. Empregamos un precursor peptídico que non se ensambla, **PC$_8$**, que consiste nun fragmento peptídico curto e aniónico (EEAAVV) equipado cunha cola alifática curta (8 átomos de carbono) que leva un grupo reactivo alcoxiamina no extremo *N*. Este péptido precursor reacciona facilmente cunha cola de aldehido hidrófobo, **T$_8$** (octanal) para xerar *in situ* o péptido anfífilo autoensamblable, **PC$_8$T$_8$**, a través dunha conexión de oxima estable. Este anfifilo está composto por dous ácidos glutámicos aniónicos, unha secuencia indutora de folla β curta (dous residuos de alanina e dous de valina) e unha cadea alifática no extremo *N*, que son cruciais para a polimerización supramolecular de **PC$_8$T$_8$**. Grazas ao ensaio de fluorimetría de tioflavina T e ás medicións de CD, puidemos confirmar a coensamblaxe de **PC$_8$T$_8$** cos seus precursores, o que resultou nun proceso fisicamente autocatalizado que acelera a reacción e, por tanto, a formación de microfibras. A polimerización supramolecular xerárquica das nanofibras individuais conduce á formación de fas de microfibras. Logo, o precursor do péptido **PC$_8$** confinouse dentro de gotiñas acuosas dunha emulsión de auga en aceite para probar se a reacción e a posterior autoensamblaxe tolerarían un límite interfacial adicional. Engadiuse **T$_8$** no medio externo e observouse fibrilación a medida que **T$_8$** se difunde a través do aceite e se divide entre as gotiñas acuosas. O perfil de reacción baixo confinamento mostrou o mesmo comportamento fisicamente autocatalizado. Curiosamente, a medida que as redes fibrilares creceron e se agruparon, as fibras reorganizáronse espacialmente desde o núcleo ata a cortiza das pingas de auga. As fibras de **PC$_8$T$_8$** que flotan libremente, en movemento aleatorio debido ao empuxe molecular durante a autoensamblaxe, tenden a acumularse nos límites das pingas cunha alta concentración local de monómeros de **PC$_8$T$_8$** (observado no ensaio de tensión infrasuperficial), o que debería impulsar a súa elongación e agrupación en conxuntos máis grandes nos bordes das pingas. Unha vez que se confirmou o proceso de fibrilación dentro das gotiñas, centramos

a nosa atención nas posibles consecuencias que estes procesos químicos e físicos axustados poderían ter nas pingas. Observouse que, despois da fibrilación, as pingas próximas tendían a maximizar o seu contacto físico con outras pingas e mostraban eventos de coalescencia estocástica que mesturaban o contido interno das pingas fusionadas, que se asignou ao agrupamento de redes fibrilares **PC_8T_8** na cortiza das pingas adxacentes. Para explorar máis a fondo a interacción das pingas coa súa contorna, estudouse o proceso de fibrilación en presenza de sondas fluorescentes exóxenas que posúen diferentes propiedades fisicoquímicas. A análise da intensidade dos píxeles permitiu estimar a absorción de colorante, revelando valores de absorción máis altos para os colorantes máis catiónicos, segundo a natureza negativa das fibras: Hoechst ~ Rodamina 6G > Rodamina B > TAMRA (56% 52% > 18% > 5% de absorción). Ademais, os colorantes catiónicos (é dicir, Rodamina 6G e Hoechst) inducen a fusión en poboacións de pingas máis grandes despois da fibrilación aniónica, o que apoia a base electrostática da funcionalidade fibrilar. Ao ser capaz de desencadear a captación molecular mediante fibrilación supramolecular confinada, imaxinouse a posibilidade de inducir o intercambio de cargas entre poboacións de gotiñas, xa que a acumulación preferente de fas fibrilares na interface entre gotiñas en contacto xeraría contactos estreitos entre gotiñas veciñas para manter a súa asociación e promover o intercambio de contidos. Esta hipótese confirmouse mediante unha fervenza encimática de dous pasos incorporada nas gotiñas, o que fixo necesario o intercambio de substrato e produto entre as poboacións de gotiñas para xerar un indicador fluoroxénico ao final da vía biocatalítica. Estes resultados mostran que a polimerización supramolecular unidimensional minimalista podería desempeñar un papel nos mecanismos funcionais que as entidades acuosas individuais poden utilizar para interactuar coa súa contorna e dentro das comunidades. En xeral, estes achados axudarán a avanzar na comprensión fundamental e a creación estrutural de complexos conxuntos biomiméticos supramoleculares unidimensionais. Ademais, desempeñarán un papel fundamental na configuración do panorama futuro de novos materiais funcionais unidimensionais, dotados de atributos realistas e un comportamento receptivo a estímulos externos.

Na segunda aplicación sintetizáronse novas sondas fluorescentes que cambian a súa fluorescencia co pH. Ademais, optimizouse a súa resposta a todo o rango de pH celular, o que permitiu identificar con precisión o pH mesmo dos compartimentos máis acedos, o que non é posible coas sondas existentes actualmente. Os principais exemplos de sondas fluorescentes de pH con fins biolóxicos son: proteínas fluorescentes, puntos cuánticos e fluoróforos orgánicos, con familias de sondas fluorescentes de moléculas pequenas amplamente utilizadas, como cumarinas, naftalimidas, xantenos, BODIPY e cianinas. Con todo, para o seguimento preciso do pH celular en orgánulos ou durante a vía endocítica, os fluoróforos que detectan o pH ratiométrico resultan ser os máis apropiados. Os fluoróforos detectores de pH ratiométricos teñen dúas bandas de emisión ou absorbancia diferenciadas en función do pH, o que permite utilizar dúas lonxitudes de onda ao mesmo tempo para rexistrar a fluorescencia e, en consecuencia, o pH. Esta propiedade permite realizar unha autocalibración, evitando posibles erros inducidos por dilución ou arrefriado, dando resultados máis precisos. Ademais do comportamento ratiométrico, existen outros requisitos funcionais dos fluoróforos para fins biolóxicos, como o seu valor de pK_a, emisión NIR, compatibilidade con microscopía de localización de molécula única, compatibilidade con fluorescencia de dous fotóns e orientación a orgánulos intracelulares. Neste segundo capítulo, seleccionamos o fluoróforo ratiométrico sensible ao pH **C.SNARF-1** para unha maior optimización con fins de seguimento do pH celular. **C.SNARF-1** presenta un alto custo de produción, estando dispoñible comercialmente só como unha mestura isomérica dos seus dous isómeros posicionais (**C5.SNARF-1** e **C6.SNARF-1**) e en escala de miligramos. Por tanto, estas limitacións sintéticas dificultan a unión destas sondas a posibles fármacos ou moléculas diana moleculares con interese biolóxico, e o seguimento do pH do híbrido resultante dentro das células. Ademais, o pK_a desta sonda, ao redor de 7,5, é demasiado alto para informar con precisión o pH das rexións intracelulares máis acedas, como os endosomas tardíos, cuxo pH pode alcanzar valores próximos a 5,0. En consecuencia, o seguimento preciso do pH ao longo da vía endocítica pode ser limitado. Para mellorar estas limitacións de **C.SNARF-1**, deseñamos unha breve síntese baseada en roteiros previamente descritos cara ao núcleo de SNARF, que consta de dous pasos sintéticos. Primeiro, faise reaccionar 3-dimetilaminofenol (3-DMAP) con anhídrido trimelítico (TMA) en tolueno para obter unha mestura dos dous isómeros posicionais intermedios 5 e 6. Estes dous compostos úsanse sen purificacións adicionais no segundo e último paso sintético, a reacción con 1,6-dihidroxinaftaleno para obter directamente a mestura dos dous isómeros posicionais de **C.SNARF-1**. Seguindo este roteiro, foi posible obter a mestura **C.SNARF-1** cun rendemento global do 45 % e escalado ata 1 gramo. A partir desta síntese de **C.SNARF-1**, o seguinte paso foi optimizar os métodos cromatográficos para permitir a separación dos dous isómeros, **C5.SANRF-1** e **C6.SNARF-1**. Así, da mestura de isómeros posicionais intermedios **5** e **6**, illouse o composto **5** mediante precipitación, mentres que o composto **6** illouse despois de 2 columnas cromatográficas consecutivas. Os illados **5** e **6** empregáronse individualmente para dar **C5.SNARF-1** e **C6.SNARF-1** cun rendemento total do 11 % e 6 %, respectivamente. Unha vez obtidos **C5.SNARF-1** e **C6.SNARF-1** procedeuse á súa caracterización fotofísica. Aínda que ambos mostran bandas acedas (584 nm) e básicas (633 nm) características de **C.SNARF-1**, **C5.SNARF-1** mostrou unha banda básica apagada. Así mesmo, en canto ao seu pK_a non se atoparon diferenzas, mostrando ambos un valor ao redor de 7,5 (7,66 e 7,65, respectivamente). Con **C.SNARF-1** e os seus isómeros xa illados e adecuadamente estudados, o seguinte paso foi tentar mellorar o seu pK_a, xa que debería ser menor para permitir a medición precisa do pH nos últimos pasos máis acedos da vía endocítica. Así, deseñamos a síntese de novos derivados fluorados de **C5.SNARF-1** e **C6.SNARF-1** con flúor na posición 2 do xanteno, os cales non foron descritos previamente. O roteiro sintético empregada baséase na roteiro de **C5.SNARF-1** e **C6.SNARF-1**, pero requírense pasos adicionais para a preparación de 7-fluoronaftaleno-1,6-diol, que substitúe ao 1,6-dihidroxinaftaleno na última reacción do roteiro anterior. O 7-fluoronaftaleno-1,6-diol prepárase realizando 4 pasos que conducen á introdución selectiva dun átomo de flúor na posición 7 do anel de naftaleno, cun rendemento final do 18 %. Así, obtivéronse o compostos **C5.SNARF-2F** e **C6.SNARF-2F** con rendementos globais do 2 % e 3 %, respectivamente. Logo, realizáronse estudos fotofísicos de **C5.SNARF-2F** e **C6.SNARF-2F**. Os parámetros estudados mostraron diferenzas importantes respecto ás súas versións non fluoradas. En primeiro lugar, observouse un cambio na posición da banda aceda e básica. O desprazamento de banda básica foi duns poucos nanómetros, pasando de 633 a 627 nm. Sen embargo, a banda básica móvese máis de 30 nm, desde 584 a 550 nm. Ademais, a banda básica parece apagada en comparación coas sondas non fluoradas, especialmente no caso do isómero C5, o que podería estar relacionado con efectos electrónicos ou de apilamiento. O mesmo fenómeno describiuse previamente noutros SNARF fluorados. En canto aos seus valores de pK_a, mostraron valores de 6,16 e 6,21 para **C5.SNARF-2F** e **C6.SNARF-2F**, respectivamente. En consecuencia, optimizouse o pK_a de **C.SNARF-1**, alcanzando unha redución próxima a 1,5 unidades de pK_a, que era un dos principais obxectivos deste capítulo de doutoramento. Por tanto, **C5.SNARF-2F** apareceu como o derivado de **C.SNARF-1** cun valor de pK_a máis baixo, o que o fai moi prometedor como sonda ratiométrica optimizada para o seguimento de fármacos durante a vía endocítica, entre outros fins biolóxicos. Finalmente, sintetizouse por primeira vez unha estrutura derivada de **C.SNARF-2F** con 4 átomos de flúor no anel aromático inferior, **SNARF-F-2F**. Para a síntese de **SNARF-F-2F** empregouse un roteiro similar ao empregado para a síntese de derivados de **C.SNARF-2F**, pero substituíndo o anhídrido trimelítico por 4,5,6,7-tetrafluoroisobenzofuran-1,3-diona na primeira reacción. O produto desta primeira reacción é o ácido 2-(4-(dimetilamino)-2-hidroxibenzoil)-3,4,5,6-tetrafluorobenzoico, que limita a presenza de dous isómeros posicionais, e proporciona unicamente, despois da segunda reacción, o **SNARF-F-2F** desexado. O rendemento global deste procedemento sintético foi do 5 %. En canto á súa caracterización fotofísica, mostrou un menor comportamento ratiométrico que o resto de sondas estudadas ao longo deste capítulo, e non presenta cambios no valor de pK_a respecto aos isómeros **C.SNARF-2F**. Os resultados obtidos durante este capítulo permitiron mellorar a síntese de **C.SNARF-1** a escala de 1 gramo, obter e caracterizar os isómeros illados **C5.SNARF-1** e **C6.SNARF-1**, e sintetizar por primeira vez novos derivados fluorados, obtendo **C5.SNARF-2F** como unha sonda ratiométrica prometedora optimizada das presente na literatura para o seguimento de fármacos durante a vía endocítica.

No terceiro caso, Sección afectada por confidencialidade: baixo protección de dereitos.

Introduction

Organic chemistry research is a broad field which try to understand and expand the knowledge related to molecules containing carbon atoms. It is precisely in carbon molecules in which life is based, so organic chemistry and biology, pharmacy or even medicine research are well related to each other. This interface between chemistry and biology is the frame of this PhD work, which is focused on the development of functional systems for cells and protocells, by combining rational design and new supramolecular concepts.

The field of supramolecular chemistry introduces significant advantages in the creation of complex organic structures. The formation of covalent bonds might result more laborious and time-consuming than the establishment of supramolecular interactions, which offers a suitable alternative exploiting non-covalent and reversible interactions. These interactions endow supramolecular systems with remarkable reversibility, allowing the desired dissociation and reassociation of complex structures. Moreover, supramolecular systems can exhibit an adaptive behaviour in response to external stimuli, broadening their applications and enhancing their functionality as sensitive systems. Apart from a sensitive behaviour, supramolecular systems can enable the assembly of macromolecular architectures with controlled size and shape, and precise alignment of functional groups in the three-dimensional space.

In this PhD work, we aim to apply them to different cell and protocell fields: amphiphilic self-assemblies for protocellular study, fluorescent probes for cellular compartments identification and new pH sensitive strategies for venom-derived antitumoral drugs.

The state-of-the-art of these three fields will be analysed along this introduction.

Field 1: Amphiphilic self-assemblies for protocellular study

1. Supramolecular chemistry and Tubular Assemblies

Supramolecular chemistry is the area of chemistry that studies the non-covalent interactions between molecules to create complex systems from simple monomers.[1,2] Supramolecular chemistry is, therefore, focused in the study of the type and strength of intermolecular interactions such as H-bonding, dipole-dipole interactions, van der Waals interactions, π-π interactions, and some others.[3] Jean-Marie Lehn is considered one of the fathers of Supramolecular Chemistry, and he was awarded with the Nobel Prize in Chemistry in 1987[4] together with Donald J. Cram[5] and Charles J. Pedersen.[6] Supramolecular chemistry is actually inspired in nature, where complex structures and functions are possible thanks to non-covalent assemblies and self-assembly, where a single molecule can guide the ordering of

---

[1] Lehn, J. M. Towards Complex Matter: Supramolecular Chemistry and Self-Organization. *Eur. Rev.* **2009**, *17* (2), 263–280.

[2] Lehn, J. M. Supramolecular Chemistry: Where from? Where To? *Chem. Soc. Rev.* **2017**, *46* (9), 2378–2379.

[3] Steed, J. W.; Turner, D. R.; Wallace, K. *Core Concepts in Supramolecular Chemistry and Nanochemistry*; Wiley: Hoboken, NJ, 2007.

[4] Lehn, J. M. Supramolecular Chemistry-Scope and Perspectives Molecules, Supermolecules, and Molecular Devices (Nobel Lecture). *Angew. Chem. Int. Ed.* **1988**, 27 (1), 89–112.

[5] Cram, D. J. The Design of Molecular Hosts, Guests, and Their Complexes (Nobel Lecture). *Angew. Chem. Int. Ed.* **1988**, *21* (3), 155–173.

[6] Pedersen, C. J. The Discovery of Crown Ethers (Noble Lecture). *Angew. Chemie Int. Ed.* **1988**, *27* (8), 1021–1027.

thousands,[7] or host-guest interactions, such as ligands in enzymatic active sites.[8] Chemists try understand and in apply these lessons from Nature to design different artificial supramolecular systems.

1.1.Synthetic supramolecular strategies towards tubular systems

Different synthetic strategies try to develop artificial surrogates that mimic nature's biomolecules structure and function.[9-13] In particular, synthetic one-dimensional (1D) supramolecular biomaterials have shown great potential for their application in biomedicine and soft nanofabrication.[14] Some of these synthetic materials imitate the hierarchical self-assembly of biological building blocks across orders of magnitude in length, spanning from short nanotubes to microfibrillar networks.[15,16] This hierarchical assembly amplifies the intramolecular and intermolecular non-covalent contacts along the resulting longitudinal assemblies.[17-20] Recent examples of such synthetic fibrillar biomaterials have demonstrated how these multivalent interactions can be used to transduce the hierarchical self-assembly of molecular entities into the macroscopic forces required to transform the size, shape and functional behaviour of soft matter.[12,21] One important work that exemplified this molecular to macroscopic transduction is the DNA-based nanomachine (Figure 1), which is actually inspired in natural virus-like assemblies, where a DNA helicity change is externally manifested in its artificial coating.[22]

---

[7] Mendes, A. C.; Baran, E. T.; Reis, R. L.; Azevedo, H. S. Self-Assembly in Nature: Using the Principles of Nature to Create Complex Nanobiomaterials. *Wiley Interdiscip. Rev. Nanomedicine Nanobiotechnology* **2013**, *5* (6), 582–612.

[8] Monod, J.; Changeux, J. P.; Jacob, F. Allosteric Proteins and Cellular Control Systems. *J. Mol. Biol.* **1963**, *6* (4), 306–329.

[9] Kim, H.-J.; Kim, T.; Lee, M. Responsive Nanostructures from Aqueous Assembly of Rigid−Flexible Block Molecules. *Acc. Chem. Res.* **2011**, *44* (1), 72–82.

[10] Danial, M.; Tran, C. M.-N.; Young, P. G.; Perrier, S.; Jolliffe, K. A. Janus Cyclic Peptide–Polymer Nanotubes. *Nat. Commun.* **2013**, *4* (1), 2780–2793.

[11] Krieg, E.; Bastings, M. M. C.; Besenius, P.; Rybtchinski, B. Supramolecular Polymers in Aqueous Media. *Chem. Rev.* **2016**, *116* (4), 2414–2477.

[12] Shimizu, T.; Ding, W.; Kameta, N. Soft-Matter Nanotubes: a Platform for Diverse Functions and Applications. *Chem. Rev.* **2020**, *120* (4), 2347–2407.

[13] Lancia, F.; Ryabchun, A.; Katsonis, N. Life-Like Motion Driven by Artificial Molecular Machines. *Nat. Rev. Chem.* **2019**, 3 (9), 536–551.

[14] Radvar, E.; Azevedo, H. S. Supramolecular Peptide/Polymer Hybrid Hydrogels for Biomedical Applications. *Macromol. Biosci.* **2018**, *19*, 1800221.

[15] Huang, Z.; Kang, S. K.; Banno, M.; Yamaguchi, T.; Lee, D.; Seok, C.; Yashima, E.; Lee, M. Pulsating Tubules from Noncovalent Macrocycles. *Science* **2012**, *337* (6101), 1521–1526

[16] Insua, I.; Montenegro, J. 1D to 2D Self Assembly of Cyclic Peptides. *J. Am. Chem. Soc.* **2020**, *142* (1), 300–307.

[17] Yagai, S.; Kitamoto, Y.; Datta, S.; Adhikari, B. Supramolecular Polymers Capable of Controlling Their Topology. *Acc. Chem. Res.* **2019**, *52* (5), 1325–1335.

[18] Ogi, S.; Sugiyasu, K.; Manna, S.; Samitsu, S.; Takeuchi, M. Living Supramolecular Polymerization Realized Through a Biomimetic Approach. *Nat. Chem.* **2014**, *6* (3), 188–195.

[19] Vázquez-González, V.; Mayoral, M. J.; Chamorro, R.; Hendrix, M. M. R. M.; Voets, I. K.; González-Rodríguez, D. Noncovalent Synthesis of Self-Assembled Nanotubes through Decoupled Hierarchical Cooperative Processes. *J. Am. Chem. Soc.* **2019**, *141* (41), 16432–16438.

[20] Chatterjee, A.; Mahato, C.; Das, D. Complex Cascade Reaction Networks Via Cross β Amyloid Nanotubes. *Angew. Chem. Int. Ed.* **2021**, *60* (1), 202–207.

[21] Insua, I.; Montenegro, J. Synthetic Supramolecular Systems in Life-like Materials and Protocell Models. *Chem* **2020**, *6* (7), 1652–1682.

[22] Kim, Y.; Li, H.; He, Y.; Chen, X.; Ma, X.; Lee, M. Collective Helicity Switching of a DNA-Coat Assembly. *Nat. Nanotechnol.* **2017**, *12* (6), 551–556.

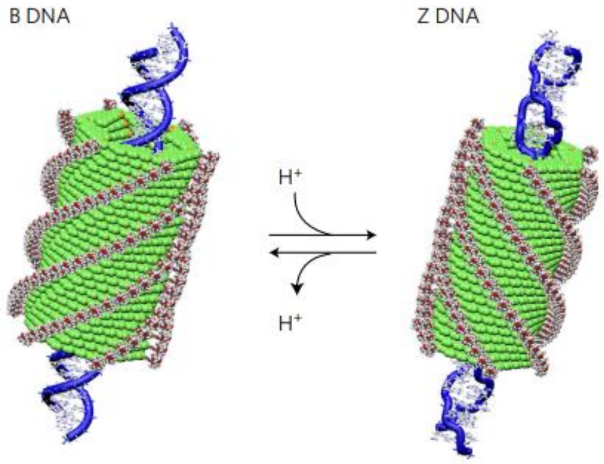

Figure 1. Collective helicity switching, first triggered in DNA helix, and transduced to its external artificial coating. [Adapted with permissions][22]

In addition, new bottom-up strategies are being developed for the artificial reconstruction of different biomimetic tubular and fibrillar materials.[21-24] For example, the rheological properties of the cellular matrix have been recently mimicked, even with spatial resolution[25,26] by hydrogelation of amphiphilic peptide nanotubes inside aqueous microdroplets.[27,28] 1D conductive supramolecular polymers, composed of artificial amino acids, can be prepared *in situ* in aqueous media by coupling a biocatalytic reaction with monomer nucleation and elongation processes.[29] Photo-responsive tubular assemblies, also made from synthetic amphiphiles in aqueous media, can encapsulate short nucleotides and control their duplex binding upon external light sources.[30] Exchange of chemical information[31] between water droplets has been recently achieved using semipermeable membranes of amphiphilic triblock copolymers.[32]

In most of these synthetic assemblies, the hydrophobic effect constitutes a primary and ubiquitous driving force in aqueous media required to build ordered ensembles, such as

---

[23] Ruiz-Mirazo, K.; Briones, C.; De La Escosura, A. Prebiotic Systems Chemistry: New Perspectives for the Origins of Life. *Chem. Rev.* **2014**, *114* (1), 285–366.

[24] Mattia, E.; Otto, S. Supramolecular Systems Chemistry. *Nat. Nanotechnol.* **2015**, *10* (2), 111–119.

[25] Spitzer, D.; Marichez, V.; Formon, G. J. M.; Besenius, P.; Hermans, T. M. Surface-Assisted Self-Assembly of a Hydrogel by Proton Diffusion. *Angew. Chem. Int. Ed.* **2018**, *57* (35), 11349–11353.

[26] Méndez-Ardoy, A.; Bayón-Fernández, A.; Yu, Z.; Abell, C.; Granja, J. R.; Montenegro, J. Spatially Controlled Supramolecular Polymerization of Peptide Nanotubes by Microfluidics. *Angew. Chemie* **2020**, *132* (17), 6969–6975.

[27] Kumar, R. K.; Harniman, R. L.; Patil, A. J.; Mann, S. Self-Transformation and Structural Reconfiguration in Coacervate-Based Protocells. *Chem. Sci.* **2016**, *7* (9), 5879–5887.

[28] Méndez-Ardoy, A.; Granja, J. R.; Montenegro, J. pH-Triggered Self-Assembly and Hydrogelation of Cyclic Peptide Nanotubes Confined in Water Micro-Droplets. *Nanoscale Horiz.* **2018**, *3* (4), 391–396.

[29] Kumar, M.; Ing, N. L.; Narang, V.; Wijerathne, N. K.; Hochbaum, A. I.; Ulijn, R. V. Amino-Acid-Encoded Biocatalytic Self-Assembly Enables the Formation of Transient Conducting Nanostructures. *Nat. Chem.* **2018**, *10* (7), 696–703.

[30] Kameta, N.; Akiyama, H. Shrinkable Nanotubes for Duplex Formation of Short Nucleotides. *Small* **2018**, *14* (34), 1–6.

[31] Martin, N.; Douliez, J. P.; Qiao, Y.; Booth, R.; Li, M.; Mann, S. Antagonistic Chemical Coupling in Self-Reconfigurable Host–Guest Protocells. *Nat. Commun.* **2018**, *9* (1), 1–12.

[32] Estirado, E. M.; Mason, A. F.; Alemán García, M. Á.; Van Hest, J. C. M.; Brunsveld, L. Supramolecular Nanoscaffolds within Cytomimetic Protocells as Signal Localization Hubs. *J. Am. Chem. Soc.* **2020**, *142* (20), 9106–9111.

micelles, bilayers, duplexes, coiled-coils, etc.[16,33,34] However, beyond hydrophobicity, 1D anisotropic growth requires the additional contribution of hydrogen bonding and/or other directional noncovalent interactions that orient and stabilize the required supramolecular elongation in water.[16,35] Importantly, small differences in the number and/or position of these directional interactions are often sufficient to switch between different assemblies such as micelles, vesicles or fibres, with completely different supramolecular ordering and functional purposes.[36,37] For example, Watson and Crick pairing is responsible of natural DNA-B structure, and micellar nanotubes (Figure 2),[37] both occurring in water media using the hydrophobic effect as the major driving force for the assembly.[34] Over the past years, the importance of the hydrophobic effect for the synthesis and assembly transitions of artificial amphiphiles have been carefully studied in the context of biomimetic compartmentalization and autopoiesis.[38-41] Physical autocatalysis has also been confirmed as a fundamental mechanism that amplifies monomer synthesis and self-assembly in many of these amphiphilic encapsulating systems.[42,43] However, very little is known about the potential functionality derived from the chemically triggered self-assembly of amphiphilic fibrillar networks inside aqueous compartments.

---

[33] Chandler, D. Hydrophobicity: Two Faces of Water. *Nature* **2002**, *417* (6888), 491.

[34] Feng, B.; Sosa, R. P.; Mårtensson, A. K. F.; Jiang, K.; Tong, A.; Dorfman, K. D.; Takahashi, M.; Lincoln, P.; Bustamante, C. J.; Westerlund, F.; Nordén, B. Hydrophobic Catalysis and a Potential Biological Role of DNA Unstacking Induced by Environment Effects. *Proc. Natl. Acad. Sci. U.S.A.* **2019**, *116* (35), 17169–17174.

[35] Díaz, S.; Insua, I.; Bhak, G.; Montenegro, J. Sequence Decoding of 1D to 2D Self-Assembling Cyclic Peptides. *Chem. Eur. J.* **2020**, *26* (64), 14765–14770.

[36] Gilroy, J. B.; Gädt, T.; Whittell, G. R.; Chabanne, L.; Mitchels, J. M.; Richardson, R. M.; Winnik, M. A.; Manners, I. Monodisperse Cylindrical Micelles by Crystallization-Driven Living Self-Assembly. *Nat. Chem.* **2010**, *2* (7), 566–570.

[37] Aparicio, F.; Chamorro, P. B.; Chamorro, R.; Casado, S.; González-Rodríguez, D. Nanostructured Micelle Nanotubes Self-Assembled from Dinucleobase Monomers in Water. *Angew. Chem. Int. Ed.* **2020**, *132* (39), 17239–17244.

[38] Flores, J.; White, B. M.; Brea, R. J.; Baskin, J. M.; Devaraj, N. K. Lipids: Chemical Tools for Their Synthesis, Modification, and Analysis. *Chem. Soc. Rev.* **2020**, *49* (14), 4602–4614.

[39] Walde, P.; Wick, R.; Fresta, M.; Mangone, A.; Luisi, P. L. Autopoietic Self-Reproduction of Fatty Acid Vesicles. *J. Am. Chem. Soc.* **1994**, *116* (26), 11649–11654.

[40] Budin, I.; Debnath, A.; Szostak, J. W. Concentration-Driven Growth of Model Protocell Membranes. *J. Am. Chem. Soc.* **2012**, *134* (51), 20812–20819.

[41] Pottanam-Chali, S.; Ravoo, B. J. Polymer Nanocontainers for Intracellular Delivery. *Angew. Chem. Int. Ed.* **2020**, *59* (8), 2962–2972.

[42] Bissette, A. J.; Odell, B.; Fletcher, S. P. Physical Autocatalysis Driven by a Bond-Forming Thiol-Ene Reaction. *Nat. Commun.* **2014**, *5* (1), 4607–4614.

[43] Budin, I.; Devaraj, N. K. Membrane Assembly Driven by a Biomimetic Coupling Reaction. *J. Am. Chem. Soc.* **2011**, *134* (2), 751–753.

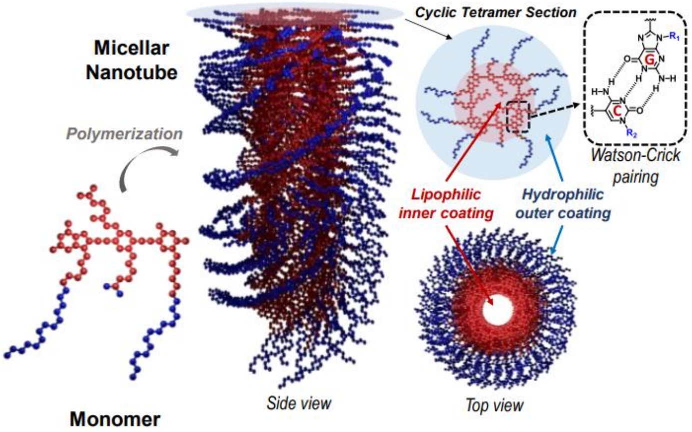

Figure 2. Micellar nanotube structure formed in water thanks to Watson and Crick base pairing. [Adapted with permissions][37]

Field 2: Fluorescent probes for cellular compartments identification

1. Fluorescence

Fluorescence is a photophysical phenomenon that some molecules can experiment and commonly observe in nature. Aurora borealis, also known as northern lights, is one of the most relevant examples. But also, hundreds of living beings emit fluorescence, being possible to find lots of examples in plants or animals, and existing, for instance, more than 180 different species of biofluorescent fishes.[44] The first example of fluorescence reported by humans was in 1595, when the Spanish Nicolás Monardes[45] described the blue fluorescence of *Lignum nephriticum* water solution. The wood of this Mexican tree was used for kidney illnesses by Azteca culture. However, it wasn’t until 300 years later when this physical phenomenon caused by the interaction with light was properly understood and explained.

From the chemical and physical point of view, fluorescence is a luminescence process. Luminescence is known as the emission of light in the UV, visible or IR region due to the relaxation of excited electrons. This name was first time employed in 1888 by the physicist E. Wiedemann with the aim of differentiate luminescence from other light emissions caused by an increase in temperature.[46] Apart from fluorescence, there is also another kind of luminescence process, which is phosphorescence. Although both phenomena have a lot of similarities, they are caused by different electronical transitions, showing therefore distinct observable behaviours. Moreover, there are another two luminescence categories: chemiluminescence and bioluminescence. In both cases, the emission of light is produced due to a chemical reaction, being inside a living organism in the second case.

When an electron in an electronic singlet ground state is excited by a source of light with enough energy, the electron will absorb a photon and ascend to an electronic singlet excited state. With this higher energy, the electron can undergo different processes, both of radiant and not radiant nature, in order to lose this excess of energy.[46,47] Jablonski diagrams (Figure 3) are

---

[44] Sparks, J. S.; Schelly, R. C.; Smith, W. L.; Davis, M. P.; Tchernov, D.; Pieribone, V. A.; Gruber, D. F. The Covert World of Fish Biofluorescence: A Phylogenetically Widespread and Phenotypically Variable Phenomenon. *PLoS One* **2014**, *9* (1): e83259.

[45] Acuña, A. U.; Amat-Guerri, F. Early History of Solution Fluorescence: The Lignum Nephriticum of Nicolás Monardes. In *Springer Series on Fluorescence*; Berberan-Santos, M. N., Ed.; Springer, 2007; Vol. 4, pp 3–20.

[46] Valeur, B. *Molecular Fluorescence: Principles and Applications*; Wiley-Vch: Weinheim; Cambridge, 2002.

[47] Lakowicz, J. R. *Principles of Fluorescence Spectroscopy*; Springer Science+Business Media: New York, 2010.

commonly used to represent these electronic transitions, making them more straightforward to understand and to explain.[48]

- Not radiant relaxation can be due to internal conversions and intersystem crossings. In the former, the electron is still in an electronic singlet excited state, but of less energy. Thus, it has moved to less energetic vibrational states of the electronic excited state, and then moved to other electronic states with less energy but the same spin. However, if it has moved to other excited states with not the same spin, we are observing an intersystem crossing. As both are not radiant, thermal dissipation is the common macroscopical manifestation.[47] Other not radiant processes could be energy transfer or solvent interactions, but they are special cases as other molecules of different nature should be present for them to occur.

- As radiant processes, we can differentiate between fluorescence and phosphorescence. When the electron is situated in the less energetic vibrational state of an electronic singlet excited state, it returns to the ground state emitting a photon and generating fluorescence. As the transition occurs between two singlet states, electronic spin change is not needed, being therefore an allowed and fast transition (half lifetimes in the order of nanoseconds). However, if the electron comes from a triplet excited state, the photon emission produces phosphorescence. In this case, the electron transition is not allowed as a switch in the electron spin is required, causing a slower process with longer half lifetimes.[47]

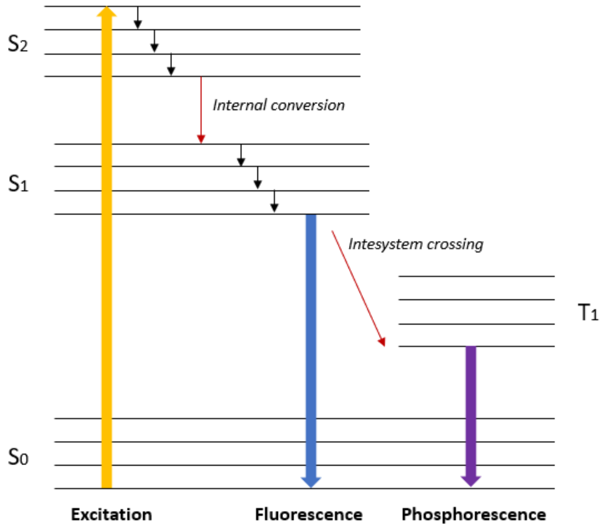

Figure 3. Jablonski diagram to illustrate different electronic transitions after electronic excitation.

Fluorescence emission has also some general characteristics which are important to completely understand the phenomenon:[47]

- The emitted photon is less energetic than the absorbed photon. This fact is called Stokes shift[49] and is caused by the internal conversions that the electron suffers in excited states, causing a loss of energy by not radiant phenomena. Once fluorescence occurs, the electron has less energy than the initially acquired with the irradiation. Thus, fluorescence emission will occur at higher wavelengths than excitation.

---

[48] Jabłoński, A. Über Den Mechanismus Der Photolumineszenz von Farbstoffphosphoren. *Z. Physik* **1935**, *94* (1-2), 38–46.

[49] Stokes, G. G. On the Change of Refrangibility of Light. *Philos. Trans. R. Soc. Lond.* **1852**, *142*, 463–562.

- The fluorescence emission is constant for a specie and independent of the energy of the excitation source, which is known as Kasha's rule.[50] Even if the electron absorbs more energy, it will lose it by different process, occurring always the fluorescence because of the photon emission between the same two energetic levels.

2. Fluorescence and fluorophores in biological applications

In the last decades, fluorescence has become an essential tool in biology and medicine applications. Fluorescence shows high sensitivity (allowing the visualization at micro or even nano concentration), good spatio-temporal resolution (making possible a detection in real-time), high biocompatibility and lack of invasiveness. Therefore, fluorescence is an appropriate technique for biological purposes with certain advantages.[51,52] Fluorescence has been used both in *in vitro* and *in vivo* experiments, and even in humans, being fluorescence imaging, detection of bioactive enzymes or enzymatic assays some examples that demonstrate its versatility.[53]

The chemical compounds that present fluorescence receive the name of fluorophores. There is a variety of them, and their fluorescent properties will depend on two important characteristics: quantum yields and fluorescence lifetimes. Quantum yield is the relation between the emitted photons and the absorbed photons. The more photons are lost by not radiant processes, the less bright will be the fluorescence and, therefore, the lower it will be the compound's quantum yield. The fluorescence lifetime gives an idea of the time that electrons expend in excited states before their return to the ground state. However, both parameters can be tuned trying to affect the rate between radiant and not radiant processes. For example, the presence of heavy atoms can cause lower values of both quantum yields and fluorescent lifetimes.[54] There are also some other important physical parameters that will be crucial depending on the specific application, as excitation and emission wavelengths, molar absorptivity coefficient or pK_a.

Regarding the nature of the fluorophores employed in the biological field, they can be classified in three different groups: organic fluorophores, fluorescent proteins and fluorescence quantum dots.

2.1. Organic fluorophores

Organic fluorophores, also named as small-molecule fluorescent probes (Figure 4), are one of the better options for bio-applications, as they are small (allowing a straightforward entrance in cells and low steric hindrance), chemically stable[55] and easy to synthesize and functionalize.[53]

In 1852 George G. Stokes was the first to understand and explain the existing relation between the absorption and emission of light processes, and coining the term "fluorescence".[49] A good example of a fluorophore in this category is quinine, which is the first defined molecule with fluorescence. Quinine's ability to emit light was described in 1845 by John F. W.

---

[50] Kasha, M. Characterization of Electronic Transitions in Complex Molecules. *Discuss. Faraday Soc.* **1950**, *9*, 14–19.

[51] Lang, W.; Yuan, C.; Zhu, L.; Du, S.; Qian, L.; Ge, J.; Yao, S. Q. Recent Advances in Construction of Small Molecule-Based Fluorophore-Drug Conjugates. *J. Pharm. Anal.* **2020**, *10* (5), 434–443.

[52] Terai, T.; Nagano, T. Small-Molecule Fluorophores and Fluorescent Probes for Bioimaging. *Pflugers Arch. Eur. J. Physiol.* **2013**, *465* (3), 347–359.

[53] Chen, Y.; Gao, Y.; He, Y.; Zhang, G.; Wen, H.; Wang, Y.; Wu, Q. P.; Cui, H. Determining Essential Requirements for Fluorophore Selection in Various Fluorescence Applications Taking Advantage of Diverse Structure-Fluorescence Information of Chromone Derivatives. *J. Med. Chem.* **2021**, *64* (2), 1001–1017.

[54] *"Quenching by halogen and heavy atoms occurs due to spin–orbit coupling and intersystem crossing to the triplet state"* (see Lakowicz, J. R. *Principles of Fluorescence Spectroscopy*; Springer Science+Business Media: New York, 2010).

[55] Lavis, L. D.; Raines, R. T. Bright Ideas for Chemical Biology. *ACS Chem. Biol.* **2008**, *3* (3), 142–155.

Herschel.[56] Although this molecule is widely known as it is present in tonic water, it also presents antimalarial properties. This medical use prompted chemists to work during decades to reach a quinine total synthesis.[57] Interestingly, the search process towards its total synthesis and the failing synthetic routes and attempts allowed the obtention of aniline-based textile dyes, which were very important during the first years of the chemical industry, at the end of the XIX century.[55]

After the discovery of quinine, plenty of other important natural molecules have been found to present fluorescence. This is the case of some amino acids as phenylalanine, tyrosine or tryptophan. The fluorescent properties of these natural amino acids were firstly published by G. Weber.[58] Tryptophan, naturally present in proteins, shows the highest fluorescence that is sensitive to environmental changes. Thus, the fluorescence of the tryptophan amino acid residue has been widely employed for protein folding determination.[59] Nicotinamide cofactors (for instance, NADH), porphyrins or flavins are other examples of fluorescent biomolecules. However, the presence of these natural fluorophores can cause a high level autofluorescence of biological tissues, which can hinder the visualization of exogenous probes.[55]

Commonly used molecular synthetic fluorescent cores include (Figure 4):[55,60]

- *Coumarins*: one of the well-known fluorophore families that can be easily prepared. With excitation wavelengths in the low UV region and low quantum yields that could hinder their applications in living systems.[61]

- *Naphtalimides*: robust fluorophores with brighter fluorescence than coumarins, although they normally show short wavelengths for both excitation and emission.

- *Xanthene dyes*: probably the most useful fluorescent molecular core that include two differentiated derivates families: fluoresceins and rhodamines. Their synthesis was first achieved in 1871 by Baeyer.[62] They are probably the brightest commonly used fluorophores with a widely spectrum of potential available wavelengths. However, their laborious synthetic routes and limited photostability due to oxidative degradation are their main drawbacks.

- *BODIPY*: their synthesis was reported for the first time in the late 60's. Their rigid molecular core, consisting in a disubstituted boron atom chelated by a dipyrromethene, is responsible for some of their most interesting properties. For example, they show a high quantum yield and high lipophilicity, which simplify their partition in cell membranes.[63]

---

[56] Herschel, J. F. W. On a Case of Superficial Colour Presented by a Homogeneous Liquid Internally Colourless. *Phil. Trans. R. Soc. London* **1845**, *135*, 143–145.

[57] Seeman, J. I. The Woodward-Doering/Rabe-Kindler Total Synthesis of Quinine: Setting the Record Straight. *Angew. Chem. Int. Ed.* **2007**, *46* (9), 1378–1413.

[58] Teale, F. W.; Weber, G. Ultraviolet Fluorescence of the Aromatic Amino Acids. *Biochem. J.* **1957**, *65* (3), 476–482.

[59] Royer, C. A. Probing Protein Folding and Conformational Transitions with Fluorescence. *Chem. Rev.* **2006**, *106* (5), 1769–1784.

[60] Fu, Y.; Finney, N. S. Small-Molecule Fluorescent Probes and Their Design. *RSC Adv.* **2018**, *8* (51), 29051–29061.

[61] Kumar, K. A.; Nagamallu, R.; Govindappa, V. K. Comprehensive Review on Coumarins : Molecules of Potential Chemical and Pharmacological Interest Comprehensive Review on Coumarins : Molecules of Potential Chemical and Pharmacological Interest. *J. Chem. Pharm. Res.* **2015**, *7* (9), 67–81.

[62] Baeyer, A. Die Drei Isomeren Reihen Wiireo Demnsch Nach Meinen Uebergangen. *Berichte der Dtsch. Chem. Gesellschaft* **1871**, *4* (2), 555–558.

[63] Loudet, A.; Burgess, K. BODIPY Dyes and Their Derivatives: Syntheses and Spectroscopic Properties. *Chem. Rev.* **2007**, *107* (11), 4891–4932.

- *Cyanines*: characterized by their polymethine chain, cyanines are very popular as they were one of the first fluorophores emitting in the red/NIR region. Although their quantum yields are commonly not very good (for instance, symmetrical Cy3 and Cy5 have quantum yields > 0.1,[64] while Alexa family members 555 and 647 present quantum yields of 0.1 and 0.33,[65] respectively), their high molar absorptivity coefficient makes them to become bright. However, they easily get photo-oxidated, which limits their use in experiments where long time irradiations are required.[66]

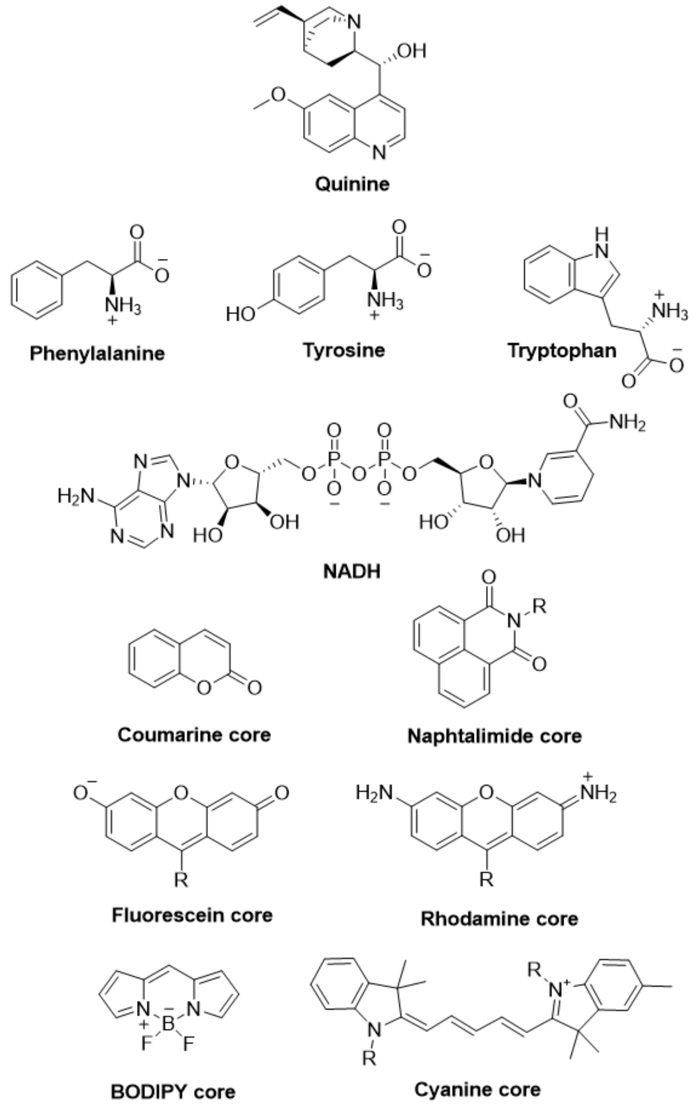

Figure 4. Most representative examples of organic fluorophores.

2.2. Fluorescent proteins

Fluorescent proteins have the ability to absorb and emit light following the physicochemical process of the fluorescence. The main advantage of this category of fluorophores compared to small organic dyes, is that they can be endogenously expressed in

---

[64] Silva, G. L.; Ediz, V.; Yaron, D.; Armitage, B. A. Experimental and Computational Investigation of Unsymmetrical Cyanine Dyes: Understanding Torsionally Responsive Fluorogenic Dyes. *J. Am. Chem. Soc.* **2007**, *129* (17), 5710–5718.

[65] Gebhardt, C.; Lehmann, M.; Reif, M. M.; Zacharias, M.; Gemmecker, G.; Cordes, T. Molecular and Spectroscopic Characterization of Green and Red Cyanine Fluorophores from the Alexa Fluor and AF Series. *ChemPhysChem* **2021**, *22* (15), 1566–1583.

[66] Shindy, H. A. Fundamentals in the Chemistry of Cyanine Dyes: A Review. *Dye. Pigment.* **2017**, *145*, 505–513.

living cells and used for labelling purposes. Fluorescent proteins can respond to a wider variety of signals and biological processes, they can also be modified to target specific cell organelles and to be introduced in more tissues and they don't suffer from photodynamic toxicity.[67]

The most important example of this class is the Green Fluorescent Protein (GFP). This protein was observed and isolated for the first time from the jellyfish A*equorea Victoria* in 1962. Protein structure consists in 238 amino acids arranged into a beta-barrel shape that protects and enhances the fluorescence of an embedded chromophore unit (Figure 3a). The chromophore is an imidazolinone dye produced from natural amino acid residues in an autocatalytic process (Figure 5a). GFP absorbs blue light (λ_{exc} of 365 nm) and emits green light (λ_{em} of 509 nm).[55,68] This protein has become one of the more important tools employed in bioscience, as it can be genetically encoded and linked to other natural proteins, allowing for the first time the intracellular tracking of fused fluorescent proteins. GFP has been modified generating a family of fluorescent protein variants with a diverse palette of fluorescent proteins where is possible to select almost a wide range of λ_{exc} and λ_{em} wavelengths. In fact, the discovery and development of the GFP was awarded in 2008 with the Nobel Prize in Chemistry to: Osamu Shimomura for first isolate and observe the fluorescence of the GFP,[69] Martin Chalfie for demonstrate the potential of GFP as a fluorescent genetic tag for multiple biological processes[68] and Roger Y. Tsien for contribute to the understanding of GFP ability to fluoresce and for generate a colour palette of GFP derivatives (Figure 5b).[70] Since this success, scientists have tried to find more fluorescent proteins in marine organisms, and although more than 30 different proteins have been already identified, just a few of them are completely characterized, such as the Red Fluorescein Protein (RFP), naturally present in coral.[67,71]

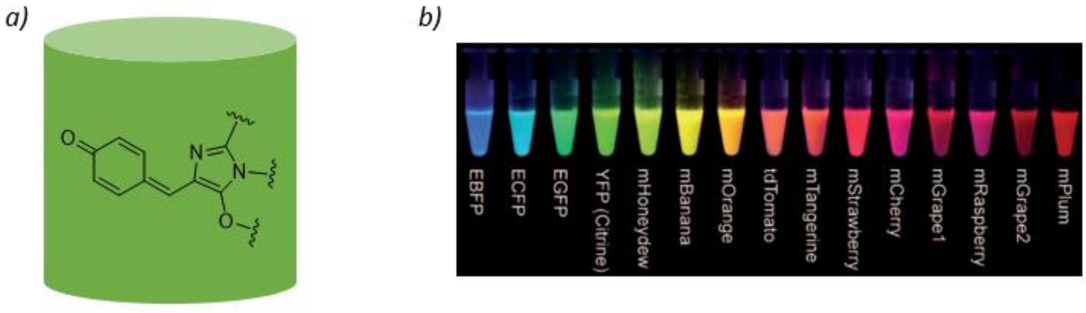

Figure 5. a) GFP diagram, with the imidazolinone chromophore embedded in a protein beta-barrel. b) Colour palette of GFP and RFP derivatives synthesized until 2004. [Adapted with permissions][71]

2.3. Quantum dots (QD)

Quantum dots (QD) are fluorescent semiconductor nanocrystals. They present a nanosized structure that will affect their fluorescent properties through quantum confinement, as their energy levels are quantized. Therefore, their fluorescent spectrum can be tuned by varying both their particle size and composition. When they have defects in their surface, quantum dots can undergo an electron or hole trap that prevents electron-hole recombination and fluorescent emission. This causes a reduction of quantum yield and an observable blinking

---

[67] Zhang, J.; Campbell, R. E.; Ting, A. Y.; Tsien, R. Y. Creating New Fluorescent Probes for Cell Biology. *Nat. Rev. Mol. Cell Biol.* **2002**, *3* (12), 906–918.

[68] Chalfie, M.; Tu, Y.; Euskirchen, G.; Ward, W. W.; Prasherf, D. C. Green Fluorescent Protein as a Marker for Gene Expression. *Science* **1994**, *263* (5148), 802–805.

[69] Shimorura, O.; Johnson, F. H.; Saiga, Y. Extraction, Purification and Properties of Aequorin, a Bioluminescent Protein from the Luminous Hydromedusan, Aequorea . *J. Cell. Comp. Physiol.* **1962**, *59* (3), 223–239.

[70] Tsien, R. Y. The Green Fluorescent Protein. *Annu. Rev. Biochem.* **1998**, *67* (1), 509–544.

[71] Tsien, R. Y. Constructing and Exploiting the Fluorescent Protein Paintbox (Nobel Lecture). *Angew. Chem. Int. Ed.* **2009**, *48* (31), 5612–5626.

effect that can be prevented by adding external layers made of a different material to increase the band gap and achieve quantum yields up to 90 %.[72] When comparing QDs with the two previous families of fluorophores, small organic dyes and fluorescent proteins, QDs commonly present better quantum yield values and higher photo stability. However, their use for biological purposes is hindered by their large size, colloidal behaviour, and their difficulties for passing through cell membranes as well as toxicity or precipitation issues.[73]

2.4. Fluorophores classification regarding labelling

Apart from previous classification of fluorescent probes by their chemical nature, we can also sort them according to their tagged counterparts:[46]

- *Intrinsic probes*: the molecule of interest present intrinsic fluorescence, such as the aromatic natural amino acids (e.g. tryptophan) previously mentioned in the category of organic fluorophores. However, this group is limited to a very few examples.

- *Extrinsic covalently bound probes*: a covalent bond is stablished between the molecules of interest and the fluorophore. This strong bond secures spatial localization and avoids dissociation in the biological medium. Amide bonds are commonly employed, to connect the amino groups of protein residues, and electrophilic functional groups of the fluorescent probes. The first example of extrinsic covalently bound probe employed was in 1942, linking the fluorophore fluorescein isothiocyanate (FITC) to an anti-pneumococcal antibody.[74] However, these covalent bonds can be difficult to obtain in selective protein positions in the aqueous media, which can hinder their biological applications.

- *Extrinsic associating probes*: as in the case of extrinsic covalently bound probes, an external fluorophore is needed but, in this case non-covalent specific interactions take place between probe and analyte. For instance, pyrene fluorophore accumulates in hydrophobic regions while pyranine in hydrophilic ones. Thus, probes sensitivity to specific environments can be exploited in this category. Although these fluorophores are straightforward to use, there is a risk of disturbing the specific area of the interaction and modify its chemical properties. To prevent it, fluorophores size and shape can be selected and optimized.

3. Cellular pH and fluorescent pH tracking

Fluorescent probes have been designed to sense and respond to environmental stimulus. One relevant aspect on biological mediums is pH such as in pH sensitive[75] or mechanosensitive[76] fluorescent probes. Cells achieve a precise spatiotemporal control of pH, which should be fixed to maintain the normal functioning of the cell machinery. In order to prevent abrupt pH changes that could be harmful for the organism, cells employ buffers formed by mixtures of weak acids and their conjugate bases such as the carbonic buffer (H_2CO_3/HCO_3^-). These biological buffers allow the maintenance of a constant and optimum pH

---

[72] Michalet, X.; Pinaud, F. F.; Bentolila, L. A.; Tsay, J. M.; Doose, S.; Li, J. J.; Sundaresan, G.; Wu, A. M.; Gambhir, S. S.; Weiss, S. Quantum Dots for Live Cells, in Vivo Imaging, and Diagnostics. *Science* **2005**, *307* (5709), 538–544.

[73] Li, H.; Vaughan, J. C. Switchable Fluorophores for Single-Molecule Localization Microscopy. *Chem. Rev.* **2018**, *118* (18), 9412–9454.

[74] Martynov, V. I.; Pakhomov, A. A.; Popova, N. V; Deyev, I. E.; Petrenko, A. G. Synthetic Fluorophores for Visualizing Biomolecules in Living Systems. *Acta Naturae* **2016**, *8* (4), 33–46.

[75] Méndez-Ardoy, A.; Reina, J. J.; Montenegro, J. Synthesis and Supramolecular Functional Assemblies of Ratiometric pH Probes. *Chem. Eur. J.* **2020**, *26* (34), 7516–7536.

[76] Colom, A.; Derivery, E.; Soleimanpour, S.; Tomba, C.; Molin, M. D.; Sakai, N.; González-Gaitán, M.; Matile, S.; Roux, A. A Fluorescent Membrane Tension Probe. *Nat. Chem.* **2018**, *10* (11), 1118–1125.

to keep biomolecules in the convenient protonated or deprotonated state.[77] Thus, pH is strictly regulated but not just for the cell as a whole, but also individually in each organelle. Organelles need a controlled pH for their function because protons participate in several metabolic reactions. Also, proton movements are critical for the generation and conversion of energy and transmission of nerve impulses.

In biological medium, pH buffering can be achieved by the intrinsic buffer effect of nucleic acid phosphate groups and acidic/basic proteins side chains, together with the pH regulation of the carbonic buffer. However, available molecules in each case are limited, and each organelle has different needs and require different strategies to maintain long-term pH homeostasis.[78]

Although pH value is always between 7.3 and 7.4 in extracellular environment, cytosolic pH is slightly more acidic (pH around 7.2). This is caused by two different phenomena that lead to a cytosolic tendency to acidification. Firstly, negatively charged anions of basic nature, such as HCO_3^-, tend to flow outside the cell due to existing electrical membrane potential. This cellular membrane potential causes a negative charge in the inner face of the membrane, which is responsible of negative molecules expulsion to the outer face. Secondly, certain metabolic reactions (e.g. ATP production through glycolysis or oxidative phosphorylation in mitochondria) generate acidic molecules. In order to correct this acidification tendency, proton pumps as ATPases and other ion carriers have an important role. Thanks to their action, H^+ are expelled out of the cells, preventing their excessive accumulation, while alkaline cations (mainly Na^+ and K^+) are transporter inside to balance the osmotic pressure. However, the mitochondria matrix has a pH around 8.0. This alkaline pH is critical for the correct function of the respiratory pathway. A more complicated situation occurs in the secretory pathway where the identification of protein sorting and processing occurs through protein-receptor interactions that are highly dependent on protonation states. Thus, on the endoplasmic reticulum, the pH value is closer to the cytosolic pH. In contrast, the *cis*-Golgi apparatus has a more acidic pH, around 6.7, and the *trans*-Golgi reaches 6.0. In the case of the secretory granules, the pH could even reach pH values close to 5. These differences are possible due to different ATPases densities, the different H^+ transport rates and the counter-ion conductance.[78]

An important and useful case of pH-cell control from the research point of view is the endocytic pathway. The endocytic pathway has a recycling and degradation function that occurs through a maturation process with strict pH regulations in each step (Figure 6). The first step is the generation of primary endocytic vesicles, which are formed by the endocytosis of external molecules through cellular membrane invaginations. These primary endocytic vesicles fuse to form early endosomes, which contain the internalized cargos, while the membrane and fluids are recycled. Early endosomes are small and present different compositions and morphologies. They are located close to cell membrane, have low Ca^{2+} concentrations and their pH is between 6.8 and 5.9. They also receive proteins from the cytosol that regulate their maturation process, as well as hydrolases from Golgi apparatus. The vacuolar subunit of early endosomes is later transformed to late endosomes, which have an oval and bigger shape, with a diameter between 250-1000 nm. Compared to early endosomes, late endosomes have higher Ca^{2+} concentrations, higher negative charge in their surface and lower pHs, with values between 6.0 and 4.9. Also, they have higher mobilities and are located closer to the nucleus. As last step of the endocytic

---

[77] Cox, M. M.; Nelson, D. L. *Principles of Biochemistry*; W H Freeman & Co, 2008.

[78] Casey, J. R.; Grinstein, S.; Orlowski, J. Sensors and Regulators of Intracellular pH. *Nat. Rev. Mol. Cell Biol.* **2010**, *11* (1), 50–61.

pathway, late endosomes fuse with lysosomes (degrading endosomes with a pH around 4.5) forming the endolysosomes, the dead-end of the degradation process.[79,80]

Due to this maturation process, the changing conditions of the endocytic pathway could be harnessed to reach plasma the cytosol inside the cell. However, cargo molecules need to escape from the endosome before the low pHs and degrading conditions are reached. Thus, viruses use endosomes to infect the cell without being identified and degraded.[81] For that purpose, viruses interact with membrane receptor in order to be endocytosed and once in the later endosome, they undergo structural modifications triggered by pH acidification that allow the viral particle to reach the cytosol.[82] Different mechanisms can lead to endosomal escape such as the formation of pores[83] or membrane fusion.[84] Similar strategies could be used to trigger the endosomal escape of a drug or therapeutic agent.[80,85,86] Therefore, fluorescent pH sensitive probes can be used to obtain information about the localization of drugs or any other molecules of interest, and to study cellular internalization pathways. Moreover, apart from these typical values and normal pH working conditions, certain diseases or infections can be caused and/or result in important pH dysregulation, such as in cancer or infections.[87] To detect these differences, again thanks to the employ of fluorescent pH sensitive probes, could be essential to identify or prevent illnesses.

---

[79] Huotari, J.; Helenius, A. Endosome Maturation. *EMBO J.* **2011**, *30* (17), 3481–3500.

[80] Rioboo, A.; Gallego, I.; Montenegro, J. Péptidos Penetrantes Celulares: Descripción, Mecanismo y Aplicaciones. *An. Química* **2019**, *115* (1), 9–21.

[81] Smith, A. E.; Helenius, A. How Viruses Enter Animal Cells. *Science* **2004**, *304* (5668), 237–242.

[82] Mercer, J.; Schelhaas, M.; Helenius, A. Virus Entry by Endocytosis. *Annu. Rev. Biochem.* **2010**, *79* (1), 803–833.

[83] Varkouhi, A. K.; Scholte, M.; Storm, G.; Haisma, H. J. Endosomal Escape Pathways for Delivery of Biologicals. *J. Control. Release* **2011**, *151* (3), 220–228.

[84] Zhang, X.; Patel, A.; Celma, C. C.; Yu, X.; Roy, P.; Zhou, Z. H. Atomic Model of a Nonenveloped Virus Reveals pH Sensors for a Coordinated Process of Cell Entry. *Nat. Struct. Mol. Biol.* **2016**, *23* (1), 74–80.

[85] Pazo, M.; Juanes, M.; Lostalé-Seijo, I.; Montenegro, J. Oligoalanine Helical Callipers for Cell Penetration. *Chem. Commun.* **2018**, *54* (50), 6919–6922.

[86] Pazo, M.; Salluce, G.; Lostalé-Seijo, I.; Juanes, M.; Gonzalez, F.; Garcia-Fandiño, R.; Montenegro, J. Short Oligoalanine Helical Peptides for Supramolecular Nanopore Assembly and Protein Cytosolic Delivery. *RSC Chem. Biol.* **2021**, *2* (2), 503–512.

[87] Webb, B. A.; Chimenti, M.; Jacobson, M. P.; Barber, D. L. Dysregulated pH: a perfect storm for cancer progression. *Nat. Rev. Cancer.* **2011**, *11*(9), 671-677.

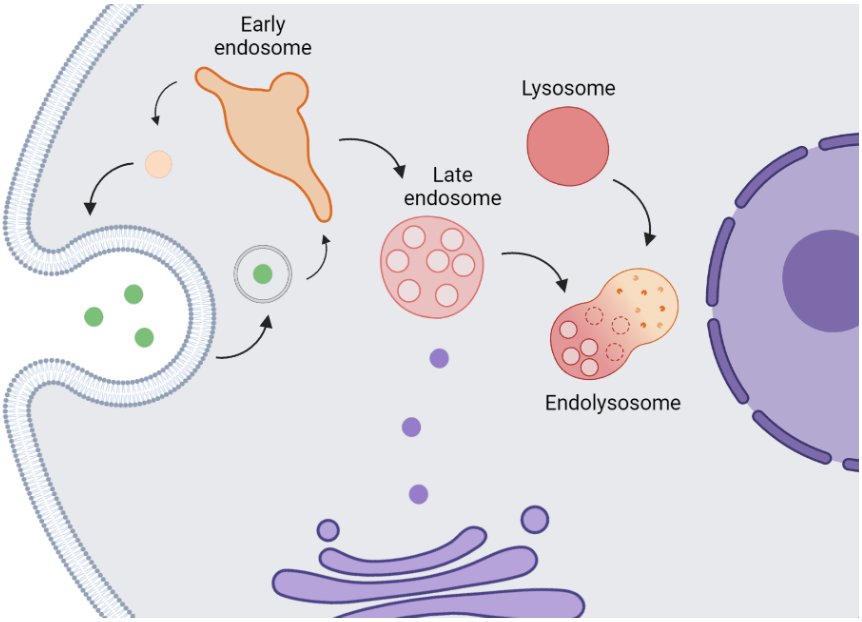

Figure 6. Endocytic pathway representation (figure elaborated with BioRender).

3.1. pH sensitive fluorophores

pH sensitive fluorophores can be suitable for intracellular tracking and, for certain applications, more practical than other techniques such as NMR, microelectrodes or absorbance, due to its high sensitivity, high spatio-temporal resolution in living cells.[88]

The ability of pH sensitive fluorophores to sense and, consequently, to report on the pH can be achieved according to two different conceptual designs (Figure 7):

- A protonable functional group such as a phenol, an amine or N-heterocycles capable of undergoing an acid-base reaction. The pK_a of this group will determine the pH range where the probe will provide an accurate pH measurement (Figure 7a).

- A reversible nucleophilic addition reaction of a hydroxyl ion in basic conditions, especially in cyanine fluorophores, in the indolinium unit (Figure 7b).

The fluorescence changes that these reactions cause in the molecule (commonly affecting π electrons resonance) will allow pH tracking at close proximity to the fluorescent probe.[89]

---

[88] Han, J.; Burgess, K. Fluorescent Indicators for Intracellular pH. *Chem. Rev.* **2010**, *110* (5), 2709–2728.

[89] Yue, Y.; Huo, F.; Lee, S.; Yin, C.; Yoon, J. A Review: The Trend of Progress about pH Probes in Cell Application in Recent Years. *Analyst* **2017**, *142* (1), 30–41.

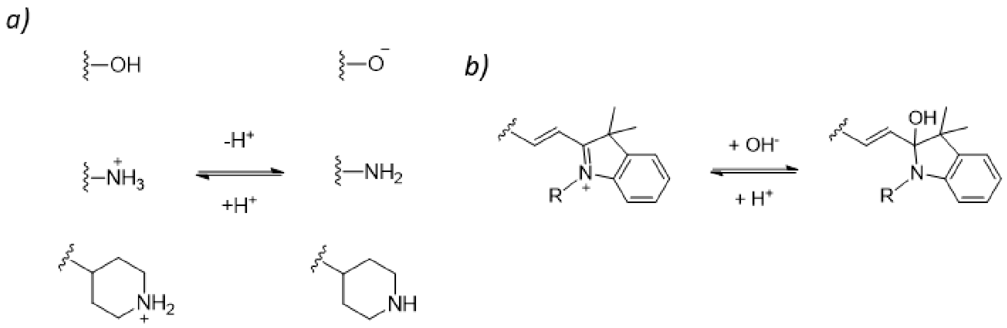

Figure 7. a) Typical acid-base neutralizations responsible of fluorophores pH sensitivity. b) Specific nucleophilic addition for pH sensing in cyanines.

Regarding their emission, there are two families of pH sensitive fluorophores (Figure 8):

- Fluorophores with an emission (on/off) switch such as molecules that only emit fluorescence above or below their pK_a value, being quenched outside this pH range.

- Ratiometric fluorescent probes that have two differentiated emission or absorbance bands depending on the pH. These probes allow the use of two wavelengths at the same time to record fluorescence and, consequently, pH. This property makes possible to perform a self-calibration, avoiding potential errors induced by dilution or quenching (caused by aggregation or precipitation, among others). Ratiometric probes are thus excellent fluorophores for cellular pH tracking, that can give more accurate results.[75]

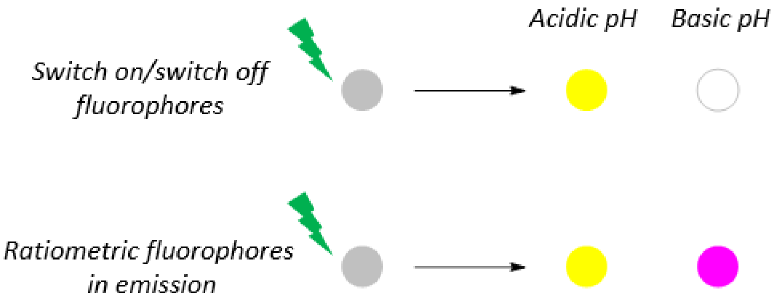

Figure 8. Characteristic fluorescent behaviour after excitation for switch on/switch off fluorophores (up) and ratiometric fluorophores (down).

3.1.1. Ratiometric fluorescent probes

Although ratiometric emissive fluorescent probes are excellent candidates for pH sensing, their structural diversity is limited. Moreover, only a few examples are commercially available at high prizes, which hinders their implementation in synthetic routes. The majority of the ratiometric pH sensitive fluorophores belong to xanthene family, and some other to cyanine and BODIPY groups. Relevant examples of each family are presented below:

- Xanthene family

This is probably the family with more examples of ratiometric probes, especially those structurally related to the fluorescein derivatives and seminaphthorhodafluor. Apart from the suitable photostability and quantum yields, this family is characterized by the capacity of the xanthene core to allow interesting reactivity and synthetic modifications, which allows the tuning and optimization of their fluorescent properties:[75,90]

- Fluorescein was one of the first examples employed due to a simple synthetic access based in two consecutive Friedel Craft’s reactions between phthalic anhydride and resorcinol.[75] Regarding its photophysical properties, the fluorescein core presents a low fluorescence below pH 5 (as it is in equilibrium with a non-fluorescent lactone form), a moderated fluorescence between pH 5 and 6.5, and a higher fluorescence over pH 6.5 (Figure 9). The fluorescein-based probes presents important cell penetration limitations due to their low negative charge.[90] Several pH sensitive fluorophores with improved characteristics were synthesized based on the fluorescein core to overcome the strong pH sensitivity and acidic-quenching such as fluorinated or sulfonated probes.[88]

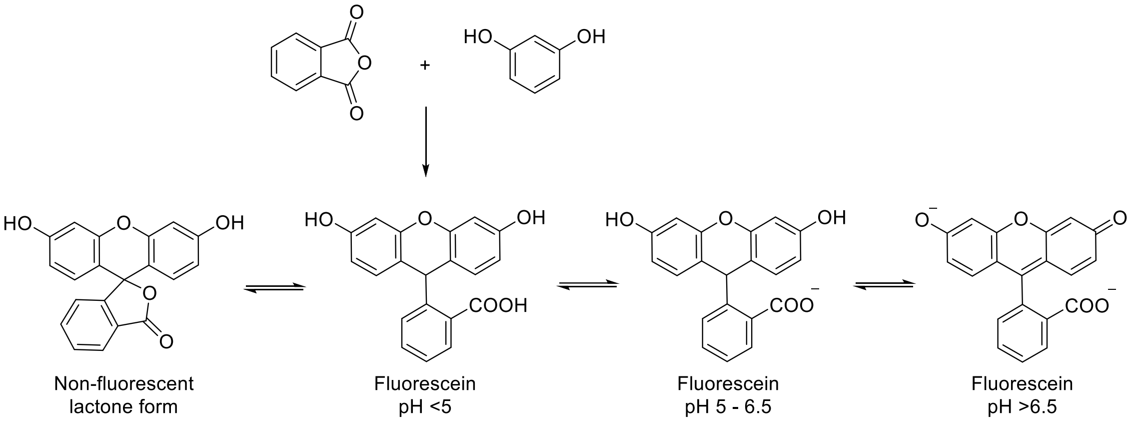

Figure 9. Fluorescein synthesis and equilibriums with pH.

- The 2′,7′-bis-(2-carboxyethyl)-5-(and-6-)carboxyfluorescein (BCECF) derivative of fluorescein was initially prepared by Roger Tsien in 1982 following a quite simple condensation reaction.[91] BCECF is ratiometric in excitation, as it has two different excitations wavelengths depending on the pH. It has been widely employed for cellular pH measurements due to its ability to be retained inside cells at neutral pH (it has 4 or 5 negative charges). BCECF pK_a is around 7 that allows an accurate measurement close to physiological pH range. This probe can be delivered into the cell in an esterified form that easily penetrates the cell membrane, and inside the cells, the carboxylic acid groups are released by intracellular esterases to recover the original fluorescence. The ionic strength of the biological medium does not affect the fluorescence profile of this probe. A similar improved analogue is 2′,7′-bis-(2-carboxypropyl)-5-(and-6-)-carboxyfluorescein (BCPCF, Figure 10), but both probes have limitations regarding fluorescence intensity differences depending on probe concentration, which could give rise to erroneous pH measurements at local high intracellular concentration.[88]

---

[90] Li, X.; Gao, X.; Shi, W.; Ma, H. Design Strategies for Water-Soluble Small Molecular Chromogenic and Fluorogenic Probes. *Chem. Rev.* **2014**, *114* (1), 590–659.

[91] Rink, T. I.; Tsien, R. Y.; Pozzan, T. Cytoplasmic pH and Free Mg^{2+} in Lymphocytes. *J. Cell Biol.* **1982**, *95* (1), 189–196.

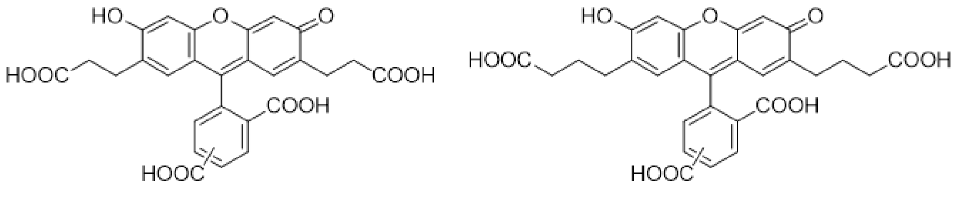

BCECF BCPCF

Figure 10. BCECF and BCEPF structures.

- SNAFLs, SNAFRs and SNARFs are three groups of pH sensitive benzo[*c*]xanthenes commercialized by Molecular Probes since the 90s. They show structural similarities, as they all have seminaphto-like molecular cores, but of fluoresceins (SNAFLs), fluorones (SNAFRs) or rhodafluors (SNARFs) in each case (Figure 9a). These probes show a ratiometric fluorescence emission with two differentiated maximums λ_{em} for the acidic and the basic forms. The synthesis of these probes consists in a condensation between the desired benzophenone (appropriately substituted for each case) and a dihydroxy naphthalene (Figure 11b).[88,92] Among this family of probes, SNARF-1, specially C.SNARF-1 (carboxy-SNARF-1), are the most widely employed, and one of the most used from all the available ratiometric pH probes.[93] The carboxy groups of the SNARF probes can also be protected as esters to enhance the probe's membrane permeability and report on intracellular pH without concentration artefacts. However, these probes can be slightly sensitive to temperature and photodegradation. The ratio between the fluorescence emission of the two emission maximums (λ_{em}) is sufficiently stable to allow precise intracellular pH tracking. In addition, the two maximum λ_{em}, between 550 and 650nm, are well suited for intracellular pH range. Nevertheless, the pK_a of SNARF probes around 7.5 turns out to be a bit high for certain acidic regions of the cells such as the endosome. Therefore, some attempts have been made to create SNARF-1 derivatives with lower pK_a, including different derivatives with halogen substitution in the lower aromatic ring[94] or versions with fluorine atoms close to the phenol group, reaching pH values of 6.4.[95]

---

[92] Whitaker, J. E.; Haugland, R. P.; Prendergast, F. G. Spectral and Photophysical Studies of Benzo[*c*]Xanthene Dyes: Dual Emission pH Sensors. *Anal. Biochem.* **1991**, *194* (2), 330–344.

[93] Seksek, O.; Henry-Toulmé, N.; Sureau, F.; Bolard, J. SNARF-1 as an Intracellular pH Indicator in Laser Microspectrofluorometry: A Critical Assessment. *Anal. Biochem.* **1991**, *193* (1), 49–54.

[94] Nakata, E.; Nazumi, Y.; Yukimachi, Y.; Uto, Y.; Maezawa, H.; Hashimoto, T.; Okamoto, Y.; Hori, H. Synthesis and Photophysical Properties of New SNARF Derivatives as Dual Emission pH Sensors. *Bioorg. Med. Chem. Lett.* **2011**, *21* (6), 1663–1666.

[95] Liu, J.; Diwu, Z.; Leung, W. Y. Synthesis and Photophysical Properties of New Fluorinated Benzo[*c*]Xanthene Dyes as Intracellular pH Indicators. *Bioorg. Med. Chem. Lett.* **2001**, *11* (22), 2903–2905.

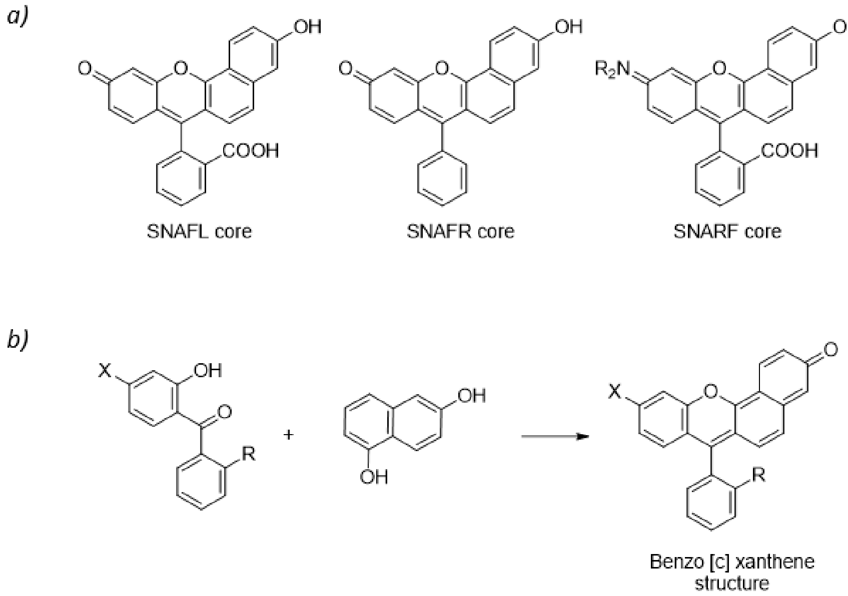

Figure 11. a) Benzo[c]xanthenes SNAFL, SNAFR and SNARF core molecular structure. b) Conventional synthesis for benzo[c]xanthenes.

- BODIPY family

Although BODIPY dyes can show pH sensing capabilities, not all of them can be used for intracellular pH tracking, as their pK_a values are commonly very low.[90] Moreover, ratiometric behaviour is not observed for many of these probes.[75] One of the very few ratiometric examples is the BODIPY equipped with *p*-dimethylaminostyryl, which extends the resonance area and allows both ratiometric absorbance and fluorescence (Figure 12a).[96]

- Cyanine family

Cyanines are also promising probes for intracellular pH tracking due to their characteristic NIR fluorescent emissions. Two different approaches can be used to implement ratiometric pH sensitive properties to cyanine probes:[88,75]

- Introduction of a phenol group or terpyridine moiety to incorporate the pH sensitive group, allowing ratiometric sensing absorbance (Figure 12b).[97]

- Conjugation of hemicyanines with other pH sensitive fluorophores, as coumarins or xanthenes. For instance, in the case of the coumarin-linked structure, depending on the pH, mainly just coumarin or just hemicyanine emission will be observed. The probe could be considered ratiometric as two differentiated wavelengths of emission are now present (Figure 12c).[98]

---

[96] Zhu, M.; Xing, P.; Zhou, Y.; Gong, L.; Zhang, J.; Qi, D.; Bian, Y.; Du, H.; Jiang, J. Lysosome-Targeting Ratiometric Fluorescent pH Probes Based on Long-Wavelength BODIPY. *J. Mater. Chem. B* **2018**, *6* (27), 4422–4426.

[97] Tang, B.; Yu, F.; Li, P.; Tong, L.; Duan, X.; Xie, T.; Wang, X. A Near-Infrared Neutral pH Fluorescent Probe for Monitoring Minor pH Changes: Imaging in Living HepG2 and HL-7702Cells. *J. Am. Chem. Soc.* **2009**, *131* (8), 3016–3023.

[98] Xia, S.; Wang, J.; Bi, J.; Wang, X.; Fang, M.; Phillips, T.; May, A.; Conner, N.; Tanasova, M.; Luo, F.-T.; Liu, H. Fluorescent Probes Based on π-Conjugation Modulation between Hemicyanine and Coumarin Moieties for Ratiometric Detection of pH Changes in Live Cells with Visible and Near- Infrared Channels. *Sens. Actuators B Chem.* **2018**, *265*, 699–708.

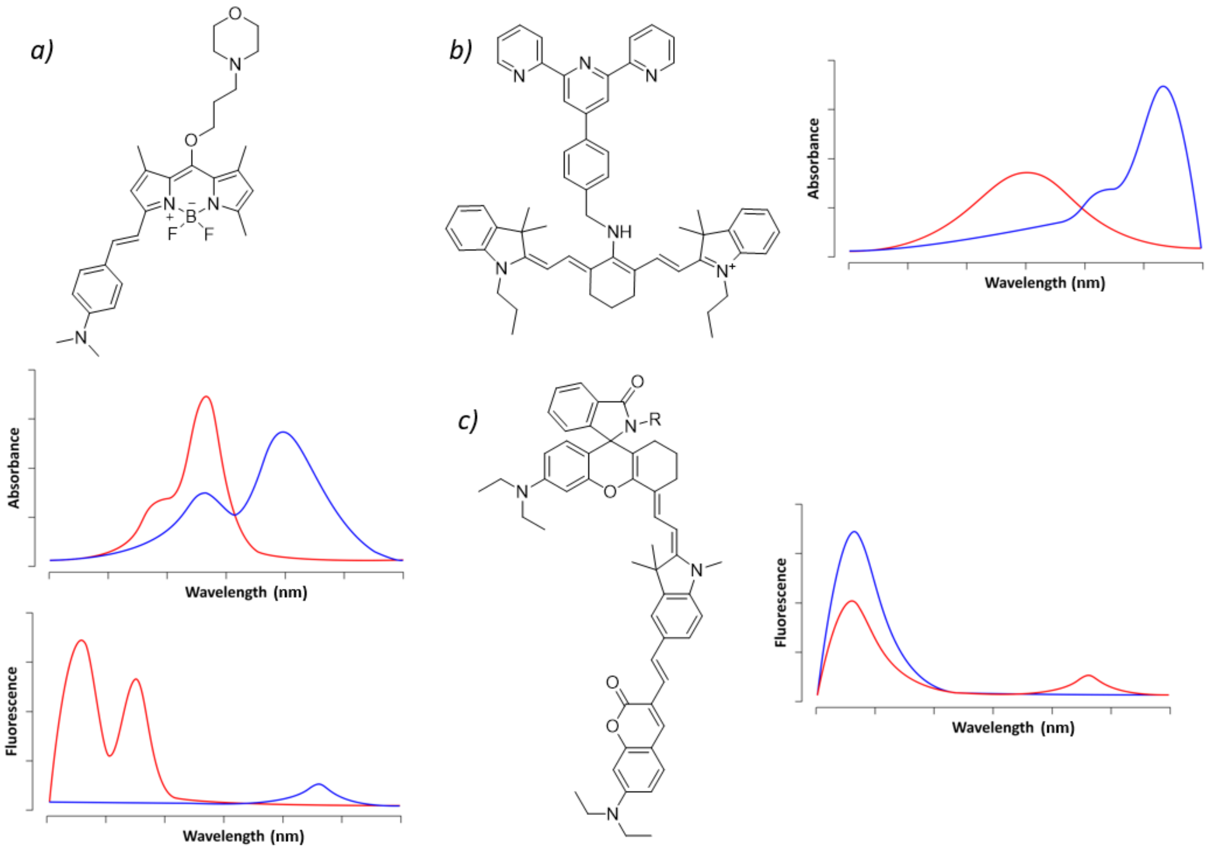

Figure 12. a) BODIPY ratiometric pH sensitive fluorophore, both in absorbance (up) and fluorescence (down).[96] b) Cyanine ratiometric pH sensitive fluorophore.[97] c) Ratiometric pH sensitive conjugation of hemicyanine and coumarin.[98] In red, their spectra (absorbance or fluorescence depending on each case) at acidic pH is represented. In blue, their spectra at basic pH.

3.1.2. Important aspects for cellular pH measurement

Apart from the applicability of ratiometric pH sensitive probes to ensure accuracy in pH determination, other important parameters should be considered when working with living systems as cells.

3.1.2.1. pK_a value

To have an adequate pK_a value it essential for intracellular pH tracking. As previously mentioned, although physiological pH is around 7.4, certain locations inside the cell have different pH values. Thus, a probe with a pK_a of 7.5 could be not ideally suited for particular applications. To lower the pK_a, a common approach is to introduce electron withdrawing atoms in the fluorescent core, as previously shown in C.SNARF-1.[94,95] Hammett coefficients help to predict how electron withdrawing atoms or other substituents affect pK_a value.

L. P. Hammett was a physical chemist who studied the effect of different substituents in the equilibrium or reaction rate of a reaction which takes place over a reacting group attached to a benzene ring.[99,100] In fact, he was able to stablish an equation that relates the ratio between the equilibrium constant with and without the substituent (K/K_0) with just two constants, one dependent on the type of reaction (ρ) and another dependent on the substituent (σ):

---

[99] Hammett, L. P. Some Relations between Reactions Rates and Equilibrium Constants. *Chem. Rev.* **1935**, *17* (1), 125–136.

[100] Hammett, L. P. The Effect of Structure upon the Reactions of Organic Compounds. Temperature and Solvent Influences. *J. Chem. Phys.* **1937**, *59* (1), 96–103.

$$\log \frac{K}{K_0} = \sigma \rho$$

Regarding the equation constant, Hammett took as a reference the reaction of deprotonation of the benzoic acid, setting it as ρ=1. Those reactions with higher values will be more sensitive to substituents effects than this ionization, and less sensitive the ones with a ρ value between 0 and 1. As in the reference reaction a negative charge is formed, those reactions where positive charge appears will have a negative ρ constant.

He determined up to 40 ρ values for ester or acid hydrolysis, esterifications, brominations, Friedel-Crafts reactions or multiple S_N2 reactions where phenols or anilines participate, among others (Table 1). In the context of this chapter, the effect of aromatic ring substituents on the pK_a values of reactions like the ionization of phenols or the deprotonation of anilinium ions should be taken into account. These two examples of reactions, which are the typical acid-base neutralizations responsible of fluorophores pH sensitivity, have ρ values of 2.008 and 2.730 respectively, which means that they are strongly affected by the presence of substituents.[100]

Table 1. Some examples of reactions studied by L. P. Hammett and their ρ constant values.[100]

Reaction	**Constant ρ**
Reaction of substituted anilines with dinitro-chloronaphthalene in ethyl alcohol at 25°	-3.690
Reaction of substituted dimethylanilines with trinitrophenol methyl ether in acetone at 35°	-2.382
Reaction of substituted anilines with formic acid in pyridine-water medium at 100°	-1.219
Acid catalyzed bromination of substituted acetophenones in an acetic acid-water-hydrochloric acid medium at 25°	-0.550
Acid catalyzed esterification of substituted benzoic esters in absolute alcohol at 25° with *N* HCl	-0.085
Hydrolysis of substituted formanilides with formic acid in pyridine-water medium at 100°	0.316
Alkaline hydrolysis of substituted phenylacetic esters in 87.83% ethyl alcohol at 30°	0.824
Hydrolysis of substituted benzenesulfonic ethyl esters in 30% ethyl alcohol at 25°	1.190
Ionization of substituted phenylboric acids in 25% ethyl alcohol at 25°	2.143
Ionization of substituted phenols in water at 25°	2.008
Acidity constants of substituted anilinium ions in water at 25°	2.730

Regarding the substituent constant, aromatic substituents showing higher positive values of the Hammett coefficient will accelerate the reaction studied, and those substituents showing negative values will slow down the reaction rate (Table 2). The effect of a substituent will depend on 3 important aspects: electrostatics (if a charge is present), σ delocalizations and π delocalizations.

σ delocalizations are transmitted across σ bonds and are directly related with the polarity of the bond and, consequently, with the electronegativity of the substituent. Those substituents with higher electronegativities will have more appetence for electrons, strongly polarizing the bond and causing an inductive effect.[101]

On the other hand, π delocalizations are transmitted across π bonds, causing resonance or mesomerism. Thus, substituents could have an electron withdrawing effect when they attract π electrons or a donating effect when they give them.[101]

Independently of which kind of delocalization is acting, if negative charge is injected into the benzoic acid (reference reaction), its acidity will increase and thus will be the reaction rate. Therefore, the substituents with higher σ values are those that present both delocalization effects (σ and π), as NO_2 (σ=0.778 and 0.710 for *para* and *meta* position) or CN (σ=1.000 and 0.678 for *para* and *meta* position). Therefore, this type of substituents (CN and NO_2) will have a high Hammett coefficient and will reduce benzoic acid pK_a. Moreover, in the case of reactions with phenols and anilines where there is a NO_2 group in *para* position, NO_2 electrons are directly in resonance with phenol or aniline, so a correction in the σ value have to be made, resulting in a higher constant value (σ=1.27). When just inductive effect is present, the σ value is considerably high, such as in the case of the halogens, with values following the order of the electronegativity (F>Cl>Br>I). However, they will not be able to reach the higher values of NO_2 and CN as just σ delocalization is present, but not π.[100]

Table 2. Some examples of substituents studied by L. P. Hammett and their σ constant values, taking the reaction of deprotonation of the benzoic acid as reference.[100]

Substituent	**Constant σ**
p CN	1,000
m CN	0,678
p NO_2	0,778
m NO_2	0,710
p F	0,062
m F	0,337
p I	0,276
m I	0,352
p CH_3	-0,170
m CH_3	-0,069
p NH_2	-0,660
m NH_2	-0,161

However, Hammett coefficients are just valid for benzene, as the rigidity of the ring inhibits the effect of other aspects that should be considered different from the type or reaction and the substituent. Moreover, these coefficients are only accurate for *meta* and *para* positions, not for *ortho*, as in this last case steric effects could interfere. Multiple corrections have been

---

[101] Krygowski, T. M.; Stępień, B. T. Sigma- and Pi-Electron Delocalization: Focus on Substituent Effects. *Chem. Rev.* **2005**, *105* (10), 3482–3512.

made in order to extend Hammett reaction rate predictions to other aromatic systems, aliphatic systems and *ortho* substituents, as those made by H. H. Jaffé[102] or R. W. Taft.[103-105]

3.1.2.2. Other considerations

Apart from pK_a, there are other important aspects that should be taking into account in the design of pH ratiometric fluorescent probes:

- **Near infrared (NIR) emission**: fluorophores with emission in the NIR region of the spectra are the best to work with cells and tissues. First, this radiation penetrates deeper in cells, which increase the potential areas to study. Also, the NIR is far from the spectra region where tissues emit, which reduce autofluorescence interferences. Finally, the lower energy of excitation lasers for NIR probes is safer and not toxic for living systems. Longer π conjugated scaffolds can lead to red shifted emissions, but also in certain cases to low quantum yields.[74,106]

- **Compatibility with single-molecule microscopy**: the optic diffraction limit of standard confocal microscopes limits fluorescence resolution of intracellular compartments and processes.[107] To remedy this limitation, super resolution microscopy allows a much better resolution of the fluorescent micrographs at the nanoscale. Depending on the super resolution technique of election, microscopists might need photoactivable probes that only emit fluorescence once irradiated.[73,108]

- **Compatibility with two-photon fluorescence**: common fluorescence is produced, as previously explained, by the excitation of an electron with a single photon of high energy. However, in the case of two-photon fluorescence, the excitation occurs simultaneously with two photons of lower energy (commonly in the NIR or NIR-II region), even lower than the emission wavelength of the probe.[109] This alternative fluorescence is less aggressive for long-time tissues visualization, penetrates deeper in tissues and reduces photodamage of the fluorophores, autofluorescence interferences or self-absorption.[110]

- **Intracellular organelle targeting:** tracking the pH of individual organelles requires targeted fluorescent probes. For that purpose, it is necessary to introduce organelle directing groups in the fluorophores without affecting their fluorescent properties. Some of the most employed are TPP for mitochondria or morpholine to lysosome, among others.[89,111]

---

[102] Jaffé, H. H. A Reëxamination of the Hammett Equation. *Chem. Rev.* **1953**, *53* (2), 191–261.

[103] Taft, R. W. Linear Free Energy Relationships from Rates of Esterification and Hydrolysis of Aliphatic and Ortho-Substituted Benzoate Esters. *J. Am. Chem. Soc.* **1952**, *74* (11), 2729–2732.

[104] Taft, R. W. Polar and Steric Substituent Constants for Aliphatic and o-Benzoate Groups from Rates of Esterification and Hydrolysis of Esters. *J. Am. Chem. Soc.* **1952**, *74* (12), 3120–3128.

[105] Taft, R. W. Linear Steric Energy Relationships. *J. Am. Chem. Soc.* **1953**, *75* (18), 4538–4539.

[106] Liu, P.; Mu, X.; Zhang, X. D.; Ming, D. The Near-Infrared-II Fluorophores and Advanced Microscopy Technologies Development and Application in Bioimaging. *Bioconjug. Chem.* **2020**, *31* (2), 260–275.

[107] Schermelleh, L.; Ferrand, A.; Huser, T.; Eggeling, C.; Sauer, M.; Biehlmaier, O.; Drummen, G. P. C. Super-Resolution Microscopy Demystified. *Nat. Cell Biol.* **2019**, *21* (1), 72–84.

[108] Thiel, Z.; Rivera-Fuentes, P. Photochemically Active Dyes for Super-Resolution Microscopy. *Chimia* **2018**, *72* (11), 764–770.

[109] Shaw, P. A.; Forsyth, E.; Haseeb, F.; Yang, S.; Bradley, M.; Klausen, M. Two-Photon Absorption: An Open Door to the NIR-II Biological Window? *Front. Chem.* **2022**, *10*:921354.

[110] Kim, H. M.; Cho, B. R. Two-Photon Probes for Intracellular Free Metal Ions, Acidic Vesicles, and Lipid Rafts in Live Tissues. *Acc. Chem. Res.* **2009**, *42* (7), 863–872.

[111] Hou, J. T.; Ren, W. X.; Li, K.; Seo, J.; Sharma, A.; Yu, X. Q.; Kim, J. S. Fluorescent Bioimaging of pH: From Design to Applications. *Chem. Soc. Rev.* **2017**, *46* (8), 2076–2090.

Although it is almost impossible to satisfy all the functional requirements of an ideal probe, it is important to consider them when searching for an appropriated labelling purpose. Current needs for new and simplified synthetic routes to smart fluorophores and stimuli-response probes are more important than ever.

Field 3: New pH sensitive strategies for venom-derived antitumoral drugs

Section affected by confidentiality: under the protection of rights.


USC
UNIVERSIDADE
DE SANTIAGO
DE COMPOSTELA

Objectives

By using chemistry as a tool, in this doctoral thesis we aim to develop new systems, sensors and drugs that can contribute to our better understanding of cell and, ultimately, lead to the development of more effective chemical tools with biological potential. However, there are specific objectives for each developed system and, consequent, field of application.

Field 1: Amphiphilic self-assemblies for protocellular study

The objectives presented in this field have been published in:

Booth, R. [a]; Insua, I. [a]; Ahmed, S. [a]; Rioboo, A. [a]; Montenegro, J. [a]* Supramolecular Fibrillation of Peptide Amphiphiles Induces Environmental Responses in Aqueous Droplets.
Nat. Commun. **2021**, *12 (1)*, 6421–6428.
DOI: 10.1038/s41467-021-26681-2

[a] Centro Singular de Investigación en Química Biolóxica e Materiais Moleculares (CiQUS), Departamento de Química Orgánica, Universidade de Santiago de Compostela (USC), 15782, Spain.

Nature Communications Impact Score: 16.6 (2022). Q1 in Biochemistry, Genetics and Molecular Biology; Chemistry; Physics and Astronomy.

Following with the research lines devoted to amphiphilic self-assemblies inside aqueous compartments,[26,28] the main objective in this field is to study the potential functional behaviour that could be triggered by the chemical reaction of dormant synthetic precursors that self-assemble into supramolecular 1D networks and confined inside water droplets.

To this end, we employed a suitable synthetic disconnection of a linear peptide amphiphile to allow the aqueous compatibility of its hydrophobic and directional hydrogen bonding blocks.

We will study the aqueous oxime condensation of these precursors to yield the corresponding hydrophobic peptide amphiphile and check the potential impact of this reaction in the assembled product and its supramolecular propagation[112,113]

We will incorporate the supramolecular system inside aqueous droplets, to study the potential assembly of fibrillar networks under confinement. We expect that the formation of amphiphilic fibrillar networks could trigger the emergence of unexpected events and potentially coupled environmental responses.

The final aim will be to study if chemically triggered 1D self-assembly can play a role in the functional properties and communication of individual aqueous entities.

---

[112] Carlsson, A. E. Dendritic Actin Filament Nucleation Causes Traveling Waves and Patches. *Phys. Rev. Lett.* **2010**, *104* (22), 4–7.

[113] Sambeth, R.; Baumgaertner, A. Autocatalytic Polymerization Generates Persistent Random Walk of Crawling Cells. *Phys. Rev. Lett.* **2001**, *86* (22), 5196–5199.

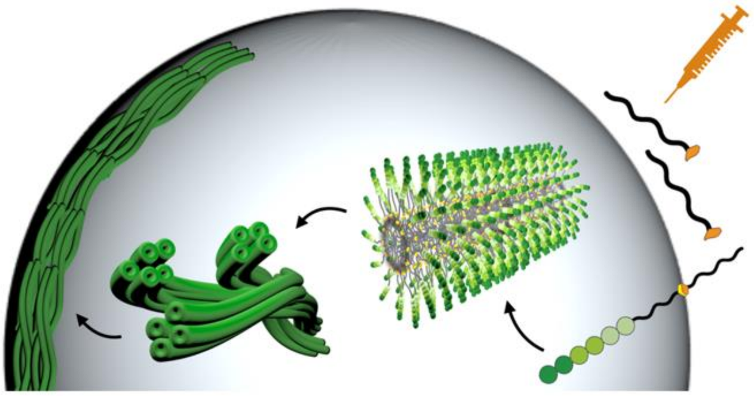

Figure 13. Schematic representation of peptide amphiphiles assembly through a self-assembly and autocatalyzed process which ends in fibres formation inside aqueous droplets.

Field 2: Fluorescent probes for cellular compartments identification

As previously discussed in the introduction, the good properties of C.SNARF-1 as pH sensitive ratiometric fluorophore turn this probe in an excellent candidate for cellular pH tracking in live cells. However, there are certain considerations that still hinder the application of this probe:

- **The pK_a value**. Although C.SNARF-1 is widely employed in cell experiments, the pK_a value of this probe, around 7.5, is too high to precisely report on the pH of the most acidic intracellular regions such as late endosomes, which pH can reach values close to 4.5. As a consequence, the precise tracking of the pH along the endocytic pathway can be limited.

- **The high production cost**. Although C.SNARF-1 is commercially available and distributed by ThermoFisher, 1mg of a mixture of its two positional isomers (C5.SNARF-1 and C6.SNARF-1, Figure 14) currently costs around 580€ (price according to catalogue 2023).[114] The high cost of this probe hinders the use of the compound for synthetic purposes. Therefore, is complicated to carry out synthetic routes with this probe and/or connect it to any synthetic peptide, drug, or target molecule of biological interest.

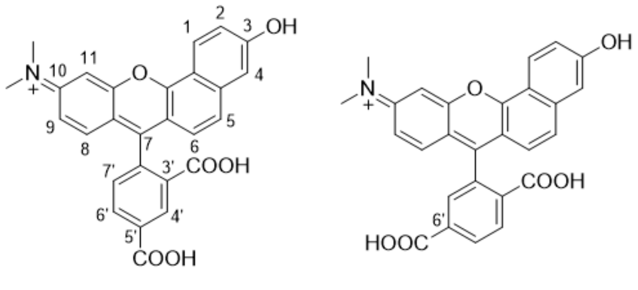

C5.SNARF-1 C6.SNARF-1

Figure 14. Two positional isomers of C.SNARF-1: C5.SNARF-1 and C6.SNARF-1.

Therefore, the objectives on this field are:

- Synthesis and isolation of the two positional isomers of C.SNARF-1, C5.SNARF-1 and C6.SNARF-1. We aim to develop a synthetic route that would allow the

---

[114] 5-(and-6)-carboxy SNARF™-1. https://www.thermofisher.com/order/catalog/product/C1270 (accessed June 28th, 2023).

separation of both positional isomers of the SNARF probe. This route is aimed to allow a robust and accessible method to access the final probe at a sufficient scale to allow its implementation in synthetic applications and connect it to molecular targets such as peptides and small molecules to track the pH along their internalization pathway.

- Synthesis and physicochemical characterization of new C.SNARF-1 derivatives with an optimized pK_a (6.0-6.5) for endosome labelling purposes. Electron withdrawing groups have shown good ability decreasing pK_a value, as previously shown in the Hammett coefficient section.[99,100] Certain fluor derivatives have been already reported with lowered pK_a values of 7.2 (for C.SNARF-5F) and 6.4 (for C.SNARF-4F),[95] and they are also commercially available (ThermoFisher). However, the potential insertion of a fluor atom at position 2 of SNARF core, which has electrons in resonance with the phenol, has not been exploited yet. Therefore, we aim to prepare C.SNARF-2F and characterized its photophysical properties in order to search for an optimized pH tracking probe. Also, fluor atoms have been introduced in the benzene pendant, outside the xanthene core, in order to increase hydrophobicity and tune photophysical properties. Additions of fluorine atoms in the extra phenyl ring have been shown to further reduce the pK_a of the probe (e.g. 7.38 for SNARF-F in Figure 15).[94] Therefore, besides fluorination in both position 2 of the xanthene core as well as multiple fluor substitution in the outer phenyl ring will be studied (Figure 15).

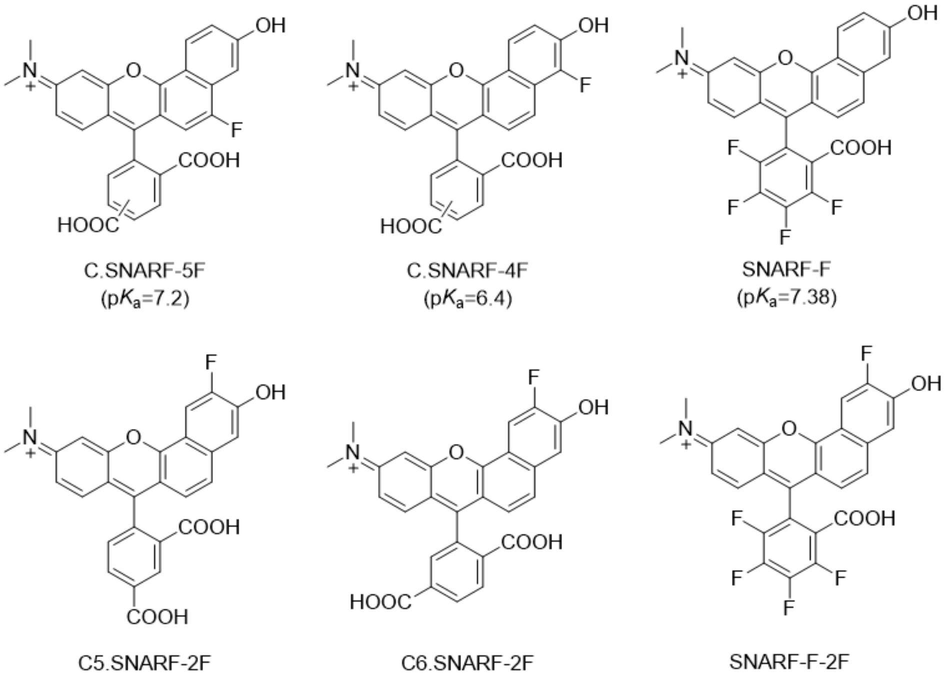

C.SNARF-5F
(pK_a=7.2)

C.SNARF-4F
(pK_a=6.4)

SNARF-F
(pK_a=7.38)

C5.SNARF-2F

C6.SNARF-2F

SNARF-F-2F

Figure 15. Three already reported fluor SNARF derivatives: C.SNARF-5F, C.SNARF-4F and SNARF-F, and three new derivatives that will be studied in this chapter: C5.SNARF-2F, C6.SNARF-2F and SNARF-F-2F.

Field 3: New pH sensitive strategies for venom-derived antitumoral drugs

Section affected by confidentiality: under the protection of rights.

Results

As the systems developed during this PhD work were oriented to three different fields of cellular research, the results are now presented following the same organization.

Field 1: Amphiphilic self-assemblies for protocellular study

The results presented in this field have been published in:

Booth, R. [a]; Insua, I. [a]; Ahmed, S. [a]; Rioboo, A. [a]; Montenegro, J. [a]* Supramolecular Fibrillation of Peptide Amphiphiles Induces Environmental Responses in Aqueous Droplets.
Nat. Commun. **2021**, *12 (1)*, 6421–6428.
DOI: 10.1038/s41467-021-26681-2

[a] Centro Singular de Investigación en Química Biolóxica e Materiais Moleculares (CiQUS), Departamento de Química Orgánica, Universidade de Santiago de Compostela (USC), 15782, Spain.

Nature Communications Impact Score: 16.6 (2022). Q1 in Biochemistry, Genetics and Molecular Biology; Chemistry; Physics and Astronomy.

1. Molecular design and fibrillation in solution

We selected linear peptide amphiphiles as scaffolds for the assembly of fibrillar supramolecular architectures.[115-117] We employed a non-assembling peptide precursor, $\mathbf{P_{C8}}$, that could readily react with a hydrophobic tail, $\mathbf{T_8}$, to generate *in situ* the self-assembling peptide amphiphile, $\mathbf{P_{C8}T_8}$ (Figure 16a). This amphiphile is composed of two anionic glutamic acids, a short β-sheet-inducer sequence (two alanine and two valine residues) and an aliphatic chain at the *N*-terminus. In this case, the obvious synthetic disconnection between the pure peptide and aliphatic segments would require the use of a potential building block of tetradecanal, which would not be soluble in aqueous media. Instead, we designed the disconnection of $\mathbf{P_{C8}T_8}$ into $\mathbf{P_{C8}}$ and $\mathbf{T_8}$, allowing the aqueous solubility and physiological compatibility of the two required molecular fragments.[115] Thus, the short non-fibrillating peptide precursor ($\mathbf{P_{C8}}$), bearing an alkoxyamine moiety, would react with octanal ($\mathbf{T_8}$) to yield the final oxime product ($\mathbf{P_{C8}T_8}$) that should be sufficiently hydrophobic to start supramolecular polymerization (Figure 16a).[116,118]

The reaction between $\mathbf{P_{C8}}$ and $\mathbf{T_8}$ was first monitored in bulk water by fluorimetry using the probe Thioflavin T (ThT) to study reaction kinetics. The increase in ThT's emission reports on the presence of peptide β-sheets and hydrophobic cavities[119] that should be formed in the final assembled $\mathbf{P_{C8}T_8}$ product. Indeed, a rapid increase in ThT emission was observed upon addition of $\mathbf{T_8}$ to an aqueous solution of the peptide head ($\mathbf{P_{C8}}$), which was consistent with the formation of the corresponding supramolecular polymers (Figure 16b). The transition from the latent peptide precursor to the final self-assembled product was also monitored by circular

---

[115] Booth, R.; Insua, I.; Bhak, G.; Montenegro, J. Self-Assembled Micro-Fibres by Oxime Connection of Linear Peptide Amphiphiles. *Org. Biomol. Chem.* **2019**, *17* (7), 1984–1991.

[116] Hendricks, M. P.; Sato, K.; Palmer, L. C.; Stupp, S. I. Supramolecular Assembly of Peptide Amphiphiles. *Acc. Chem. Res.* **2017**, *50* (10), 2440–2448.

[117] Wester, J. R.; Lewis, J. A.; Freeman, R.; Sai, H.; Palmer, L. C.; Henrich, S. E.; Stupp, S. I. Supramolecular Exchange among Assemblies of Opposite Charge Leads to Hierarchical Structures. *J. Am. Chem. Soc.* **2020**, *142* (28), 12216–12225.

[118] Ortony, J. H.; Newcomb, C. J.; Matson, J. B.; Palmer, L. C.; Doan, P. E.; Hoffman, B. M.; Stupp, S. I. Internal Dynamics of a Supramolecular Nanofibre. *Nat. Mater.* **2014**, *13* (8), 812–816.

[119] Wolfe, L. S.; Calabrese, M. F.; Nath, A.; Blaho, D. V.; Miranker, A. D.; Xiong, Y. Protein-Induced Photophysical Changes to the Amyloid Indicator Dye Thioflavin T. *Proc. Natl. Acad. Sci.* **2010**, *107* (39), 16863–16868.

dichroism (CD), showing an exponential increase in the expected β-sheet-like signal as the reaction proceeds, which suggested a cooperative reaction-assembly mechanism (Figure 16c, d). Indeed, the aqueous self-assembly of linear peptide amphiphiles, such as $\mathbf{P_{C8}T_{8}}$, is driven by hydrophobic tail packing and β-sheet H-bonding between hydrophobic amino acids; Ala and Val in this case.[116,118] High-performance liquid chromatography (HPLC) analysis of the reaction kinetics showed a lag time preceding the formation of the final product (Figure 16e and S1.1). However, we could demonstrate that this delay could be reduced by doping the reaction mixture with seeds of the preformed product $\mathbf{P_{C8}T_{8}}$ (5 % mol ratio), which caused an approximate fourfold enhancement of the reaction rate (Figure 16e).

Analysis of the samples by epifluorescence microscopic imaging revealed the sudden emergence of long aster-like fibrillar networks, around 2 um in diameter, 5 min after the addition of $\mathbf{T_{8}}$ to an aqueous sample containing the reactive peptide precursor $\mathbf{P_{C8}}$ (Figure 16 and Movie 1). Electron microscopic analysis of these $\mathbf{P_{C8}T_{8}}$ samples showed the expected nanofibrillar morphology with progressive bundling into micron-sized 1D networks with increasing concentration, whereas no fibrillar structures were formed by the precursor $\mathbf{P_{C8}}$ (Figure S1.2). It should be noted that decreasing pH or increasing salt concentration of the aqueous medium will promote peptide fibrillation due to protonation or ionic shielding of the glutamic acid residues, respectively.[115] However, in this chapter, the external buffer conditions were not modified at any point to solely rely on the chemical trigger $\mathbf{T_{8}}$ to induce peptide fibrillation and potential functional responses.

The observed reaction-assembly profile (Figure 16d, e) is consistent with the initial formation of micellar aggregates from the reaction product $\mathbf{P_{C8}T_{8}}$, as evidenced by pyrene fluorescence titrations that showed a critical micellar concentration (CMC) of *ca.* 34 uM (Figure S1.3). From a supramolecular perspective, these micelles can establish a phase separation between an inner hydrophobic core and polar peptide shell, which drives the accumulation of precursor $\mathbf{P_{C8}}$ and $\mathbf{T_{8}}$ at either phase, thus increasing the reaction rate (Figure 16a).[118,120] Beyond the self-assembly of $\mathbf{P_{C8}T_{8}}$ at its CMC, the reaction product displayed a second supramolecular transition at ca. 200 uM, which would correspond to the elongation of micelles into fibres (Figure S1.3). The precursor $\mathbf{P_{C8}}$ did not show any evidence of micelle formation with this same pyrene assay, even at concentrations as high as 1 mM. However, a 12-fold ThT emission increase was observed in $\mathbf{P_{C8}}$ samples (1 mM) doped with sub-fibrillar concentrations of $\mathbf{P_{C8}T_{8}}$ (20–150 uM), demonstrating the co-assembly of the precursor and product (Figure S1.4).[118,120] Taken together, these experimental observations were consistent with a physical autocatalytic reaction mechanism, which is triggered by the phase separation at micellar and fibrillar interfaces and the co-assembly of precursors and products (Figure 16a).

---

[120] Shi, Y.; Ferreira, D. S.; Banerjee, J.; Pickford, A. R.; Azevedo, H. S. Tuning the Matrix Metalloproteinase-1 Degradability of Peptide Amphiphile Nanofibres through Supramolecular Engineering. *Biomater. Sci.* **2019**, *7* (12), 5132–5142.

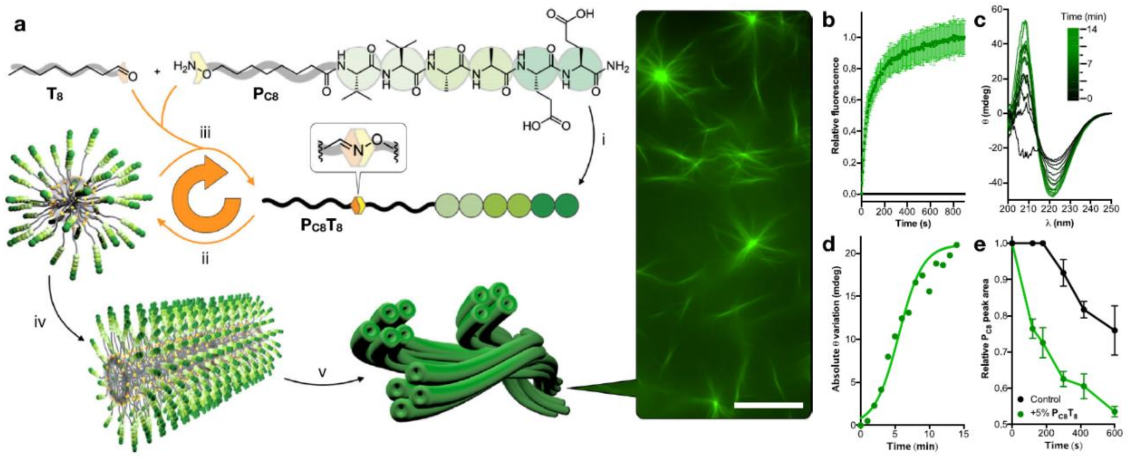

Figure 16. Autocatalytic formation of peptide-based microfibres. A) Schematic showing: (i) precursor peptide **P$_{C8}$** *reacting with octanal (***T$_8$***) to form the peptide amphiphile product,* **P$_{C8}$T$_8$***, though an oxime connection; (ii) micellar aggregation of the product* **P$_{C8}$T$_8$***; (iii) co-assembly of* **P$_{C8}$T$_8$** *with its precursors and the resulting physically autocatalytic behaviour (circular orange arrow); (iv, v) Hierarchical elongation into individual nanofibers and microfibrillar bundles, which can be seen by fluorescence microscopy stained with ThT. Scale bar = 20 um. B) Time-dependent ThT emission from an aqueous* **P$_{C8}$** *solution after addition of* **T$_8$** *(green) and without* **T$_8$** *(black); n = 3 (mean ± SD). C) Time-dependent CD spectra of the reaction after addition of* **T$_8$***. D) Change in CD signal (222 nm) during the reaction. E)* **P$_{C8}$** *consumption in reaction with* **T$_8$** *(1 mM) either in the absence (control) or presence of preformed* **P$_{C8}$T$_8$** *product (5 % mol/mol) followed by HPLC (222 nm); n= 3 (mean ± SD).*

2. Confined fibrillation in aqueous droplets

Having established that the reaction proceeds by physical autocatalysis across the interface of amphiphilic assemblies, the **P$_{C8}$** peptide was confined inside aqueous droplets of a water-in-oil (w/o) emulsion to test whether the reaction and subsequent self-assembly would tolerate an additional interfacial boundary (Figure 17a). Reaction kinetics were first monitored by fluorescence spectroscopy in the presence of ThT, showing a lag time followed by an abrupt increase of the probe's emission (Figure 17b). This emission profile suggested the successful reaction between **P$_{C8}$** and **T$_8$** and the subsequent self-assembly process. As expected, the lag phase observed was gradually shortened when doping the droplets with increasing concentrations of the final product **P$_{C8}$T$_8$** (Figure 17b).[121] To study the importance of the hydrophobic effect, competition experiments were carried out in the presence of a second reactive peptide bearing a shorter two carbon tail (**P$_{C2}$**). Thus, **P$_{C8}$** and **P$_{C2}$** were mixed in equal amounts inside the water droplets and reacted against each other by addition of **T$_8$**. HPLC analysis confirmed the faster reaction of the peptide precursor **P$_{C8}$** compared to its shorter analogue **P$_{C2}$**, as it could be expected from the less amphiphilic structure of **P$_{C2}$** and its product, **P$_{C2}$T$_8$**, which is unable to self-assemble into fibres (Figure 17c).[115]

To image the confined fibrillation process, water droplets containing the peptide precursor **P$_{C8}$** and ThT were placed on a microscopy slide and octanal (**T$_8$**) was added at the top-right end of the emulsion for it to diffuse and react across the slide (Figure 17d–f and Movie 2). After approximately 3 min, microfibrillar structures emerged from the lumen of the droplets and distributed homogeneously across the whole aqueous compartment (Figure 17d). Intriguingly, as the fibrillar networks grew longer and bundled together, fibres reorganized spatially from the core to the cortex of the water droplets (Figure 17e, f and Movie 3). Confocal fluorescence microscopy confirmed the accumulation of fibres at the cortex of the droplets by the end of the fibrillation–migration process, as found in z-stacked slices of droplets (Movie 4). As shown by pixel quantified time-lapse analysis, **P$_{C8}$T$_8$** fibrillation originates at both the

---

[121] Jain, A.; Dhiman, S.; Dhayani, A.; Vemula, P. K.; George, S. J. Chemical Fuel-Driven Living and Transient Supramolecular Polymerization. *Nat. Commun.* **2019**, *10* (1), 450–458.

interior and border of droplets at a very similar space, but after approximately 1 min, ThT emission in the edge starts increasing at the expense of that in the centre (Figure S1.5, t ~ 240 s), indicative of the outward movement of the fibres towards the border of the droplets. It is expected that free-floating $\mathbf{P_{C8}T_8}$ fibres, in random motion due to molecular thrust during self-assembly,[122,123] tend to accumulate at droplet boundaries with high local concentration of $\mathbf{P_{C8}T_8}$ monomers (*vide* infra surface tension assay), which should drive their elongation and bundling into larger assemblies at droplet edges.

Once found that confinement allowed the physically autocatalytic process and triggered a spatial reorganization of the microfibres within the water microdroplets, we focused our attention on the potential consequences that these coupled chemical and physical processes could have on the droplet containers. It was observed that, after fibrillation, droplets in proximity tended to maximize their physical contact with other droplets in close proximity and showed stochastic coalescence events that mixed the internal content of the fused droplets (Figure 18b and Movie 5). This coalescence, triggered by the formation of $\mathbf{P_{C8}T_8}$ and its supramolecular polymerization, can be assigned to the bundling of fibrillar networks at the cortex of adjacent droplets, resulting in the mixing and eventual fusion of the aqueous compartments (Movies 2 and 5). Dynamic surface tension[124] measurements showed that both the peptide precursor and the final amphiphile decreased the surface tension of the water phase (Figure S1.6), an effect that should stabilize the emulsion droplets,[125,126] thus ruling out variations in surface tension as the driving force for droplet coalescence. It should be noted that the surfactant Span 80 was employed in all water droplet experiments to stabilize the emulsions (Figure 17a). To investigate any potential interaction between this surfactant and the fibrillar assemblies, the β-sheet signal of $\mathbf{P_{C8}T_8}$ fibres was monitored by CD with increasing concentrations of Span 80, which showed nearly identical profiles for all cases (Figure S1.7). In addition, no morphological differences could be noticed in the bundling fibres within droplets or in the bulk buffer (Figure 16a and Figure 17e), further suggesting no significant interference of the non-ionic surfactant Span 80 in the growth and bundling of the supramolecular fibres (Figure 17a).

---

[122] Leckie, J.; Hope, A.; Hughes, M.; Debnath, S.; Fleming, S.; Wark, A. W.; Ulijn, R. V.; Haw, M. D. Nanopropulsion by Biocatalytic Self-Assembly. *ACS Nano* **2014**, *8* (9), 9580–9589.

[123] Inaba, H.; Hatta, K.; Matsuura, K. Directional Propulsion of DNA Microspheres Based on Light-Induced Asymmetric Growth of Peptide Nanofibres. *ACS Appl. Bio. Mater.* **2021**, *4* (7), 5425–5434.

[124] Miller, D. Dynamic Surface Tension: Industrial Applications and Characterisation of Commercial Surfactants. *Tenside, Surfactants, Deterg.* **2005**, *42* (4), 204–209.

[125] Schroën, K.; de Ruiter, J.; Berton-Carabin, C. The Importance of Interfacial Tension in Emulsification: Connecting Scaling Relations Used in Large Scale Preparation with Microfluidic Measurement Methods. *ChemEngineering* **2020**, *4* (4), 1–22.

[126] Bai, S.; Pappas, C.; Debnath, S.; Frederix, P. W. J. M.; Leckie, J.; Fleming, S.; Ulijn, R. V. Stable Emulsions Formed by Self-Assembly of Interfacial Networks of Dipeptide Derivatives. *ACS Nano* **2014**, *8* (7), 7005–7013.

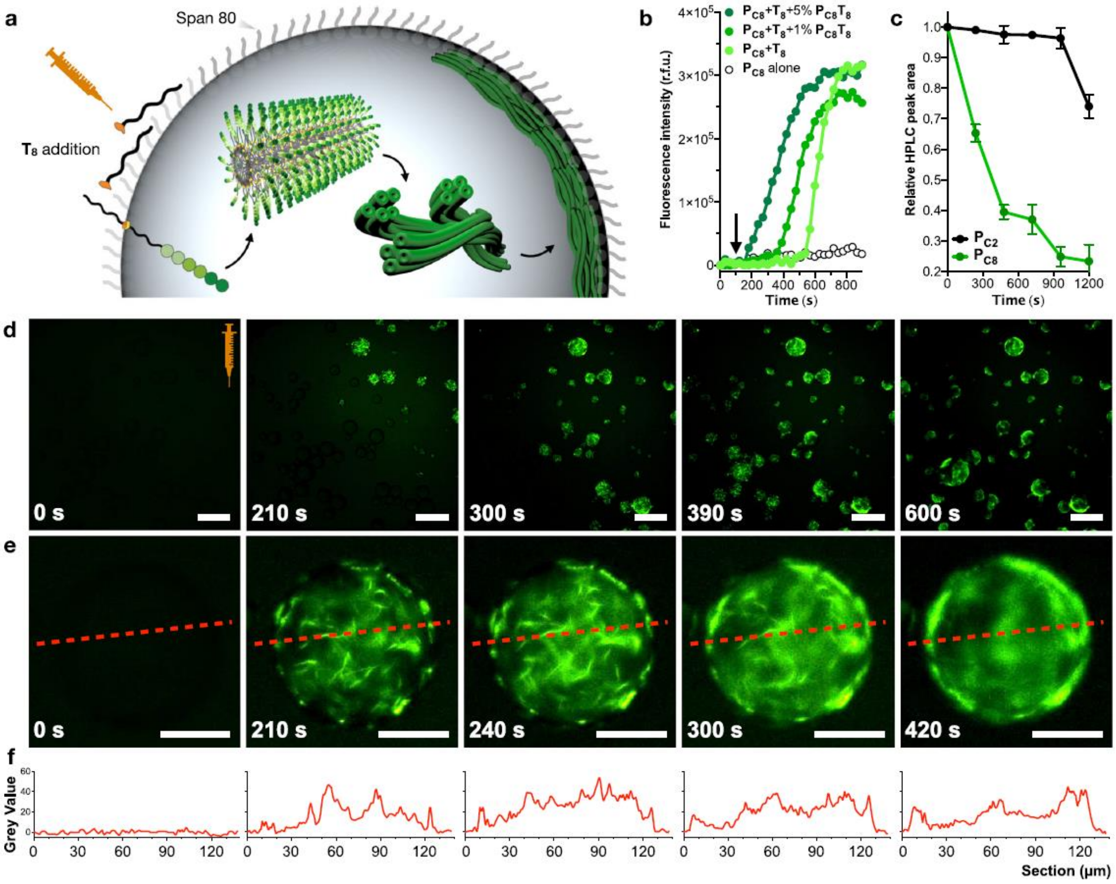

Figure 17. Physical autocatalysis in water-in-oil emulsion. A) Schematic showing the autocatalytic fibre forming reaction in aqueous droplets. Dormant **P_{C8}** *precursor loaded into the microdroplets reacts with* **T_8** *added to the external oil phase, thus triggering* **$P_{C8}T_8$** *production and fibrillation, ultimately generating cortical microfibrillar bundles at droplet interfaces. Note all droplets in this chapter contain the surfactant Span 80. B) Time-dependent ThT emission in the presence of the confined reaction between* **P_{C8}** *and* **T_8** *doped with their product* **$P_{C8}T_8$** *(1–5% mol, dark greens), no doping (light green) and negative reaction control without* **T_8** *(white). Octanal (***T_8***) is added to the samples after 100 s (arrow). C) Plots showing the competition between* **P_{C8}** *(green) and* **P_{C2}** *(black) in droplets; data collected by HPLC (222 nm); n=3 (mean ± SD). D, e) Fluorescence micrographs showing diffusion-dependent reaction after addition of* **T_8***. The syringe indicates the point of addition of* **T_8***. Scale bars =200 um (d) and 50 um I. f) Intensity profiles of droplets shown in e).*

3. Fibrillation-induced molecular uptake and coalescence

To further explore the interaction of droplets with their environment, the fibrillation process was studied in the presence of exogenous fluorescent probes possessing different physicochemical properties (Figure 18). Fibrillation experiments were initially performed in the presence of cationic Rhodamine 6G, which was quickly taken up inside droplets by the anionic fibrillar network (Figure 18d). Surprisingly, in addition to the uptake of this dye, an increase in the rate of droplet coalescence was observed compared to samples in the absence of any dye (Figure S1.8 and Movies 6a, b). This intriguing behaviour can be explained by the neutralization of anionic **$P_{C8}T_8$** fibres by this cationic dye, which shields charge repulsions between fibrillar networks and thus promotes the bundling of neighbouring fibres and droplet fusion (Figure 18b). Indeed, fibrillation experiments in the presence of the zwitterionic Rhodamine B dye showed efficient uptake of this dye but very limited droplet coalescence, reinforcing the role of the exogenous cargo to modulate fibre neutralization and droplet coalescence (Figure 18d, Movies 7a, b and Figure S1.8). An alternative cationic dye, Hoechst, which binds to the minor groove of double stranded DNA, confirmed the enhancement in droplet coalescence when the supramolecular fibres capture an oppositely charged molecule (Figure 18d, Figure S1.8 and Movie 8). Finally, the anionic dye TAMRA was explored as negative coalescence control of the proposed charge neutralization principle. As expected, this anionic dye showed a slight reduction in the coalescence degree of fibrillating droplets below the number of original events observed in the absence of any external dye (Figure 18c, Figure S1.8 and Movie 9). Pixel intensity analysis allowed the estimation of dye uptake, revealing higher uptake values for more cationic dyes: Hoechst ~ Rhodamine 6G > Rhodamine B > TAMRA (56% ~ 52% > 18% > 5% uptake; Figure S1.9). The extent of dye uptake follows the same trend as found for dye-mediated droplet coalescence (Figure 18c and Figure S1.10), in which cationic dyes (*i.e.*, Rhodamine 6G and Hoechst) induce fusion into larger droplet populations after anionic fibrillation, supporting the electrostatic foundation of fibrillar functionality.

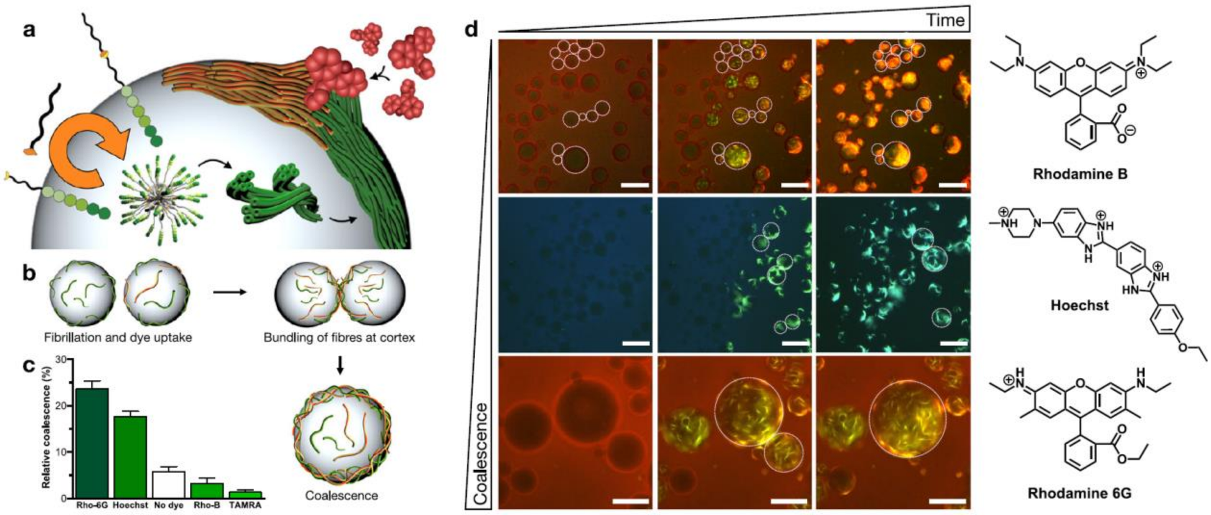

Figure 18. Fibre-mediated uptake of external molecules and droplet coalescence. a) Schematic showing fibre-forming autocatalytic reaction in a w/o emulsion triggering the uptake of external dyes. Note that Span 80 has not been drawn for clarity. b) Schematic showing dye-mediated coalescence of adjacent droplets induced by confined fibrillation. c) Relative coalescence of droplets undergoing fusion in the presence of external dyes (n ≥ 65, see Figure S1.10). These values are calculated as the relative increase (%) in average droplet diameter after the addition of **T_8** *(see Methodology Section). d) Fluorescence micrographs showing coalescence of adjacent droplets in the presence of different external dyes (see structures on the right). Contoured droplets are representative positive/negative coalescence examples. Scale bars= 80 um. All experiments contain ThT at 5 uM.*

4. Enzymatic cascade across droplet populations

Being able to trigger molecular uptake by confined supramolecular fibrillation, the possibility of inducing contact-based exchange of cargoes between droplet populations was envisioned.[32,127] ThT emission profiles along droplet contacts revealed the preferential accumulation of fibrillar bundles at the interface between contacting droplets (Figure S1.11). Such fibre focalization results from a partial inter-droplet bundling of fibres, which would generate tight contacts between neighbouring droplets to maintain their association and promote content exchange (Figure 19). To test this hypothesis, a two-step enzymatic cascade was incorporated into droplets, making substrate and product exchange between droplet populations necessary to generate a fluorogenic reporter at the end of the biocatalytic pathway (Figure 19a). Therefore, catalysts and substrates of the enzymatic cascade between glucose oxidase (GOx) and horseradish peroxidase (HRP) were orthogonally encapsulated into two different

---

[127] Mason, A. F.; Buddingh, B. C.; Williams, D. S.; Van Hest, J. C. M. Hierarchical Self-Assembly of a Copolymer-Stabilized Coacervate Protocell. *J. Am. Chem. Soc.* **2017**, *139* (48), 17309–17312.

populations of droplets.[128] In this coupled pathway, HRP uses H_2O_2, which is produced by GOx from glucose, to oxidase Amplex Red into fluorescent resorufin (red). DyLight 405 (blue) was attached to GOx to differentiate and visualize this droplet population. The two populations were mixed and **T$_8$** was added to the emulsion to initiate the fibrillation reaction while monitoring by fluorescence microscopy (Figure 19b and Movie 10a). The appearance of red fluorescence in the HRP droplets confirmed the completion of the biocatalytic pathway and hence the exchange of cargoes between the two droplet populations. HRP droplets (colorless) in proximity to GOx droplets (blue) showed a fast increase in red fluorescence (Figure 19b). The red emission found in blue Gox droplets confirmed the two-way exchange of substrates (*i.e.* glucose and Amplex Red) and products (*i.e.* H_2O_2 and resorufin) between populations, while macromolecular cargoes like blue tagged GOx remained unexchanged (Figure 19b and Movies 10a, b).

Red resorufin emission was observed at short reaction times before microfibrillation due to the assembly of short peptide 1D nanofibers, which could not be resolved by epifluorescence microscopy. The formation of these shorter 1D nanofibers was confirmed to occur right after **T$_8$** addition and to progressively bundle into larger microfibres with increasing reaction times (Figures S1.12). Individual droplet analysis demonstrated that populations in direct contact *via* cortical fibre clusters generate faster and more intense red emission than distant droplets (Movie 10b and Figure S1.12c). Control experiments in the absence of the fibrillation trigger **T$_8$** did not show any red-emitting droplets, demonstrating the role of the peptide fibres as transport and communication promoters between droplets (Figure 19c and Movie 11). It must be noted that emulsions are dynamic systems that can inherently exchange material across their discontinuous phase, a phenomenon that is promoted in the presence of amphiphilic molecules.[129,130] However, a control experiment with a non-fibrillating yet amphiphilic analogue, **P$_{C2}$T$_8$**,[115] showed a threefold lower red emission than **P$_{C8}$T$_8$**, supporting the role of supramolecular fibres in enhancing the exchange of chemicals between droplet communities (Figure 19d). Combining all experimental evidence, we propose a dual synergistic role of **P$_{C8}$T$_8$** in promoting droplet communication: (i) fibrillar bundles across droplet interfaces establish tight contacts that might generate local points of phase continuity, allowing the direct exchange of aqueous content (Figures S1.11); (ii) the amphiphilic nature of **P$_{C8}$T$_8$** can increase chemical transport and droplet cross-talk,[129,130] which would also be reinforced by the fibre-mediated clustering of droplets.

---

[128] Tang, T. Y. D.; Cecchi, D.; Fracasso, G.; Accardi, D.; Coutable-Pennarun, A.; Mansy, S. S.; Perriman, A. W.; Anderson, J. L. R.; Mann, S. Gene-Mediated Chemical Communication in Synthetic Protocell Communities. *ACS Synth. Biol.* **2018**, *7* (2), 339–346.

[129] Gruner, P.; Riechers, B.; Semin, B.; Lim, J.; Johnston, A.; Short, K.; Baret, J. C. Controlling Molecular Transport in Minimal Emulsions. *Nat. Commun.* **2016**, *7*, 10392–10400.

[130] Etienne, G.; Vian, A.; Biočanin, M.; Deplancke, B.; Amstad, E. Cross-Talk between Emulsion Drops: How Are Hydrophilic Reagents Transported across Oil Phases? *Lab Chip* **2018**, *18* (24), 3903–3912.

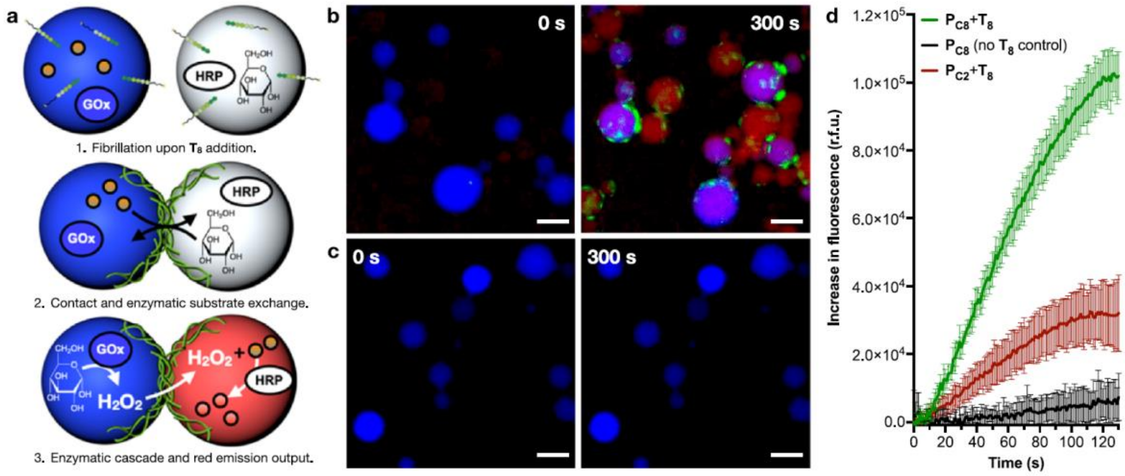

*Figure 19. Microfibre-mediated exchange of chemical contents between droplets to trigger a biocatalytic pathway. a) Scheme illustrating the steps involved in content exchange between droplets and resulting enzymatic reactions. The non-emissive Amplex Red precursor (orange dots) is converted into red emissive resorufin (red dots). b, c) Fluorescence micrographs before and 300 s after the addition of octanal (**T_8**). Experiments carried out in the presence (b) and absence (c) of the aldehyde precursor **T_8**. Scale bars = 70 um. All experiments contain ThT at 5 uM. d) Bulk red emission of emulsions containing both droplet populations, either in the presence (red) or absence (black) of **T_8**, corresponding to a fibrillating and non-fibrillating system, respectively. The red profile shows a control sample with both droplet populations loaded with **P_{C2}**, whose product **$P_{C2}T_8$** is unable to self-assemble into fibres;*[115] *n = 3 (mean ± SD).*

Field 2: Fluorescent probes for cellular compartments identification

1. C5.SNARF-1 and C6.SNARF-1 synthesis and characterization

A simple route of two synthetic steps was designed to prepare **C.SNARF-1**. This strategy was based on the previously described condensations between 1,6-dihydroxynaphtalene and resorcinols[92] or aminophenols,[92,94] depending on the desired benzo[c]xanthene member. In the first step, 3-dimethylaminophenol (3-DMAP) **1** is reacted with trimellitic anhydride (TMA) **2** in toluene, to obtain a mixture of the two positional isomers **5** and **6**. These two compounds are used without further purifications in the second and last synthetic step, the reaction with 1,6-dihydroxynaphtalene **7** to directly obtain the mixture of the two positional isomers of **C.SNARF-1** (Figure 20).

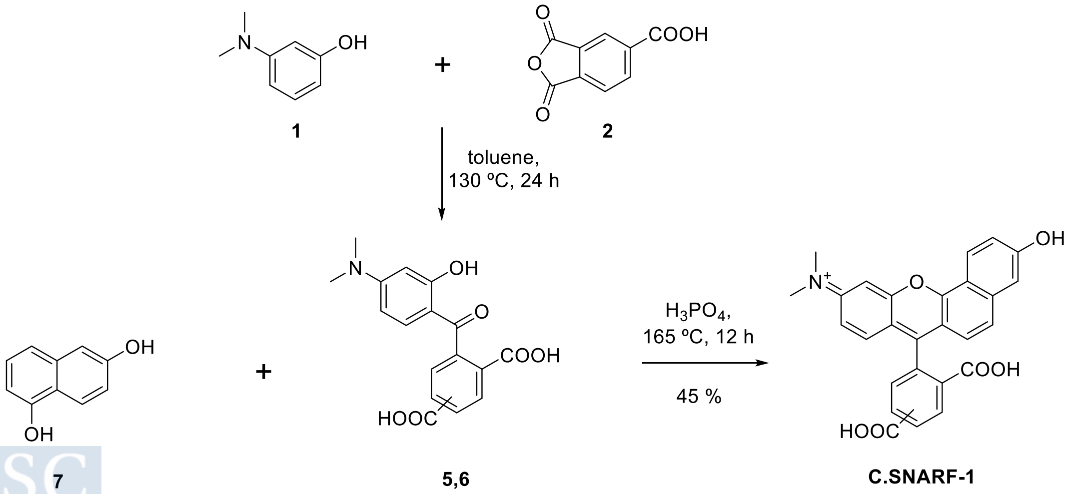

*Figure 20. Synthetic route employed to obtain **C.SNARF-1**.*

Regarding this synthetic route, it is important to comment that the two positional isomers are formed during the first reaction. This result is a consequence of the nucleophilic attack from 3-DMAP enolate to one of the two potential carbonyl groups in TMA. As the two TMA carbonyls have similar steric hindrance, a similar ratio of the **5** and **6** isomers is obtained (Figure 21).

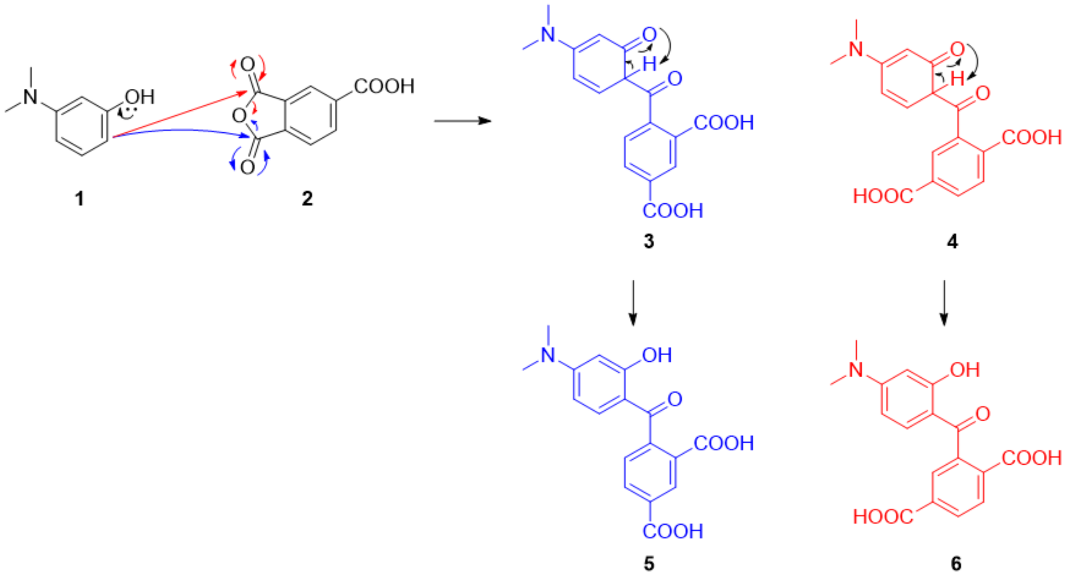

Figure 21. First synthetic step, where the mechanistic formation of the two isomers ***5*** *and* ***6*** *is shown.*

It should be mentioned that we could noticed the formation of **TAMRA** as an undesired side product during this first reaction. **TAMRA** fluorophore is formed by the reaction between the **5** and **6** diacids and the excess of 3-dimethylaminophenol **1** (Figure 22). **TAMRA** is always observed in TLC under UV light as a more retained yellow dot and it can be separated during **C.SNARF-1** chromatographic purification step (DCM/MeOH/formic acid 5:1:0.1) (Figure 23).

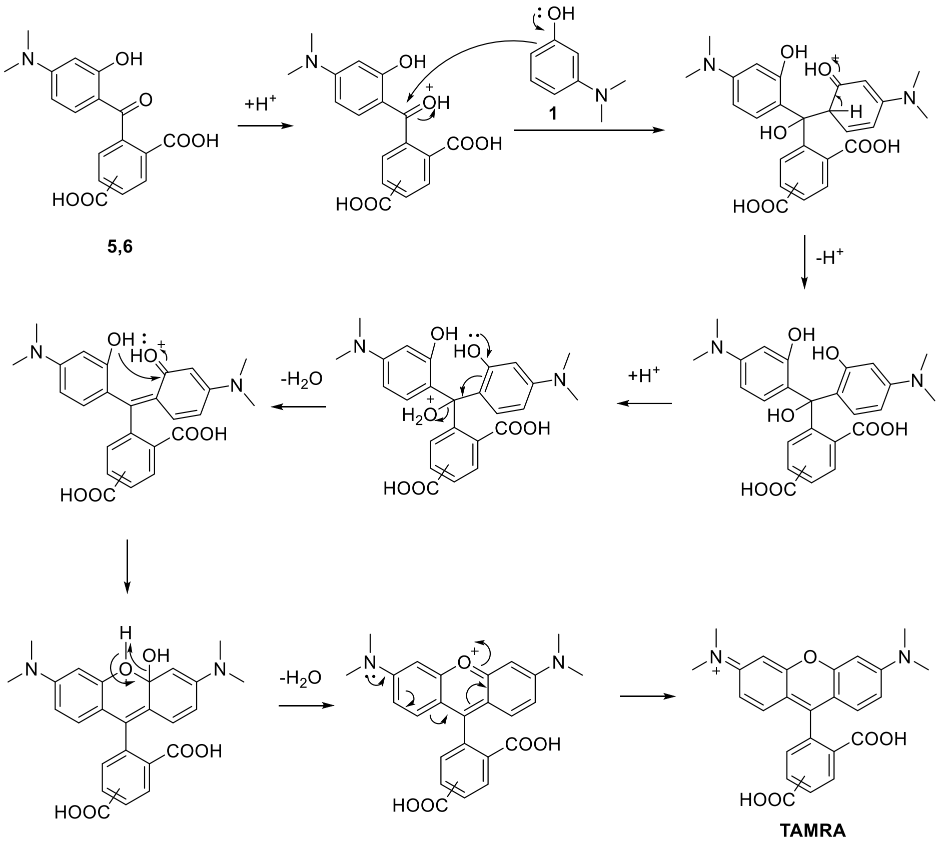

*Figure 22. Proposed mechanism for the side reaction that takes place between diacids **5**, **6** and the dimethylaminophenol **1** during the first step of the **C.SNARF-1** synthetic route, leading to the obtention of **TAMRA** fluorophore.*

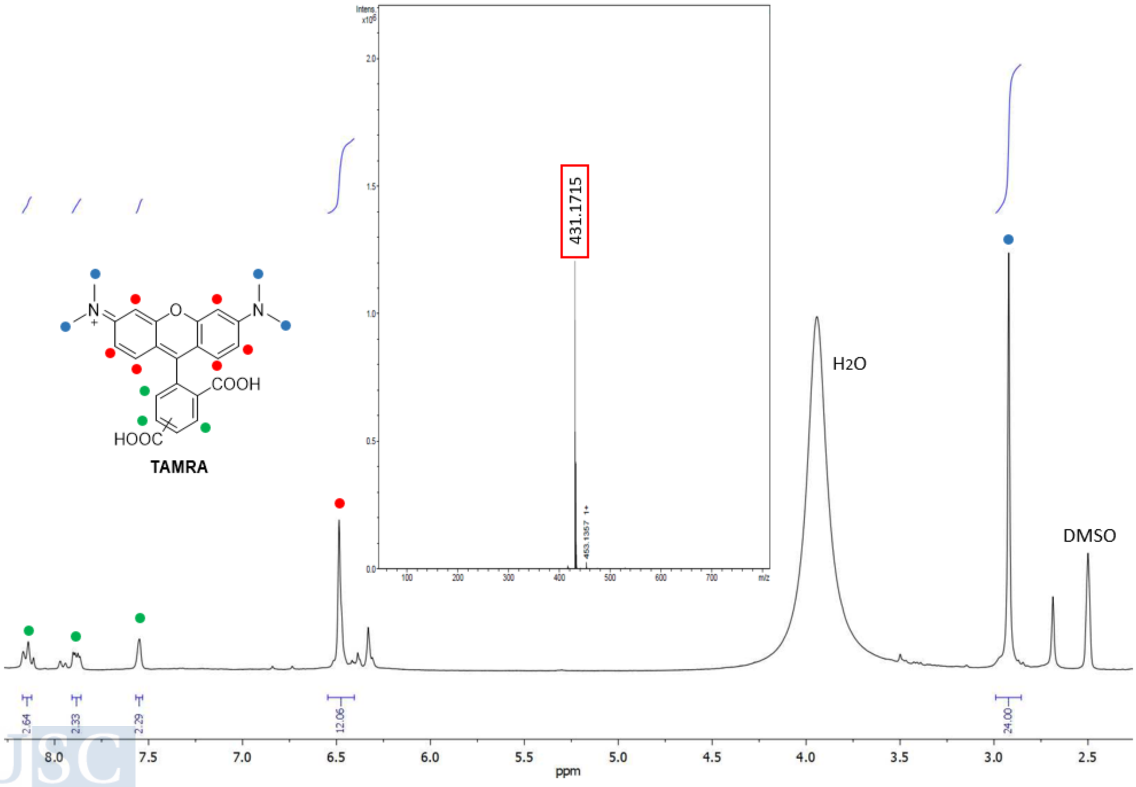

*Figure 23. **TAMRA** ^1H NMR in DMSO, where the chemical shift of each proton can be checked, and MS spectrum, where its corresponding mass is remarked in red.*

The resulting diacids **5** and **6** were then reacted with 1,6-dihydroxynaphtalene **7**, in the presence of phosphoric acid to give the mixture of **C.SNARF-1** positional isomers (Figure 20). We tried to optimize the reaction, so methanesulfonic acid was employed as solvent. The use of methanesulfonic acids allowed the reaction to take place in 15 minutes, while the reaction in phosphoric acid need to take place over night. However, analysis of the reaction crude by TLC showed a better reaction profile and less side products spots for the phosphoric acid. Thus, better isolated yields (~ 45 %) were obtained for **C.SNARF-1** with the phosphoric acid. If In addition, if the reaction is carried out in methanesulfonic acid, the chromatographic purification should be usually repeated (at least twice) and yields do not go over 20 %. Therefore, the reaction with phosphoric acid was selected for all future analogous condensations. It is also important to mention than, before chromatography, **C.SNARF-1** was first separated from crude impurities by precipitation in water. The water solvent from this precipitation step should be carefully removed under high vacuum to avoid problems in the chromatography.

Next, we tried to address the isolation of both **C.SNARF-1** positional isomers, **C5.SNARF-1** and **C6.SNARF-1**, which was not previously described in the literature. Unfortunately, it was not possible to achieve optimized chromatographic conditions to effectively separate both **C.SNARF-1** isomers. In all tested conditions, both compounds show almost the same retention factor. Therefore, we decided to alternatively perform the isolation of precursors **5** and **6**. Thus, fluorophores **C5.SNARF-1** and **C6.SNARF-1** would be then individually obtained by reacting 1,6-dihydroxynaphtalene **7** with intermediate compound **5** or **6** (Figure 24).

Interestingly, we could first isolate isomer **5** by crystallization in MeOH and filtration. The high purity of these crystals avoids the requirement of any chromatographic purification step, allowing a good isolation yield of 30%. However, the separation of the other positional isomer **6** from the small amounts of **5** and other impurities that remained in solution was more tedious and additional purification steps were required. A first chromatographic column (MeOH/DCM/formic acid 98:2:0.1) was performed to separate the two isomers from other impurities observed in reaction crude TLC. Then, a second column was required to properly separate the amount of **5** that remained in solution (MeOH/DCM/NH_3 7N in MeOH 50:50:0.1). Good isolation yield was obtained for the isomer **6**, with a 25 %.

The last condensation reaction of the individual isomers **5** and **6** with 1,6-dihydroxynaphtalene **7** afforded the **C5.SNARF-1** and **C6.SNARF-1**, respectively (Figure 24). The reaction conditions were analogous as the employed for the synthesis and purification of **C.SNARF-1**, but in this case using each individual isomer **5** or **6**, depending on the desired final product. **C5.SNARF-1** was obtained with a yield of 37 % in this second reaction (global synthesis yield of 11%); and **C6.SNARF-1** with a yield of 15 % in this second reaction (global synthesis yield of 4%). It should be noted for future synthetic efforts that high polarity and π-π stacking of this type of xanthene core dyes can enhance the self-aggregation and attachment to the silica during chromatography.

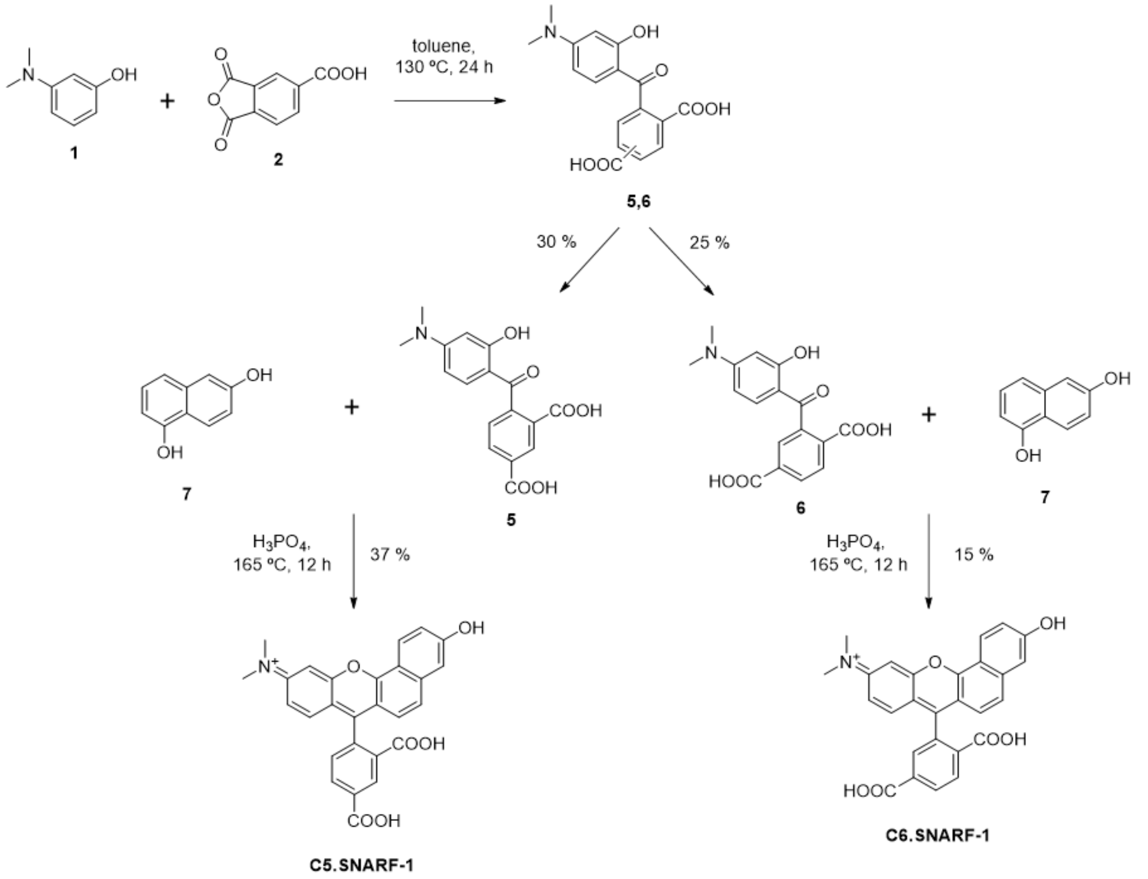

*Figure 24. Synthetic route to obtain separately **C5.SNARF-1** and **C6.SNARF-1**.*

After the purification of **C5.SNARF-1** and **C6.SNARF-1**, their photophysical characterization was carried out. When dissolved in water, both isomers showed a different colour at different pHs, going from pink in acidic media to violet in basic conditions. Under UV light, naked eye different fluorescent emission is also observed depending on the pH and according to their ratiometric behaviour: orange colour for acidic media, while pink colour for basic one (Figure 25).

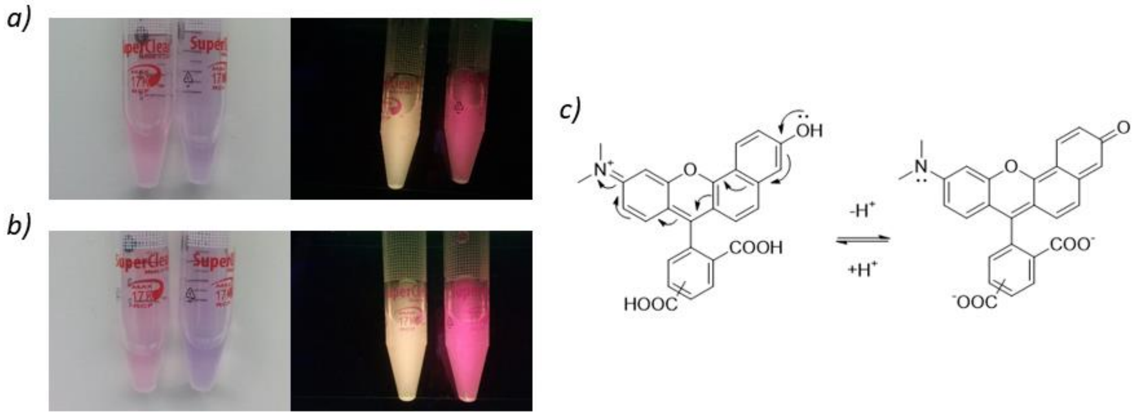

*Figure 25. a) **C5.SNARF-1** at acidic (left vial) and basic pH (right vial) under sun light (left image) and UV light at 480 nm (right image). b) **C6.SNARF-1** at acidic (left vial) and basic pH (right vial) under sun light (left image) and UV light at 480 nm (right image). c) **C.SNARF-1** structures at acidic (left) and basic pH (right), showing electronic movements of the push-pull system.*

The absorbance spectrum of the mixture of **C.SNARF-1** isomers matches well with the reported data for the commercially available **C.SNARF-1** mixture (ThermoFisher),[131] as shown in the methodology section (Figure S2.1). In the case of the absorbance of the two isolated positional isomers, **C5.SNARF-1** and **C6.SNARF-1** at different pHs, a similar pH dependence was also observed in both cases (Figure 26).

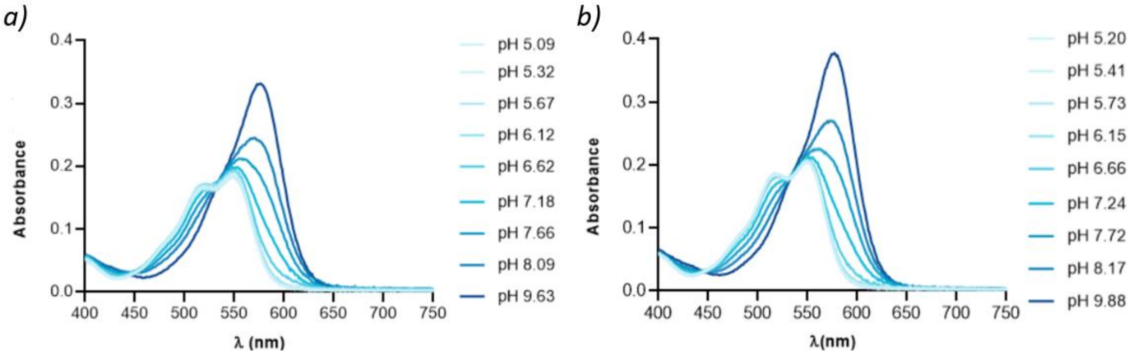

Figure 26. Absorbance spectrum of a) ***C5.SNARF-1*** *and b)* ***C6.SNARF-1****.*

Fluorescence spectra were then recorded at two different excitation wavelengths: 488 nm and 533 nm (Figure 27). The first wavelength at 488 nm was selected as one of the most common working wavelength of the microscopes, being therefore the most appropriated for future general imaging in living cells. A second wavelength of 533 nm was selected at the isosbestic point of absorbance spectra, where both acidic and basic forms will have the same absorbance. Spectra of **C.SNARF-1** mixture of **5** and **6** isomers were also recorded following the same protocol (available in methodology section, Figure S2.2.).

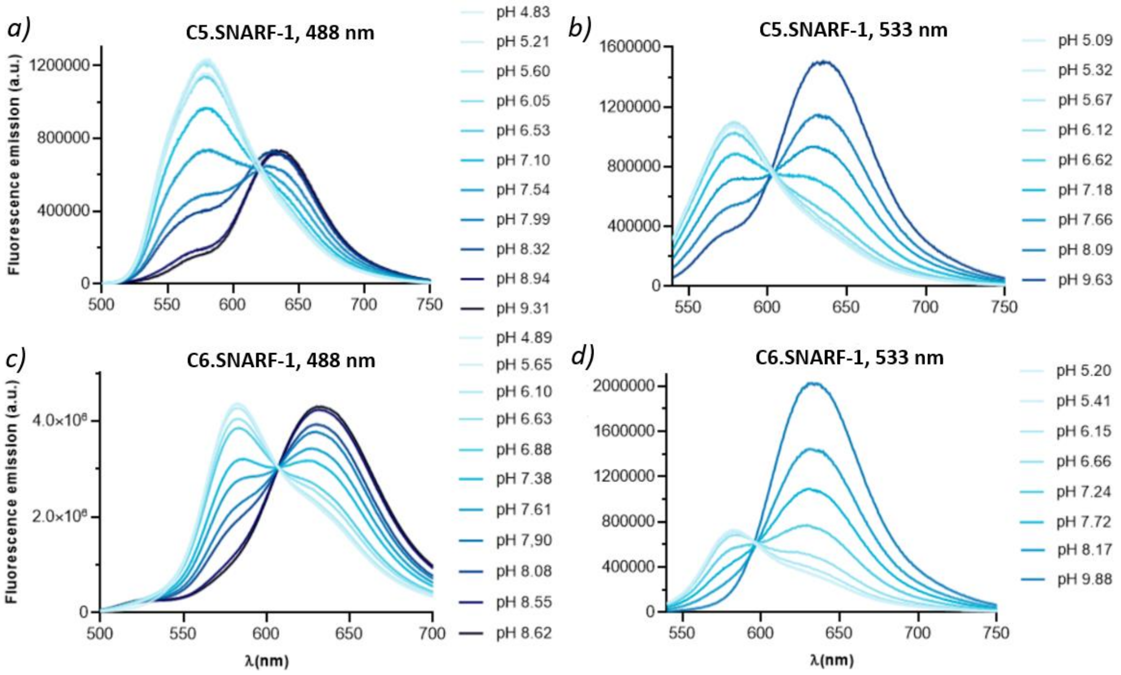

Figure 27. Fluorescence spectra of ***C5.SNARF-1*** *at excitation wavelength of a) 488 nm and b) 533 nm, and* ***C6.SNARF-1*** *at excitation wavelength of c) 488 nm and d) 533 nm.*

The emission bands of the acidic (584 nm) and basic (633 nm) forms were located at the same wavelength for both isomers. However, the ratio of the intensities between those two

---

[131] Snarf pH Indicators. *ThermoFisher Scientific.* https://assets.thermofisher.com/TFS-Assets/LSG/manuals/mp01270.pdf (accessed October 4th, 2022).

bands was different. In general, the basic band of **C6.SNARF-1** is more intense than the acidic band at each excitation wavelength. However, in the case of **C5.SNARF-1**, the basic band generally showed a lower emission intensity. Although the reason behind this decrease in the intensity is not clear, we speculate that a stronger stacking of the deprotonated form of the C5 isomer could be quenching the emission. The C6 carboxylic group of **C6.SNARF-1** would hinder this stacking as will be out of the plane after rotation of the phenyl ring (Figure 28). However, the C5 carboxylic group of **C5.SNARF-1** would be on the same plane than the xanthene ring.

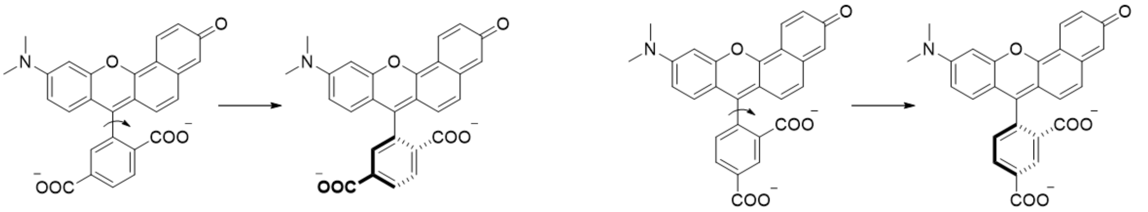

C6.SNARF-1

C5.SNARF-1

*Figure 28. Differences between the plane where the carboxylic group of **C5.SNARF-1** and **C6.SNARF-1** is positioned.*

By representing the intensity of the basic or acidic emission band against the pH (at λ_{exc} = 488 nm), the pK_a was calculated through GraphPad Prism “log(agonist) *vs* response -- Find ECanything” equation. When F value is fixed to 50, we are focusing on the middle of the sigmoidal curve: the inflection point. Therefore, obtained logECF parameter (F = 50) corresponds to pK_a value. Slight differences were observed between the pK_a obtained from the acidic or from the basic band representation, so real pK_a was considered as the average of both values. In the case of **C5.SNARF-1**, a pK_a of 7.66 was obtained, while for **C6.SNARF-1,** the obtained pK_a was 7.65 (Figure 29). Thus, we can conclude that does not exist a difference of pK_a between both positional isomers. Following the same protocol, the pK_a value obtained for the mixture of isomers of **C.SNARF-1** was 7.56, matching the already reported 7.5 value[114] (available in methodology section, Figure S2.3.).

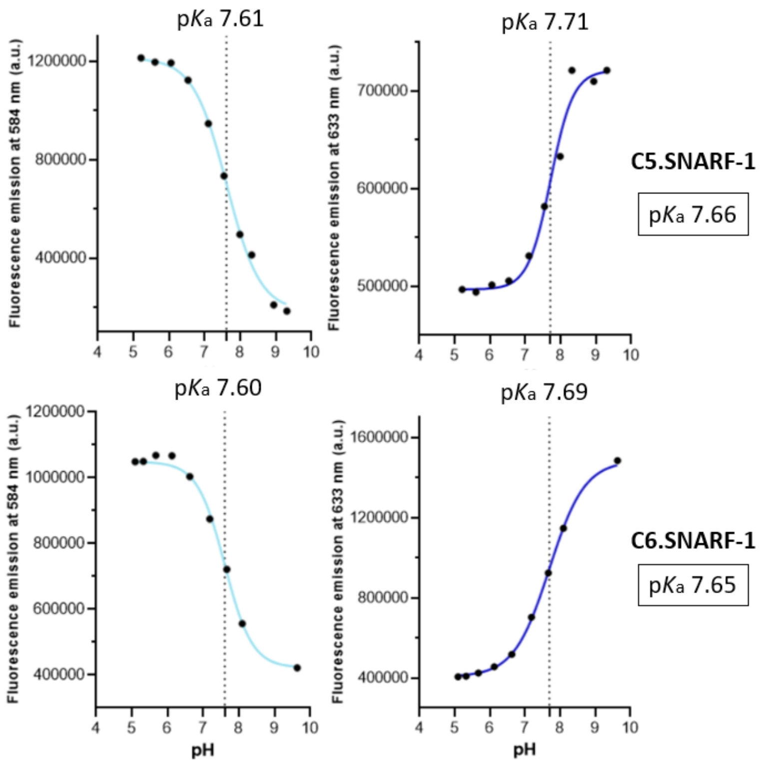

Figure 29. Graphs representing the variation of the fluorescence emission (at λ_{exc} = 488 nm) with pH for ***C5.SNARF-1*** *(up) and* ***C6.SNARF-1*** *(down), and their obtained pK_a values.*

2. Fluor C.SNARF-1 derivatives

For the preparation of the new fluor derivatives **C5.SNARF-2F** and **C6.SNARF-2F**, the synthetic approach was analogous to that of **C5.SNARF-1** and **C6.SNARF.1**. However, it was necessary to substitute the previously used dialcohol **7** (commercially available) by the 7-fluoronaphthalene-1,6-diol (**11**). The synthesis of this synthon can be easily achieved in 4 synthetic additional steps with a total yield of 18 % (Figure 30).

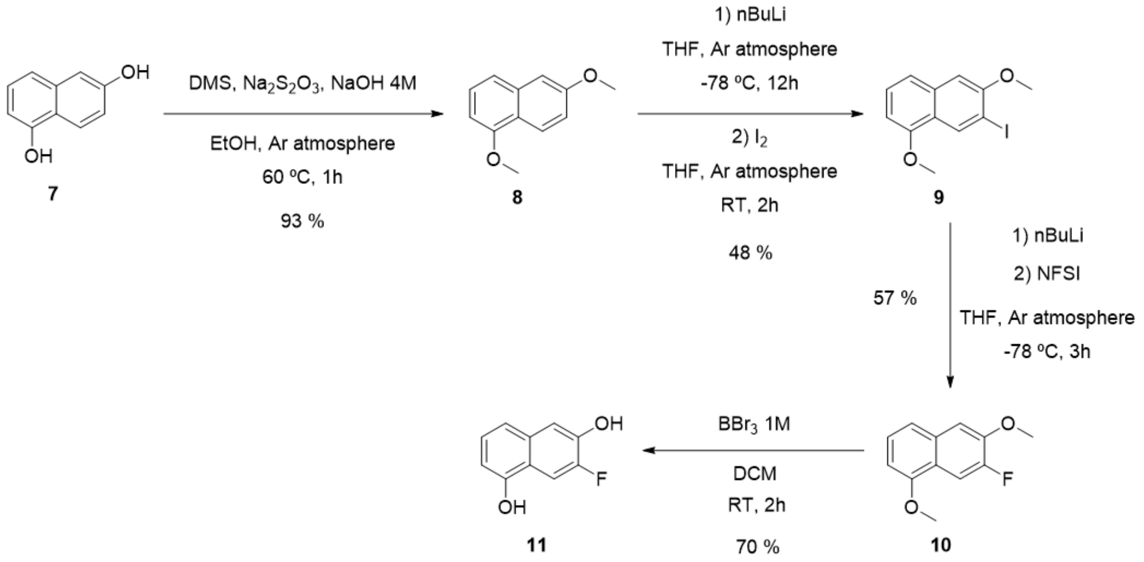

Figure 30. Synthetic route to prepare 7-fluoronaphthalene-1,6-diol ***12*** *from naphthalene-1,6-diol* ***7****.*

First, the two hydroxyl groups of **7** are methylated by reaction with dimethyl sulfate (DMS) in the presence of NaOH, leading to compound **8** with a yield of 93 %. Chromatographic purification is not needed, and it was possible to precipitate the product in water and isolate it in high purity by filtration. The product was characterized by ^{1}H NMR, where the signals of the new two methyl groups appear at 3.92 and 3.99 ppm (Figure 31).

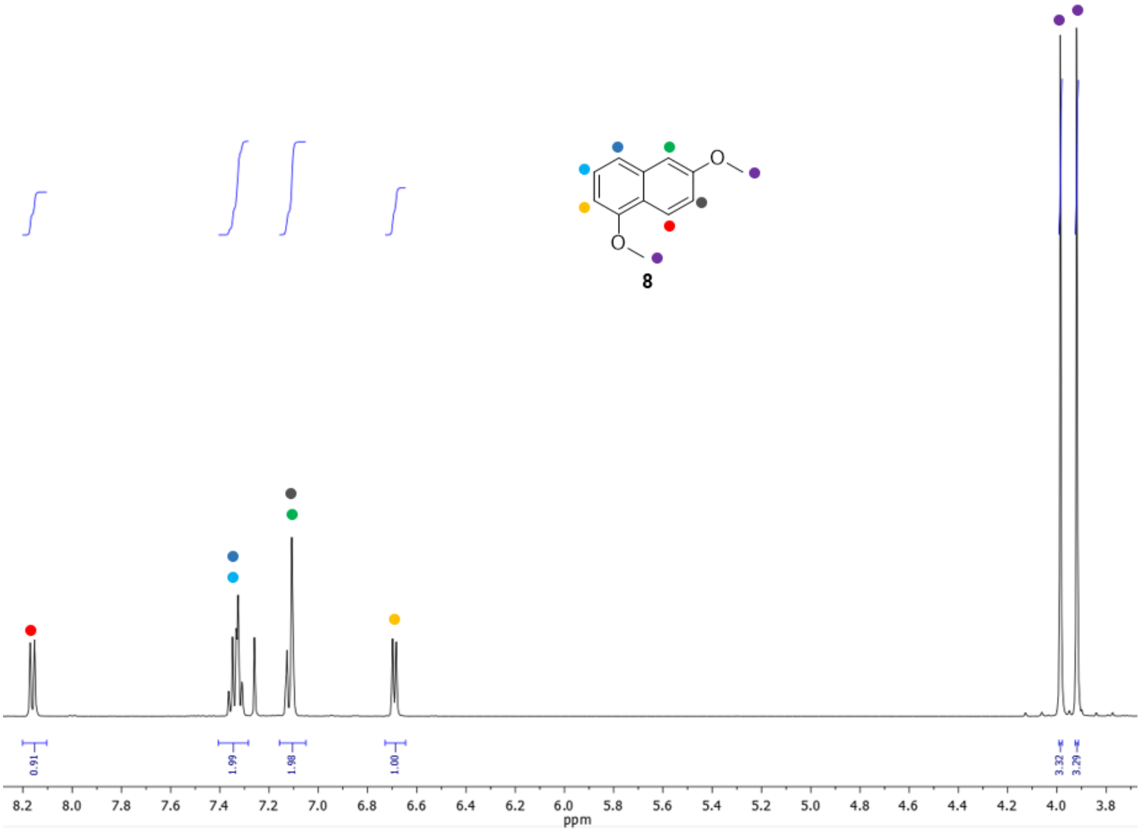

*Figure 31.Compound **8** ^{1}H NMR, where characteristic methyl signals are remarked in violet.*

Selective introduction of the iodine group at position 7 of the naphthalene core was achieved by treatment of compound **8** with *n*BuLi and trapping of the generated anion with I_2. The resulting final product **9** was obtained with a yield of 48 % after a chromatographic column (hexane/DCM 7:1).

Iodine to fluorine exchange was performed by treatment with *n*BuLi and trapping of the resulting ion with the *N*-fluorobenzenesulfonimide (NFSI) as fluorine electrophile. The reaction proceeded in THF solvent for a total of 3 hours at -78 °C. Once room temperature was reached, the reaction was quenched by addition of MilliQ H_2O. After extraction with AcOEt, the crude was purified by column chromatography (hexane/THF 100:5) to obtain compound **10** with a yield of 57 %. Fluorine insertion can be monitored by ^{1}H NMR by following the chemical shift of the protons in close proximity to the halogen. A small downfield (0.1 ppm) for proton 5 (green) and a strong upfield (1 ppm) for proton 8 (red) can be observed in compound **10** ^{1}H NMR. The strong shielding of proton 8 could be due to the impact of the electronegativity of fluorine atom, as compared to the iodine, for substituents in the *ortho* position. Moreover, the spin coupling between proton and fluorine nucleus in compound **10** caused the splitting of the signals of these protons, singlets in iodide derivative **9**, but doublets in the ^{1}H NMR of fluorinated compound **10**.

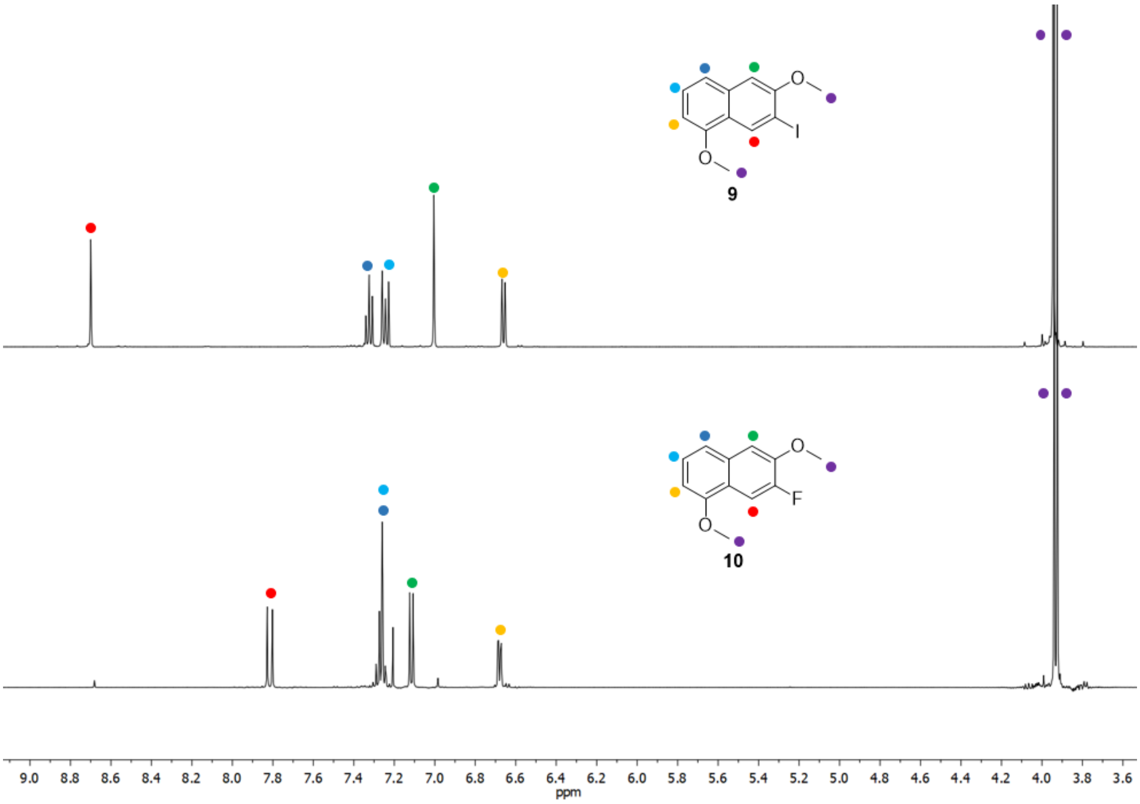

*Figure 32. Comparison between ^{1}H NMR of compounds **9** (up) and **10** (down), where the chemical shift of each proton can be checked.*

The subsequent methyl deprotection was achieved by treatment of **10** with BBr_3, leading to the dialcohol **11**, which was ready for reaction with isomers **5** and **6**. The deprotection proceeded in dried DCM solvent for 2 hours at RT, and the reaction was quenched by addition of ice. After extraction with ethyl ether, the reaction crude was purified by chromatography (hexane/ethyl ether 1:1) to yield product **11** with a 70 % yield. The ^{1}H NMR comparison between compounds **10** and **11** confirmed the disappearance of the methyl signal at ~3.9 ppm (Figure 33).

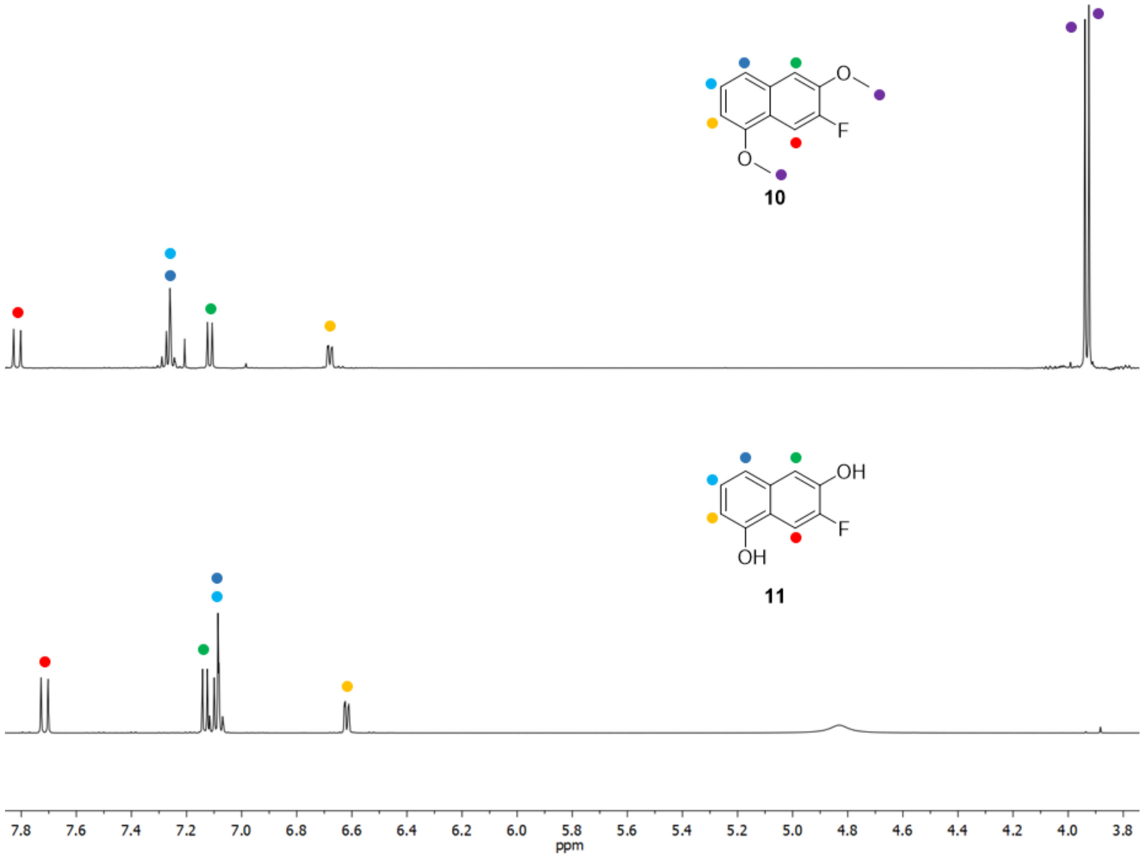

*Figure 33. Comparison between ^{1}H NMR of compounds **10** and **11**, where the disappearance of methyl signals is remarked in violet.*

An analogous synthetic route to the previously employed for the original **C.SNARF-1** isomers (see Figure 24), was also employed to prepare the fluor derivatives (Figure 34). Thus, it was possible to obtain separately both positional isomers **C5.SNARF-2F** and **C6.SNARF-2F**. Comparing with the original **C5.SNARF-1** and **C6.SNARF-1**, the fluorine derivatives require less polar conditions in their chromatographic purification. The original **C.SNARF-1** required DCM/MeOH/formic acid (9:1:0.1), while the fluorinated analogous could be purified with DCM/MeOH/formic acid (5:1:0.1) as mobile phase. The yields of these last reactions were 30 % for **C5.SNARF-2F**, and 76 % for **C6.SNARF-2F**. The **C5.SNARF-2F** was obtained with an overall yield of 2%, and the **C6.SNARF-2F** with an overall yield of 3%. Differences between the ^{1}H NMR of non-halogenated (**C.SNARF-1**) and halogenated (**C.SNARF-2F**) derivatives are exemplified with C5 derivatives comparison (Figure 35). Mainly observed differences are related with the proton disappearance when fluorine atom is introduced (dark green colour) and the upfield shift suffered by the proton in *ortho* to fluorine (orange colour). Also, analysis of the molecular ions ($[M]^+$) by HRMS showed clear m/z peaks of 454 and 472 for **C.SNARF-1** and the **C.SNARF-2F** compounds, respectively (Figure 36).

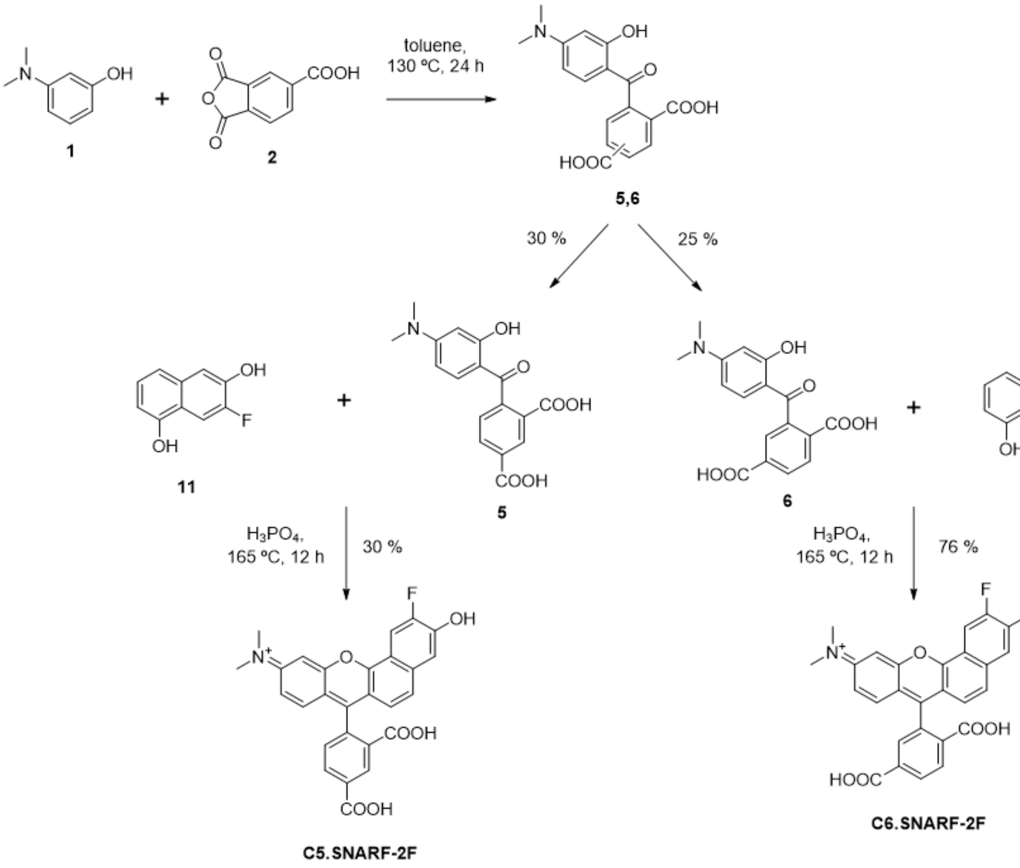

Figure 34. Synthetic route employed to obtain separately ***C5.SNARF-2F*** *and* ***C6.SNARF-2F****.*

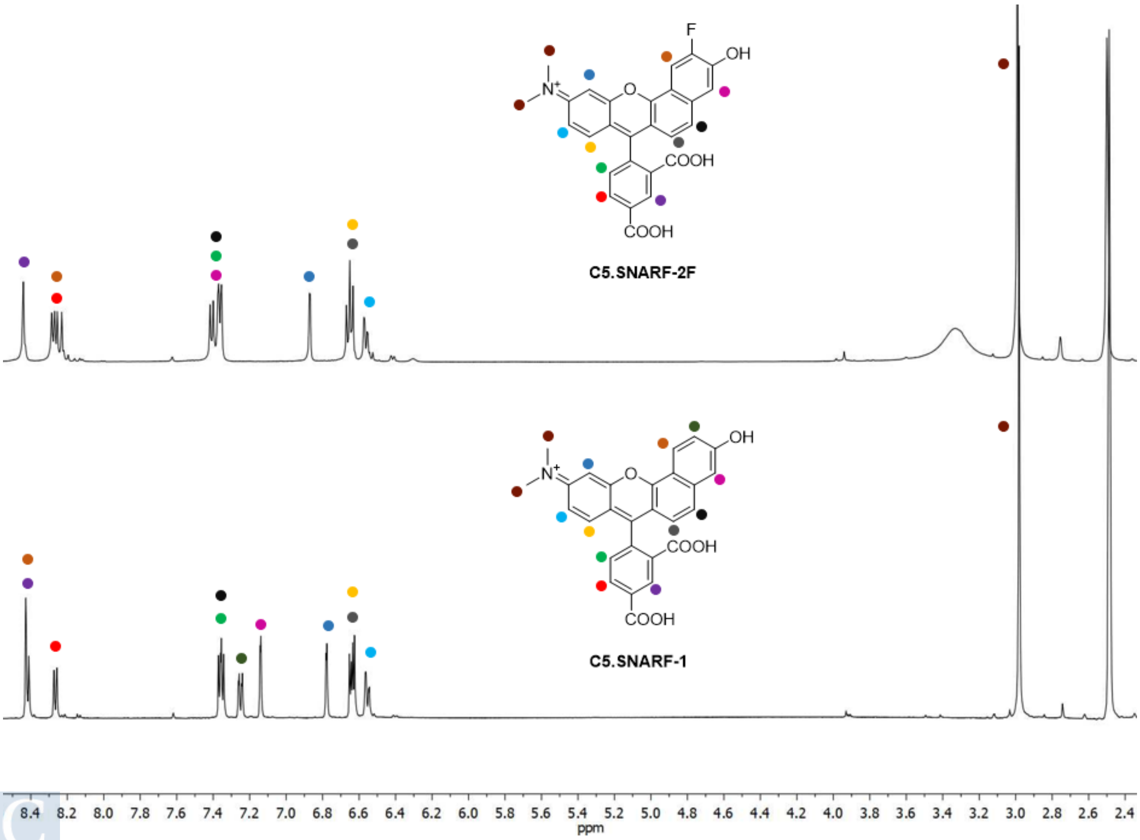

Figure 35. Comparison between ^{1}H NMR of compounds ***C5.SNARF-2F*** *(up) and* ***C5.SNARF-1*** *(down), where the chemical shift of each proton can be checked.*

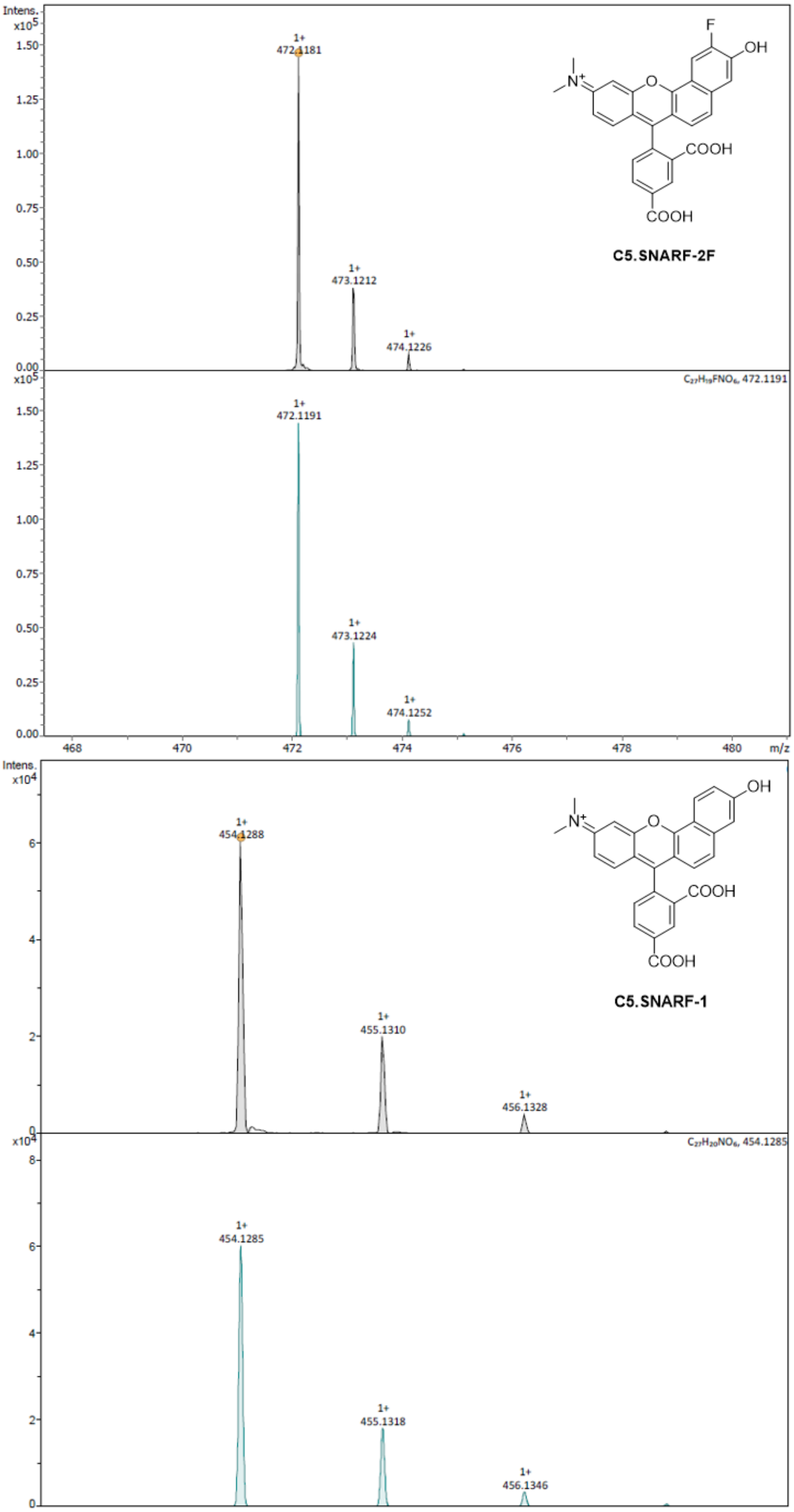

*Figure 36. HRMS of **C5.SNARF-2F** (up) and **C5.SNARF-1** (down).*

Having completed the synthesis of the **C.SNARF-2F** derivatives, their photophysical characterization was carried out. Absorbance spectra were first obtained at pH intervals in the range 4-10. Both isomers showed analogous spectra that were also comparable to the

C5.SNARF-1 and **C6.SNARF-1** ones with a slightly lower definition of the two absorbance bands. However, their absorbance wavelengths remain unaltered (Figure 37).

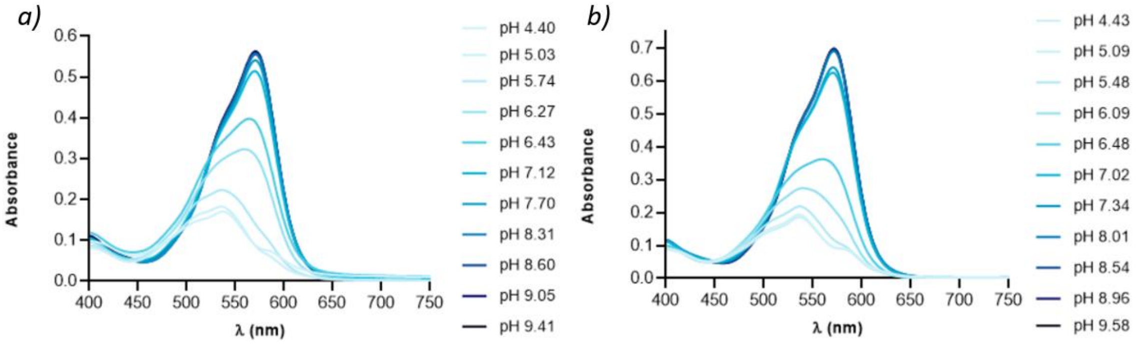

Figure 37. Absorbance spectrum of a) ***C5.SNARF-2F*** *and b)* ***C6.SNARF-2F****.*

The fluorescence emission, however, showed differences at the two selected excitation wavelengths (Figure 38):

- An hypsochromic shift is observed for the maximums emissions of the fluorinated analogues. The basic band, at 633 nm in non-functionalized **C.SNARFs-1**, is now located at 627 nm, while the acidic band, at 584 nm in **C.SNARFs-1**, suffered a stronger blue-shift up to 550 nm. This decrease in the maximum emission wavelengths could be explained by an increase of the energetic difference between the ground and excited electronic states, which would be due to the stabilization of the charge by the fluorine.

- Second, there is a decrease in the intensity of the acidic band, especially in the case of **C6.SNARF-2F**. Although probe precipitation was not experimentally observed, the reduction of intensity might be due to the chromophore stacking, or by a potential electronic effect that would decrease the emission of the acidic species. This decrease of the emission band of the acidic form has been previously reported for the SNARF-5F.[95] For both isomers, C5 and C6, an increase of the wavelength of excitation further reduce the basic/acidic band intensity ratio.

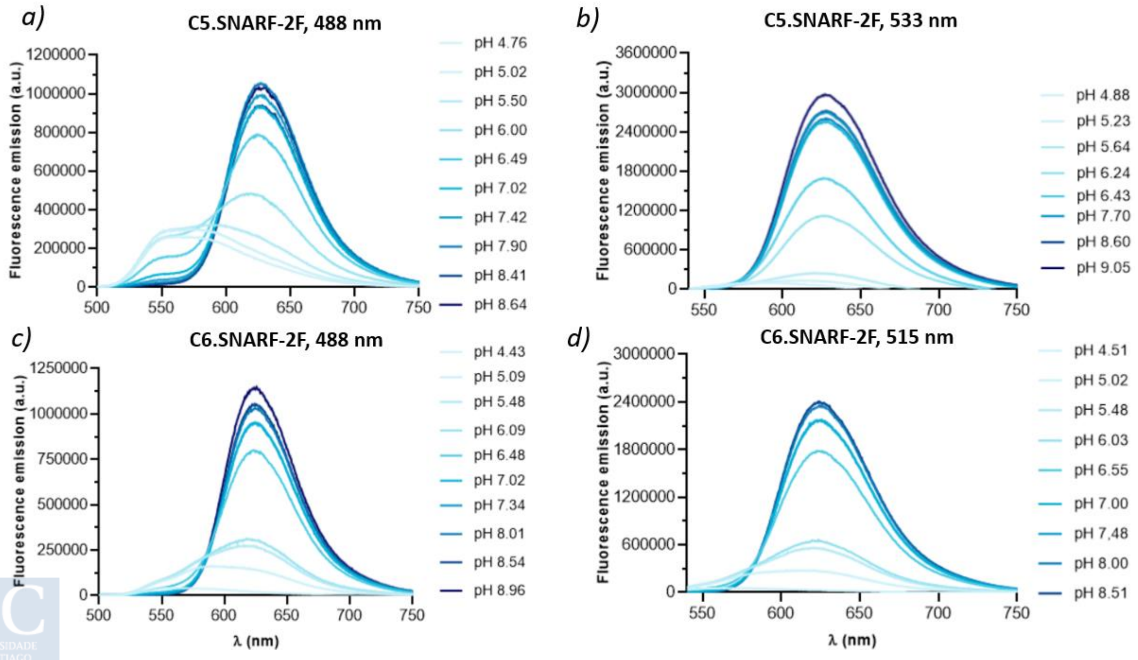

Figure 38. Fluorescence spectra of ***C5.SNARF-2F*** *at excitation wavelength of a) 488 nm and b) 533 nm, and* ***C6.SNARF-2F*** *at excitation wavelength of c) 488 nm and d) 515 nm.*

To determine their pK_a, the same protocol employed with **C.SNARF-1** was performed. Thus, the fluorescent basic emission pH (at λ_{exc} = 488 nm) was recorded against the pH and the obtained values were fit to a sigmoidal curve. Interestingly, both isomers present a lower pK_a, which turn these new molecules into suitable ratiometric fluorescent probes for cellular purposes. The obtained pK_a values are 6.16 and 6.21 for **C5.SNARF-2F** and **C6.SNARF-2F** respectively (Figure 39), which represents a decrease of 1.5 units of pK_a as compared with the original unsubstituted **C.SNARF-1**. To the best of our knowledge, the newly prepared **C5.SNARF-2F** is the **C.SNARF-1** derivative with the lower pK_a reported up to date, which turn this probe as an interesting candidate for tracking the lysosomal pH of carriers and/or cargo molecules.

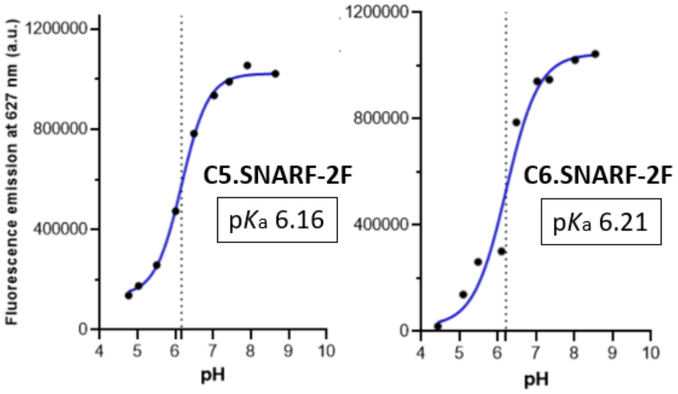

Figure 39. Graphs representing the variation of the fluorescence emission (at λ_{exc} = 488 nm) with pH for ***C5.SNARF-2F*** *and* ***C6.SNARF-2F****, and their value of pK_a obtained.*

When we compare our new fluorinated SNARF derivatives with previously reported ones, SNARF-5F and SNARF-4F,[95] important differences could be observed:

- Regarding SNARF-5F (Figure 40a), its fluorescent behavior is very similar to that shown by our **C6.SNARF-2F** (Figure 38c,d). Thus, emission bands are located at similar wavelengths: the acidic band is almost at the same wavelength (628 versus 627 nm) and the basic band is just 25 nm higher in the case of SNARF-5F (575 versus 550 nm). The acidic band is extremely quenched in both compounds, SNARF-5F and **C6.SNARF-2F**. However, the pK_a of SNARF-5F is considerably higher, with a reported value of 7.2, while our new compounds show a pK_a around 6.2 (Figure 39).

- Regarding SNARF-4F (Figure 40b), we can first note that the position of its fluorescence bands is different to that of our new fluorinated derivatives. Thus, SNARF-4F bands position (587 and 650 nm for acidic and basic form, respectively) is more similar to that shown by original **C.SNARF-1** compounds (584 and 633 nm for acidic and basic form, respectively) (Figure 27). Moreover, SNARF-4F acidic and basic fluorescence bands show the same intensity. However, its pK_a is slightly higher than in our **C5.SNARF-2F** derivative, with a reported value of 6.4. It is important to mention that SNARF-4F can be obtained with 3 % overall yield after 9 synthetic steps and as a mixture of isomers, while our **C5.SNARF-2F** single isomer can be obtained with 2 % yield after 6 synthetic steps.

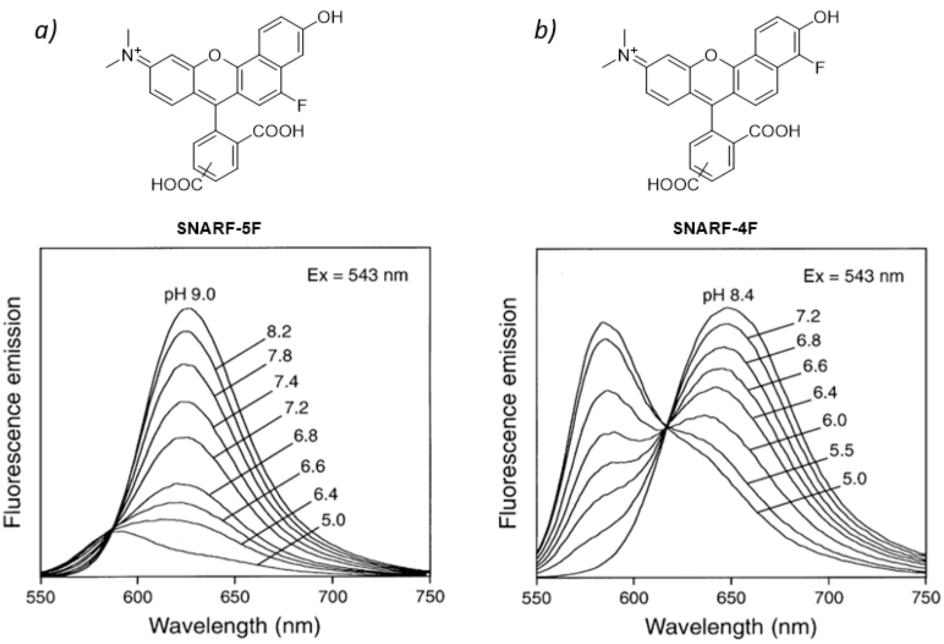

Figure 40. Fluorescence spectrum of previously reported fluorinated SNARF derivatives, a) SNARF-5F and b) SNARF-4F. [Adapted with permissions][95]

We next decided to introduce 4 fluorine atoms in the external phenyl ring in **SNARF-F-2F**, as this pattern has been already reported to additionally decrease the hydroxyl p*K*a.[94]

A similar route to that of Figure 34 was been employed, but substituting trimellitic anhydride by 4,5,6,7-tetrafluoroisobenzofuran-1,3-dione **12** in the first condensation reaction (Figure 41). The product of this first reaction is 2-(4-(dimethylamino)-2-hydroxybenzoyl)-3,4,5,6-tetrafluorobenzoic acid **13**, which only has one carboxy positional isomer, and thus leads to the desired **SNARF-F-2F** after condensation with **11** with a good overall synthetic yield of 5 %.

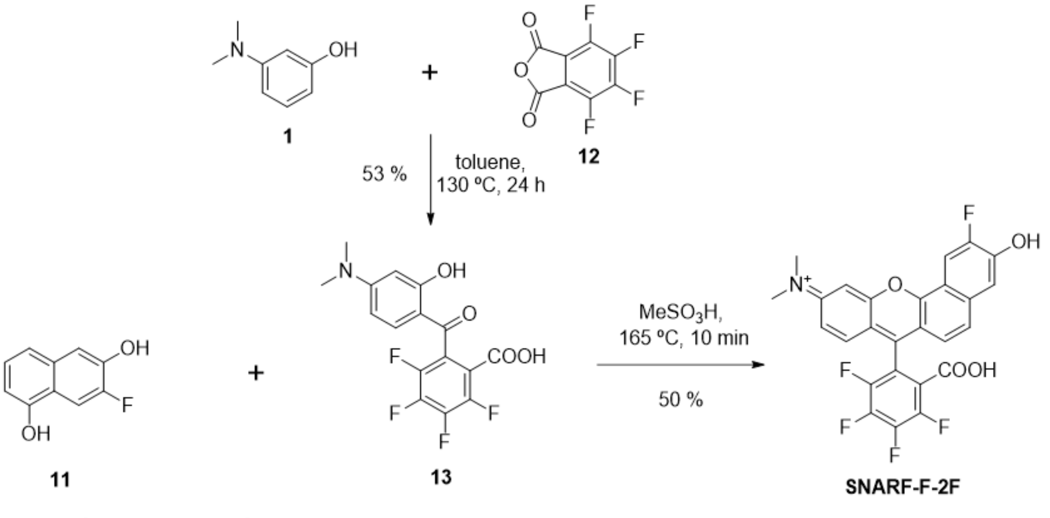

*Figure 41. Synthetic route to obtain **SNARF-F-2F**.*

Regarding the first synthetic step, compound **13** was prepared in the same conditions as compounds **5** and **6**. However, compound **13** was then purified in conditions DCM/MeOH/formic acid 9:1:0.1 (the same employed for **C5.SNARF-2F** and **C6.SNARF-2F** purification), affording the corresponding products with a 53 % yield. When characterizing compound **13**, it is important to note that the ^{1}H NMR is simpler than compound **5** ^{1}H NMR, as just three aromatic protons are now present (Figure 42).

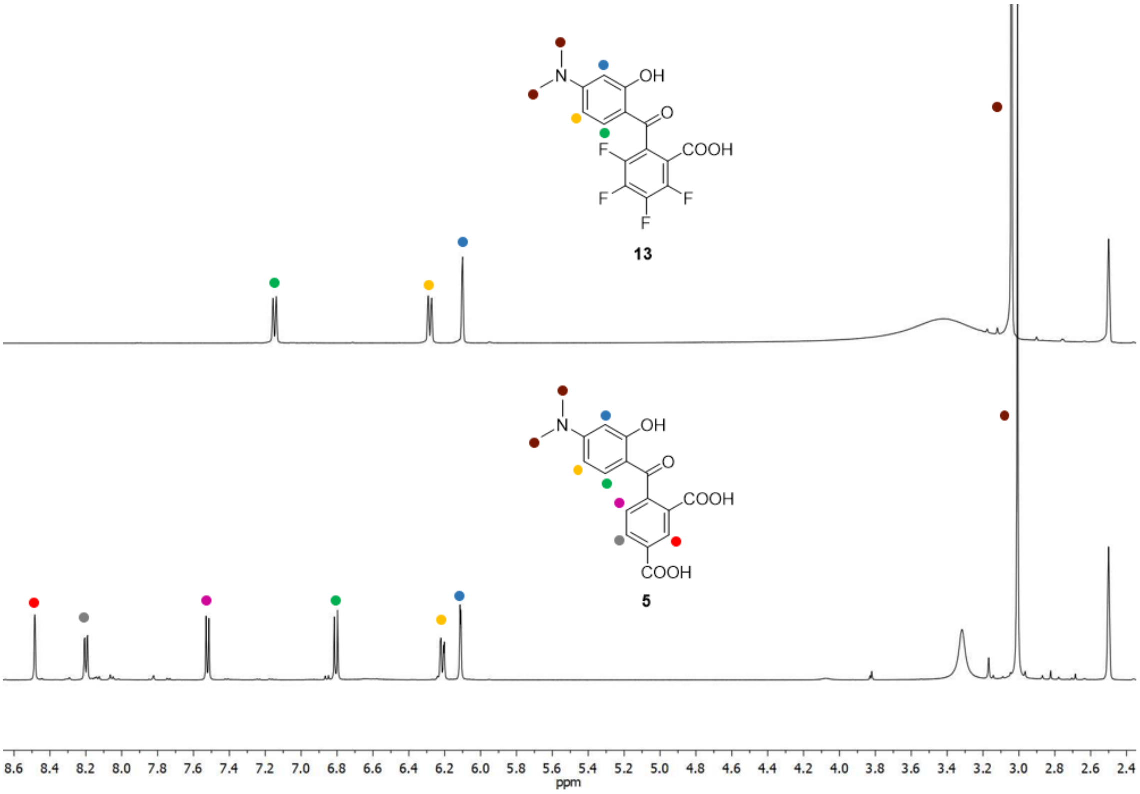

*Figure 42. ^{1}H NMR of compound **13** ^{1}H NMR (up) and compound **5** (down), where chemical shift of each proton can be checked.*

To prepare **SNARF-F-2F**, compound **13** reacted with fluorinated di-alcohol **11**. In this case, the use of $MeSO_3H$ as solvent gave good results, leading to fast reaction times (10 min) and a clean reaction crude. **SNARF-F-2** was obtained with a 50 % of yield by water precipitation. No chromatographic purification was required. Again, due to the reduction of proton signals, **SNARF-F-2F** ^{1}H NMR is considerably simpler than **C5.SNARF-2F** ^{1}H NMR (Figure 43).

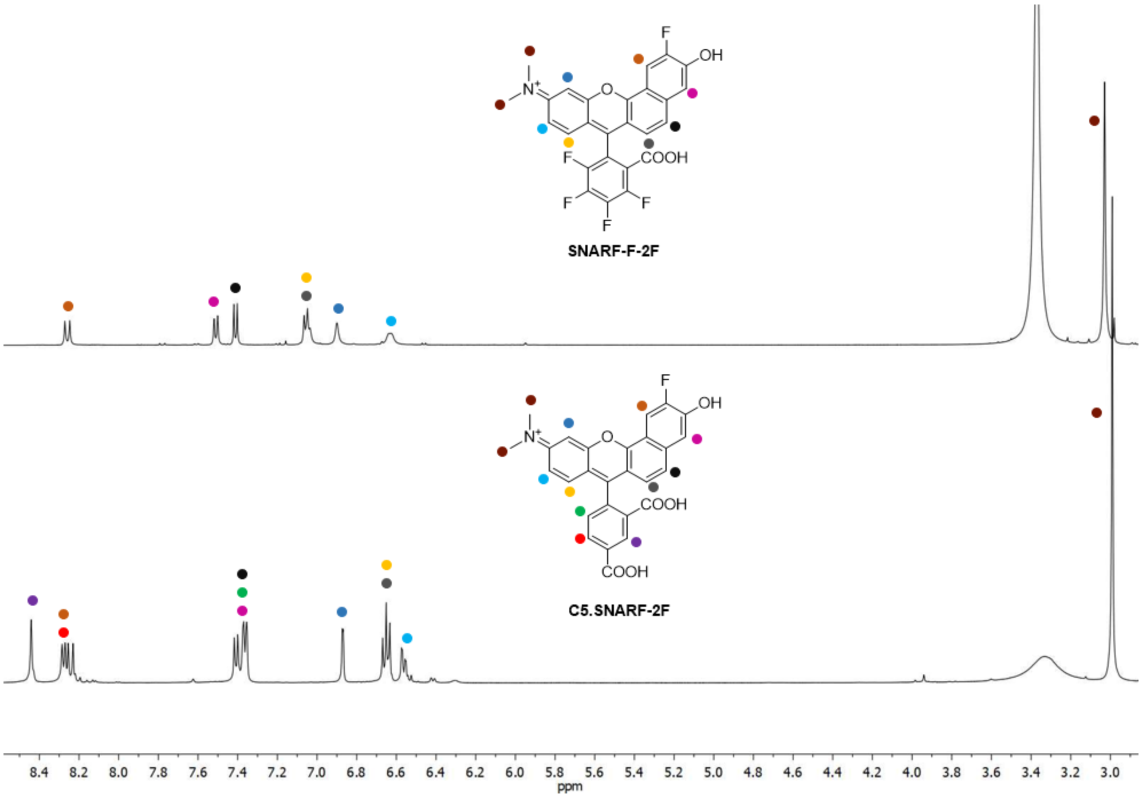

*Figure 43. ^{1}H NMR of **SNARF-F-2F** (up) and **C5.SNARF-2F** (down), where chemical shift of each proton can be checked.*

SNARF-F-2F absorbance spectrum showed two maximums at 550 and 600 nm that increase with basification (Figure 44a). The fluorescence emission of this perflourinated analogue showed a strong decrease in the acidic form emission that could affect its potential ratiometric properties. The relative intensity of this band was decreased at higher excitation wavelengths (Figure 44b,c). The obtained pK_a of 6.27 by fluorescence titration was similar to that of **C5.SNARF-2F** and **C6.SNARF-2F** (Figure 44d). We could conclude that the presence of fluorine atoms in the external phenyl ring affected the position of the fluorescent emission bands but did not influence the pK_a value, contrary to expectations. In previously reported cases,[94] the introduction of this perfluorinated pattern only reduced the pK_a in 0.2 units.

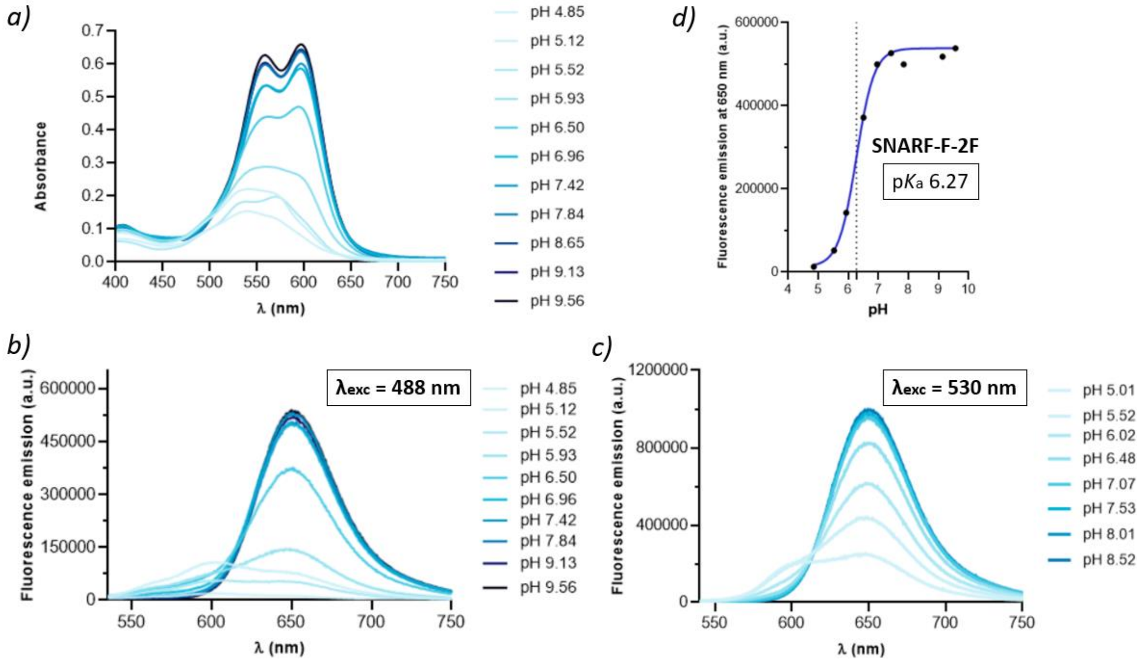

Figure 44. a) Absorbance spectrum of ***SNARF-F-2F****. Fluorescence spectra of* ***SNARF-F-2F*** *at excitation wavelength of b) 488 nm and c) 530 nm. d) Graph representing the variation of the fluorescence emission with the pH for* ***SNARF-F-2F*** *and its value of pK_a obtained.*

Field 3: New pH sensitive strategies for venom-derived antitumoral drugs

Section affected by confidentiality: under the protection of rights.

Methodology

Each field of application and systems developed were performed employed different methodologies, which can be consulted in the following section.

Field 1: Amphiphilic self-assemblies for protocellular study

The methodology presented in this field have been published in:

Booth, R. [a]; Insua, I. [a]; Ahmed, S. [a]; Rioboo, A. [a]; Montenegro, J. [a]* Supramolecular Fibrillation of Peptide Amphiphiles Induces Environmental Responses in Aqueous Droplets.
Nat. Commun. **2021**, *12 (1)*, 6421–6428.
DOI: 10.1038/s41467-021-26681-2

[a] Centro Singular de Investigación en Química Biolóxica e Materiais Moleculares (CiQUS), Departamento de Química Orgánica, Universidade de Santiago de Compostela (USC), 15782, Spain.

Nature Communications Impact Score: 16.6 (2022). Q1 in Biochemistry, Genetics and Molecular Biology; Chemistry; Physics and Astronomy.

1. General description of reagents and instrumentation

All reagents have been purchased to commercial brands as Sigma-Aldrich, TCI, Iris Biotech or Fisher Scientific and were employed with sale quality without further purification. Purified water was obtained from Millipore Milli-Q integral 5 water purification system.

For reactions monitorization, thin layer chromatography (TLC) with silica gel 60 F_{254} has been employed. For chromatographic purification, we have employed silica gel 60 (0.0015-0.0040mm).

Analytical HPLC was carried out using an Agilent 1260 Infinity II equipped with an Agilent SB-C18 column and connected to a 6120 Quadrupole LC-MS.

HR-MS was acquired using a Bruker MicroTOF instrument.

^{1}H NMR and ^{13}C NMR spectra were acquired using a Varian 300 MHz spectrometer or a DRX 500 MHz spectrometer. When analysing spectrums, chemical shifts (δ) were measured in ppm, while coupling constants (J) were measured in Hz. Also, following initials were employed: s (singlet), d (doublet), dd (doublet of doublets), m (multiplet), t (triplet), M (molecular ion).

2. Compounds synthesis and characterization

Methyl-8-bromooctanoate

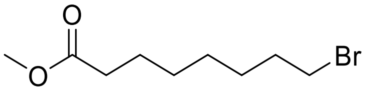

8-bromooctanoic acid (2 g, 8.96 mmol) was dissolved in 10 mL of methanol and stirred at room temperature for 10 min. H_2SO_4 (0.2 mL, 0.1 mL per gram of acid) was added and the solution was refluxed for 16 h. Methanol was removed under reduced pressure and afterwards the resultant solution was neutralized by addition of 10 mL of saturated $NaHCO_3$. The product was extracted from the aqueous solution by addition of DCM (3 x 2 mL). The organic phase was dried with anhydrous $MgSO_4$ and then removed under reduced pressure. The desired product was obtained as a light-yellow liquid (2.01 g, 95%).

NMR spectra: Compound already characterized[132] and commercially available.

---

[132] Perlikowska, W. Mikołajczyk, M. A Short Synthesis of Enantiomeric Phytoprostanes B1 Type I. *Synthesis* **2009**, 16, 2715–2718.

Methyl-8-[Boc](aminooxy)]octanoate

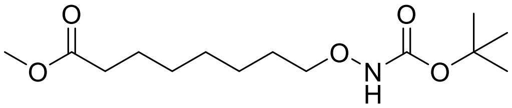

Methyl 8-Bromooctanoate (2 g, 8.44 mmol) was dissolved in anhydrous MeCN (40 mL), was kept under argon and stirred for 10 min at room temperature. *Tert*-butyl N-hydroxycarbamate (1.13 g, 8.44 mmol) and 1,8-diazabicyclo(5.4.0)undec-7-ene (3.78 mL, 25.32 mmol) were added and the solution was refluxed under argon for 16 h. The solution was neutralized by addition of saturated NH_4Cl (40 mL) and the subsequent solution was concentrated under reduced pressure. Once the MeCN was eliminated, the resulting aqueous solution was extracted by addition of DCM (3 x 15mL) to yield a yellow liquid which was purified by column chromatography (5:1 hexane/ethyl acetate) affording methyl-8-[boc](aminooxy)]octanoate as a colourless liquid (500 mg, 20 %).

^{1}**H NMR** ($CDCl_3$, 500 MHz): δ (ppm) 7.11 (s, 1H NH), 3.83 (t, *J*=6.6 Hz, 2H, OCH_2), 3.66 (s, 3H, OCH_3), 2.29 (t, *J*=7.5 Hz, 2H, $COCH_2$), 1.65-1.56 (m, 4H, CH_2 x 2), 1.47 (s, 9H, CH_3 x 3), 1.39-1.28 (m, 6H, CH_2 x 3).

^{13}**C NMR** ($CDCl_3$, 125 MHz): δ (ppm) 174.38 (C=O), 157.05 (C=O), 81.68 (*C*$O(CH_3)_3$), 77.17 (CH_2O), 51.58 (CH_3), 34.17 (CH_2), 29.15 (CH_2), 29.11 (CH_2), 28.37 (CH_3 x 3), 28.07 (CH_2), 25.82 (CH_2), 24.97 (CH_2).

HRMS (ESI): Calculated for $C_{14}H_{27}NNaO_5$: 312.1781; found: 312.1782 ($[M+Na]^+$).

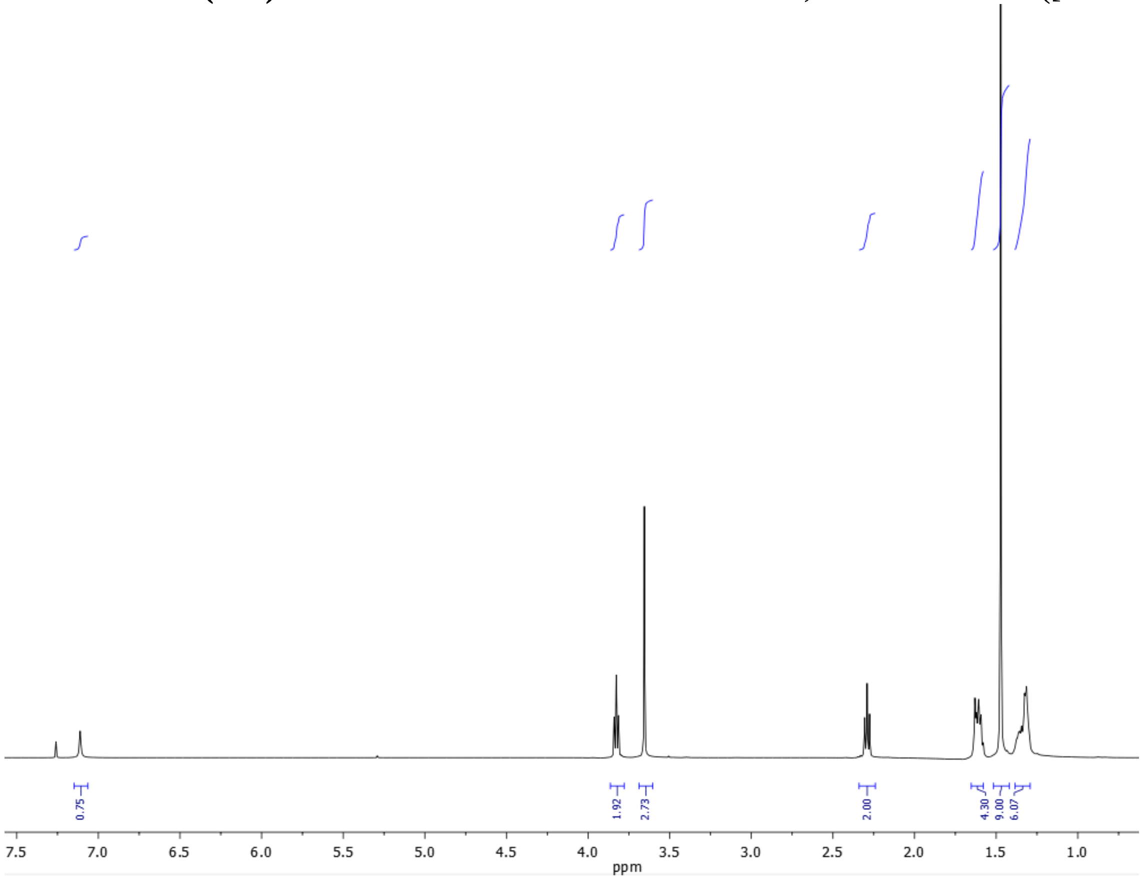

^{1}H NMR ($CDCl_3$, 500 MHz)

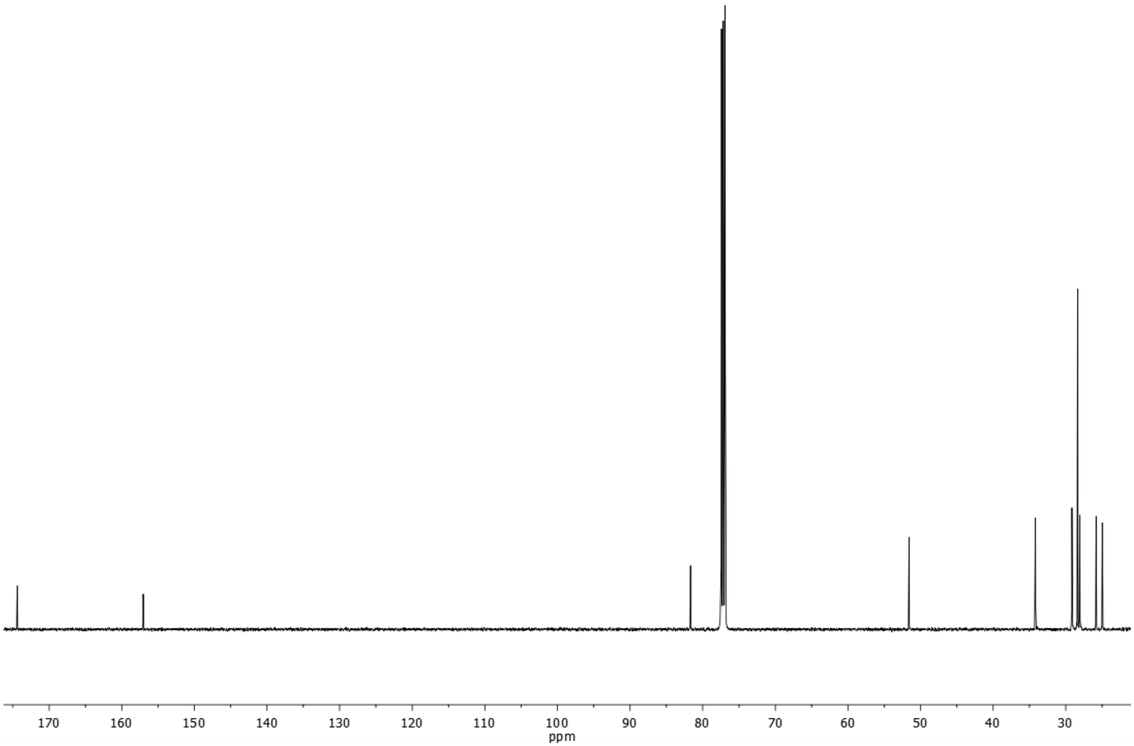

^{13}C NMR ($CDCl_3$, 125 MHz)

8-[Boc](aminooxy)]octanoic acid

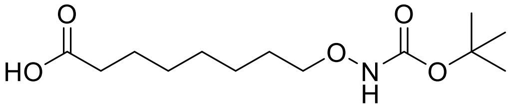

Methyl-8-[boc](aminooxy)]octanoate (350 mg, 1.21 mmol) was dissolved in 10 mL of methanol. To this solution, a solution of NaOH 2N was added until a white turbidity has been observed. The solution was stirred at 40°C for 3 h. The methanol was removed under reduced pressure and the subsequent aqueous phase was acidified to pH 3.5 by addition of HCl (10 %). The product was extracted from the aqueous solution by addition of DCM (3 x 10 mL). The organic phase was dried with anhydrous $MgSO_4$ and removed under reduced pressure to obtains the product as a colourless liquid (295 mg, 89 %).

^{1}H NMR ($CDCl_3$, 500 MHz): δ (ppm) 7.29 (s, 1H NH), 3.83 (t, *J*=6.6 Hz, 2H, OCH_2), 2.34 (t, *J*=7.5 Hz, 2H, $COCH_2$), 1.68-1.58 (m, 4H, CH_2 x 2), 1.48 (s, 9H, CH_3 x 3), 1.41-1.30 (m, 6H, CH_2 x 3).

^{13}C NMR ($CDCl_3$, 125 MHz): δ (ppm) 179.42 (C=O), 157.26 (C=O), 81.84 ($\mathit{C}O(CH_3)_3$), 77.18 (CH_2O), 34.05 (CH_2), 29.12 (CH_2), 29.03 (CH_2), 28.38 (CH_3 x 3), 28.06 (CH_2), 25.80 (CH_2), 24.71 (CH_2).

HRMS (ESI): Calculated for $C_{13}H_{25}NNaO_5$: 298.1625; found: 298.1625 ([M+Na]$^+$).

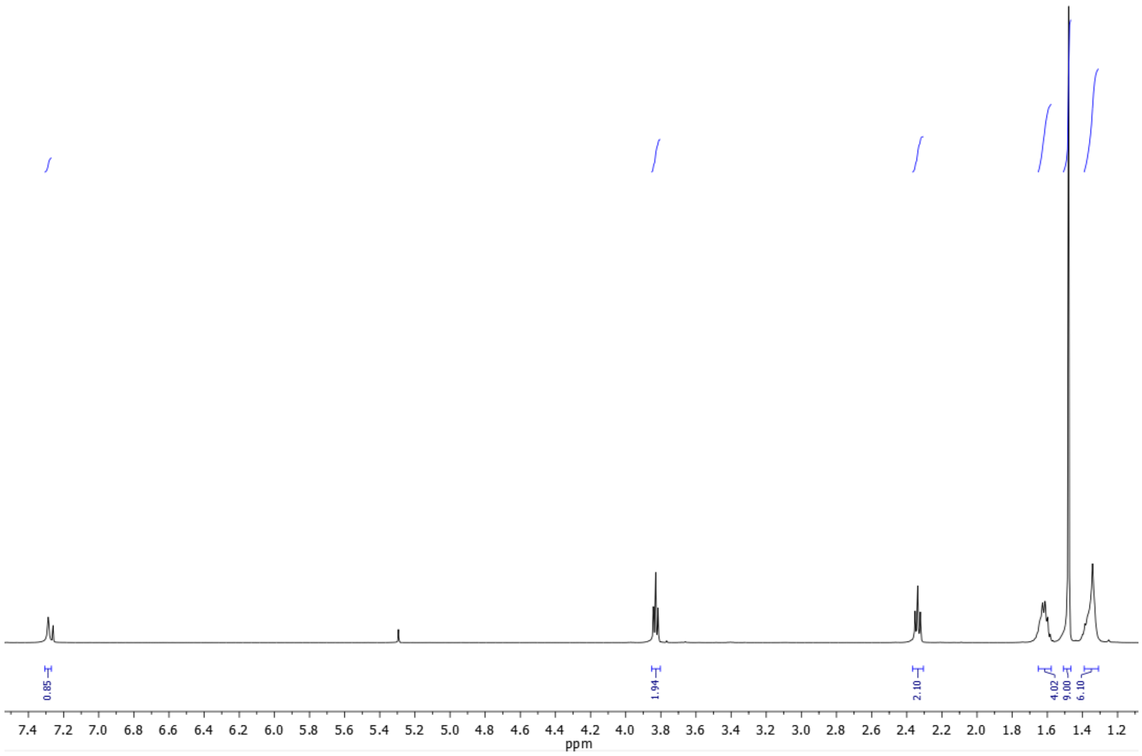

^{1}H NMR ($CDCl_3$, 500 MHz)

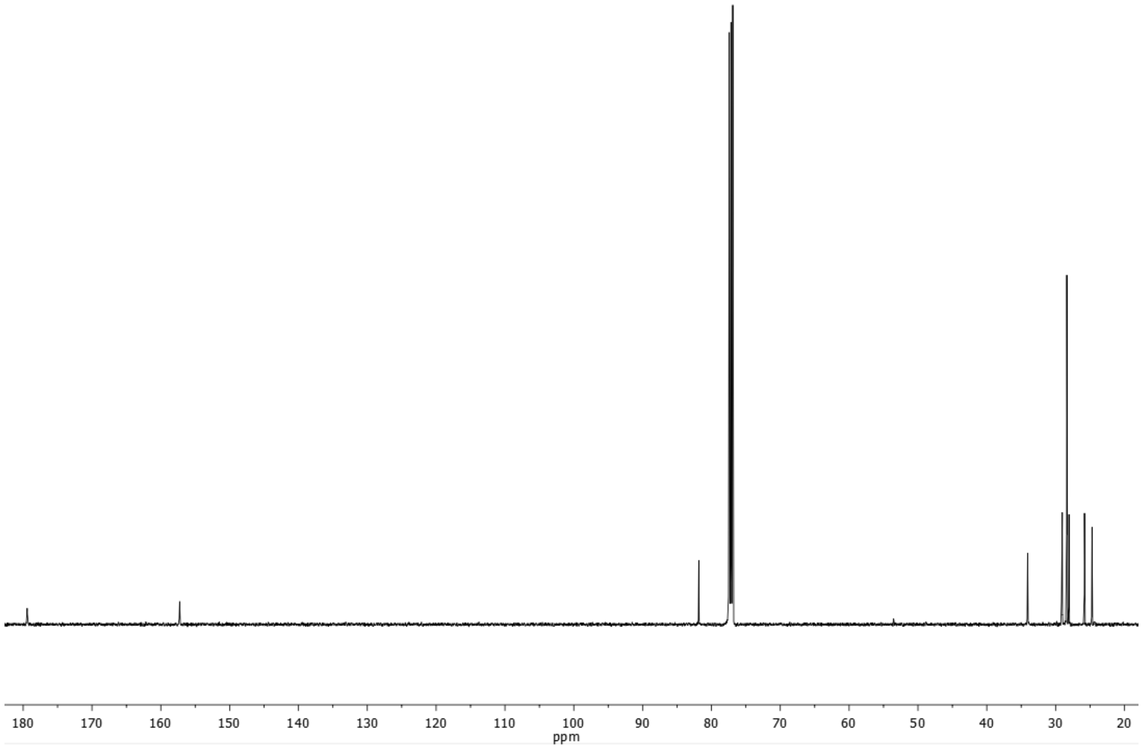

^{13}C NMR ($CDCl_3$, 125 MHz)

Peptide head (P_{C8} and P_{C2}) synthesis: General Procedure A

The peptide head was synthesized using Fmoc-Rink Amide resin (0.74 mmol/g) using standard solid phase peptide synthesis techniques. Each coupling was carried out using 3 equivalents Fmoc protected amino acid, 2.8 equivalents of *N*-HBTU and 4 equivalents of DIEA in DMF. The Fmoc protecting group was removed each time using 20 % piperidine in DMF. The 8-(Boc)octanoic acid or (Boc-aminooxy)acetic acid linker were added in the last step of the synthesis using 2 equivalents, 1.8 equivalents of *N*-HBTU and 3 equivalents of DIEA. The synthesized peptide was washed with DMF and DCM and was cleaved from the resin using a cocktail of TFA : DCM : TIS : H_2O (90:5:2.5:2.5 in % v/v). The resulting solution from the cleavage was concentrated reducing its volume with a N_2 flow, and the peptide was precipitated in diethyl ether afforded the crude peptide. It was purified by preparative HPLC from crude aqueous solutions of the peptide at approximately 10 mg/mL and filtered through 0.2 micrometres filters. The conditions of purification were H_2O (0.1 % TFA)/CH_3CN (0.1 % TFA) 100:0 (0→5 min), 100:0→50:50 (5→35 min).

P$_{C8}$

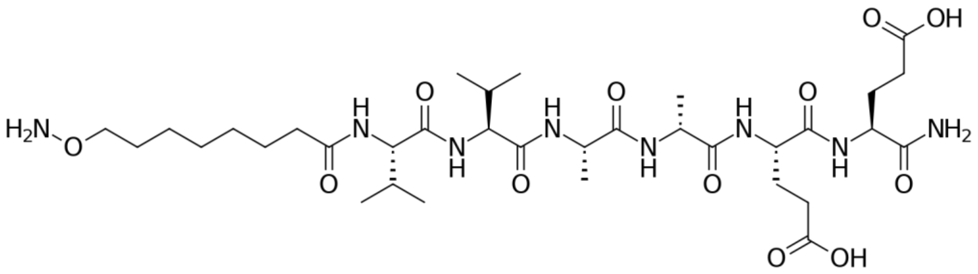

P$_{C8}$ was synthesized following the General Procedure A, starting from a 0.1 mmol scale of Rink Amide resin. The desired product has been obtained as a white powder (29.4 mg, 38 %).

^{1}H NMR (D_2O, 300 MHz): δ (ppm) 4.39-4.20 (m, 4H, Hα), 4.14-3.99 (m, 4H, Hα x 2 + aliphatic OCH_2), 2.53-2.41 (m, 4H, Asp -CH_2- x 2), 2.34-2.22 (m, 2H, aliphatic $COCH_2$), 2.20-1.91 (m, 6H, Asp -CH_2- x 2 + Val -CH- x 2), 1.72-1.49 (m, 4H, aliphatic CH_2 x 2), 1.43-1.22 (m, 12H, Ala -CH_3 x 2 + aliphatic CH_2 x 3), 0.98-0.84 (m, 12H, Val -CH-(CH_3)$_2$ x 2).

ESI-HPLC (C18, H_2O (0.1 % TFA)/CH_3CN (0.1 % TFA) 100:0 (0→2 min), 100:0→50:50 (2→15 min), ESI, +*e*V). R*t* = 11.2 min. m/z = 773.5 (100, $[M+H]^+$), 387.4 (24, $[M+2H]^{2+}$).

HRMS (ESI, m/z): Calculated for $C_{34}H_{61}N_8O_{12}$: 773.4403; found: 773.4408 ($[M+H]^+$).

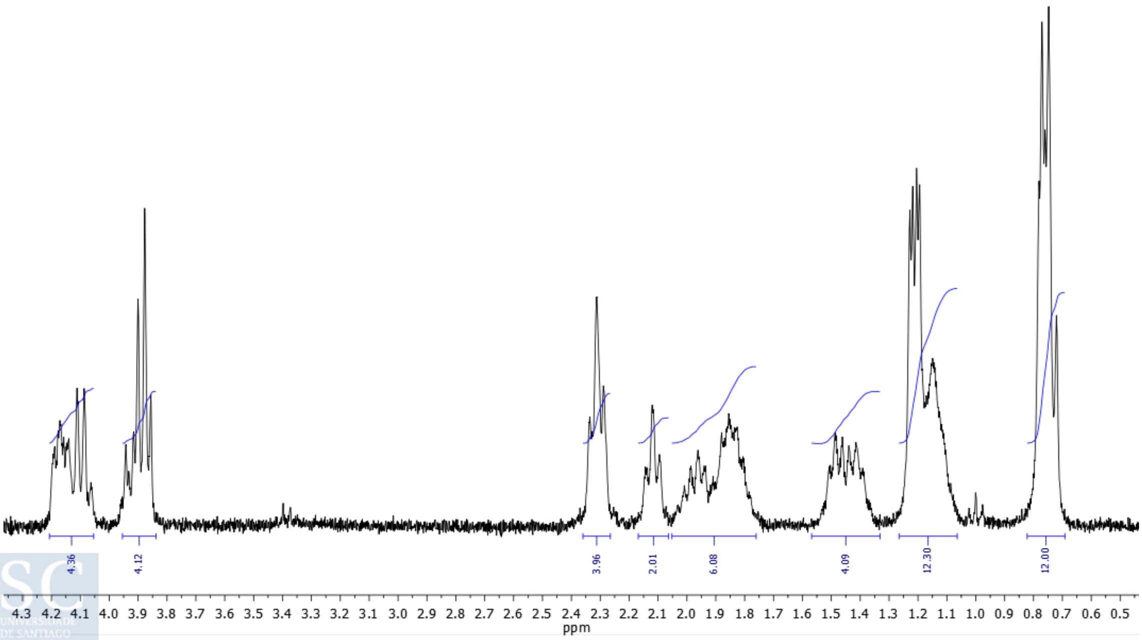

^{1}H NMR (D_2O, 300 MHz)

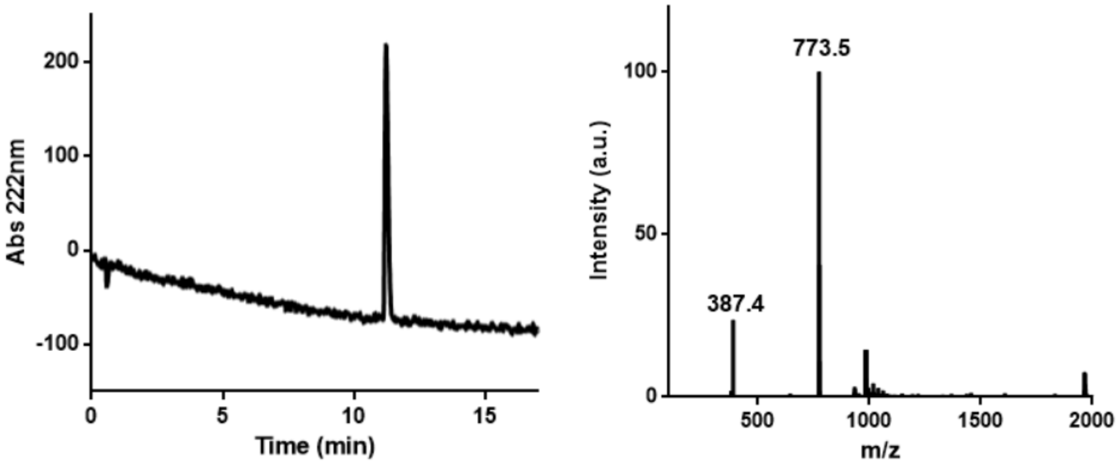

ESI-HPLC

P$_{C2}$

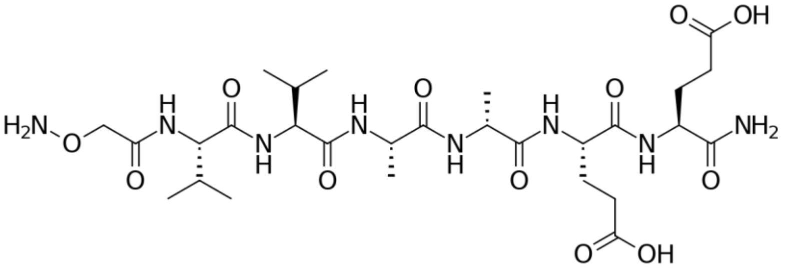

P$_{C2}$ was synthesized following the General Procedure A, starting from a 0.1 mmol scale of Rink Amide resin. The desired product has been obtained as a white powder (21.1 mg, 31 %).

^{1}H NMR (D_2O, 300 MHz): δ (ppm) 4.33-4.21 (m, 4H, Hα x 4), 4.25 (s, 2H, aliphatic CH_2), 4.18 (d, J=8.0Hz, 1H, Val Hα), 4.12 (d, J=8.2Hz, 1H, Val Hα), 2.36-2.23 (m, 4H, Asp -CH_2- x 2), 2.14-1.86 (m, 6H, Asp -CH_2- x 2 + Val -CH- x 2), 1.39 (d, J=7.2Hz, 3H, Ala -CH_3), 1.39 (d, J=7.2Hz, 3H, Ala -CH_3), 1.01-0.85 (m, 12H, Val -CH-(CH_3)$_2$ x 2).

ESI-HPLC (C18, H_2O (0.1 % TFA)/CH_3CN (0.1 % TFA) 100:0 (0→2 min), 100:0→50:50 (2→15 min), ESI, +*e*V). R*t* = 9.2 min. m/z = 1377.2 (22, $[2M+H]^+$), 689.4 (100, $[M+H]^+$), 345.25 (21, $[M+2H]^{2+}$).

HRMS (ESI, m/z): Calculated for $C_{28}H_{49}N_8O_{12}$: 689.3464; found: 689.3466 ($[M+H]^+$).

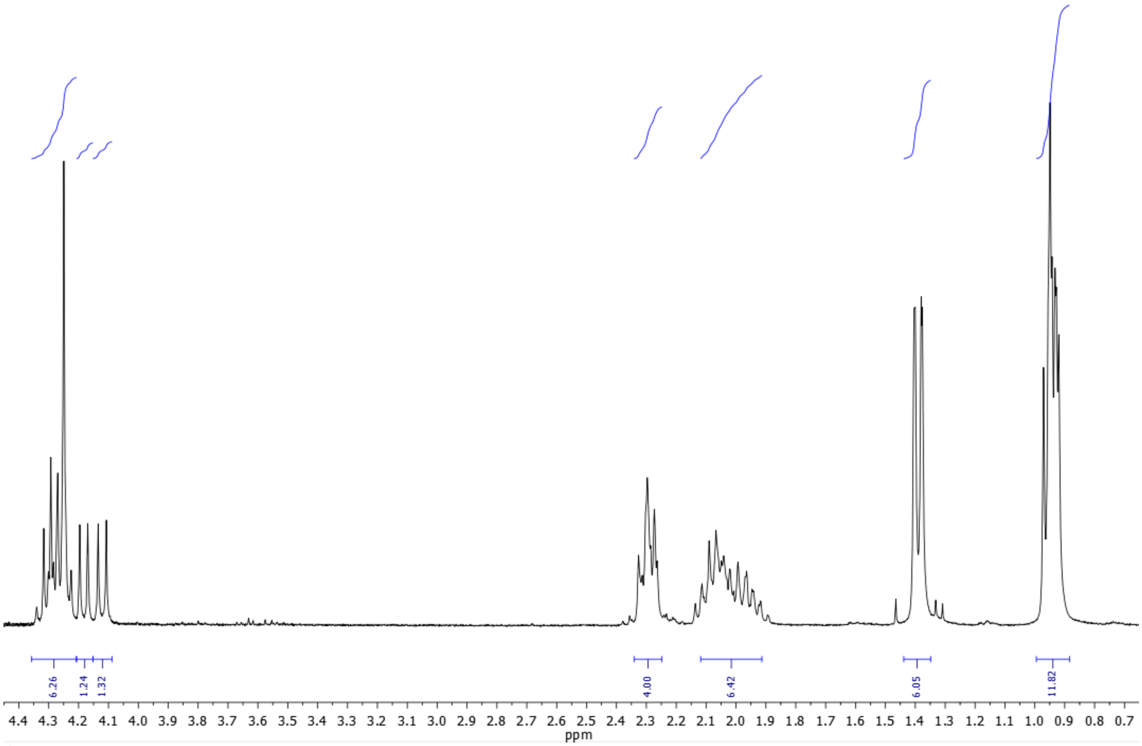

^{1}H NMR (D_2O, 300 MHz)

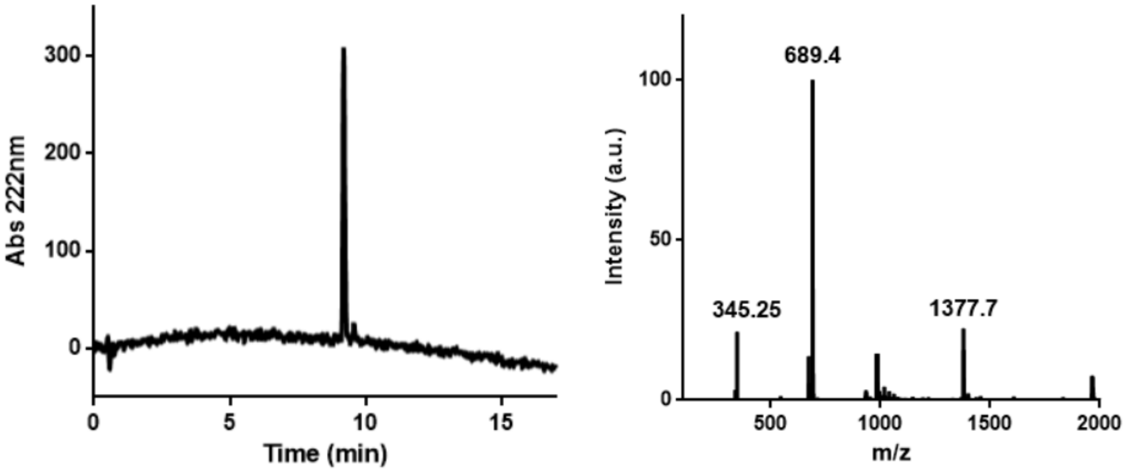

ESI-HPLC

Peptide amphiphile ($P_{C8}T_8$ and $P_{C2}T_8$) synthesis: General Procedure B

Peptide amphiphiles were synthesized by the addition of octanal (**T_8**) (1.1 eq) to each individual peptide head (1 eq) in DMSO (5 mg/mL of peptide head); the solution was shaken and heated to 60 °C until the reaction was confirmed to have proceeded to completion by HPLC-MS. The solution was precipitated three times in cold diethyl ether, dissolved in water and lyophilized.

PC8T8

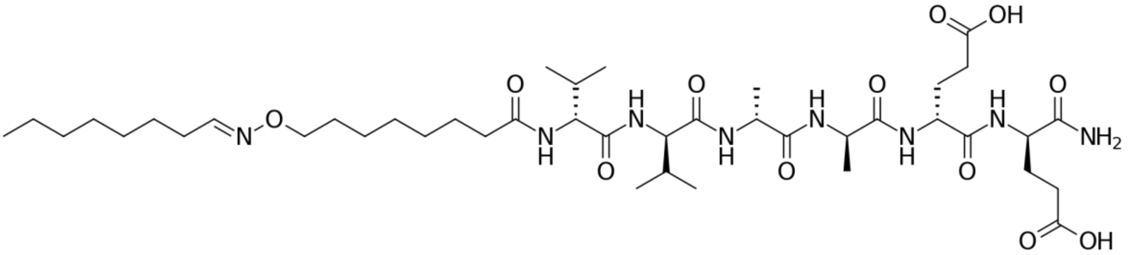

PC8T8 was synthesized following the General Procedure B, starting from 5 mg of **PC8**. The desired product has been obtained as a white powder (5.5 mg, 96 %).

^{1}H NMR (DMSO, 300 MHz): δ (ppm) 8.18 (d, *J*=7.2Hz, 1H, CONH), 8.04 (d, *J*=6.8Hz, 2H, CONH x 2), 7.94-7.78 (m, 2H, CONH x 2), 7.76 (d, *J*=7.6Hz, 1H, CONH), 7.37 (t, *J*=6.2Hz, 0.5H, NCH oxime *trans*), 7.21 (s, 1H, NH_2 C terminus), 7.06 (s, 1H, NH_2 C terminus), 6.69 (t, *J*=5.4Hz, 0.5H, NCH oxime *cis*), 4.36-4.03 (m, 6H, Hα x 6), 4.01-3.83 (m, 2H, aliphatic OCH_2), 2.30-2.04 (m, 8H, Asp -CH_2- x 2 + aliphatic $COCH_2$ + aliphatic C*H*$_2$CHNO), 2.04-1.85 (m, 4H, Asp -CH_2- x 2), 1.85-1.66 (m, 2H, Val -CH- x 2), 1.62-1.36 (m, 6H, aliphatic CH_2 x 3), 1.36-1.12 (m, 20H, Ala -CH_3 x 2 + aliphatic CH_2 x 7), 0.87-0.77 (m, 15H, Val -CH-(C*H*$_3$)$_2$ x 2 + aliphatic CH_3).

HPLC (C18, H_2O (0.1 % TFA)/CH_3CN (0.1 % TFA) 100:0 (0→2 min), 100:0→75:25 (2→22 min). R*t* = 19.8 min.

HRMS (ESI, m/z): Calculated for $C_{42}H_{75}N_8O_{12}$: 883.5499; found: 883.5516 ($[M+H]^+$).

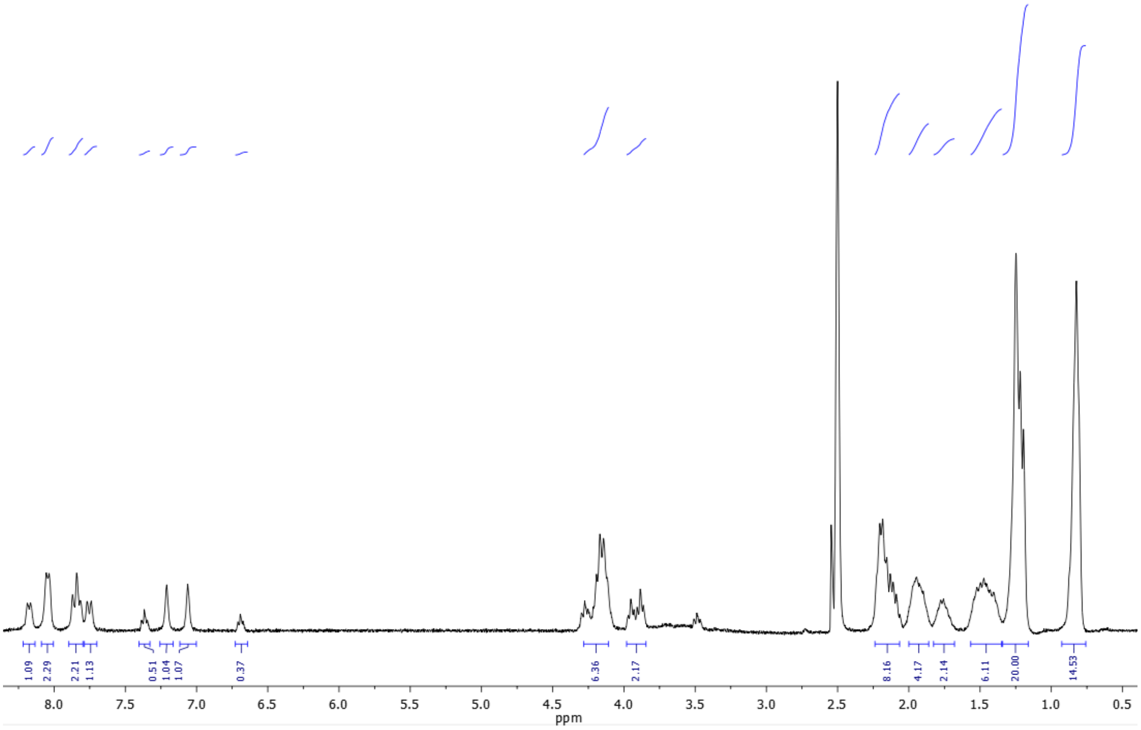

^{1}H NMR (DMSO, 300 MHz)

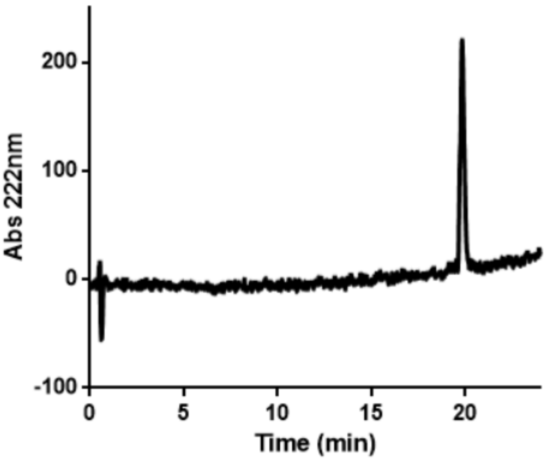

HPLC

$P_{C2}T_8$

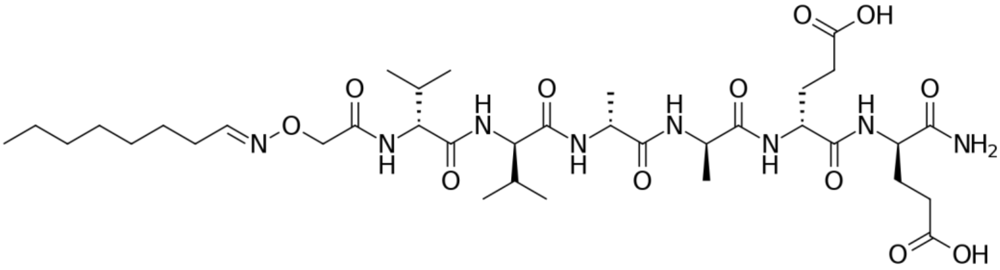

$P_{C2}T_8$ was synthesized following the peptide General Procedure B, starting from 5 mg of **P_{C8}**. The desired product has been obtained as a white powder (5.1 mg, 91 %).

^{1}H NMR (DMSO, 300 MHz): δ (ppm) 8.11-7.90 (m, 3H, CONH x 3), 7.82 (d, *J*=7.8Hz, 1H, CONH), 7.61-7.54 (m, 1H, CONH), 7.41 (d, *J*=8.8Hz, 1H, CONH), 7.35-7.30 (m, 0.5H, NCH oxime *trans*), 7.26 (s, 1H, NH_2 C terminus), 7.07 (s, 1H, NH_2 C terminus), 6.88-6.82 (m, 0.5H, NCH oxime *cis*), 4.49-4.08 (m, 8H, Hα x 6 + aliphatic OCH_2), 2.38-2.05 (m, 8H, Asp -CH_2- x 2 + Val -CH- x 2 + aliphatic CH_2CHNO), 2.05-1.84 (m, 4H, Asp -CH_2- x 2), 1.83-1.64 (m, 2H, aliphatic CH_2), 1.51-1.34 (m, 2H, aliphatic CH_2), 1.35-1.12 (m, 12H, Ala -CH_3 x 2 + aliphatic CH_2 x 3), 0.94-0.71 (m, 15H, Val -CH-$(CH_3)_2$ x 2 + aliphatic CH_3).

HPLC (C18, H_2O (0.1 % TFA)/CH_3CN (0.1 % TFA) 100:0 (0→2 min), 100:0→75:25 (2→22 min). R*t* = 16.7 min.

HRMS (ESI, m/z): Calculated for $C_{36}H_{63}N_8O_{12}$: 799.4560; found: 799.4569 ($[M+H]^+$).

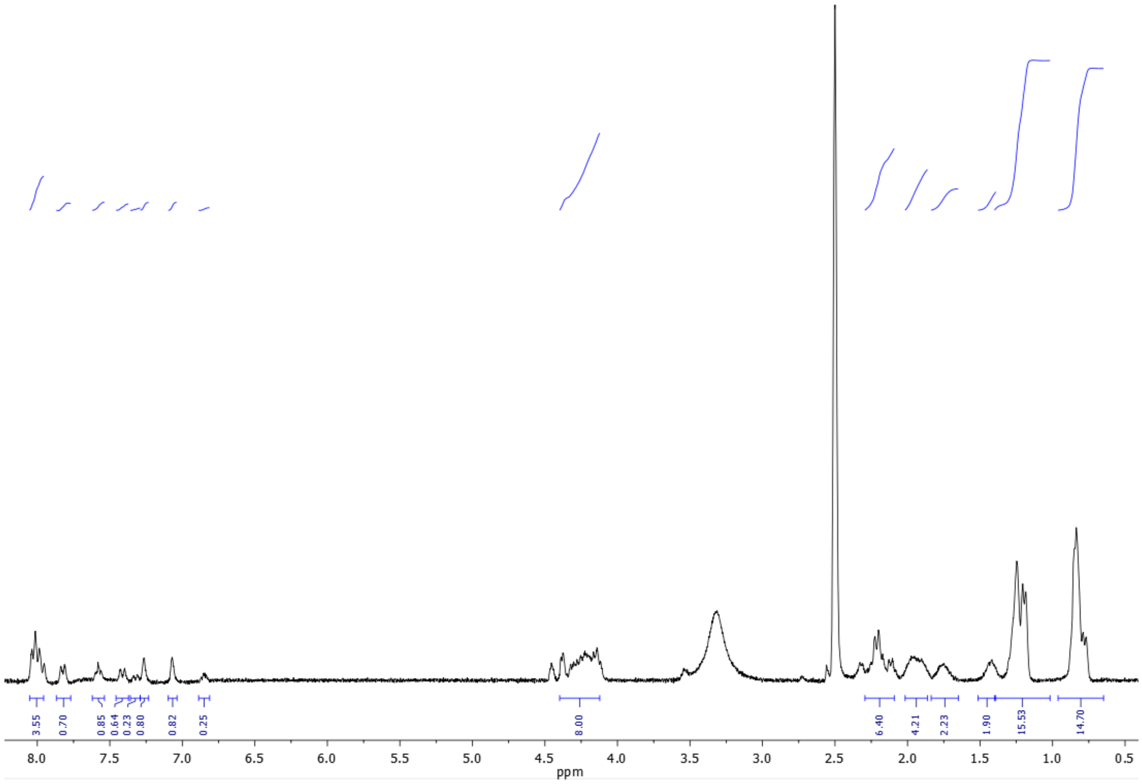

^{1}H NMR (DMSO, 300 MHz)

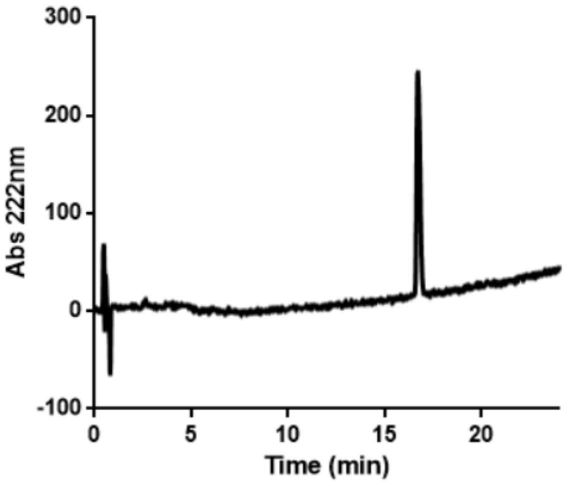

HPLC

5. Fluorescence measurements

Fluorescence measurements were carried out on a Horiba FluoroMax-3 fluorometer and were acquired with stirring at 25°C. Thioflavin T at 10 uM was used as the fluorescent probe for all experiments, using an excitation wavelength of 450 nm and an emission wavelength of 482 nm.

6. Fluorescence microscopy

Fluorescence microscopy was carried out using a Nikon Ti microscope equipped with an Andro Zyla sCMOS camera with images taken at either 10x or 60x magnification and using an FITC filter cube for Thioflavin T fluorescence (excitation: 480/30 nm, emission: 535/45 nm), a TRITC filter cube for resorufin fluorescence (excitation: 540/25 nm, emission: 605/55 nm) and a DAPI filter cube for DyLight-405 (excitation: 375/28 nm, emission: 460/60 nm). All images were taken at 25 °C.

7. Circular dichroism experiments

Circular dichroism spectra were acquired in a Jasco J-1100 CD spectrometer. Data was obtained at 25°C in a 2 mm light path quartz cuvette after subtraction of the solvent background signal.

8. Critical micellar and fibrillar concentration (CMC and CFC)

500 uL solutions of $\mathbf{P_{C8}T_8}$ from 2.5 to 80 uM were prepared in 50 mM MES buffer pH 6.0 in triplicate. 1 uL of a pyrene stock solution in tetrahydrofuran (1 mM) was added to each sample. Pyrene fluorescence emission was recorded (excitation: 334 nm, emission: 345 - 500 nm). Then, the $I_3 : I_1$ ratio (Figure S1.3) was calculated for each spectrum by dividing the emission intensity at 383 nm (third emission band) by that at 372 nm (first emission band). The CMC was calculated as the intercept between the two linear regimes found in the $I_3 : I_1$ plot. High concentrations (up to 1 mM) of $\mathbf{P_{C8}T_8}$ and $\mathbf{P_{C8}}$ were studied likewise, only in one replicate due to the higher amounts of material needed for this concentration range. $\mathbf{P_{C8}T_8}$'s CFC was identified as the second I_3:I_1 transition found in this higher concentration regime, corresponding to the one-dimensional elongation of micelles into fibres, whereas $\mathbf{P_{C8}}$ did not display neither CMC nor CFC at concentrations as high as 1 mM.

9. Co-assembly of precursor and product

Samples containing $\mathbf{P_{C8}}$ (1 mM) and increasing amounts of doping $\mathbf{P_{C8}T_8}$ (0, 2, 5, 10 and 15 % mol/mol) in 50 mM MES buffer pH 6.0 were stained with 0.1 % v/v of a ThT solution in water (5 mM). Dopant blanks were prepared likewise without $\mathbf{P_{C8}}$, only containing $\mathbf{P_{C8}T_8}$ in buffer with ThT at the same concentration. Fluorescence spectra were recorded for all samples (excitation: 430 nm, emission: 440 - 600 nm). The fluorescence spectrum of each dopant blank (*e.g.* $\mathbf{P_{C8}T_8}$ 5 %) was subtracted from the corresponding doped samples (*e.g.* $\mathbf{P_{C8}}$ 1 mM + $\mathbf{P_{C8}T_8}$ 5 %) to remove the contribution of the dopant in the mixture (Figure S1.4 *left*). The maximum emission intensity of these blank-subtracted spectra was normalized to that of pure $\mathbf{P_{C8}}$ (*i.e.* 0 % doping) in Figure S1.4c.

10. HPLC kinetics in aqueous solution

Kinetic experiments in aqueous solution were carried out by first preparing 300 uL of an aqueous solution containing peptide head $\mathbf{P_{C8}}$ (1 mM) and MES buffer (50 mM, pH 6). 50 uL of this solution was added to an aqueous solution of *O*-benzylhydroxylamine (10 uL, 6.5 mM) to be used as the t_0 time-point. The reaction was initiated by addition of octanal ($\mathbf{T_8}$) (5 uL, 250 mM in dodecane) and stirred for the duration of the reaction. The subsequent time-points were taken out at the required intervals in the same manner as t_0. The solutions of the individual time points were each washed with hexane (2 x, 1 mL), the residual hexane was evaporated and the aqueous solution basified with ammonia (10 uL, 10 % w/v) and MeCN (40 uL) was added to aid solubility of the sample before HPLC analysis (C18, H_2O/MeCN + 0.1 % v/v TFA). The solutions were sonicated for 5 min, filtered and analysed by HPLC-MS. The seeding experiments were carried as before but the aqueous solution was doped with the pre-formed $\mathbf{P_{C8}T_8}$ (5 % mol/mol, 50 uM) and the reaction was initiated with 1 mM octanal.

11. HPLC kinetics in the water-in-oil emulsion

Typically, the water phase of the emulsion was prepared by mixing peptide head $\mathbf{P_{C8}}$ (52.5 uL, 10 mM), MES buffer (52.5 uL, 500 mM, pH 6) and 420 uL of Milli-Q water. The oil phase was prepared by adding 350 uL of Span 80 (80 mg/mL) dissolved in dodecane to 6125 uL of pure dodecane and the w/o emulsion was made by mixing the two phases together at an aqueous/oil volume fraction (φ_W) of 0.08. 1 mL of this solution was added to an aqueous solution of *O*-benzylhydroxylamine (10 uL, 6.5 mM) to be used as the t_0 time-point. The reaction was initiated by addition of octanal (**T_8**) (8.7 uL, 1.8 M) and rotated during the reaction to avoid sedimentation. The subsequent time-points were taken out at the required intervals in the same manner as t_0. The solutions of the individual time points were centrifuged and the oil layer removed. The subsequent solutions of the individual time-points were worked up and analysed in the same manner as the aqueous solutions. The competition experiments were carried out in the same manner but with the additional peptide head **P_{C2}** (1 mM final concentration) was added to the aqueous solution prior to emulsification. The seeding experiments were carried out by addition of the pre-formed peptide amphiphile, **$P_{C8}T_8$**, to the aqueous solution (5 % mol/mol, 50 uM) prior to emulsification.

12. HPLC kinetics data analysis

The collected data was analysed by taking the ratio of the integrals of the starting material peak and the product peak and converting this number into relative peak area of peptide starting material remaining, expressed as a percentage. This was done to mitigate the effect of unknown levels of dilution due to the extensive work-up procedure. The HPLC signals of the starting materials and products were analysed and an experiment specific extinction coefficient was calculated, the ratios of the coefficients were used to correct for the different HPLC signals of the starting material and product where necessary. The reactions were completed in triplicate with an average taken.

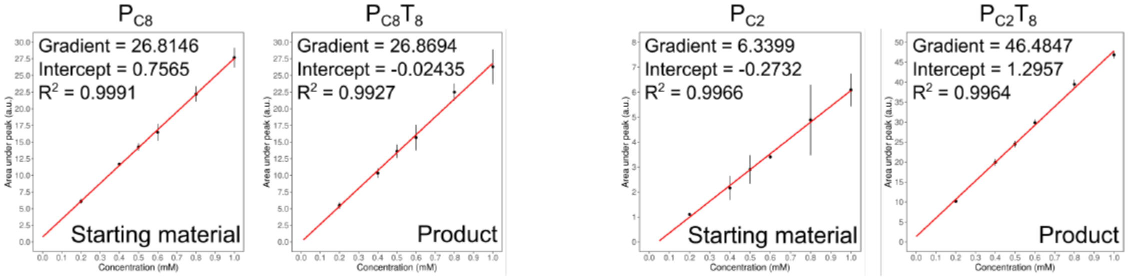

13. Fluorescence measurements of $P_{C8}T_8$ in water

Typically, an aqueous solution containing **P_{C8}** (40 uL, 10 mM), MES buffer at pH 6 (40 uL, 500 mM), Thioflavin T (40 uL, 100mM) and 280 uL Milli-Q water was prepared and the reaction was initiated by addition of octanal (5 uL, 405 mM in dodecane). The reaction and self-assembly process was monitored by fluorescence emission of Thioflavin T (excitation = 450 nm; emission = 482 nm) every 30 s for a total of 900 s. The control experiment was carried out using the same aqueous solution as above but by replacing the octanal with pure dodecane.

14. Fluorescence measurements of $P_{C8}T_8$ in emulsion

Typically, the water phase of the emulsion was prepared by mixing peptide head **P_{C8}** (11.25 uL, 10 mM), MES buffer at pH 6 (11.25 uL, 500 mM), Thioflavin T (11.25 uL, 100 mM) and 78.25 uL of Milli-Q water. The oil phase was prepared by adding 75 µL of Span 80 (80 mg/mL) dissolved in dodecane to 1312.5 uL of pure dodecane. The two solutions were mixed and shaken vigorously for 10 s to form a water-in-oil emulsion (aqueous/oil volume fraction, φ_W of 0.08). The emulsion was stirred and heated to 25°C and the reaction and subsequent self-assembly was initiated by addition of 20.5 uL of octanal (**T_8**) to a final concentration of 100 mM (oil phase). The reaction and self-assembly process was monitored by fluorescence emission of Thioflavin T (excitation = 450 nm; emission = 482 nm) every 30 s for a total of 900 s. The self-assembly in the absence of octanal was carried out following the same procedure but by substituting the volume of octanal added for dodecane. The autocatalysis experiments were carried out by adding the pre-formed peptide amphiphile (**$P_{C8}T_8$**) to the water phase of the emulsion to a mole fraction of either 0.5 or 0.1 %. As an example, in order to obtain a mole fraction of 0.1 %, 4.6 uL of a 0.025 mM solution of the pre-formed **$P_{C8}T_8$** was added to the water phase prior to emulsification, keeping the volumes constant. The reaction was initiated by addition of octanal (20.5 uL, 320 mM in dodecane) to a final octanal concentration of 5 mM, the reaction and self-assembly process was followed using the standard procedure.

15. Fluorescence microscopy of synthesis and subsequent self-assembly of $P_{C8}T_8$

Typically, the water phase of the emulsion was prepared by mixing peptide head **P_{C8}** (2 uL, 10 mM), MES buffer at pH 6 (2 uL, 500 mM), Thioflavin T (2 uL, 10 mM) and 14 uL of Milli-Q water. The oil phase was prepared by adding Span 80 (12.5 uL, 80 mg/mL) dissolved in dodecane to 237.5 uL of pure dodecane. The two solutions were mixed and shaken vigorously for 10 s to form a water-in-oil emulsion (aqueous/oil volume fraction, φ_W of 0.08). The freshly shaken emulsion was added to a microscope slide (9 uL) and the focus was adjusted to the droplets using the brightfield. The reaction and self-assembly process was initiated by addition of octanal (**T_8**) (1 uL, 1.74 M in dodecane) and monitored using the fluorescence emission of Thioflavin T and the FITC filter (see 5.2.), taking images every 30 s for approximately 10 min.

16. Calculation of droplet coalescence induced by fibrillation and dye uptake

Dye uptake microscopy experiments were the same as previously but with the addition of the corresponding fluorescent dye (10 uM final concentration, stocks prepared in water) to the emulsion before fibrillation. Relative coalescence was calculated as a percentage difference between the mean diameter of at least 65 droplets before and after the fibre-forming reaction.

17. Fluorescence microscopy of communication between droplets

Two separate emulsions were prepared in the same method as discussed previously but with the addition of glucose oxidase that was tagged with DyLight 405 dye to aid visualization (0.1 mg/mL) and Amplex Red (10 uM) to the water phase of one emulsion and horseradish peroxidase (10 U/mL) and glucose (50 mM) to the water phase of the second emulsion prior to emulsification. The two emulsions were added sequentially and very gently to a microscope slide and the reaction was initiated by addition of octanal (**T_8**) (1 uL, 1.74 M in dodecane) and monitored using the fluorescence emission of Thioflavin T and the FITC filter for fibre formation, the DAPI filter for visualization of GOx-DyLight 405 and the TRITC filter for resorufin production (from Amplex Red), (see 5.2.), taking images every 30 s for approximately 10 min.

18. Measurements of enzyme mediated communication between droplets

Two separate emulsions were prepared in the same method as discussed previously but with the addition of glucose oxidase (untagged, 0.1 mg/mL) and Amplex Red (10 uM) to the water phase of one emulsion and horseradish peroxidase (10 U/mL) and glucose (50 mM) to the water phase of the second emulsion. The two emulsions were gently mixed together and heated to 25°C, the reaction and subsequent self-assembly was initiated by addition of 20.5 uL of octanal (**T_8**) to a final concentration of 100 mM (oil phase). The communication between the two populations was monitored by fluorescence emission of resorufin (excitation = 570 nm; emission = 585 nm) every 1 s for a total of 130 s. The control without **T_8** was carried out by replacing the octanal used to initiate the reaction with an equivalent volume of pure dodecane.

19. Scanning-transmission electron microscopy (STEM)

Scanning-transmission electron microscopy (STEM) images were acquired on a FESEM Ultra plus (Zeiss) operating at 20 kV. Liquid samples (MES buffer, pH 6.0) were cast on Cu grids (carbon type-B, 300 mesh, purchased from Ted Pella) and the excess sample was absorbed after 2 min of contact. The grid was then washed with Milli-Q water (3 x 40 uL) and stained with gadolinium (III) acetate.

20. Dynamic Surface Tension (DST) measurements

Dynamic surface tension (DST) measurements were carried out on a Krü ss K100 using the maximum bubble pressure method,[124] with all measurements performed at 20°C and screening to the maximum surface age (*i.e.* inverse to bubble production rate) allowed by the instrument, $2.5\cdot 10^7$ ms. Due to intense foaming, DST data from 1 mM **P$_{C8}$T$_8$** samples could only be acquired from surface age values of $7.5\cdot 10^5$ ms onwards. Buffered **P$_{C8}$** (1 mM) samples represent a pre-fibrillated state, whereas increasing concentrations of buffered **P$_{C8}$T$_8$** simulate its progressive formation and fibrillation.

21. Complementary figures

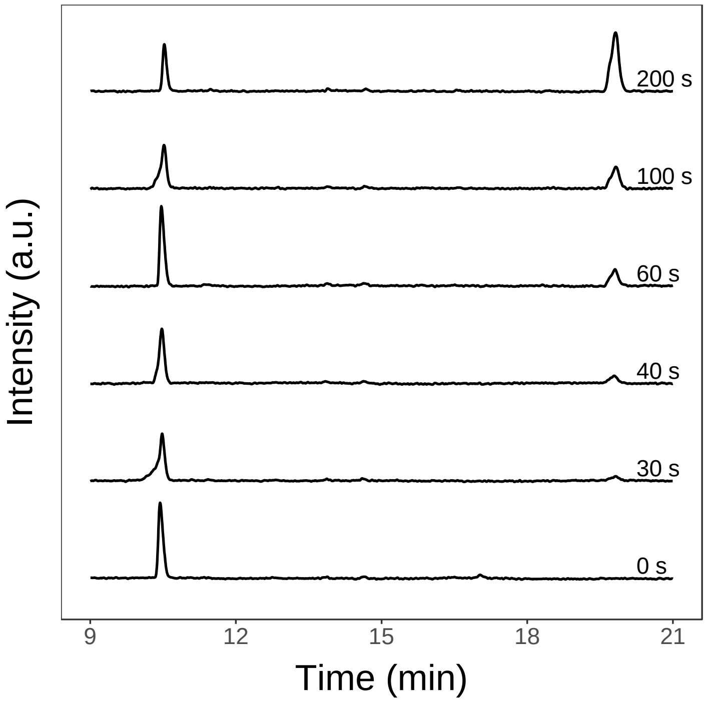

*Figure S1.1. HPLC chromatograms (222 nm) showing the conversion of the peptide head (**P$_{C8}$**, Rt = 10.5 min) to peptide amphiphile (**P$_{C8}$T$_8$**, Rt = 20 min) over time after the addition of octanal (**T$_8$**).*

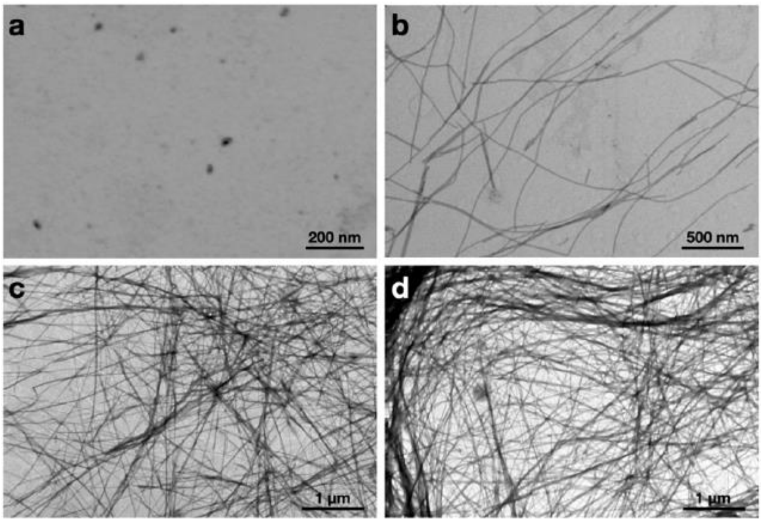

Figure S1.2. STEM images of $\mathbf{P_{C8}}$ *precursor (250 uM, a)) and* $\mathbf{P_{C8}T_8}$ *fibres (increasing concentrations up to 1 mM, b)-d)).*

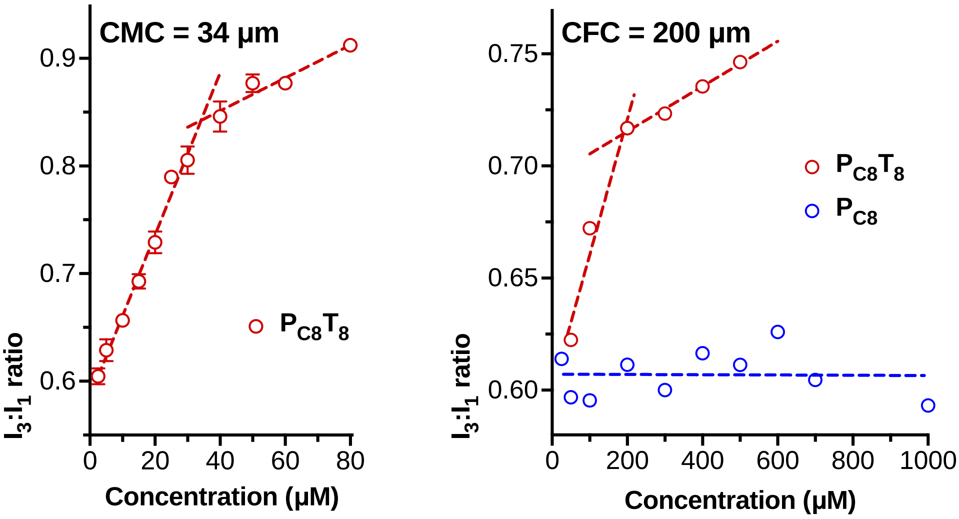

Figure S1.3. Relative pyrene emission ($I_3 : I_1$ *ratio; see methods above) in presence of* $\mathbf{P_{C8}T_8}$ *and* $\mathbf{P_{C8}}$ *at low (left, n = 3) and high concentrations (right, n = 1). The calculated critical micellar and fibrillar concentrations, CMC and CFC respectively, are indicated above the intercept of the corresponding linear regressions.*

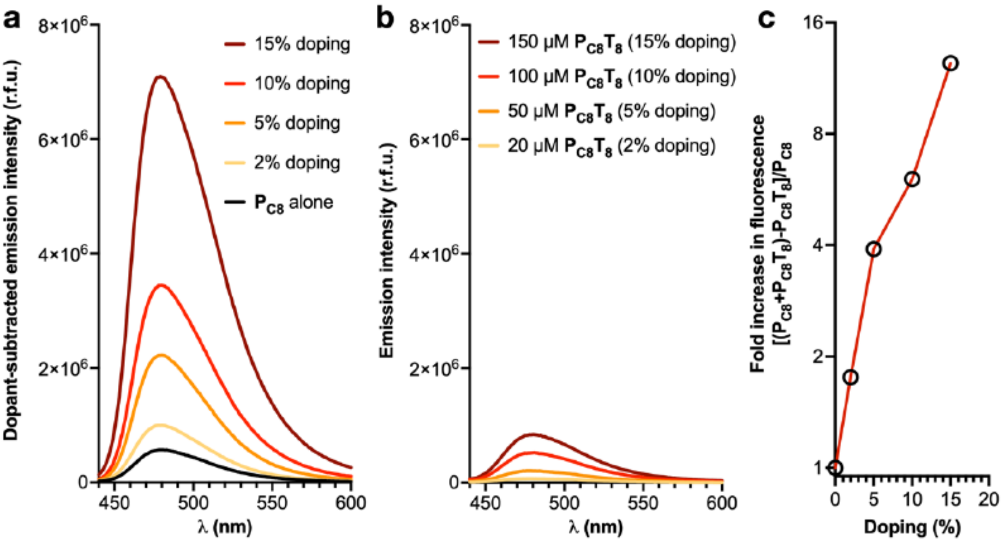

Figure S1.4. a) ThT emission spectra in presence of **P_{C8}** *(1 mM) doped with increasing amounts of its reaction product* **$P_{C8}T_8$** *(0-15% mol/mol). The contribution of the doping* **$P_{C8}T_8$** *has been subtracted (see methods). b) ThT emission in presence of the dopants alone as controls. c) Fold increase in dopant- corrected emission -plot (a))- relative to doping % (mol/mol).*

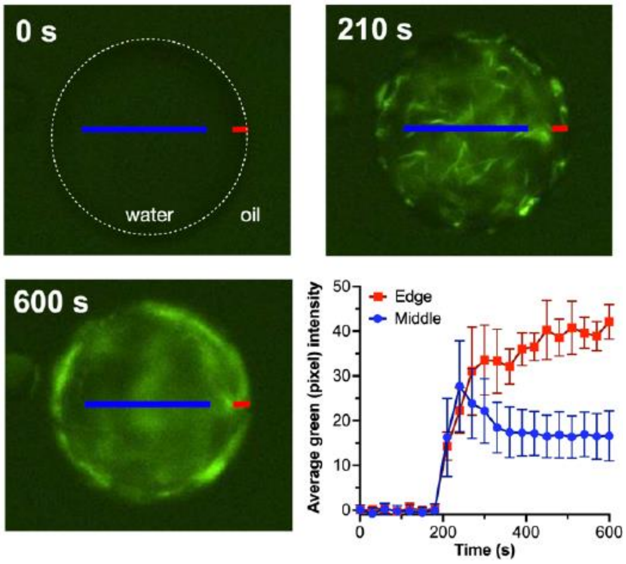

Figure S1.5. Representative time-lapse epifluorescence micrographs of a single droplet loaded with **P_{C8}** *undergoing fibrillation with* **T_8** *(see Figure 2e)). Fibres stained with ThT (green emission). The plot represents the average pixel intensity (green emission) of the blue (middle) and red (edge) cross-sections.*

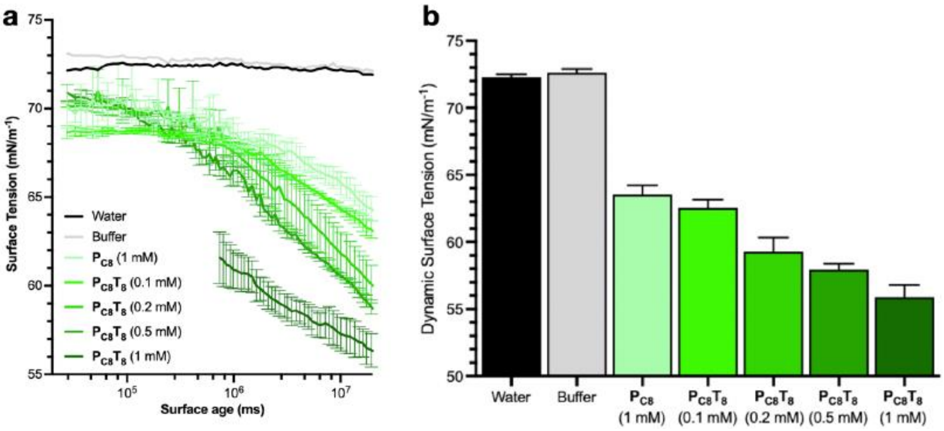

Figure S1.6. a) Dynamic surface tension (DST) profiles obtained from the maximum bubble pressure method representing surface tension of different solutions versus slower bubble production rates (i.e. increasing surface ages).[124] *All* **P_{C8}** *and* **$P_{C8}T_8$** *samples were prepared in buffer (50 mM MES pH 6.0); n = 3 (mean ± SD). b) DST values at the highest surface age measured ($2.5 \cdot 10^7$ ms). For water and plain buffer (with static surface tensions) the value plotted is the average of all surface ages.*

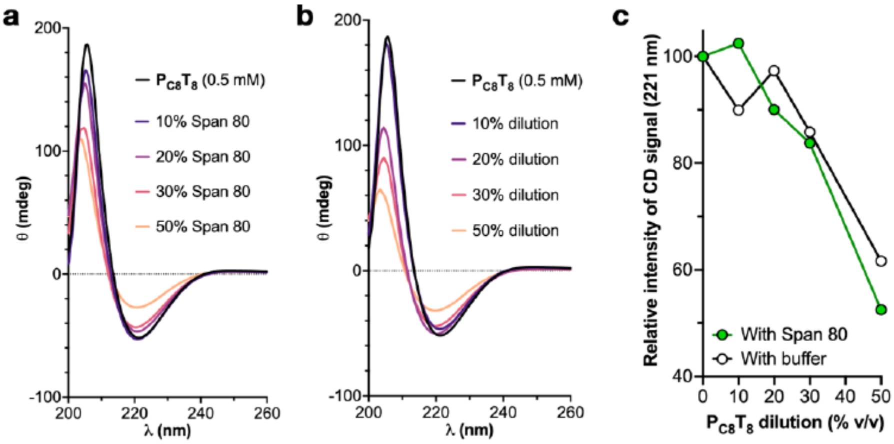

Figure S1.7. Circular dichroism spectra of **$P_{C8}T_8$** *fibres (0.5 mM) in buffer (50 mM MES, pH 6.0) diluted with a 0.5 mM stock of the a) surfactant Span 80 or b) buffer. Percentages indicate % vol/vol. Being* **$P_{C8}T_8$** *and Span 80 stocks at the same concentration, % vol/vol = % mol/mol. c) Relative intensity of the 221 nm band vs. dilution with Span 80 (green) or buffer (white). Pure* **$P_{C8}T_8$** *0.5 mM = 100 % signal.*

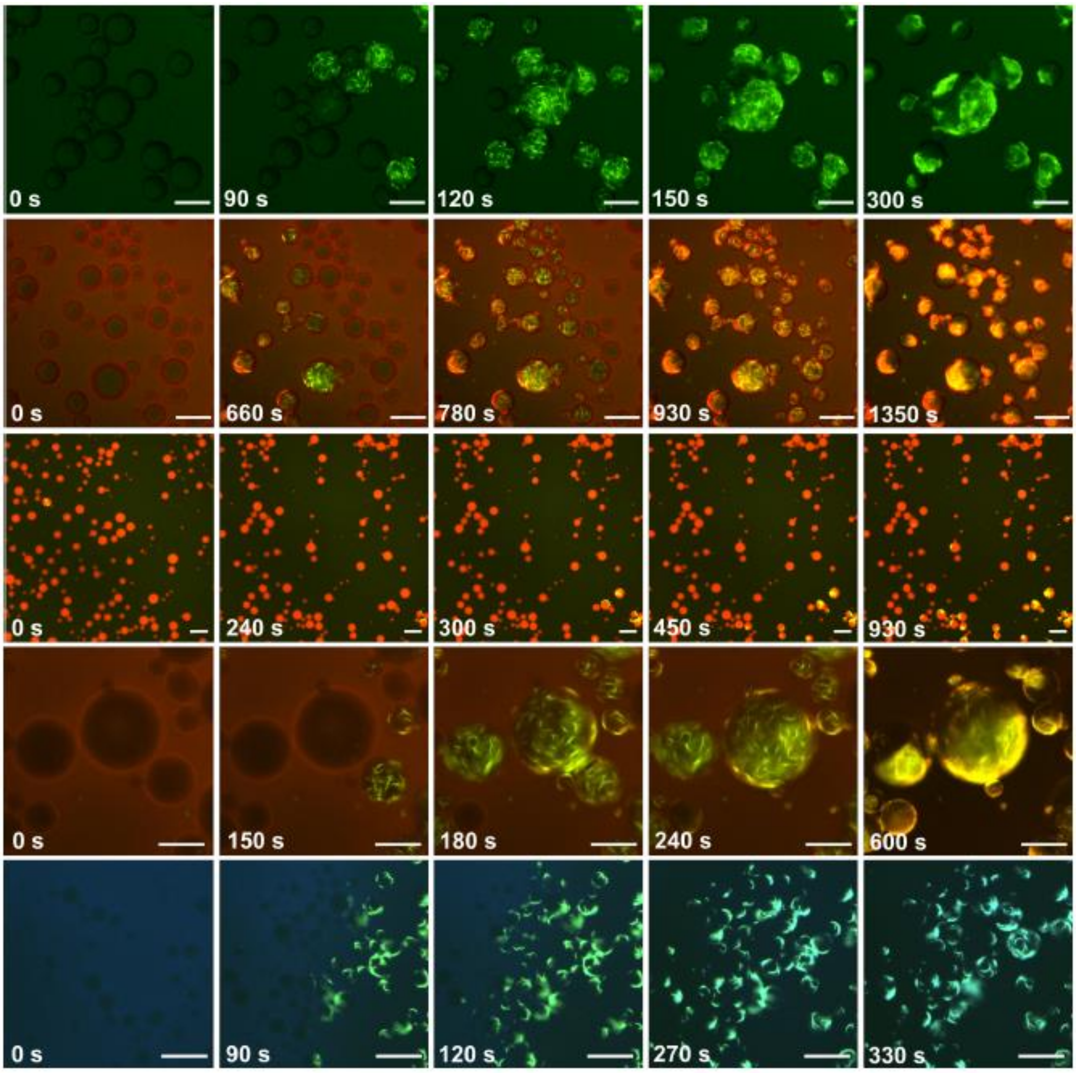

Figure S1.8. Fluorescence microscopy images showing the coalescence of droplets without any external dye (top row), not showing any coalescence in the presence of the zwitterionic Rhodamine B (2nd row), or any coalescence in the presence of the anionic Rhodamine-based TAMRA (3rd row), while exhibiting enhanced coalescence in the presence of the cationic dyes Rhodamine 6G (4th row) and Hoechst 33342 (5th row). Times are since the addition of octanal (**T_8** *). All scale bars = 100 um.*

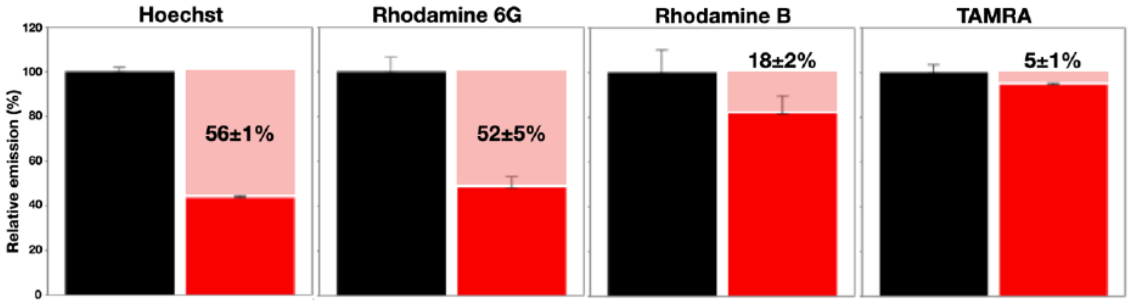

Figure S1.9. Average emission of each dye in the oil phase of the emulsion before (black) and after (red) fibrillation. Dye emission before fibrillation is normalized to 100 %. The difference in dye emission before and after fibrillation is represented in light pink and labelled numerically, representing the relative amount of dye taken up by droplets; n = 5 (mean ± SD).

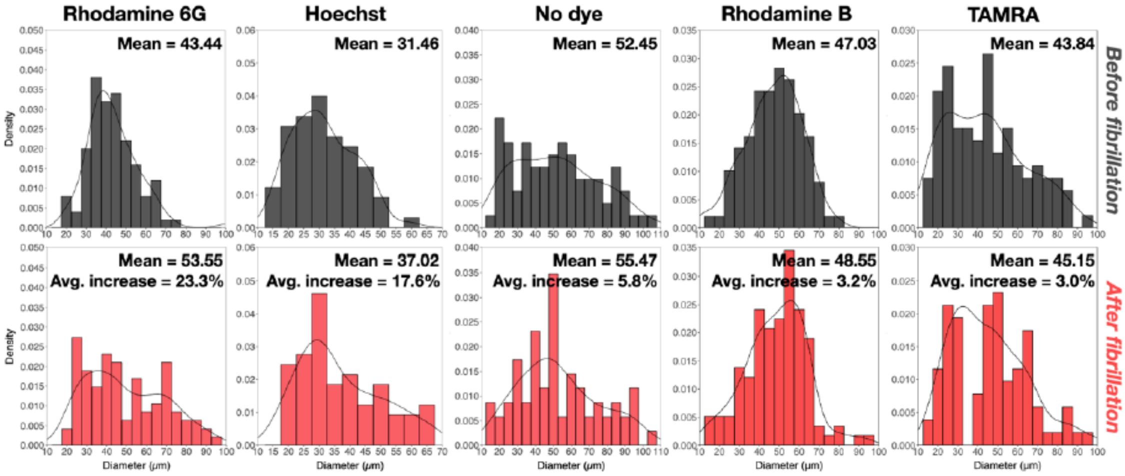

Figure S1.10. Size distribution of droplets loaded with $\mathbf{P_{C8}}$ *before (top row) and after (bottom row) addition of* $\mathbf{T_8}$ *–and subsequent fibrillation– in presence of different fluorescent dyes (see labels). The average increase ('Avg. increase') in droplet size -which is the value plotted in Figure 3c (mean ± SD)- represents the difference in mean size ('mean') after fibrillation divided by the mean size before fibrillation (%). n ≥ 65.*

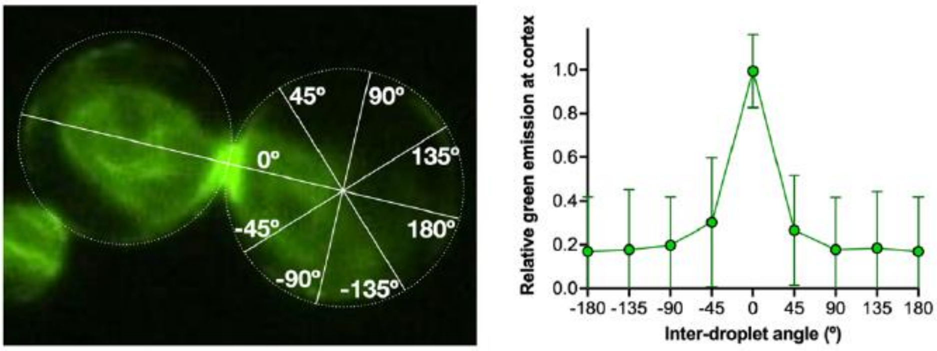

Figure S1.11. Representative epifluorescence micrograph of two contacting droplets with their centres connected through a straight line (0°). Angles drawn from each droplet centre on either direction (see labels). The plot represents the average pixel intensity (green emission) at the cortex of the droplets measured at each of the angles indicated on the left; n = 24 (mean ± SD). Note - 180° = 180°.

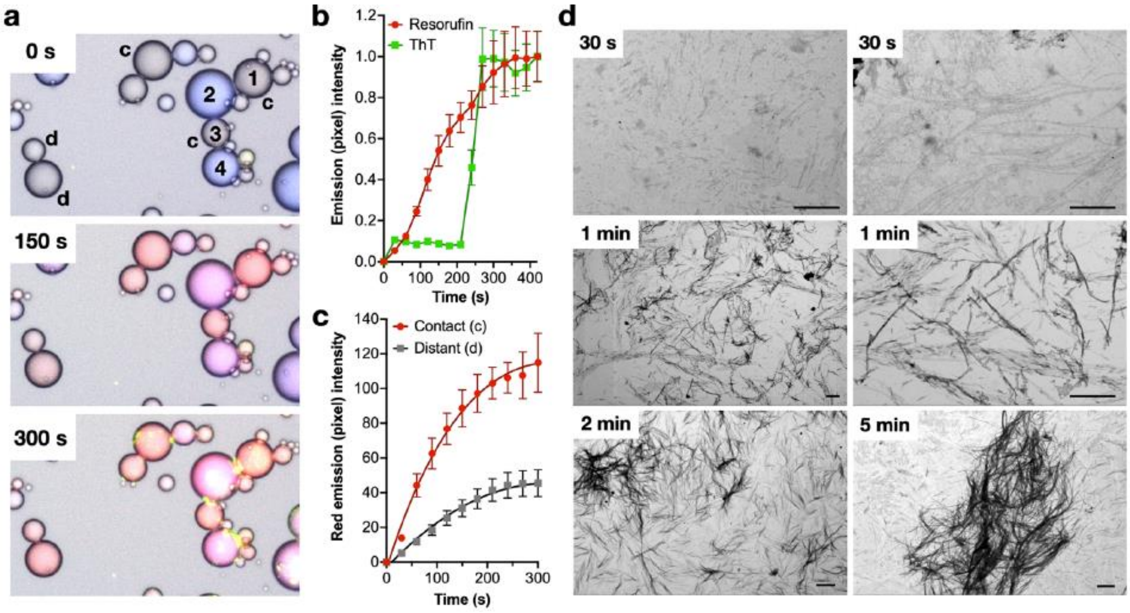

Figures S1.12. a) Epifluorescence time-lapse images of droplet populations containing either GOx (blue) or HRP (colourless), both loaded with **P_{C8}**, *after addition of octanal (*$\mathbf{T_8}$*) at t = 0 s (see Movie 10b). Merged channels: GOx (blue), resorufin reporter (red), ThT-stained microfibres (green). b) Average microfibre (ThT) and red (resorufin) emission intensity of droplets 1 - 4 (see labels) normalized to the maximum value observed for each channel; n = 4 (mean ± SD). c) Average red emission intensity of HRP droplets in contact (c)) or distant (d)) from GOx droplets – see labels; n = 3 (mean ± SD). d) STEM images of* **P_{C8}** *in reaction with* $\mathbf{T_8}$ *evidencing rapid nanofiber production (30 s) with progressive bundling over time (1 - 5 min). Scale bars = 1 um.*

22. Complementary videos

Supplementary videos can be consulted in 10.1038/s41467-021-26681-2.

Supplementary Movie 1

Epifluorescence microscopy video showing the microfibre forming reaction in water, imaged using Thioflavin T (green) to help visualize the fibres. Total video length is 5 s and is shown at a real-time speed of x60 at 1 frame per second.

Supplementary Movie 2

Epifluorescence microscopy video showing the microfibre forming reaction in water-in-oil emulsion droplets, imaged using Thioflavin T (green) to help visualize the fibres. Total video length is 20 s and is shown at a real-time speed of x30 at 1 frame per second.

Supplementary Movie 3

Cropped video of Movie 2. Length of video, frames per second and real-time speed is the same as Movie 2.

Supplementary Movie 4

Confocal microscopy video of a z-stack taken of droplets containing microfibres after the reaction and self-assembly, imaged using Thioflavin T (green) to help visualize the fibres. The video consists of 43 slices taken in 10 um increments and is shown at a speed of 5 frames per second.

Supplementary Movie 5

Cropped video of Movie 2. Length of video and recorded interval between each frame is the same as Movie 2 but the video itself is shown at 120x real-time speed.

Supplementary Movie 6a

Epifluorescence microscopy video showing the microfibre forming reaction in water-in-oil emulsion droplets and the subsequent uptake of Rhodamine 6G (red). Total video length is 13 s and is shown at a real-time speed of x60 at 2 frames per second.

Supplementary Movie 6b

Epifluorescence microscopy video showing the microfibre forming reaction in water-in-oil emulsion droplets and the subsequent uptake of Rhodamine 6G (red). The microfibres are imaged using Thioflavin T (green). Total video length is 10 s and is shown at a real-time speed of x60 at 2 frames per second.

Supplementary Movie 7a

Epifluorescence microscopy video showing the microfibre forming reaction in water-in-oil emulsion droplets and the subsequent uptake of Rhodamine B (red). Total video length is 15 s and is shown at a real-time speed of x60 at 2 frames per second.

Supplementary Movie 7b

Epifluorescence microscopy video showing the microfibre forming reaction in water-in-oil emulsion droplets and the subsequent uptake of Rhodamine B (red). The microfibres are imaged using Thioflavin T (green). Total video length is 9 s and is shown at a real-time speed of x150 at 5 frames per second.

Supplementary Movie 8

Epifluorescence microscopy video showing the microfibre forming reaction in water-in-oil emulsion droplets and the subsequent uptake of Hoechst (blue). The microfibres are imaged using Thioflavin T (green). Total video length is 10 s and is shown at a real-time speed of x60 at 2 frames per second.

Supplementary Movie 9

Epifluorescence microscopy video showing the microfibre forming reaction in water-in-oil emulsion droplets and the subsequent uptake of TAMRA (red). The microfibres are imaged using Thioflavin T (green). Total video length is 10 s and is shown at a real-time speed of x150 at 5 frames per second.

Supplementary Movie 10a and 10b

Epifluorescence microscopy video showing the microfibre forming reaction in water-in-oil emulsion droplets and the subsequent communication between two populations of droplets each containing one enzyme in a two-enzyme cascade. The microfibres are imaged using Thioflavin T (green). The separate enzyme populations are distinguished by GOx-DyLight 405 (blue) and the communication is demonstrated by the appearance of resorufin (red). Total video length is 10 s and is shown at a real-time speed of x30 at 2 frames per second. The two movies represent different areas of the same sample, with Movie 10a not showing the brightfield channel, whereas Movie 10b does include brightfield in the merged channels.

Supplementary Movie 11

Epifluorescence microscopy video showing the control experiment (without octanal = $\mathbf{T_8}$) of Movie 10. All other aspects of the video such as the length of video, frames per second and real-time speed is the same as Movie 10.

Field 2: Fluorescent probes for cellular compartments identification

1. General description of reagents and instrumentation

All reagents have been purchased to commercial brands as Sigma-Aldrich, Merck, TIC, Carbosynth or Alfa Aesar, and employed with sale quality without further purification.

For reactions monitorization, thin layer chromatography (TLC) with silica gel 60 F_{254} has been employed. For chromatographic purification, we have employed silica gel 60 (0.0015-0.0040mm).

Regarding instrumentation, for NMR analysis, Varian Mercury 300MHz y Bruker DRX 500MHz were employed. High resolution mass spectra were measured in ESI-TOF Bruker MicroTof and APCI-TOF Bruker MicroTof. When analyzing spectra, chemical shifts (δ) were measured in ppm, while coupling constants (*J*) were measured in Hz. Also, following initials were employed: s (singlet), d (doblet), dd (doblet of doblets), m (multiplet), t (triplet), M (molecular ion).

pH measurements and adjustments were carried out with a pH-meter SensION^{TM}+ PH3 HANCH-LANGE. Regarding spectra, absorbance was measured in a spectrophotometer UV-Vis Libra S60 Biochrom, while fluorescence was measured in FluoroMax-3 Horiba Jobin Yvon with temperature controler Wavelenght electronics 5Amp-40Watt model LFI-3751. The employed cuvette was SUPRASIL de 10x4mm de Hellma Analytics, made with high resolution quartz.

For graphs representations, program GraphPad Prism 6 was employed.

2. Compounds synthesis and characterization

4-(4-(dimethylamino)-2-hydroxybenzoyl) isophthalic acid (5)

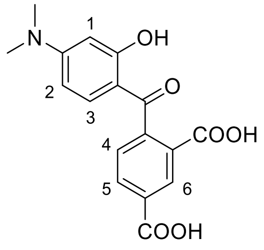

5

3-DMAP **1** (8.60 g, 62.69 mmol) was dissolved in toluene (200 mL) and stirred while heated at 60 ºC. TMA **2** (14.4 g, 74.95 mmol) was converted in a thin powder employing mortar and pestle, and then added to the stirring solution. The temperature of the resulting solution was settled to 130 ºC and let it reflux during 24 h.

Once the reaction reached room temperature, the dark solid that was formed on the reaction mixture was filtered and washed with toluene. It was pulverized employing a spatula until it adopted the aspect of a loose dark violet powder. The powder was introduced on a round-bottom flask and MeOH (150 mL) was added. The resulting solution was refluxed during 10 min. Then, acetic acid (50 mL) was added and it was concentrated to eliminate all the solvent. The solid was scratched from the flask walls and more MeOH was added. This process was repeated until all the acetic acid was co-evaporated and the solid was obtained as a loose violet powder.

Finally, MeOH was added (100 mL), refluxed for 1 h, let it reach room temperature and cooled on the fridge overnight. The precipitated solid was then filtered and washed with cold MeOH. The desired product was obtained as a dark violet powder (3006 mg, 30 %).

^{1}H RMN (DMSO, 500 MHz): δ (ppm) 3.00 (s, 6 H, 2x CH_3), 6.10 (d, 1 H, *J* = 2.5 Hz, H1), 6.20 (dd, 1 H, *J* = 9.2, 2.5 Hz, H2), 6.80 (d, 1 H, *J* = 9.1 Hz, H3), 7.51 (d, 1 H, *J* = 7.9 Hz, H4), 8.19 (dd, 1 H, *J* = 7.9, 1.7 Hz, H5), 8.47 (d, 1 H, *J* = 1.7 Hz, H6), 12.34 (s, 1 H, COOH).

^{13}C RMN (DMSO, 125 MHz): δ (ppm) 39.97 (2x CH_3), 97.39 (C1), 104.87 (C2), 109.84, 128.63 (C4), 130.40, 131.06 (C6), 132.03, 133.04 (C5), 134.17 (C3), 144.14, 156.21, 164.53, 166.46 (2x COOH), 197.98 (C=O).

HRMS (ESI, m/z): Calculated for $C_{17}H_{16}NO_6$: 330.097214; found: 330.097190 ($[M+H]^+$).

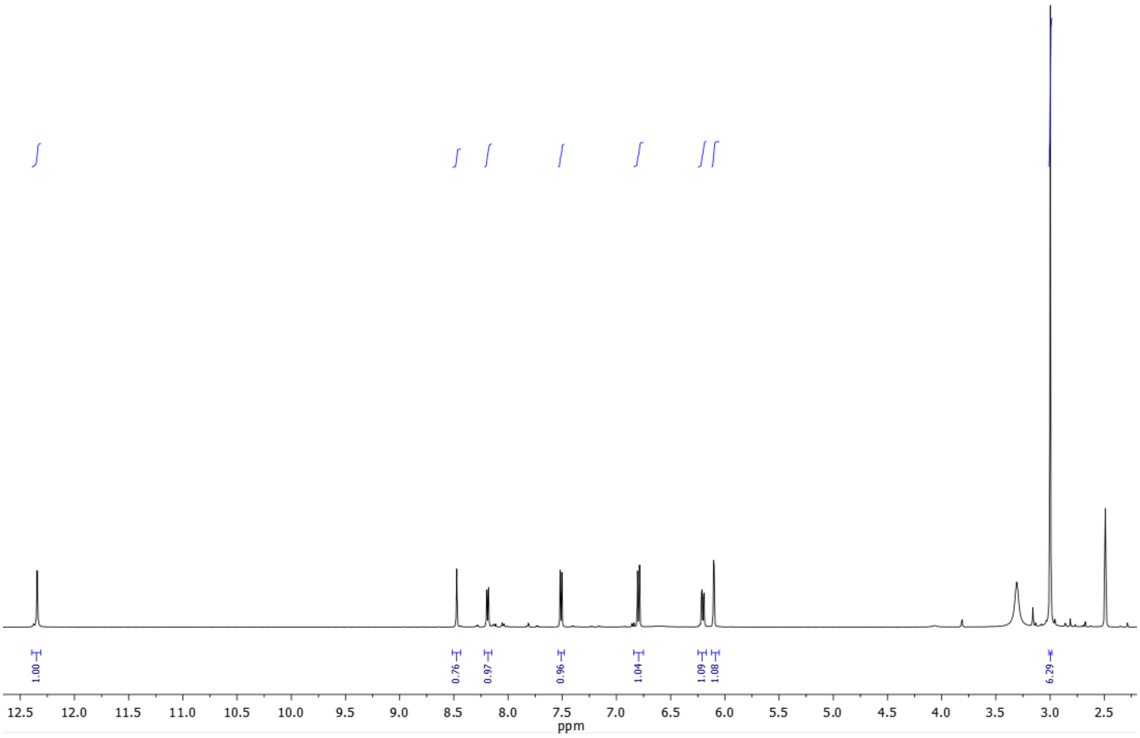

^{1}H NMR

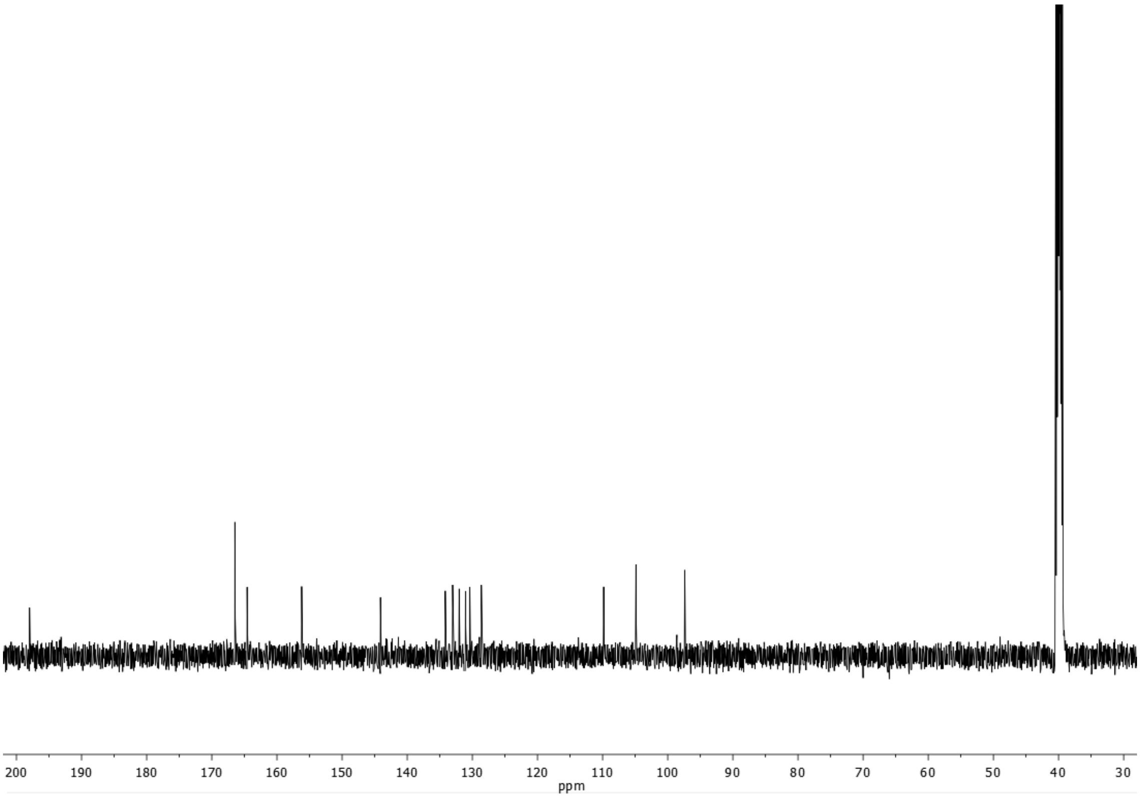

^{13}C NMR

2-(4-(dimethylamino)-2-hydroxybenzoyl) terephthalic acid (6)

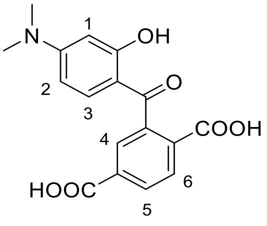

6

The same solution that was filtered to obtain the molecule **5** (but in less scale) was purified by two chromatographic columns (first one was in MeOH/DCM/formic acid 98:2:0.1; second one was in MeOH/DCM/NH_3 7 N in MeOH 50:50:0.1), allowing the separation of the desired product from the amount of **5** that has not precipitated. The product **6** was obtained as a dark violet powder (682.5 mg, 25 %).

^{1}H RMN (DMSO, 500 MHz): δ (ppm) 2.98 (s, 6 H, 2x CH_3), 6.07 (d, 1 H, *J* = 2.3 Hz, H1), 6.17 (dd, 1 H, *J* = 9.0, 2.5 Hz, H2), 6.82 (dd, 1 H, *J* = 9.0, 1.4 Hz, H3), 7.64 (d, 1 H, *J* = 1.7 Hz, H4), 7.86 (dd, 1 H, *J* = 8.0, 1.5 Hz, H5), 7.95 (dd, 1 H, *J* = 8.0, 1.6 Hz, H6).

^{13}C RMN (DMSO, 125 MHz): δ (ppm) 45.08 (2x CH_3), 97.12 (C1), 103.84 (C2), 110.69, 127.24 (C4), 129.07 (C5), 129.23 (C6), 133.74 (C3 + C_{quat}), 139.29 ($\underline{C}$-COOH x2), 155.27, 163.77, 167.56 (COOH), 168.19 (COOH), 200.37 (C=O).

HRMS (ESI, m/z): Calculated for $C_{17}H_{16}NO_6$: 330.0972; found: 330.0972 ($[M+H]^+$).

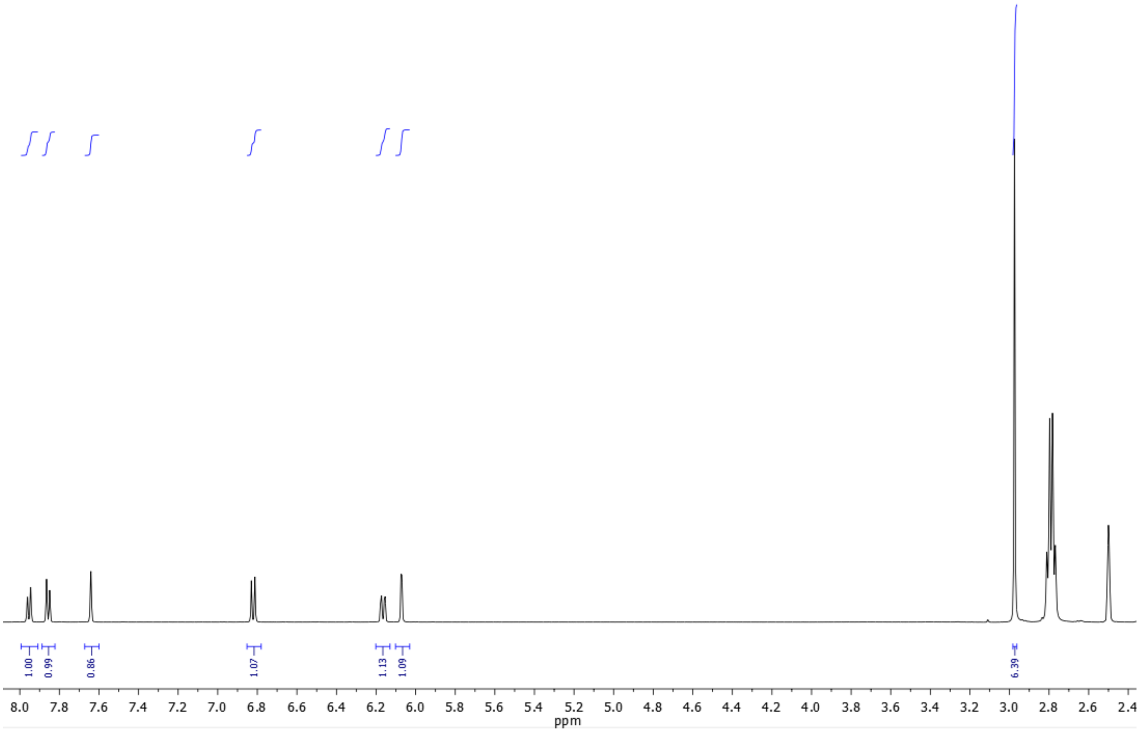

^{1}H NMR (DMSO, 500 MHz)

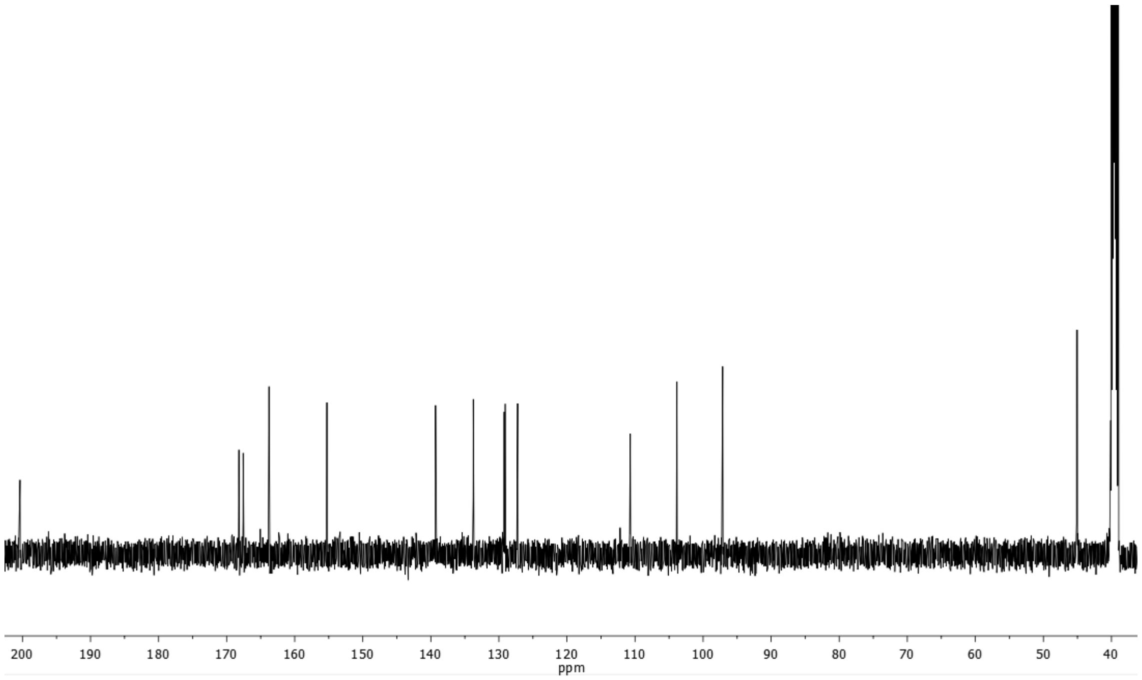

^{13}C NMR (DMSO, 125 MHz)

N-(7-(2,4-dicarboxyphenyl)-3-hydroxy-10H-benzo[c]xanthen-10-ylidene)-N-methylmethanaminium (C5.SNARF-1)

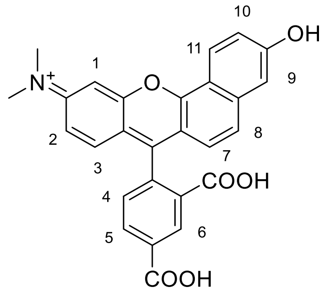

C5.SNARF-1

Compound **5** (300 mg, 0.91 mmol) and 1,6-dihydroxynaphtalene **7** (161 mg, 1.00 mmol) were suspended in phosphoric acid (3 ml), and they were under stirring and reflux during 12 h (temperature set to 165 °C).

After this time, reaction crude has suffered a colour change, switching from intense brown to dark violet. Reaction is stopped by the addition of MQ-H_2O (20 ml), which cause the appearance of the product as a violet precipitate. This solid is filtered and washed with cold MQ-H_2O (5 ml), and let it dry under vacuum during 2 h, always protect from light with aluminium foil. Then, the solid was move to a round-bottom flask. The solid retained in the filter plate were solved in MeOH, and also transferred to the same round-bottom flask. The resulting solution was concentrated and adhered over silica to perform a chromatographic purification (DCM/MeOH/formic acid 5:1:0.1). **C5.SNARF-1** was obtained as a dark violet solid (152 mg, 37 %).

^{1}H RMN (DMSO, 500 MHz): δ (ppm) 3.01 (s, 6H, 2x CH_3), 6.58 (dd, 1H, *J*=8.9, 2.6Hz, H2), 6.65 (d, 1H, *J*=9.0Hz, H3), 6.67 (d, 1H, *J*=8.7Hz, H7), 6.80 (d, 1H, *J*=2.6Hz, H1), 7.16 (d, 1H, *J*=2.5Hz, H9), 7.27 (dd, 1H, *J*=9.1, 2.4Hz, H10), 7.38 (d, 1H, *J*=8.7Hz, H8), 7.39 (d, 1H, *J*=7.9Hz, H4), 8.27-8.31 (m, 1H, H5), 8.43 (m, 1H, H11), 8.45 (d, 1H, *J*=2.5Hz, H6).

^{13}C RMN (DMSO, 125 MHz): δ (ppm) 39.9 (2x CH_3), 84.5, 93.8, 98.6 (C1), 105.2, 109.6, 109.7 (C9), 110.1 (C2), 117.5, 119.4 (C10), 122.3 (C8), 124.0 (C7), 124.4 (C4), 125.0

(C11), 125.9 (C6), 127.2, 128.9 (C3), 133.3, 136.3 (C5), 147.2, 151.9, 152.5, 156.9, 157.7, 166.4 (COOH), 168.4 (COOH).

HR-MS (ESI, m/z): Calculated for $C_{27}H_{20}NO_6^+$: 454,1285; found: 454.1294 ($[M]^+$).

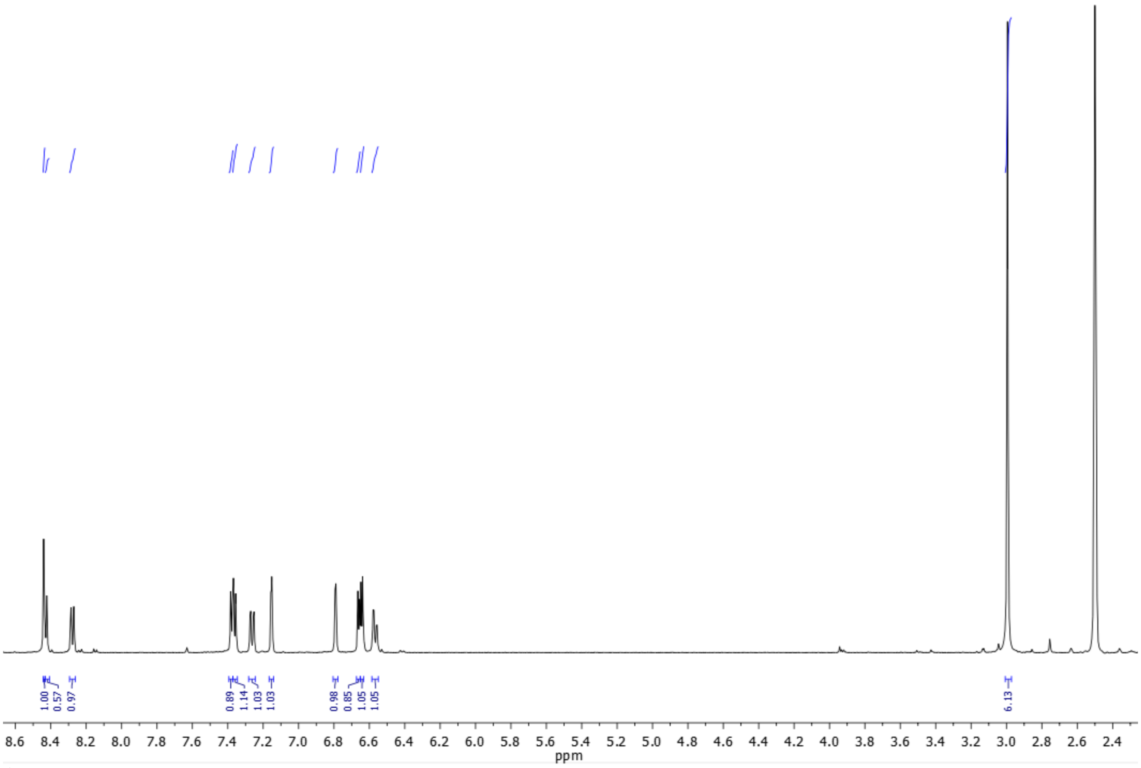

^{1}H NMR (DMSO, 500 MHz)

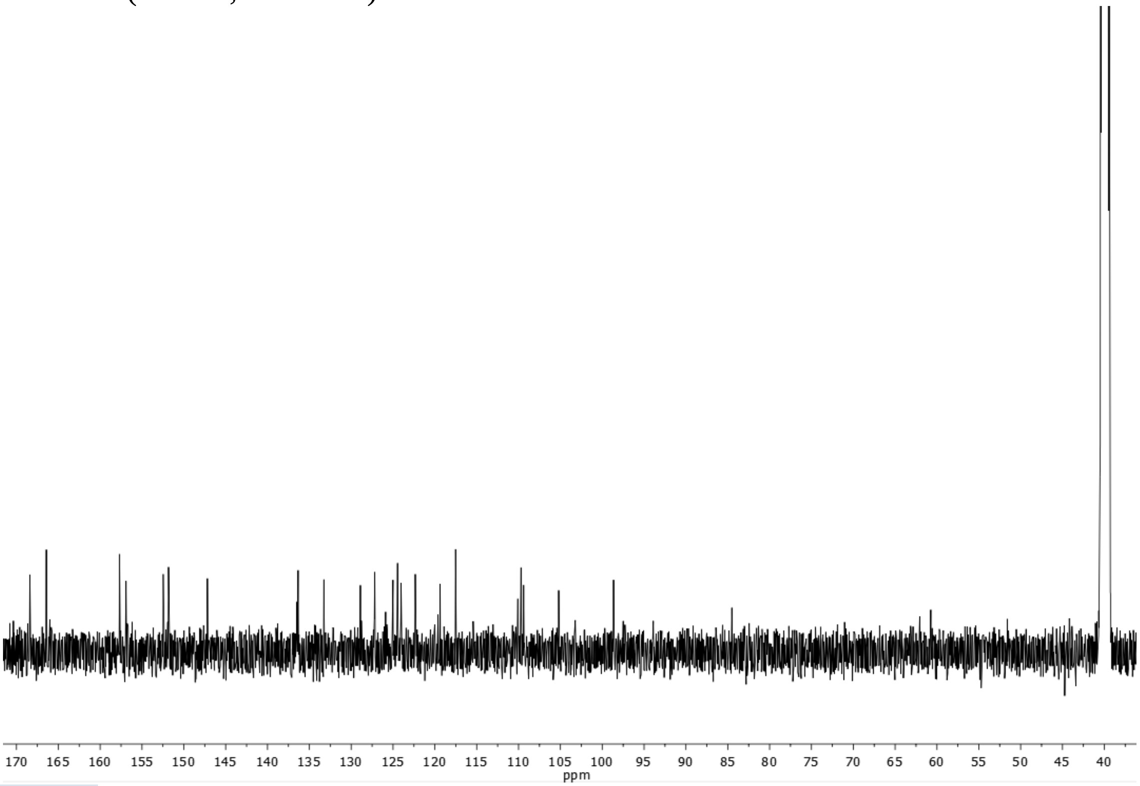

^{13}C NMR (DMSO, 125 MHz)

N-(7-(2,5-dicarboxyphenyl)-3-hydroxy-10H-benzo[c]xanthen-10-ylidene)-N-methylmethanaminium (6)

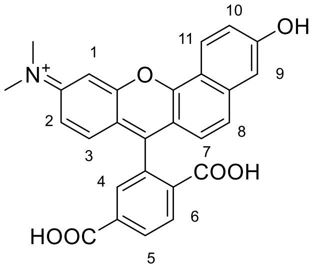

C6.SNARF-1

Same procedure than for the synthesis of **C5.SNARF-1** was employed, but making the reaction between compound **6** (1.0 g, 3.04 mmol) and **7** (535 mg, 3.34 mmol), in the corresponding proportion of phosphoric acid (7 ml). Elaboration and purification were also the same. **C6.SNARF-1** was obtained as a dark violet powder (200 mg, 15%).

^{1}H RMN (DMSO, 500 MHz): δ (ppm) 2.99 (s, 6H, 2x CH_3), 6.57 (dd, 1H, *J*=9.0, 2.4Hz, H2), 6.61 (d, 1H, *J*=8.8Hz, H3), 6.63 (d, 1H, *J*=8.7Hz, H7), 6.79 (d, 1H, *J*=2.4Hz, H1), 7.16 (d, 1H, *J*=2.4Hz, H9), 7.28 (dd, 1H, *J*=9.0, 2.1Hz, H10), 7.35 (d, 1H, *J*=8.8Hz, H8), 7.58 (s, 1H, H4), 7.97 (d, 1H, *J*=7.9Hz, H5), 8.19 (d, 1H, *J*=8.0Hz, H6), 8.43 (d, 1H, *J*=9.1Hz, H11).

^{13}C RMN (DMSO, 125 MHz): δ (ppm) 39.8 (2x CH_3), 83.6, 98.3 (C1), 105.5, 109.3 (C9), 109.62, 109.68 (C2), 117.1, 119.0 (C10), 121.9 (C8), 123.6 (C11), 123.87 (C5), 123.92, 124.03 (C4), 124.06 (C7), 128.4 (C3), 128.7, 130.7 (C6), 135.8, 146.7, 151.4, 151.9, 153.1, 157.4, 168.8 (2x COOH).

HR-MS (ESI, m/z): Calculated for $C_{27}H_{20}NO_6^+$: 454,1285; found: 454.1283 ($[M]^+$).

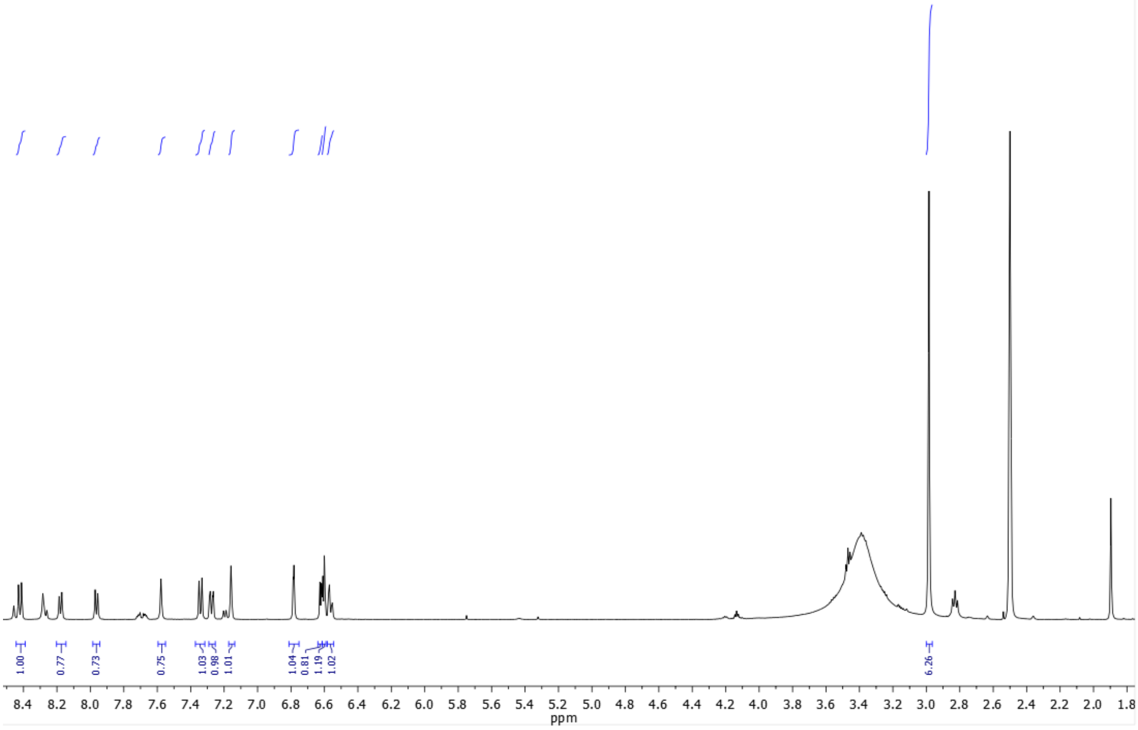

^{1}H NMR (DMSO, 500 MHz)

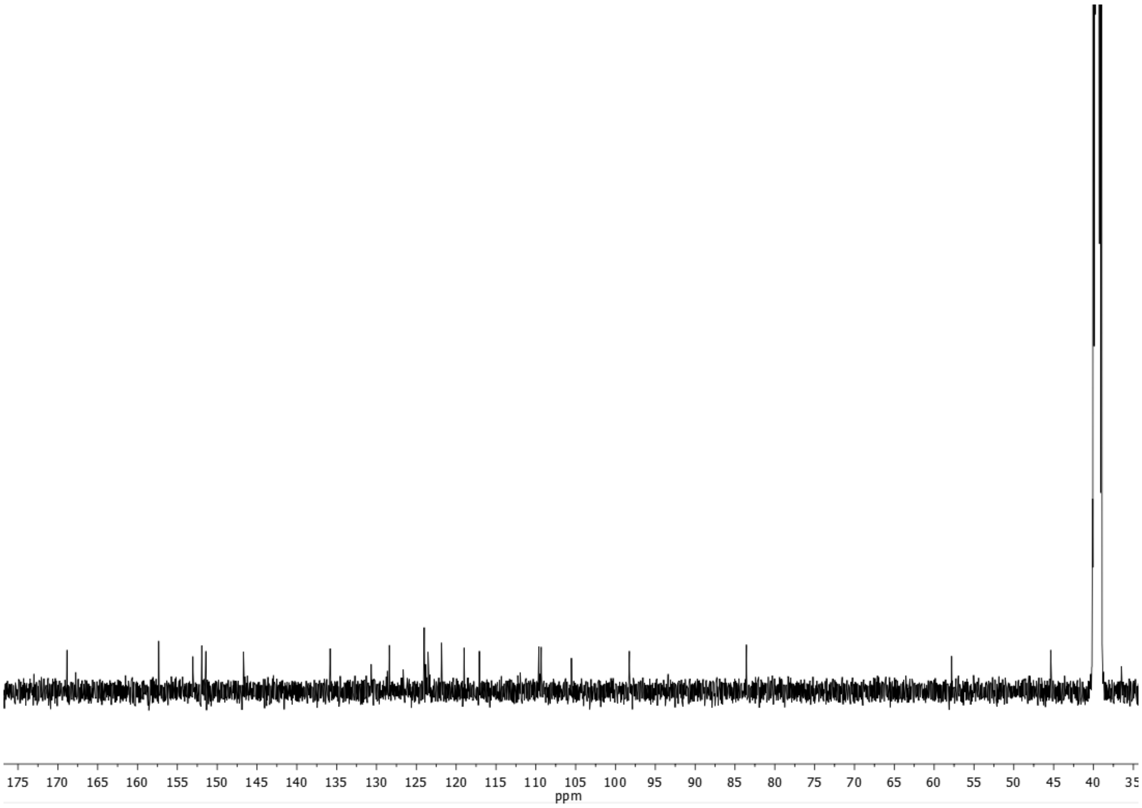

^{13}C NMR (DMSO, 125 MHz)

N-(7-(2,4-dicarboxyphenyl)-3-hydroxy-10H-benzo[c]xanthen-10-ylidene)-N-methylmethanaminium and N-(7-(2,5-dicarboxyphenyl)-3-hydroxy-10H-benzo[c]xanthen-10-ylidene)-N-methylmethanaminium (C5,6.SNARF-1)

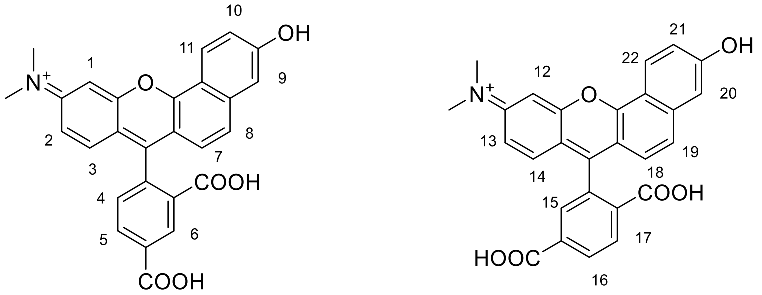

C5,6.SNARF-1

Same procedure than for the synthesis of **C5.SNARF-1** was employed, but making the reaction between a not previous purified mixture of **5** and **6** (1.57g, 4.77 mmol) and **7** (838.92 mg, 5.24 mmol), in the corresponding proportion of phosphoric acid (15 ml). Elaboration and purification were also the same. **C5,6.SNARF-1** mixture was obtained as a dark violet powder (985 mg, 45%).

^{1}H NMR (500 MHz, DMSO): δ (ppm) 2.98 (s, 12H, 4x CH_3), 6.56 (dd, *J* = 9.0, 2.4 Hz, 2H, H2 + H13), 6.61 (dd, *J* = 8.9, 8.9 Hz, 4H, H3 + H14 + H7 + H18), 6.78 (d, *J* = 2.4 Hz, 2H, H1 + H12), 7.14 (d, *J* = 2.4 Hz, 2H, H9 + H20), 7.26 (dd, *J* = 9.1, 2.4 Hz, 2H, H10 + H21), 7.33 (d, *J* = 8.8 Hz, 2H, H8 + H19), 7.51 (s, 2H, H6 + H15), 7.92 (d, *J* = 7.9 Hz, 2H, H5 + H16), 8.14 (d, *J* = 7.9 Hz, 2H, H4 + H17), 8.42 (d, *J* = 9.1 Hz, 2H, H11 + H22).

^{13}C NMR (125 MHz, DMSO): δ (ppm) 40.4 (4x CH_3), 82.9, 97.6 (C1 + C12), 105.0, 108.7 (C9 + C20), 109.0 (C2 + C13), 116.45, 118.3 (C10 + C21), 121.2, 122.9 (C8 + C19), 123.4 (C7 + C18), 123.9 (C11 + 22), 124.1 (C6 + C15), 124.3 (C5 + C16), 127.7 (C3 + C14), 128.0, 129.9, 130.9, (C5 + C17), 135.2, 146.1, 150.9, 151.3, 152.4, 156.6, 166.3 (2x COOH), 168.3 (2x COOH).

HRMS (ESI, m/z): Calculated for $C_{27}H_{20}NO_6^+$: 454.1285; found: 454.1294 ($[M]^+$).

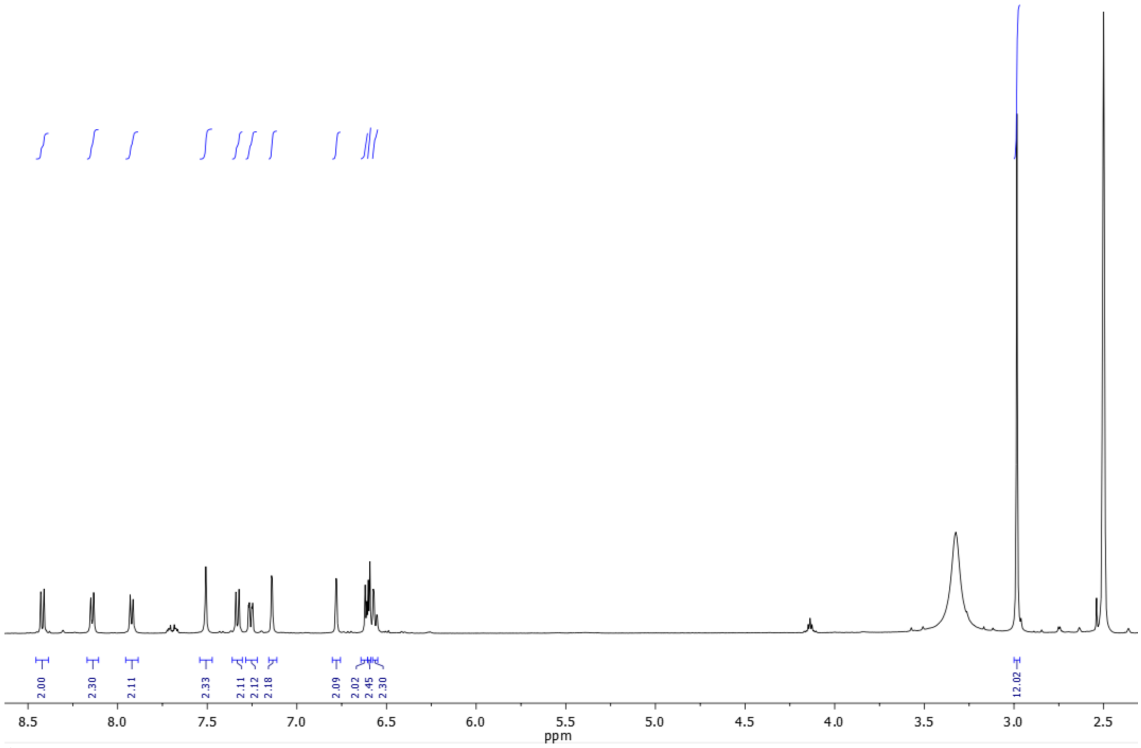

^{1}H NMR (DMSO, 500 MHz)

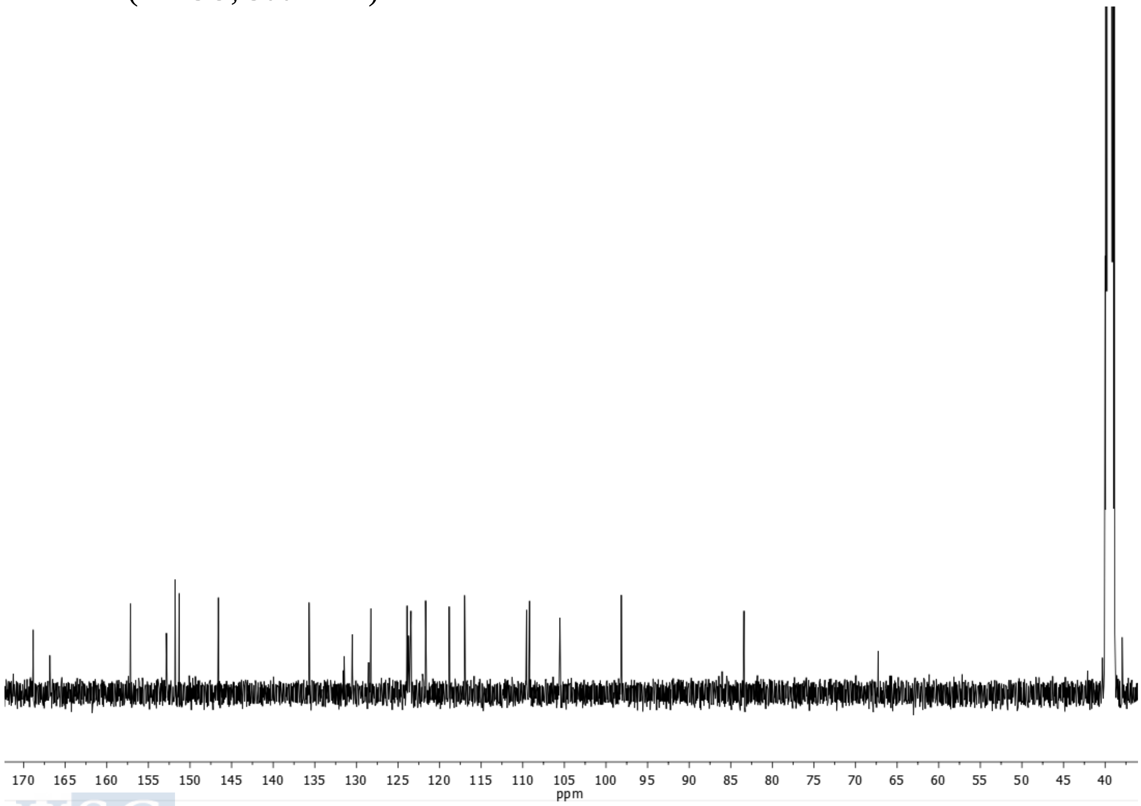

^{13}C NMR (DMSO, 125 MHz)

1,6-dimethoxynaphthalene (8)

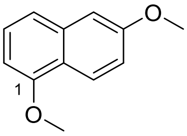

8

A solution of 1,6-dihydroxynaphthalene **7** (1 g, 6.24 mmol), dimethyl sulphate (DMS) (1.42 ml, 14.98 mmol) and sodium thiosulfate (additive, catalytic amount) was prepared in ethanol (4 ml) under argon atmosphere. A solution of NaOH 4M (4.12 ml) was added dropwise during 15 min, and the resulting solution was stirred and heated at 60°C for 1 h. After that, the product was precipitated in water, separated by filtration and dried under vacuum. The desired product was obtained (1.09 g, 93%) as a black solid.

^{1}H NMR ($CDCl_3$, 500 MHz): δ (ppm) 3.92 (s, 3 H, OCH_3), 3.99 (s, 3 H, OCH_3), 6.69 (dd, 1 H, *J* = 7.1, 1.6 Hz, H2), 7.08-7.15 (m, 2 H, H7 + H5), 7.28-7.39 (m, 2 H, H3 + H4), 8.16 (d, 1 H, *J* = 9.8 Hz, H8).

^{13}C NMR ($CDCl_3$, 125 MHz): δ (ppm) 55.39 (OCH_3), 55.58 (OCH_3), 102.15 (C2), 105.89 (C5), 117.64 (C7), 119.39 (C4), 120.94, 123.86 (C8), 126.79 (C3), 136.05, 155.82 (C1), 158.28 (C6).

HRMS (APCI, m/z): Calculated for $C_{12}H_{13}O_2$: 189.0910; found: 189.0917 ($[M+H]^+$).

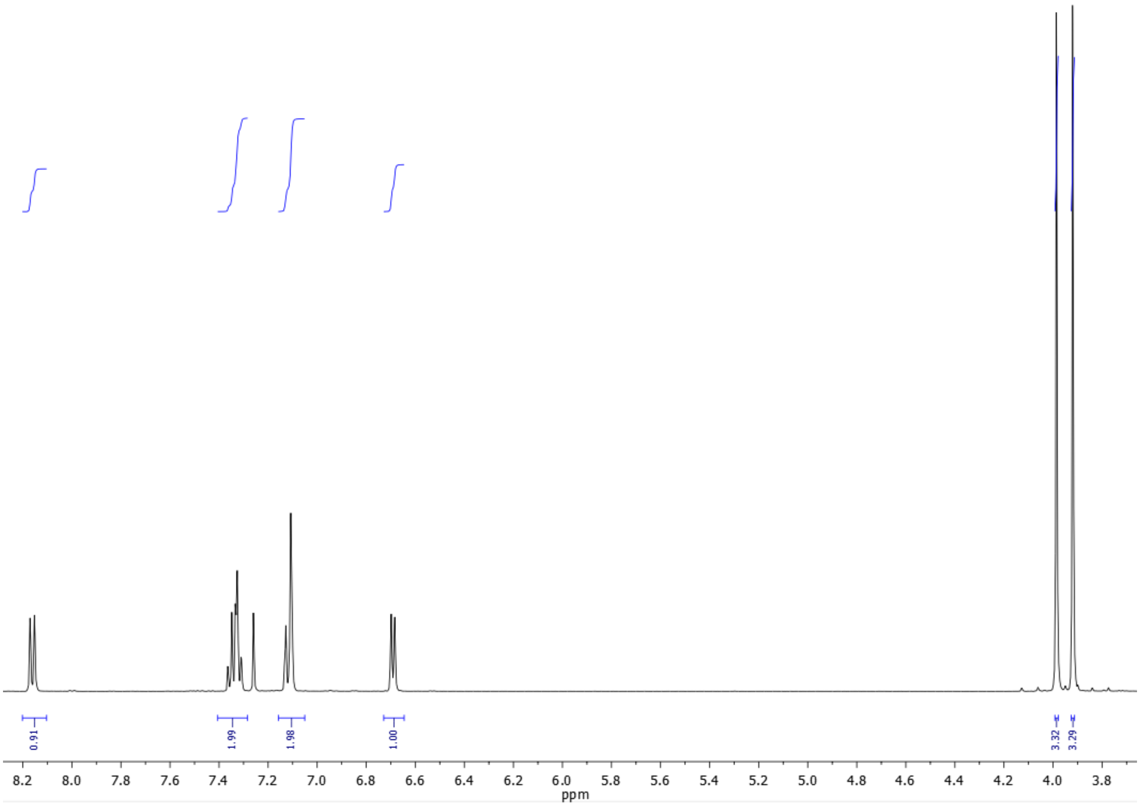

^{1}H NMR ($CDCl_3$, 500 MHz)

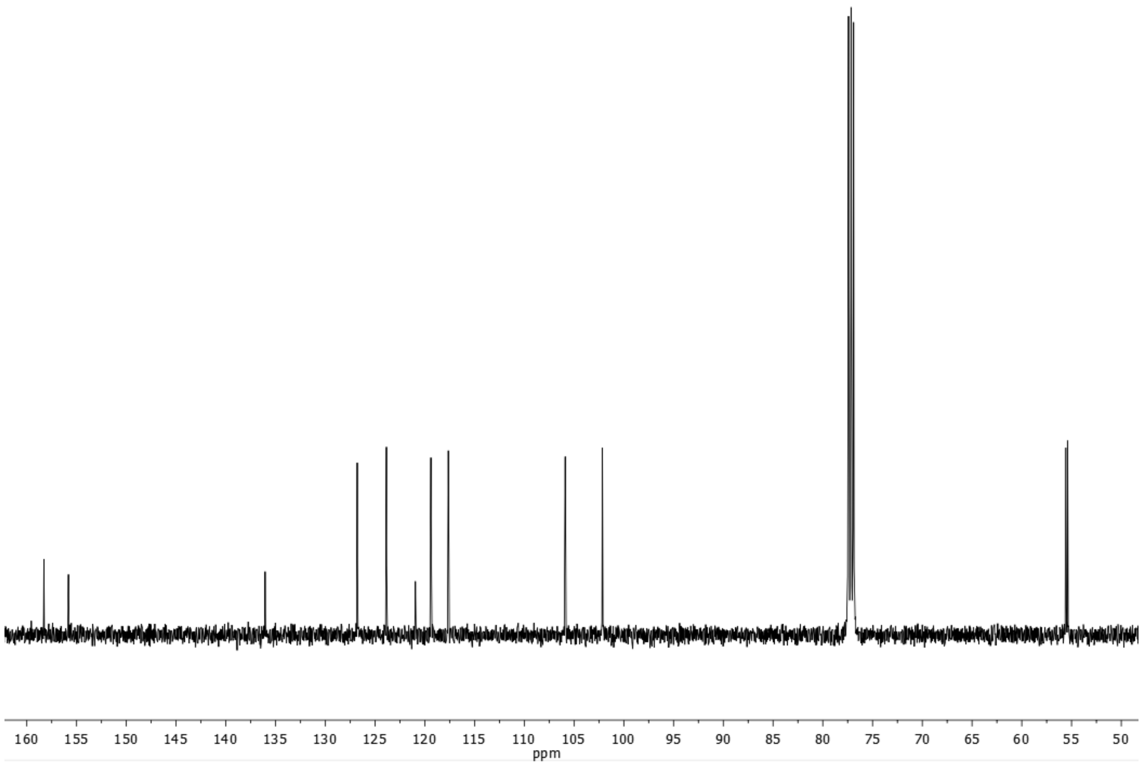

^{13}C NMR ($CDCl_3$, 125 MHz)

7-iodo-1,6-dimethoxynaphtalene (9)

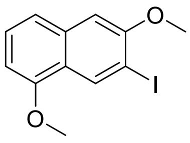

9

Compound 1,6-dimethoxynaphthalene **8** (2.00 g, 10.63 mmol) is introduced in a doble-neck bottom-round flask extremely dried, and Ar atmosphere is generated inside. Then, dried THF is added (20 mL), and the resulting solution is introduced in an acetone/solid CO_2 bath at -78 °C. Once the temperature is fixed, *n*BuLi (4.25 mL, 10.63 mmol) is added dropwise. Then, the reaction is stirring during 12 h, while the bath is returning to room temperature.

After this time, another bath of acetone/solid CO_2 at -78 °C is prepared, and the reaction flask is put inside it. Once the temperature is fixed, an under-Ar I_2 solution in THF (2.7 g, 10.63 mmol, in 20 mL of THF) is added dropwise during 1 h. Once the addition has finished, the reaction is 10 min more stirring at -78 °C and then the cold bath is removed. After 2 h stirring at room temperature, the reaction is quenched by the addition of NH_4Cl saturated solution (6 mL) and $Na_2S_2O_3$ saturated solution (6 mL).

Resulting reaction is concentrated in rotavapor to eliminate the THF. Then, it is diluted in ethyl ether (150 mL) and washed with MQ-H_2O (150 mL). Organic phase has been dried over magnesium sulphate anhydrous and concentrated. Finally, the product was purified by chromatographic column (hexane/DCM 7:1). Desired product **9** was obtained as a yellow solid (1.59 g, 48 %).

^{1}H NMR ($CDCl_3$, 500 MHz): δ (ppm) 3.94 (s, 6H), 6.66 (d, 1 H, *J* = 7.6 Hz, H2), 7.00 (s, 1 H, H5), 7.21-7.27 (m, 1 H, H4), 7.32 (t, 1 H, *J* = 7.9 Hz, H3), 8.70 (d, 1 H, H8).

^{13}C NMR ($CDCl_3$, 125 MHz): δ (ppm) 55.64 (OCH_3), 56.44 (OCH_3), 86.97 (C7), 102.68 (C2), 105.41 (C5), 119.10 (C4), 122.37, 127.41(C3), 134.14 (C8), 135.71, 154.70 (C1), 155.80 (C6).

HRMS (APCI, m/z): Calculated for $C_{12}H_{12}IO_2$: 314.9877; found: 314.9887 ($[M+H]^+$).

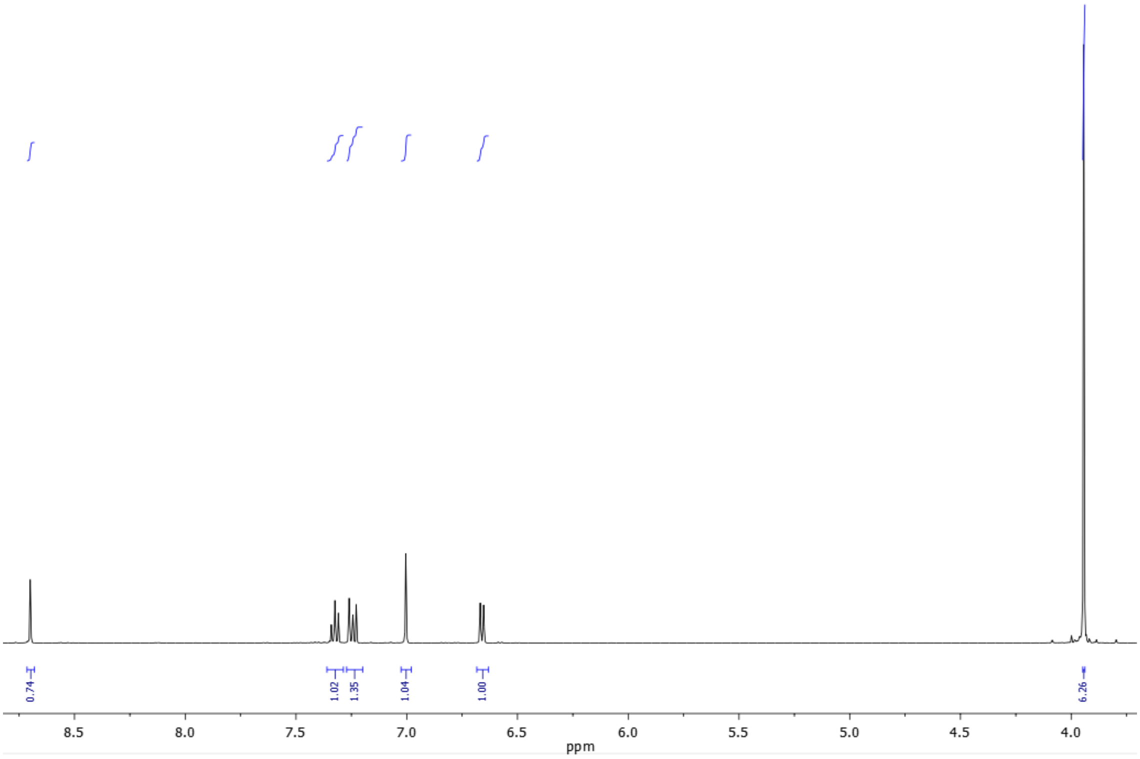

^{1}H NMR ($CDCl_3$, 500 MHz)

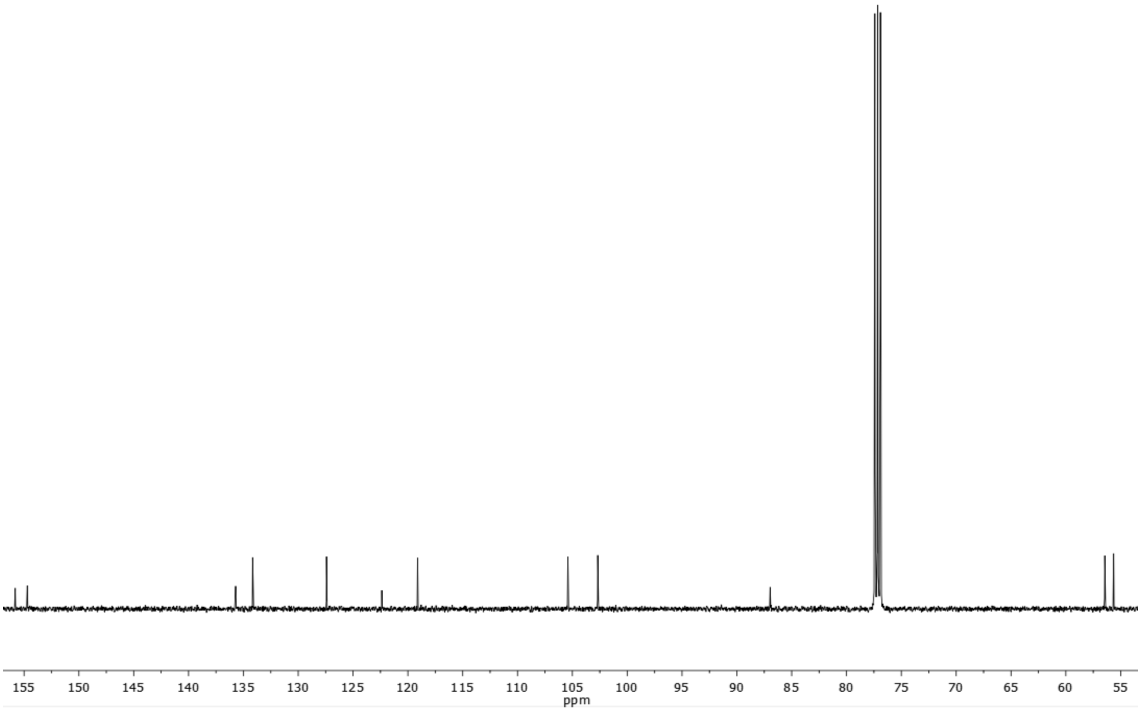

^{13}C NMR ($CDCl_3$, 125 MHz)

7-fluoro-1,6-dimethoxynapththalene (10)

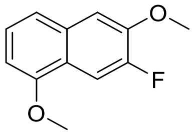

10

Compound 7-iodo-1,6-dimethoxynaphtalene **9** (160 mg, 0.51 mmol) is introduced in a doble-neck bottom-round flask extremely dried, and Ar atmosphere is generated inside. Then, dried THF is added (4 mL), and the resulting solution is introduced in an acetone/solid CO_2 bath at -78 ^{o}C. Once the temperature is fixed, *n*BuLi (265 uL, 0.66 mmol) is added dropwise. Then, the reaction is stirring during 30 min at -78 ^{o}C.

After this time, an under-Ar *N*-fluorobenzenesulfonimide (NFSI) solution in THF (194.5 mg, 0.62 mmol, in 1.5 mL of THF) is added dropwise during 30 min. The reaction is stirring in the cold bath during 2 h, and then is stirring outside the bath until room temperature is reached.

The reaction is quenched by the addition of MQ-H_2O (5 mL). The product is extracted to an AcOEt phase (25 mL), and dried over magnesium sulphate anhydrous and concentrated. Finally, the product was purified by chromatographic column (hexane:THF 100:5). Desired product **10** was obtained as a yellow solid (60 mg, 57 %).

^{1}H NMR (500 MHz, $CDCl_3$): δ (ppm) 3.90 (s, 3H), 3.91 (s, 3H), 6.65 (dd, 1H, *J* = 6.8, 1.9 Hz, H2), 7.09 (d, 1H, *J* = 8.4 Hz, H5), 7.21 – 7.27 (m, 2H, H3+H4), 7.79 (d, 1H, *J* = 12.8 Hz, H8).

^{13}C NMR (125 MHz, $CDCl_3$): δ (ppm) 55.9 (OCH_3), 56.3 (OCH_3), 103.2 (C2), 107.6 (C8), 108.3 (C5), 119.3 (C4), 120.6, 126.2 (C3), 132.5, 148.5 (C6), 151.3 (C7), 155.4 (C1).

HRMS (ESI, m/z): Calculated for $C_{12}H_{11}FO_2$: 207.0816; found: 207.0818 ($[M+H]^+$).

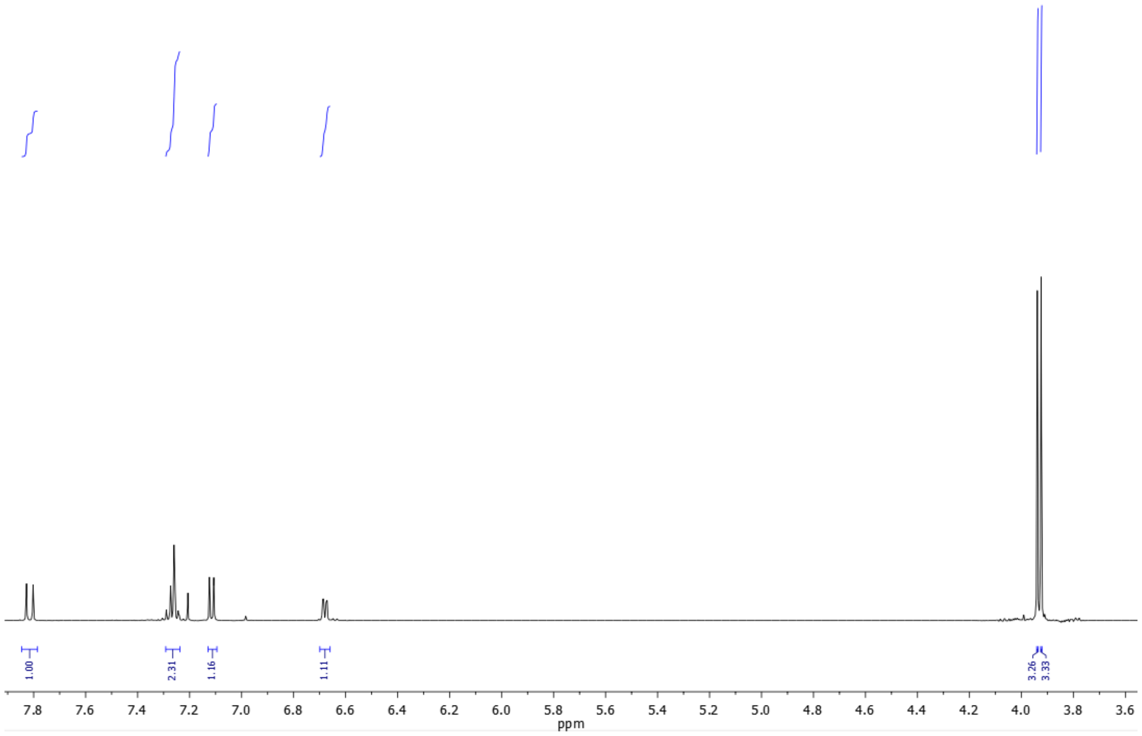

^{1}H NMR ($CDCl_3$, 500 MHz)

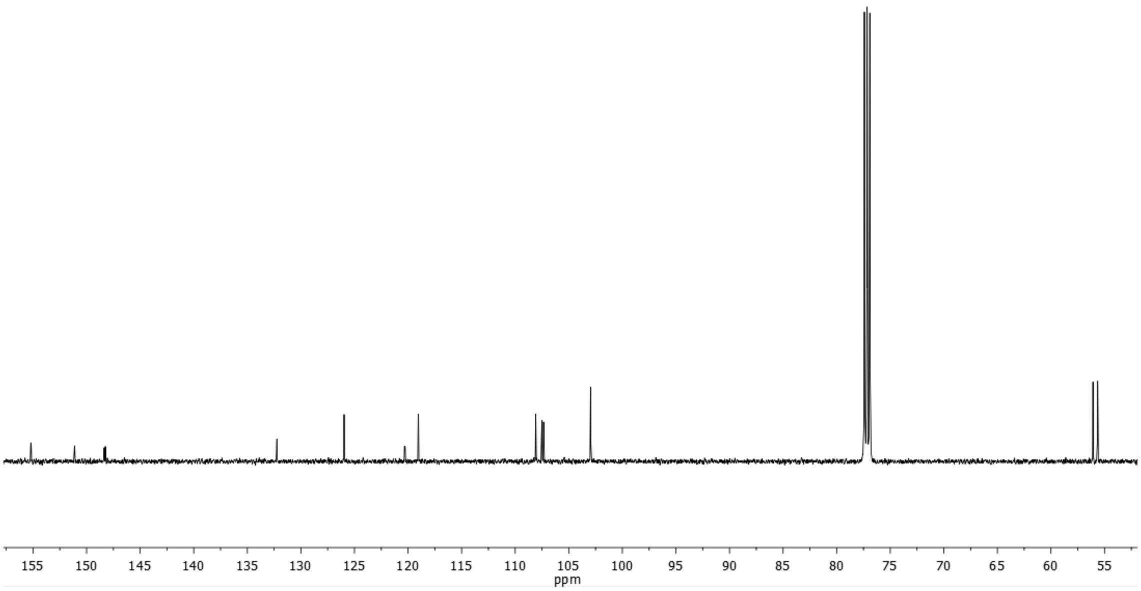

^{13}C NMR ($CDCl_3$, 125 MHz)

7-fluoronapthalene-1,6-diol (11)

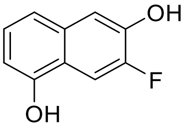

11

7-fluoro-1,6-dimethoxynapththalene **10** (100 mg, 0.485 mmol) is dissolved in dried DCM (1 mL) and BBr_3 1M in DCM (1.94 mL, 1,94 mmol) is added. After 2 h stirring at room temperature, ice is added inside the bottom-round flask of the reaction. Once melted, the product is extracted to an ethyl ether phase (3 mL), which is then dried over magnesium sulphate anhydrous and concentrated. Finally, the product was purified by a chromatographic column (hexane/ethyl ether 1:1). Desired product **11** was obtained as a pallid yellow solid (60.8 mg, 70 %).

^{1}H NMR (500 MHz, CD_3OD): δ (ppm) 6.68 (ddd, 1H, *J* = 6.7, 1.9, 0.8 Hz, H2), 7.12 – 7.18 (m, 2H, H3+H4), 7.19 (d, 1H, *J* = 8.8 Hz, H5), 7.78 (d, 1H, *J* = 12.7 Hz, H8).

^{13}C NMR (125 MHz, CD_3OD): δ (ppm) 107.6 (C2), 108.3 (C8), 113.4 (C5), 118.8 (C4), 121.2, 127.4 (C3), 134.8, 146.7 (C6), 152.3 (C1), 154.4 (C7).

HRMS (APCI, m/z): Calculated for $C_{10}H_7FO_2$: 179.0503; found: 179.0497 ($[M+H]^+$).

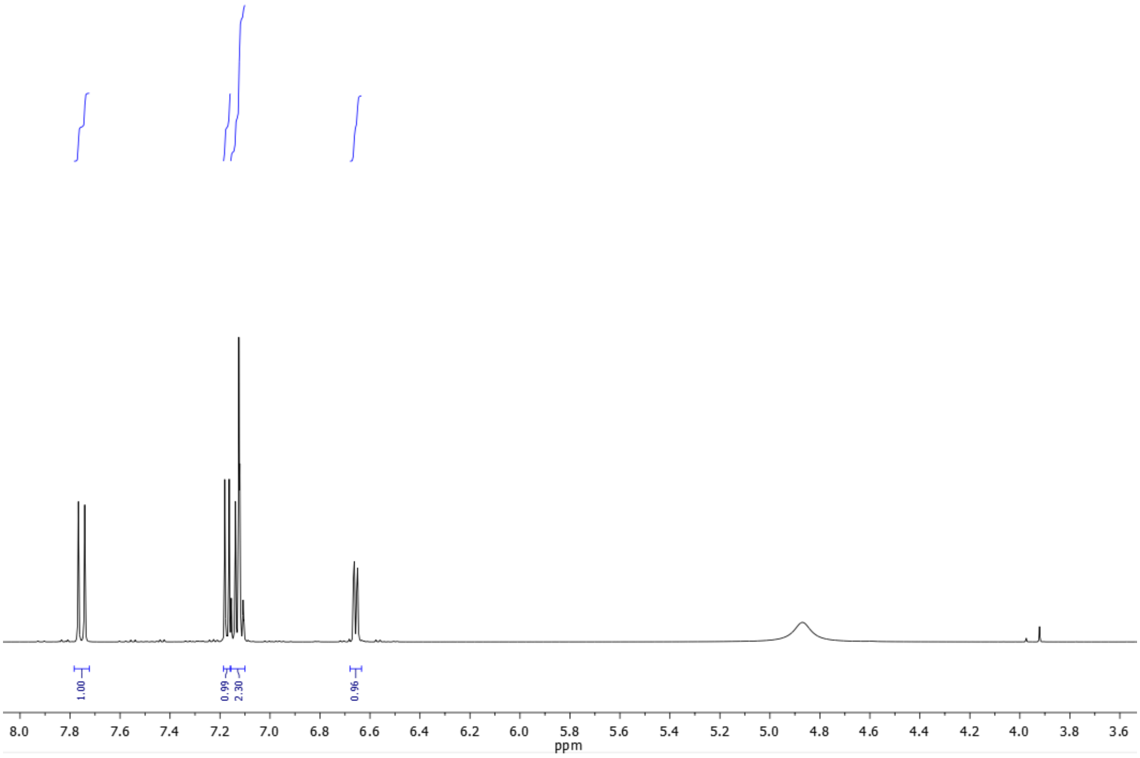

^{1}H NMR (CD_3OD, 500 MHz)

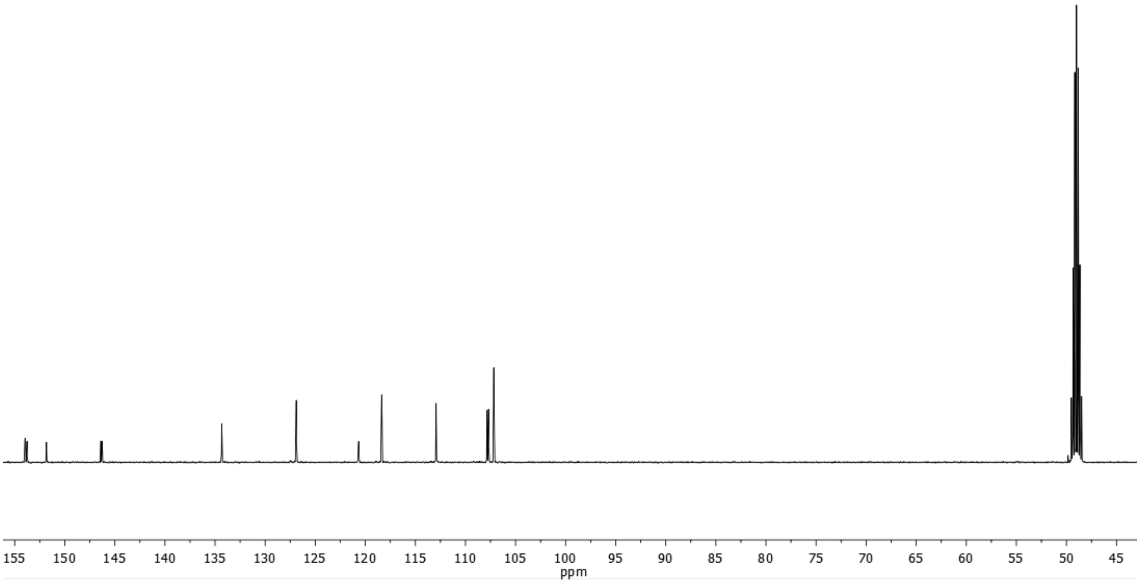

^{13}C NMR (CD_3OD, 125 MHz)

N-(7-(2,4-dicarboxyphenyl)-2-fluoro-3-hydroxy-10H-benzo[c]xanthen-10-ylidene)-N-methylmethanaminium (C5.SNARF-2F)

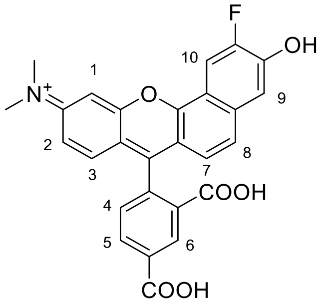

C5.SNARF-2F

Same procedure than for the synthesis of **C5.SNARF-1** was employed, but making the reaction between compound **5** (103 mg, 0.314 mmol) and **11** (56 mg, 0.314 mmol), in the corresponding proportion of phosphoric acid (2 ml). Elaboration was also the same, and the purification was in condition DCM/MeOH/formic acid (9:1:0.1). **C5.SNARF-2F** was obtained as a dark violet powder (45 mg, 30%).

^{1}H NMR (500 MHz, DMSO): δ (ppm) 2.99 (s, 6H, 2x CH_3), 6.56 (dd, 1H, *J* = 8.9, 2.5 Hz, H2), 6.65 (t, 2H, *J* = 9.0 Hz, H3 + H7), 6.87 (d, 1H, *J* = 2.5 Hz, H1), 7.33-7.44 (m, 3H, H4 + H8 + H9), 8.24 (d, 1H, *J* = 12.2 Hz, H10), 8.28 (d, 1H, *J* = 8.1 Hz, H5), 8.44 (s, 1H, H6).

^{13}C NMR (125 MHz, DMSO): δ (ppm) 40.0 (2x CH_3), 84.3, 98.9 (C1), 105.2, 107.7 (C10), 107.9, 110.2 (C2), 110.7, 112.9 (C4), 117.4, 122.2 (C8), 123.9 (C7), 125.0 (C9), 125.9 (C6), 127.2, 128.9 (C3), 132.7, 136.6 (C5), 146.7, 147.4, 147.4, 151.9, 152.6, 153.9, 166.7 (COOH), 168.6 (COOH).

HRMS (ESI, m/Z): Calculated for $C_{27}H_{19}FNO_6^+$: 472,1191; found: 472.1181 ($[M]^+$).

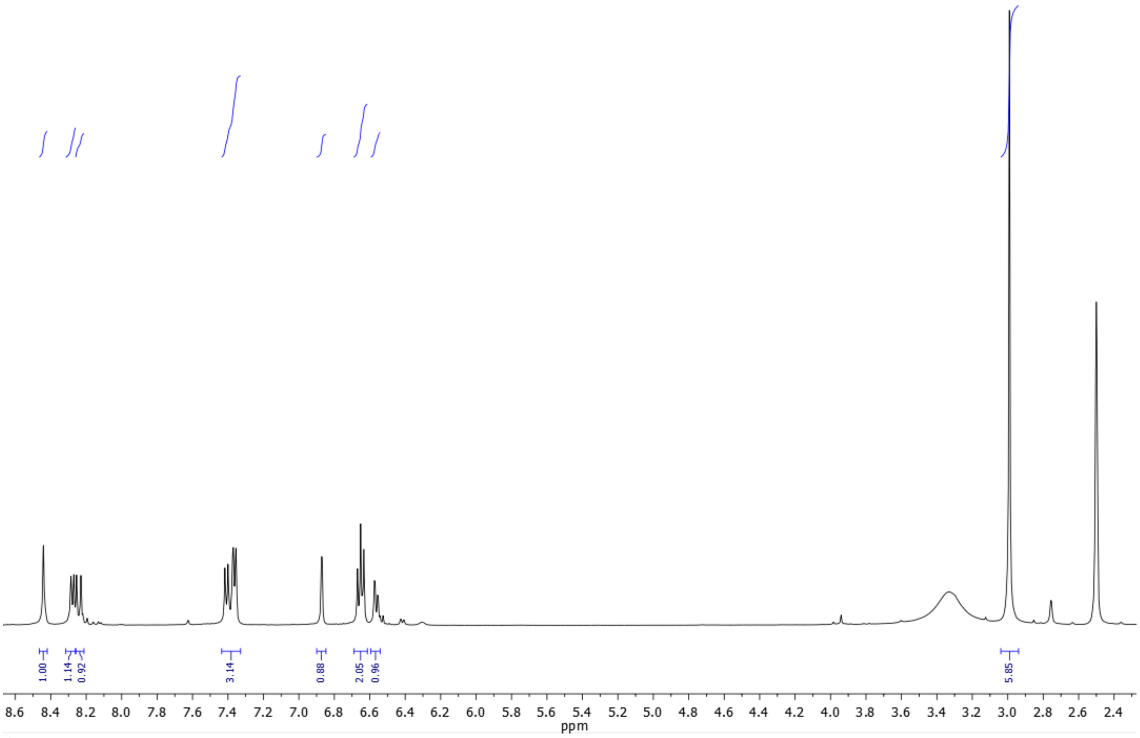

^{1}H NMR (DMSO, 500 MHz)

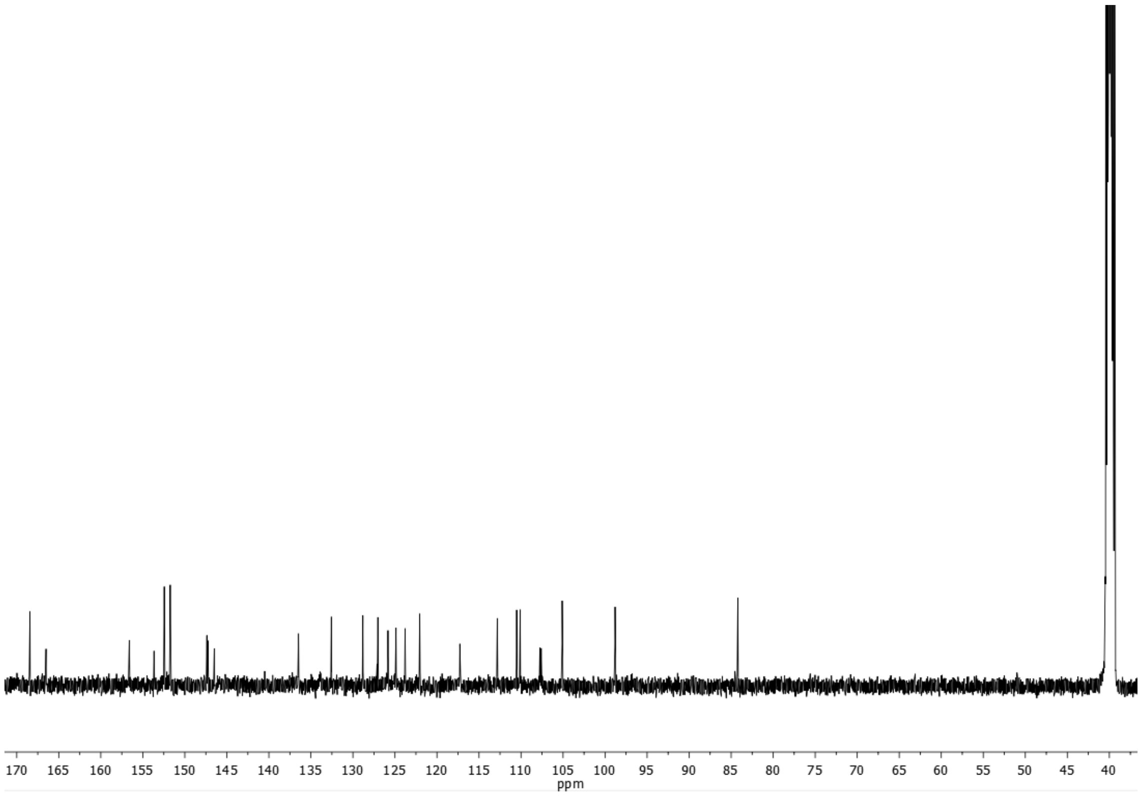

^{13}C NMR (DMSO, 125 MHz)

N-(7-(2,5-dicarboxyphenyl)-2-fluoro-3-hydroxy-10H-benzo[c]xanthen-10-ylidene)-N-methylmethanaminium (C6.SNARF-2F)

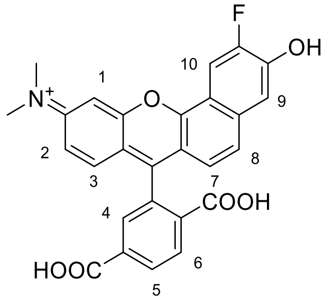

C6.SNARF-2F

Same procedure than for the synthesis of **C5.SNARF-1** was employed, but making the reaction between compound **6** (50 mg, 0.094 mmol) and **11** (16 mg, 0.094 mmol), in the corresponding proportion of phosphoric acid (1 ml). Elaboration was also the same, and the purification was in condition DCM/MeOH/formic acid (9:1:0.1), as for **C5.SNARF-2F**. **C6.SNARF-2F** was obtained as a dark violet powder (34 mg, 76%).

^{1}H NMR (500 MHz, DMSO): δ (ppm) 2.99 (s, 6H, 2x CH_3), 6.57 (dd, 1H, *J* = 8.9, 2.4 Hz, H2), 6.62 (d, 1H, *J* = 7.9 Hz, H7), 6.64 (d, 1H, *J* = 8.3 Hz, H3), 6.87 (d, 1H, *J* = 2.4 Hz, H1), 7.40 (d, 2H, *J* = 8.1 Hz, H8 + H9), 7.65 (s, 1H, H4), 8.02 (d, 1H, *J* = 7.8 Hz, H5), 8.18-8.27 (m, 2H, H6 + H10).

^{13}C NMR (125 MHz, DMSO): δ (ppm) 40.0 (2x CH_3), 83.8, 98.9 (C1), 105.7, 107.7, 107.8 (C10), 110.2 (C2), 111.1, 112.9 (C9), 117.3, 117.3, 122.1 (C8), 123.9 (C3), 124.7 (C5), 124.8 (C4), 128.9 (C7), 131.2 (C6), 132.6, 146.5, 146.5, 147.6, 151.8, 152.5, 153.7, 169.2 (2x COOH).

HRMS (ESI, m/Z): Calculated for $C_{27}H_{19}FNO_6^+$: 472,1191; found: 472.1195 ([M]$^+$).

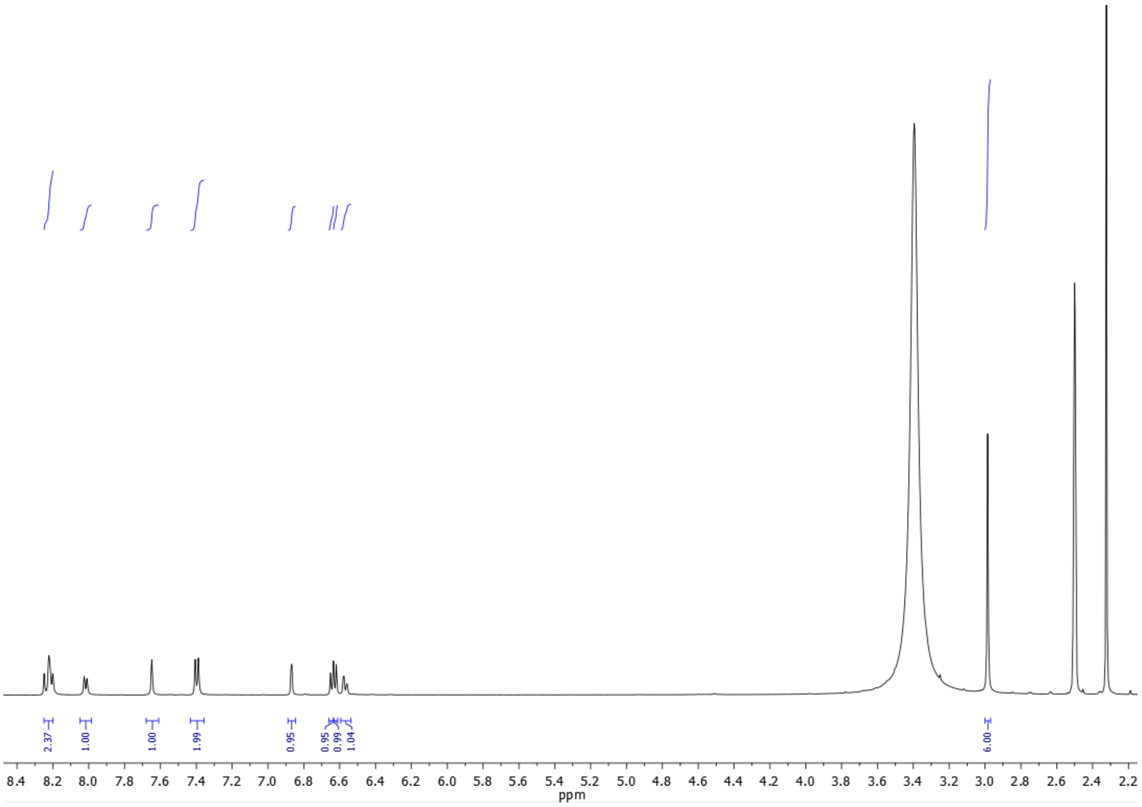

^{1}H NMR (DMSO, 500 MHz)

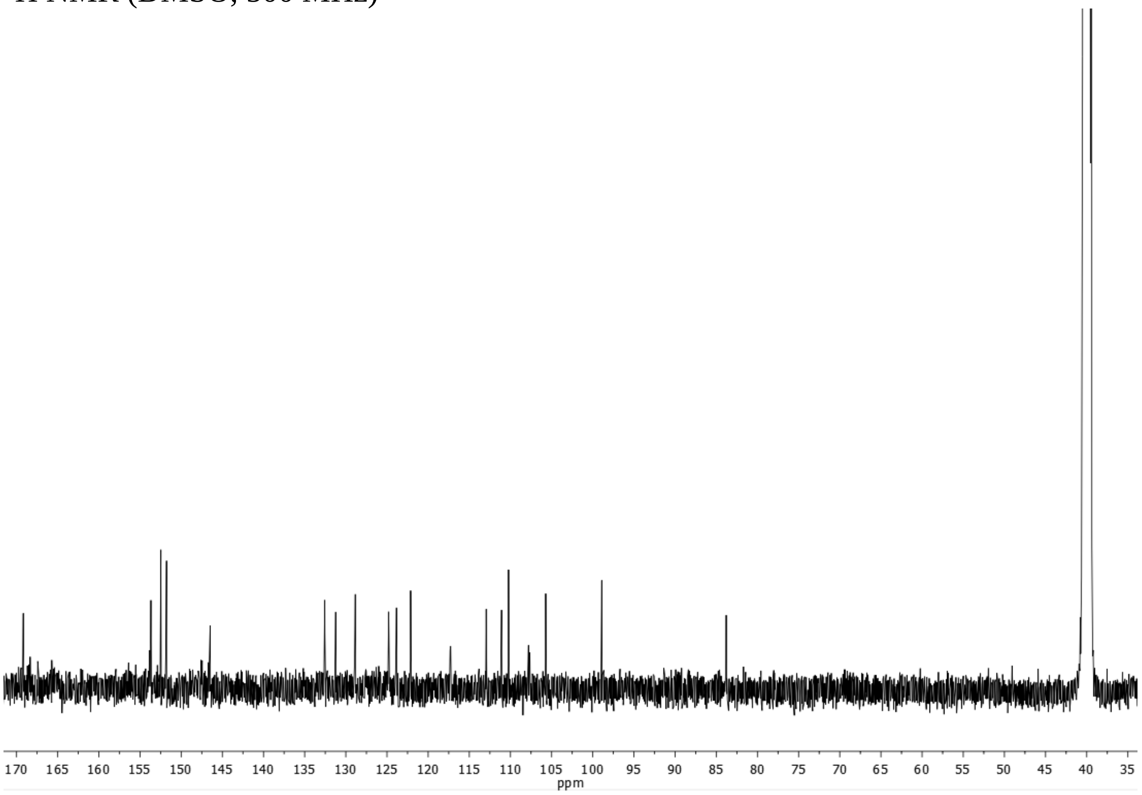

^{13}C NMR (DMSO, 125 MHz)

2-(4-(dimethylamino)-2-hydroxybenzoyl)-3,4,5,6-tetrafluorobenzoic acid (13)

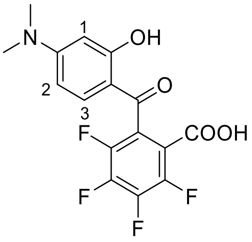

13

A solution of 3-DMAP (94 mg, 0.682 mmol) and tetrafluorophthalic anhydride (150mg, 0.682 mmol) in toluene (3 mL) was stirring under reflux (130 °C) for 12 hours. After this time, the resulting solution was concentrated and the solid was purified by chromatographic column (DCM/MeOH/formic acid 9:1:0.1). The desired product **13** was obtained as a dark solid (130 mg, 53%).

^{1}H RMN (DMSO, 500 MHz): δ (ppm) 3.04 (s, 6 H, 2x CH_3), 6.10 (d, 1 H, *J* = 2.3 Hz, H1), 6.28 (dd, 1 H, *J* = 9.2, 2.2 Hz, H2), 7.15 (dd, 1 H, *J* = 9.2, 1.7 Hz, H3).

^{13}C RMN (DMSO, 125 MHz): δ (ppm) 39.52 (2x CH_3), 96.71 (C1), 105.10 (C2), 110.08, 117.03, 123.37, 133.89 (C3), 142.22, 144.15, 144.76, 146.76, 156.37, 162.35 (COOH), 163.87, 188.08 (C=O).

HRMS (ESI, m/z): Calculated for $C_{16}H_{12}F_4NO_4$: 358.0697; found: 358.0707 ($[M+H]^+$).

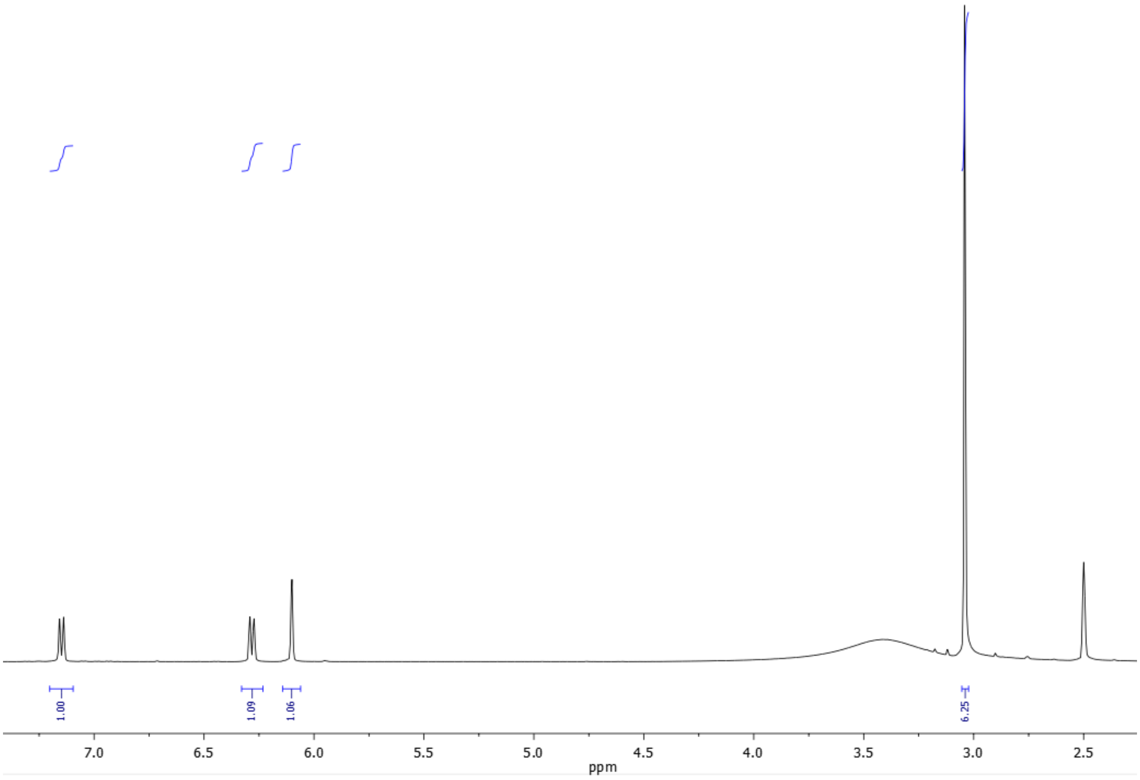

^{1}H NMR (DMSO, 500 MHz)

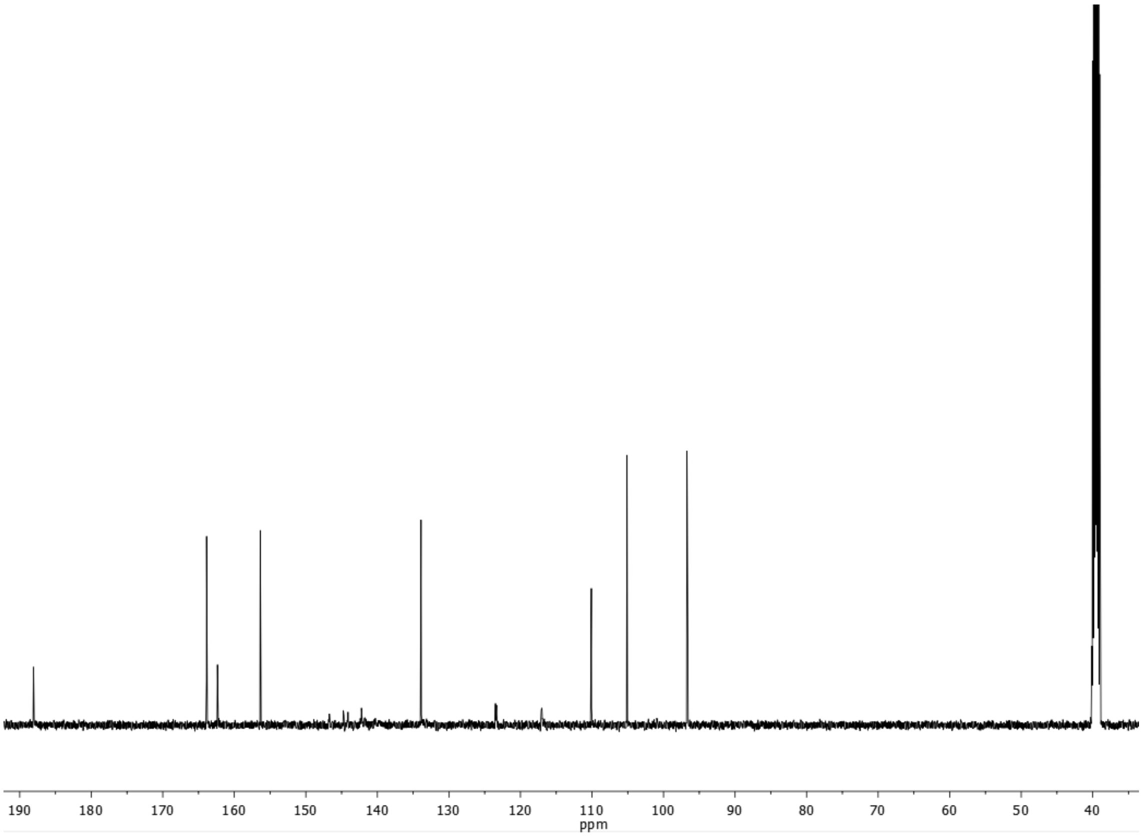

^{13}C NMR (DMSO, 125 MHz)

N-(7-(2-carboxy-3,4,5,6-tetrafluorophenyl)-2-fluoro-3-hydroxy-10H-benzo[c]xanthen-10-ylidene)-N-methylmethanaminium (SNARF-F-2F)

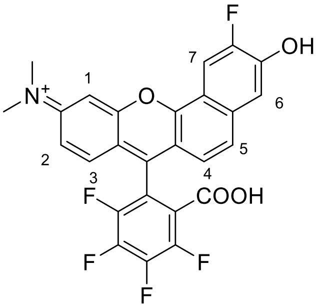

SNARF-F-2F

Compound **13** (20 mg, 0.056 mmol) and **11** (10 mg, 0.056 mmol) were dissolved in methanesulfonic acid (1 ml). Reaction was carried out at 165 °C during 10 min under stirring. The desired product was then precipitated in water and obtained as a dark violet powder (14mg, 50%).

^{1}H NMR (500 MHz, DMSO): δ (ppm) 3.02 (s, 6H), 6.57-6.66 (m, 1H, H2), 6.87-6.90 (m, 1H, H1), 7.0-7.07 (m, 2H, H3 + H4), 7.40 (t, 1H, *J* = 9.2 Hz, H5), 7.50 (d, 1H, *J* = 9.3 Hz, H6), 8.25 (d, 1H, *J* = 12.4 Hz, H7).

^{13}C NMR (125 MHz, DMSO): δ (ppm) 39.4 (2x CH_3), 98.4 (C1), 107.5 (C7), 108.7, 109.8 (C2), 111.5, 112.3 (C5), 116.8, 122.1 (C6), 123.0 (C3) 128.3 (C4), 132.7, 139.8, 140.5, 141.8, 142.6, 143.8, 144.8, 145.8, 146.3, 147.2, 151.4, 152.6, 153.4, 162.7 (COOH).

HRMS (ESI, m/z): Calculated for $C_{26}H_{15}F_5NO_4^+$: 500.0916; found: 500.0914 ([M]$^+$).

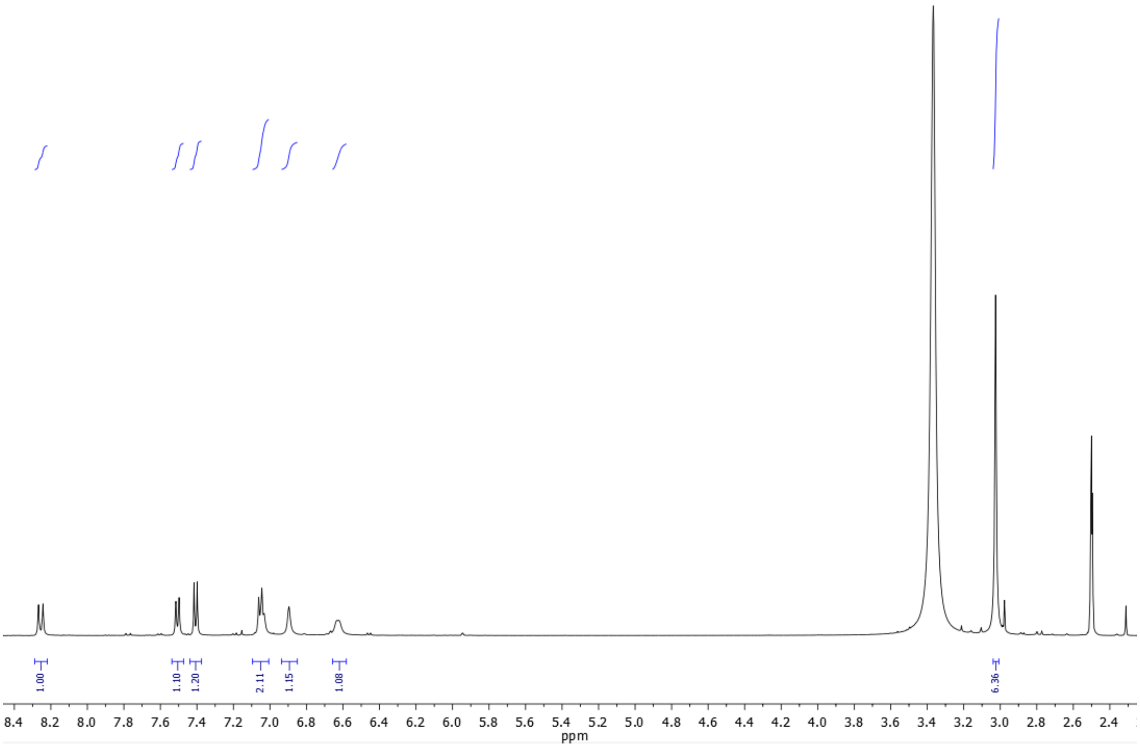

^{1}H NMR (DMSO, 500 MHz)

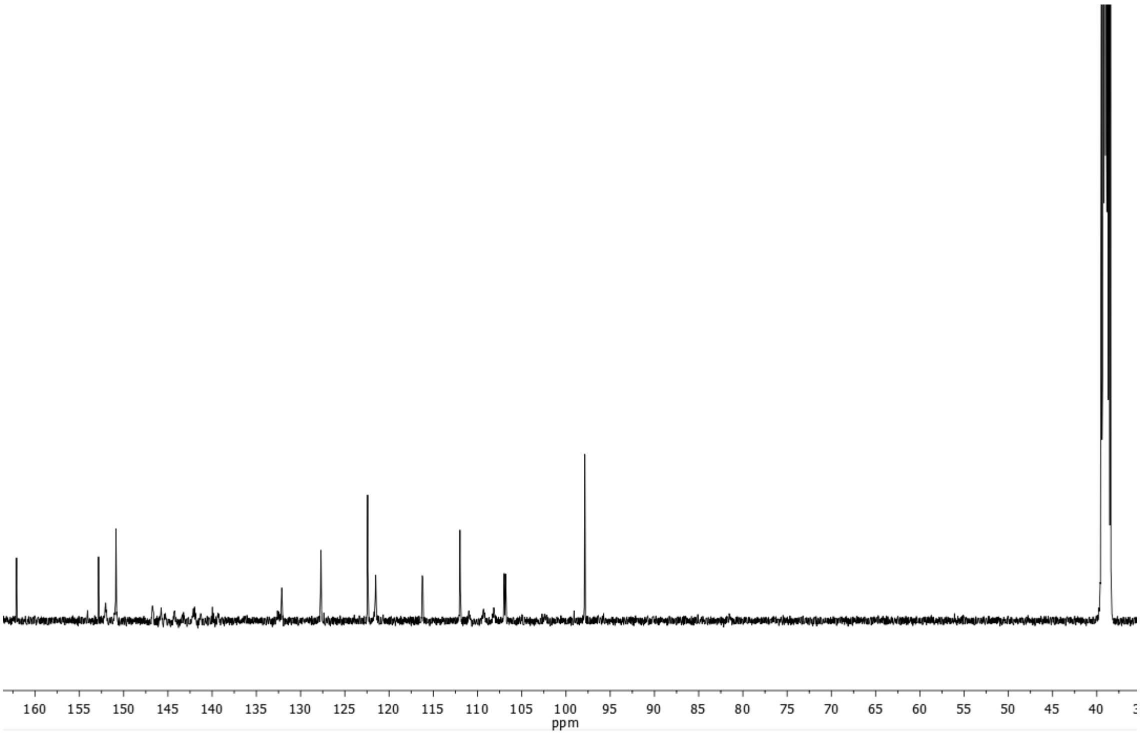

^{13}C NMR (DMSO, 125 MHz)

3. General procedure for spectra measurement and representation

To carry out both absorbance and fluorescence emission spectra of the different SNARF derivatives, firstly, several buffers[133] are prepared with adjusted pH between 4.5 and 9.5. These

---

[133] Lucien, F.; Harper, K.; Pelletier, P. P.; Volkov, L.; Dubois, C. M. Simultaneous pH Measurement in Endocytic and Cytosolic Compartments in Living Cells Using Confocal Microscopy. *J. Vis. Exp.* **2014**, *86*: e51395.

buffers are aqueous solutions with 10 mM MES, 10 mM HEPES, 20 mM glucose, 1 mM $CaCl_2$, 1 mM $MgCl_2$, 135 mM KCl and 20 mM NaCl, and the pH is adjusted with few drops of 1M HCl or 1M NaOH.

By other side, a stock solution of the studied fluorophore is prepared. MQ-H_2O (30 g) are weighed, and its pH is adjusted to ≈ 9.5 with 10 % NH_3 (aq). Few milligrams of the fluorophore are added, and absorbance is adjusted around 0.7 a.u. in its maximum wavelength, avoiding saturation of the spectrophotometer lamp and guaranteeing a similar concentration in all cases.

Next, final solutions are prepared by mixing 3 mL of the stock solution and another 3 mL of the corresponding buffer for each case. The pH is measured again for each one of them, which varies slightly when adding the stock solution, and their absorption or fluorescence emission spectra are recorded.

All curves are normalized to start at 0 a.u. at the maximum or minimum wavelength recorded.

For few cases of fluorescence emission, if not all the curves intersect at the isosbestic point, a correction is made to eliminate alterations introduced by concentration differences due to pipetting errors or partial precipitation at certain pHs. This correction is made by selecting the emission intensity value for the isosbestic point of one of the curves and dividing the emission intensity at that wavelength on the rest of the curves by that selected value. In this way, a normalization factor is obtained for each curve. Next, all the emission intensity values of each curve are divided by the corresponding normalization factor. Thus, all curves intersect at the isosbestic point.

4.1. General procedure for pK_a calculation

For pK_a value determination, the fluorescence intensity at the acidic or basic maximum wavelength is represented *versus* its pH. Data adjustment to determine pK_a value was performed with a “log(agonist) vs. response -- Find ECanything” equation, fixing F to 50 and bottom and top values to minimum and maximum represented values, respectively. pK_a value corresponds with logECF obtained value.

4. Complementary figures

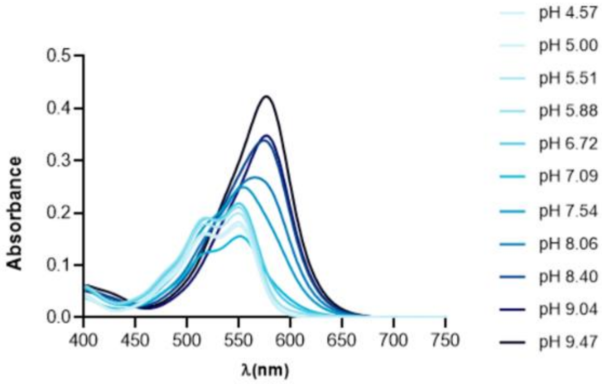

Figure S2.1. Absorbance spectrum of ***C5,6.SNARF-****1 mixture.*

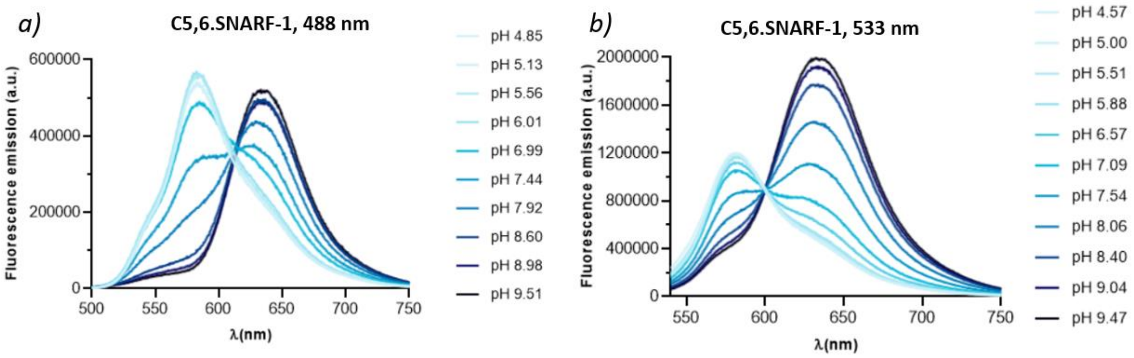

*Figure S2.2. Fluorescence spectra of **C5,6.SNARF-1** mixture at excitation wavelength of (a) 488 nm and (b) 533 nm.*

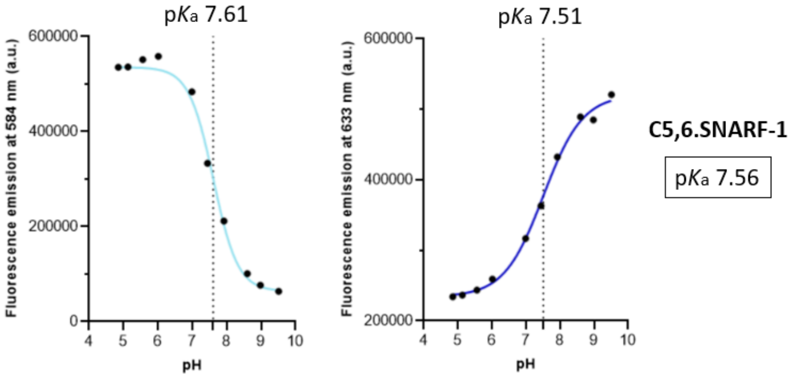

*Figure S2.3. Graphs representing the variation of the fluorescence emission with the pH for **C5,6.SNARF-1**, and its value of pK$_a$ obtained.*

Field 3: New pH sensitive strategies for venom-derived antitumoral drugs

Section affected by confidentiality: under the protection of rights.

Conclusions

Along this PhD work, we have used chemistry as a tool to develop new supramolecular concepts and sensitive systems to mimic and interfere with diverse cellular functional applications. More in detail, we have applied it to three different fields: amphiphilic self-assemblies for protocellular study, fluorescent probes for cellular compartments identification and new pH sensitive strategies for venom-derived antitumoral drugs.

In the first case (Figure 45), a new one-dimensional protofilament system has been developed, which allows to better understand the functional behaviour of more complex fibrillar systems that could have been formed in protocells. Thus, the assembly of fibrillar supramolecular peptide architectures was obtained *in situ* through an oxime connection by the self-assembly of a non-assembling peptide ($\mathbf{P_{C8}}$) and a hydrophobic peptide tail ($\mathbf{T_8}$), producing a peptide amphiphile, namely $\mathbf{P_{C8}T_8}$. The supramolecular aggregation starts with a micellar state of $\mathbf{P_{C8}T_8}$ and a subsequent elongation from micelles to fibres according to a physical autocatalytic reaction. Moreover, it was demonstrated that this fibrillation phenomenon, when carried out inside confined aqueous droplets, can mediate in the interaction with environment, taking up exogenous fluorescent probes selectively depending on their charge. Even, the contact base-exchange between droplets have been studied, showing the key role of $\mathbf{P_{C8}T_8}$ increasing chemical transport between them.

More in detail, it was possible to achieve several goals and conclusions:

- The reaction of a dormant non-assembling peptide ($\mathbf{P_{C8}}$) with a hydrophobic aldehyde tail ($\mathbf{T_8}$) led to the production of the peptide amphiphile $\mathbf{P_{C8}T_8}$.

- After this reaction, a micellar aggregation of the $\mathbf{P_{C8}T_8}$ amphiphile triggered a physical autocatalytic reaction, where initial $\mathbf{P_{C8}T_8}$ aggregates facilitate and accelerate the reaction and the subsequent self-assembly of the peptide amphiphiles into nanofibers that were bundled into filaments at the micro scale.

- The fibrillation phenomenon has been carried out in confined spaces as aqueous droplets. When these droplets are filled with $\mathbf{P_{C8}}$, and $\mathbf{T_8}$ is exogenously added, fibres are formed inside the droplets. Interestingly, as fibres number starts to grow, they tend to move from the core to droplet cortex of the droplet containers. This phenomenon was explained as the favourable interaction of the fibres with other $\mathbf{P_{C8}T_8}$ units, which are more concentrated in the interface (as $\mathbf{T_8}$ is coming to the droplet from outside).

- The ability of interaction of fibrillated droplets with their environment has also been studied. For example, the fibrillation process triggered the uptake of exogenous fluorescent probes that had an impact in the droplet populations. Cationic probes were easily taken up by droplets, as fibres are negatively charged, and the coalescence between droplets increase probably due to a fibre neutralization and the following reduction of the charge repulsion between fibres. Externally added zwitterionic probes were also internalized, but not important effects in coalescence were observed. In contrast, the addition of negatively charged probes decreased the coalescence rate.

- Finally, a two-step enzymatic cascade between two droplets populations was tested. The exchange of molecular information between the droplets was demonstrated by generation of the fluorescent product resulting from an enzymatic cascade between droplets containing mixtures of orthogonally distributed reagents. The critical role of $\mathbf{P_{C8}T_8}$ fibres is generating local points of face continuity between droplets and also its ability to increase chemical transport.

From a more general point of view, the work developed in this field have given interesting results regarding elongated structures and fibrillar networks, which are commonly identified in cells and in the semiliquid protoplasm.[134] Intriguing discoveries on primitive fibrillar networks have confirmed the presence of different early supramolecular biopolymers that were involved in functional processes such as the emergence of basic phagocytic behaviour and perhaps also in symbiotic engulfment.[135] The experiments reported here constitute a first proof of principle that 1D hierarchical self-assembly can indeed trigger coordinated complex functional behaviour between individual aqueous entities (*i.e.* physical autocatalysis, self-assembly, uptake, coalescence and exchange of materials) without the need of a complex molecular machinery. It also transpires from these results that minimalistic 1D supramolecular polymerization plays a role in the functional mechanisms that individual aqueous entities may have used to interact with their environment and within communities. Overall, these results will contribute to the bottom-up design and basic understanding of more complex 1D supramolecular biomimetic assemblies and the future development of new 1D functional materials with life-like properties and stimuli-responsive behaviour.

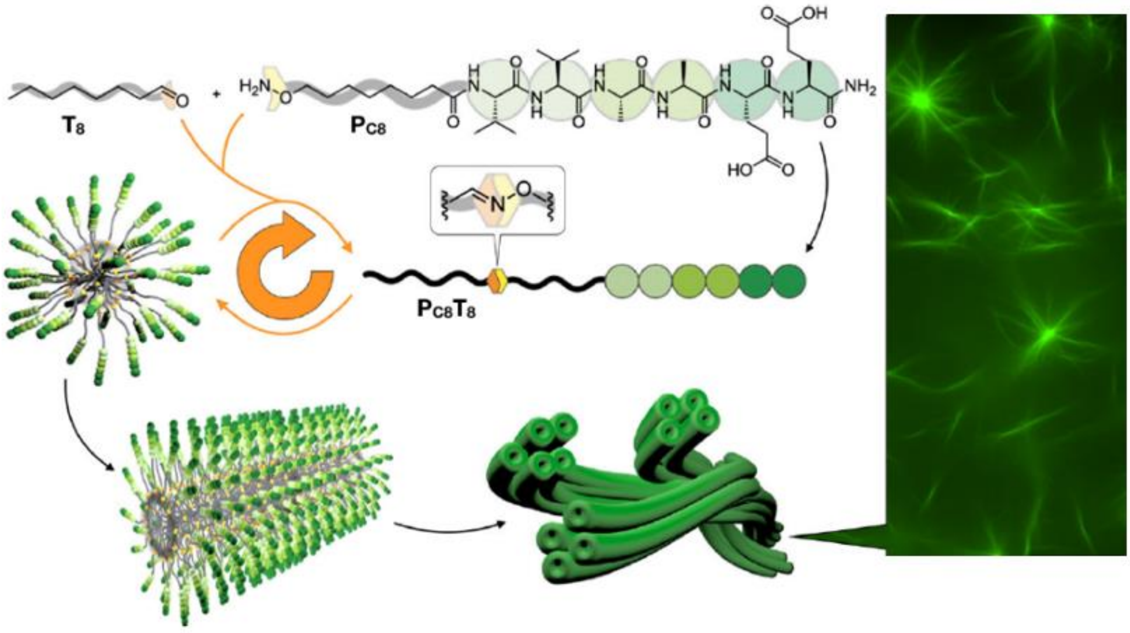

Figure 45. Field 1: Amphiphilic self-assemblies for protocellular study. Schematic representation of supramolecular $\mathbf{P_{C8}T_8}$ *formation and autocatalytic aggregation into final fibrillar cytoskeleton mimetic structures.*

In the second field (Figure 46), a synthetic route towards ratiometric fluorophore structures has been optimized to prepare fluorinated SNARF analogues with low pK_a. As a first step, the research have started with the development of a two steps synthetic route for **C.SNARF-1** production in up to 1 gram scale with an overall yield of 45 %. Also, the optimization of a chromatographic method was carried out allowing, for the first time, the separation of the two positional isomers of **C.SNARF-1**, namely **C5.SNARF-1** and **C6.SNARF-1**, followed by a complete photophysical characterization of both isolated compounds. New fluorinated derivatives of **C5.SNARF-1** and **C6.SNARF-1** have also been

---

[134] Oparin, A. I. *The Origin of Life*; Foreign Languages Publishing House, 1924.

[135] Ettema, T. J. G.; Lindås, A. C.; Bernander, R. An Actin-Based Cytoskeleton in Archaea. *Mol. Microbiol.* **2011**, *80* (4), 1052–1061.

synthesized and characterized for the first time. Although both of them present a fluorescent quenching of their acidic band, their phenol pK_a value is more than one unit lower, presenting **C5.SNARF-2F** a pK_a of 6.16 and **C6.SNARF-2F** a pK_a of 6.21. Thus, **C5.SNARF-2F** has appeared as the **C.SNARF-1** derivative with lower pK_a value reported, which make it very promising as an optimized ratiometric probe for drug tracking during endocytic pathway, among other biological purposes. Finally, perfluorinated derivative **SNARF-F-2F** has been synthesized for the first time, but improvements in its pK_a were not observed.

Therefore, the next bullet points have been achieved:

- Based on previously reported SNARF synthetic approaches,[94] we have developed a synthetic route that allow the production of **C.SNARF-1** with an overall yield of 45 %. This synthetic approach consists on just two successive reactions, where only a purifications step is required at the end of the route in conditions DCM/MeOH/formic acid 5:1:0.1. Moreover, this protocol can be scaled up to the gram scale, which allows the employ of the probe for other synthetic purposes, and to attach this probe to any molecules of interest to be observed in cells.

- A separation method has been optimized for the isolation of the two positional isomers of **C.SNARF-1**, namely: **C5.SNARF-1** and **C6.SNARF-1**. Both isomers are not currently commercially available and, to the best of our knowledge, have not been isolated and characterized independently before. To make possible the separation of the **5** and **6** positional isomers, compound **5** is first separated from the crude through a precipitation in methanol. Compound **6** is then isolated after two chromatographic columns, the first in conditions MeOH/DCM/formic acid 98:2:0.1, and the second in MeOH/DCM/NH_3 7N in MeOH 50:50:0.1. The reaction of either **5** or **6** with 1,6-dihydroxynaphtalene leads to **C5.SNARF-1** and **C6.SNARF-1** in excellent isolated yields of 37 % and 15 % respectively, which means a total yield of 11 % for the synthesis **C5.SNARF-1** and 4 % for **C6.SNARF-1**.

- The photophysical properties of **C5.SNARF-1** and **C6.SNARF-1** have been characterized and compared. Analysing the position of their bands, corresponding with the acidic form (584 nm) and basic form (633 nm), no differences were observed. However, when comparing their relative intensities, **C5.SNARF-1** presents a quenched basic band. This observation could be rationalized by the potential stacking between fluorescent molecules, a phenomenon which is just possible in **C5.SNARF-1**, but hindered for the isomer **C6.SNARF-1**. Their pK_a values were in the same range (7.65 and 7.66), which perfectly matches with the reported 7.5 value for commercially available C.SNARF-1 mixture.

- **C5.SNARF-2F** and **C6.SNARF-2F**, new fluorinated **C.SNARF-1** positional isomers derivatives, has been synthesized for the first time following an analogous synthetic scheme to **C5.SNARF-1** and **C6.SNARF-1** route, but only 4 additional steps required for the preparation of 7-fluoronaphthalene-1,6-diol (compound **11**). Compound **11** is prepared to introduce a fluorine atom selectively in the position 7 of the naphthalene ring, with a final yield of 18 % after 4 synthetic steps. Reaction of **11** with the corresponding intermediates **5** or **6** lead to the obtention of **C5.SNARF-2F** and **C6.SNARF-2F** with overall yields of 2 % and 3 %, respectively.

- **C5.SNARF-2F** and **C6.SNARF-2F** photophysical study has shown important differences compared to their non-fluorinated versions. First, a shift in the position of acidic and basic band has been observed. Basic band shift was of few nanometers, moving from 633 to 627 nm. However, acidic band moves more than 30 nm, from 584 to 550 nm. This fact is explained as the fluorine stabilization of charge and the consequent energetic change of basal and excited electronic states. Moreover, acidic band seems quenched compared to non-fluorinated probes, especially in the case of C6 isomer, which could be related with stacking or electronic effects. Same phenomenon was previously described in other fluorinated SNARFs, as in the case of SNARF-5.[95]

- The pK_a values of SNARF fluorinated (at position 2) analogues showed values of 6.16 and 6.21 for **C5.SNARF-2F** and **C6.SNARF-2F**, respectively, which was determined employing basic band. **C5.SNARF-2F** emerges as the C.SNARF-1 probe with the lowest pK_a value reported with potential applications as a useful ratiometric probe for intracellular tracking of endocytosis and acidic organelles.

- The fluorinated **C5.SNARF-2F** can be obtained in just 6 synthetic steps with an overall yield of 2 %. Regarding other previously reported C.SNARF-1 fluorinated derivatives, SNARF-4F showed the lowest pK_a (6.4) and can be obtained with a yield of 3 % through 9 synthetic steps.[95] Therefore, our new optimized **C.SNARF-1** probe has close to 0.3 units less of pK_a and can be obtained with almost the same yield in 3 steps less.

- The C.SNARF-2F analogue with 4 fluorine atoms in the phenyl pendant, **SNARF-F-2F**, has been synthesized for the first time, with an overall yield of 5 %. This probe loses certain ratiometric behaviour and it does not improve the pK_a value of the C.SNARF-2F isomers.

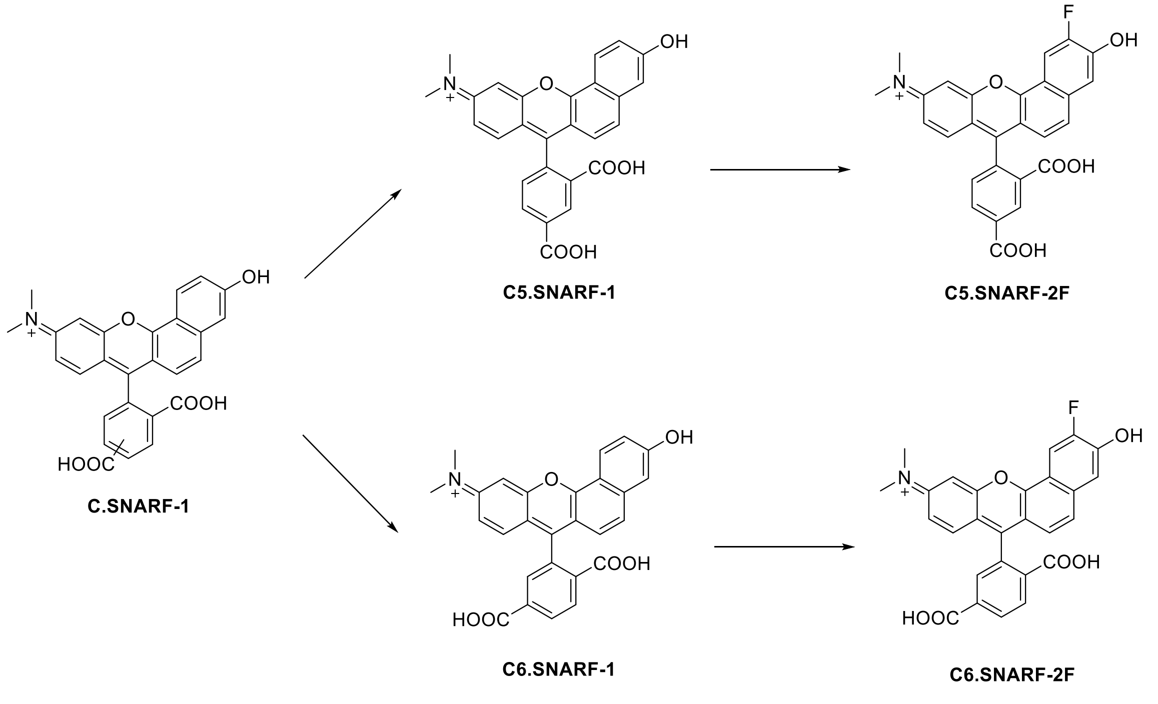

Figure 46. Chapter II. Schematic representation of the different main fluorophore structures synthesized during this chapter, being from left to right: ***C.SNARF-1*** *mixture,* ***C5.SNARF-1*** *and* ***C6.SNARF-1*** *isomers, and derived fluorinated new structures,* ***C5.SNARF-2F*** *and* ***C6.SNARF-2F****.*

Finally, in the third field Section affected by confidentiality: under the protection of rights.

The conclusions presented in the first case have been published in:

Booth, R. [a]; Insua, I. [a]; Ahmed, S. [a]; Rioboo, A. [a]; Montenegro, J. [a]* Supramolecular Fibrillation of Peptide Amphiphiles Induces Environmental Responses in Aqueous Droplets.
Nat. Commun. **2021**, *12 (1)*, 6421–6428.
DOI: 10.1038/s41467-021-26681-2

[a] Centro Singular de Investigación en Química Biolóxica e Materiais Moleculares (CiQUS), Departamento de Química Orgánica, Universidade de Santiago de Compostela (USC), 15782, Spain.

Nature Communications Impact Score: 16.6 (2022). Q1 in Biochemistry, Genetics and Molecular Biology; Chemistry; Physics and Astronomy.

Bibliography

[1] Lehn, J. M. Towards Complex Matter: Supramolecular Chemistry and Self-Organization. *Eur. Rev.* **2009**, *17* (2), 263–280.

[2] Lehn, J. M. Supramolecular Chemistry: Where from? Where To? *Chem. Soc. Rev.* **2017**, *46* (9), 2378–2379.

[3] Steed, J. W.; Turner, D. R.; Wallace, K. *Core Concepts in Supramolecular Chemistry and Nanochemistry*; Wiley: Hoboken, NJ, 2007.

[4] Lehn, J. M. Supramolecular Chemistry-Scope and Perspectives Molecules, Supermolecules, and Molecular Devices (Nobel Lecture). *Angew. Chem. Int. Ed.* **1988**, 27 (1), 89–112.

[5] Cram, D. J. The Design of Molecular Hosts, Guests, and Their Complexes (Nobel Lecture). *Angew. Chem. Int. Ed.* **1988**, *21* (3), 155–173.

[6] Pedersen, C. J. The Discovery of Crown Ethers (Noble Lecture). *Angew. Chemie Int. Ed.* **1988**, *27* (8), 1021–1027.

[7] Mendes, A. C.; Baran, E. T.; Reis, R. L.; Azevedo, H. S. Self-Assembly in Nature: Using the Principles of Nature to Create Complex Nanobiomaterials. *Wiley Interdiscip. Rev. Nanomedicine Nanobiotechnology* **2013**, *5* (6), 582–612.

[8] Monod, J.; Changeux, J. P.; Jacob, F. Allosteric Proteins and Cellular Control Systems. *J. Mol. Biol.* **1963**, *6* (4), 306–329.

[9] Kim, H.-J.; Kim, T.; Lee, M. Responsive Nanostructures from Aqueous Assembly of Rigid−Flexible Block Molecules. *Acc. Chem. Res.* **2011**, *44* (1), 72–82.

[10] Danial, M.; Tran, C. M.-N.; Young, P. G.; Perrier, S.; Jolliffe, K. A. Janus Cyclic Peptide–Polymer Nanotubes. *Nat. Commun.* **2013**, *4* (1), 2780–2793.

[11] Krieg, E.; Bastings, M. M. C.; Besenius, P.; Rybtchinski, B. Supramolecular Polymers in Aqueous Media. *Chem. Rev.* **2016**, *116* (4), 2414–2477.

[12] Shimizu, T.; Ding, W.; Kameta, N. Soft-Matter Nanotubes: a Platform for Diverse Functions and Applications. *Chem. Rev.* **2020**, *120* (4), 2347–2407.

[13] Lancia, F.; Ryabchun, A.; Katsonis, N. Life-Like Motion Driven by Artificial Molecular Machines. *Nat. Rev. Chem.* **2019**, 3 (9), 536–551.

[14] Radvar, E.; Azevedo, H. S. Supramolecular Peptide/Polymer Hybrid Hydrogels for Biomedical Applications. *Macromol. Biosci.* **2018**, *19*, 1800221.

[15] Huang, Z.; Kang, S. K.; Banno, M.; Yamaguchi, T.; Lee, D.; Seok, C.; Yashima, E.; Lee, M. Pulsating Tubules from Noncovalent Macrocycles. *Science* **2012**, *337* (6101), 1521–1526

[16] Insua, I.; Montenegro, J. 1D to 2D Self Assembly of Cyclic Peptides. *J. Am. Chem. Soc.* **2020**, *142* (1), 300–307.

[17] Yagai, S.; Kitamoto, Y.; Datta, S.; Adhikari, B. Supramolecular Polymers Capable of Controlling Their Topology. *Acc. Chem. Res.* **2019**, *52* (5), 1325–1335.

[18] Ogi, S.; Sugiyasu, K.; Manna, S.; Samitsu, S.; Takeuchi, M. Living Supramolecular Polymerization Realized Through a Biomimetic Approach. *Nat. Chem.* **2014**, *6* (3), 188–195.

[19] Vázquez-González, V.; Mayoral, M. J.; Chamorro, R.; Hendrix, M. M. R. M.; Voets, I. K.; González-Rodríguez, D. Noncovalent Synthesis of Self-Assembled Nanotubes through Decoupled Hierarchical Cooperative Processes. *J. Am. Chem. Soc.* **2019**, *141* (41), 16432–16438.

[20] Chatterjee, A.; Mahato, C.; Das, D. Complex Cascade Reaction Networks Via Cross β Amyloid Nanotubes. *Angew. Chem. Int. Ed.* **2021**, *60* (1), 202–207.

[21] Insua, I.; Montenegro, J. Synthetic Supramolecular Systems in Life-like Materials and Protocell Models. *Chem* **2020**, *6* (7), 1652–1682.

[22] Kim, Y.; Li, H.; He, Y.; Chen, X.; Ma, X.; Lee, M. Collective Helicity Switching of a DNA-Coat Assembly. *Nat. Nanotechnol.* **2017**, *12* (6), 551–556.

[23] Ruiz-Mirazo, K.; Briones, C.; De La Escosura, A. Prebiotic Systems Chemistry: New Perspectives for the Origins of Life. *Chem. Rev.* **2014**, *114* (1), 285–366.

[24] Mattia, E.; Otto, S. Supramolecular Systems Chemistry. *Nat. Nanotechnol.* **2015**, *10* (2), 111–119.

[25] Spitzer, D.; Marichez, V.; Formon, G. J. M.; Besenius, P.; Hermans, T. M. Surface-Assisted Self-Assembly of a Hydrogel by Proton Diffusion. *Angew. Chem. Int. Ed.* **2018**, *57* (35), 11349–11353.

[26] Méndez-Ardoy, A.; Bayón-Fernández, A.; Yu, Z.; Abell, C.; Granja, J. R.; Montenegro, J. Spatially Controlled Supramolecular Polymerization of Peptide Nanotubes by Microfluidics. *Angew. Chemie* **2020**, *132* (17), 6969–6975.

[27] Kumar, R. K.; Harniman, R. L.; Patil, A. J.; Mann, S. Self-Transformation and Structural Reconfiguration in Coacervate-Based Protocells. *Chem. Sci.* **2016**, *7* (9), 5879–5887.

[28] Méndez-Ardoy, A.; Granja, J. R.; Montenegro, J. pH-Triggered Self-Assembly and Hydrogelation of Cyclic Peptide Nanotubes Confined in Water Micro-Droplets. *Nanoscale Horiz.* **2018**, *3* (4), 391–396.

[29] Kumar, M.; Ing, N. L.; Narang, V.; Wijerathne, N. K.; Hochbaum, A. I.; Ulijn, R. V. Amino-Acid-Encoded Biocatalytic Self-Assembly Enables the Formation of Transient Conducting Nanostructures. *Nat. Chem.* **2018**, *10* (7), 696–703.

[30] Kameta, N.; Akiyama, H. Shrinkable Nanotubes for Duplex Formation of Short Nucleotides. *Small* **2018**, *14* (34), 1–6.

[31] Martin, N.; Douliez, J. P.; Qiao, Y.; Booth, R.; Li, M.; Mann, S. Antagonistic Chemical Coupling in Self-Reconfigurable Host–Guest Protocells. *Nat. Commun.* **2018**, *9* (1), 1–12.

[32] Estirado, E. M.; Mason, A. F.; Alemán García, M. Á.; Van Hest, J. C. M.; Brunsveld, L. Supramolecular Nanoscaffolds within Cytomimetic Protocells as Signal Localization Hubs. *J. Am. Chem. Soc.* **2020**, *142* (20), 9106–9111.

[33] Chandler, D. Hydrophobicity: Two Faces of Water. *Nature* **2002**, *417* (6888), 491.

[34] Feng, B.; Sosa, R. P.; Mårtensson, A. K. F.; Jiang, K.; Tong, A.; Dorfman, K. D.; Takahashi, M.; Lincoln, P.; Bustamante, C. J.; Westerlund, F.; Nordén, B. Hydrophobic Catalysis and a Potential Biological Role of DNA Unstacking Induced by Environment Effects. *Proc. Natl. Acad. Sci. U.S.A.* **2019**, *116* (35), 17169–17174.

[35] Díaz, S.; Insua, I.; Bhak, G.; Montenegro, J. Sequence Decoding of 1D to 2D Self-Assembling Cyclic Peptides. *Chem. Eur. J.* **2020**, *26* (64), 14765–14770.

[36] Gilroy, J. B.; Gädt, T.; Whittell, G. R.; Chabanne, L.; Mitchels, J. M.; Richardson, R. M.; Winnik, M. A.; Manners, I. Monodisperse Cylindrical Micelles by Crystallization-Driven Living Self-Assembly. *Nat. Chem.* **2010**, *2* (7), 566–570.

[37] Aparicio, F.; Chamorro, P. B.; Chamorro, R.; Casado, S.; González-Rodríguez, D. Nanostructured Micelle Nanotubes Self-Assembled from Dinucleobase Monomers in Water. *Angew. Chem. Int. Ed.* **2020**, *132* (39), 17239–17244.

[38] Flores, J.; White, B. M.; Brea, R. J.; Baskin, J. M.; Devaraj, N. K. Lipids: Chemical Tools for Their Synthesis, Modification, and Analysis. *Chem. Soc. Rev.* **2020**, *49* (14), 4602–4614.

[39] Walde, P.; Wick, R.; Fresta, M.; Mangone, A.; Luisi, P. L. Autopoietic Self-Reproduction of Fatty Acid Vesicles. *J. Am. Chem. Soc.* **1994**, *116* (26), 11649–11654.

[40] Budin, I.; Debnath, A.; Szostak, J. W. Concentration-Driven Growth of Model Protocell Membranes. *J. Am. Chem. Soc.* **2012**, *134* (51), 20812–20819.

[41] Pottanam-Chali, S.; Ravoo, B. J. Polymer Nanocontainers for Intracellular Delivery. *Angew. Chem. Int. Ed.* **2020**, *59* (8), 2962–2972.

[42] Bissette, A. J.; Odell, B.; Fletcher, S. P. Physical Autocatalysis Driven by a Bond-Forming Thiol-Ene Reaction. *Nat. Commun.* **2014**, *5* (1), 4607–4614.

[43] Budin, I.; Devaraj, N. K. Membrane Assembly Driven by a Biomimetic Coupling Reaction. *J. Am. Chem. Soc.* **2011**, *134* (2), 751–753.

[44] Sparks, J. S.; Schelly, R. C.; Smith, W. L.; Davis, M. P.; Tchernov, D.; Pieribone, V. A.; Gruber, D. F. The Covert World of Fish Biofluorescence: A Phylogenetically Widespread and Phenotypically Variable Phenomenon. *PLoS One* **2014**, *9* (1): e83259.

[45] Acuña, A. U.; Amat-Guerri, F. Early History of Solution Fluorescence: The Lignum Nephriticum of Nicolás Monardes. In *Springer Series on Fluorescence*; Berberan-Santos, M. N., Ed.; Springer, 2007; Vol. 4, pp 3–20.

[46] Valeur, B. *Molecular Fluorescence: Principles and Applications*; Wiley-Vch: Weinheim; Cambridge, 2002.

[47] Lakowicz, J. R. *Principles of Fluorescence Spectroscopy*; Springer Science+Business Media: New York, 2010.

[48] Jabłoński, A. Über Den Mechanismus Der Photolumineszenz von Farbstoffphosphoren. *Z. Physik* **1935**, *94* (1-2), 38–46.

[49] Stokes, G. G. On the Change of Refrangibility of Light. *Philos. Trans. R. Soc. Lond.* **1852**, *142*, 463–562.

[50] Kasha, M. Characterization of Electronic Transitions in Complex Molecules. *Discuss. Faraday Soc.* **1950**, *9*, 14–19.

[51] Lang, W.; Yuan, C.; Zhu, L.; Du, S.; Qian, L.; Ge, J.; Yao, S. Q. Recent Advances in Construction of Small Molecule-Based Fluorophore-Drug Conjugates. *J. Pharm. Anal.* **2020**, *10* (5), 434–443.

[52] Terai, T.; Nagano, T. Small-Molecule Fluorophores and Fluorescent Probes for Bioimaging. *Pflugers Arch. Eur. J. Physiol.* **2013**, *465* (3), 347–359.

[53] Chen, Y.; Gao, Y.; He, Y.; Zhang, G.; Wen, H.; Wang, Y.; Wu, Q. P.; Cui, H. Determining Essential Requirements for Fluorophore Selection in Various Fluorescence Applications Taking Advantage of Diverse Structure-Fluorescence Information of Chromone Derivatives. *J. Med. Chem.* **2021**, *64* (2), 1001–1017.

[54] *"Quenching by halogen and heavy atoms occurs due to spin–orbit coupling and intersystem crossing to the triplet state"* (see Lakowicz, J. R. *Principles of Fluorescence Spectroscopy*; Springer Science+Business Media: New York, 2010).

[55] Lavis, L. D.; Raines, R. T. Bright Ideas for Chemical Biology. *ACS Chem. Biol.* **2008**, *3* (3), 142–155.

[56] Herschel, J. F. W. On a Case of Superficial Colour Presented by a Homogeneous Liquid Internally Colourless. *Phil. Trans. R. Soc. London* **1845**, *135*, 143–145.

[57] Seeman, J. I. The Woodward-Doering/Rabe-Kindler Total Synthesis of Quinine: Setting the Record Straight. *Angew. Chem. Int. Ed.* **2007**, *46* (9), 1378–1413.

[58] Teale, F. W.; Weber, G. Ultraviolet Fluorescence of the Aromatic Amino Acids. *Biochem. J.* **1957**, *65* (3), 476–482.

[59] Royer, C. A. Probing Protein Folding and Conformational Transitions with Fluorescence. *Chem. Rev.* **2006**, *106* (5), 1769–1784.

[60] Fu, Y.; Finney, N. S. Small-Molecule Fluorescent Probes and Their Design. *RSC Adv.* **2018**, *8* (51), 29051–29061.

[61] Kumar, K. A.; Nagamallu, R.; Govindappa, V. K. Comprehensive Review on Coumarins : Molecules of Potential Chemical and Pharmacological Interest Comprehensive Review on Coumarins : Molecules of Potential Chemical and Pharmacological Interest. *J. Chem. Pharm. Res.* **2015**, *7* (9), 67–81.

[62] Baeyer, A. Die Drei Isomeren Reihen Wiireo Demnsch Nach Meinen Uebergangen. *Berichte der Dtsch. Chem. Gesellschaft* **1871**, *4* (2), 555–558.

[63] Loudet, A.; Burgess, K. BODIPY Dyes and Their Derivatives: Syntheses and Spectroscopic Properties. *Chem. Rev.* **2007**, *107* (11), 4891–4932.

[64] Silva, G. L.; Ediz, V.; Yaron, D.; Armitage, B. A. Experimental and Computational Investigation of Unsymmetrical Cyanine Dyes: Understanding Torsionally Responsive Fluorogenic Dyes. *J. Am. Chem. Soc.* **2007**, *129* (17), 5710–5718.

[65] Gebhardt, C.; Lehmann, M.; Reif, M. M.; Zacharias, M.; Gemmecker, G.; Cordes, T. Molecular and Spectroscopic Characterization of Green and Red Cyanine Fluorophores from the Alexa Fluor and AF Series. *ChemPhysChem* **2021**, *22* (15), 1566–1583.

[66] Shindy, H. A. Fundamentals in the Chemistry of Cyanine Dyes: A Review. *Dye. Pigment.* **2017**, *145*, 505–513.

[67] Zhang, J.; Campbell, R. E.; Ting, A. Y.; Tsien, R. Y. Creating New Fluorescent Probes for Cell Biology. *Nat. Rev. Mol. Cell Biol.* **2002**, *3* (12), 906–918.

[68] Chalfie, M.; Tu, Y.; Euskirchen, G.; Ward, W. W.; Prasherf, D. C. Green Fluorescent Protein as a Marker for Gene Expression. *Science* **1994**, *263* (5148), 802–805.

[69] Shimorura, O.; Johnson, F. H.; Saiga, Y. Extraction, Purification and Properties of Aequorin, a Bioluminescent Protein from the Luminous Hydromedusan, Aequorea . *J. Cell. Comp. Physiol.* **1962**, *59* (3), 223–239.

[70] Tsien, R. Y. The Green Fluorescent Protein. *Annu. Rev. Biochem.* **1998**, *67* (1), 509–544.

[71] Tsien, R. Y. Constructing and Exploiting the Fluorescent Protein Paintbox (Nobel Lecture). *Angew. Chem. Int. Ed.* **2009**, *48* (31), 5612–5626.

[72] Michalet, X.; Pinaud, F. F.; Bentolila, L. A.; Tsay, J. M.; Doose, S.; Li, J. J.; Sundaresan, G.; Wu, A. M.; Gambhir, S. S.; Weiss, S. Quantum Dots for Live Cells, in Vivo Imaging, and Diagnostics. *Science* **2005**, *307* (5709), 538–544.

[73] Li, H.; Vaughan, J. C. Switchable Fluorophores for Single-Molecule Localization Microscopy. *Chem. Rev.* **2018**, *118* (18), 9412–9454.

[74] Martynov, V. I.; Pakhomov, A. A.; Popova, N. V; Deyev, I. E.; Petrenko, A. G. Synthetic Fluorophores for Visualizing Biomolecules in Living Systems. *Acta Naturae* **2016**, *8* (4), 33–46.

[75] Méndez-Ardoy, A.; Reina, J. J.; Montenegro, J. Synthesis and Supramolecular Functional Assemblies of Ratiometric pH Probes. *Chem. Eur. J.* **2020**, *26* (34), 7516–7536.

[76] Colom, A.; Derivery, E.; Soleimanpour, S.; Tomba, C.; Molin, M. D.; Sakai, N.; González-Gaitán, M.; Matile, S.; Roux, A. A Fluorescent Membrane Tension Probe. *Nat. Chem.* **2018**, *10* (11), 1118–1125.

[77] Cox, M. M.; Nelson, D. L. *Principles of Biochemistry*; W H Freeman & Co, 2008.

[78] Casey, J. R.; Grinstein, S.; Orlowski, J. Sensors and Regulators of Intracellular pH. *Nat. Rev. Mol. Cell Biol.* **2010**, *11* (1), 50–61.

[79] Huotari, J.; Helenius, A. Endosome Maturation. *EMBO J.* **2011**, *30* (17), 3481–3500.

[80] Rioboo, A.; Gallego, I.; Montenegro, J. Péptidos Penetrantes Celulares: Descripción, Mecanismo y Aplicaciones. *An. Química* **2019**, *115* (1), 9–21.

[81] Smith, A. E.; Helenius, A. How Viruses Enter Animal Cells. *Science* **2004**, *304* (5668), 237–242.

[82] Mercer, J.; Schelhaas, M.; Helenius, A. Virus Entry by Endocytosis. *Annu. Rev. Biochem.* **2010**, *79* (1), 803–833.

[83] Varkouhi, A. K.; Scholte, M.; Storm, G.; Haisma, H. J. Endosomal Escape Pathways for Delivery of Biologicals. *J. Control. Release* **2011**, *151* (3), 220–228.

[84] Zhang, X.; Patel, A.; Celma, C. C.; Yu, X.; Roy, P.; Zhou, Z. H. Atomic Model of a Nonenveloped Virus Reveals pH Sensors for a Coordinated Process of Cell Entry. *Nat. Struct. Mol. Biol.* **2016**, *23* (1), 74–80.

[85] Pazo, M.; Juanes, M.; Lostalé-Seijo, I.; Montenegro, J. Oligoalanine Helical Callipers for Cell Penetration. *Chem. Commun.* **2018**, *54* (50), 6919–6922.

[86] Pazo, M.; Salluce, G.; Lostalé-Seijo, I.; Juanes, M.; Gonzalez, F.; Garcia-Fandiño, R.; Montenegro, J. Short Oligoalanine Helical Peptides for Supramolecular Nanopore Assembly and Protein Cytosolic Delivery. *RSC Chem. Biol.* **2021**, *2* (2), 503–512.

[87] Webb, B. A.; Chimenti, M.; Jacobson, M. P.; Barber, D. L. Dysregulated pH: a perfect storm for cancer progression. *Nat. Rev. Cancer.* **2011**, *11*(9), 671-677.

[88] Han, J.; Burgess, K. Fluorescent Indicators for Intracellular pH. *Chem. Rev.* **2010**, *110* (5), 2709–2728.

[89] Yue, Y.; Huo, F.; Lee, S.; Yin, C.; Yoon, J. A Review: The Trend of Progress about pH Probes in Cell Application in Recent Years. *Analyst* **2017**, *142* (1), 30–41.

[90] Li, X.; Gao, X.; Shi, W.; Ma, H. Design Strategies for Water-Soluble Small Molecular Chromogenic and Fluorogenic Probes. *Chem. Rev.* **2014**, *114* (1), 590–659.

[91] Rink, T. I.; Tsien, R. Y.; Pozzan, T. Cytoplasmic pH and Free Mg^{2+} in Lymphocytes. *J. Cell Biol.* **1982**, *95* (1), 189–196.

[92] Whitaker, J. E.; Haugland, R. P.; Prendergast, F. G. Spectral and Photophysical Studies of Benzo[*c*]Xanthene Dyes: Dual Emission pH Sensors. *Anal. Biochem.* **1991**, *194* (2), 330–344.

[93] Seksek, O.; Henry-Toulmé, N.; Sureau, F.; Bolard, J. SNARF-1 as an Intracellular pH Indicator in Laser Microspectrofluorometry: A Critical Assessment. *Anal. Biochem.* **1991**, *193* (1), 49–54.

[94] Nakata, E.; Nazumi, Y.; Yukimachi, Y.; Uto, Y.; Maezawa, H.; Hashimoto, T.; Okamoto, Y.; Hori, H. Synthesis and Photophysical Properties of New SNARF Derivatives as Dual Emission pH Sensors. *Bioorg. Med. Chem. Lett.* **2011**, *21* (6), 1663–1666.

[95] Liu, J.; Diwu, Z.; Leung, W. Y. Synthesis and Photophysical Properties of New Fluorinated Benzo[*c*]Xanthene Dyes as Intracellular pH Indicators. *Bioorg. Med. Chem. Lett.* **2001**, *11* (22), 2903–2905.

[96] Zhu, M.; Xing, P.; Zhou, Y.; Gong, L.; Zhang, J.; Qi, D.; Bian, Y.; Du, H.; Jiang, J. Lysosome-Targeting Ratiometric Fluorescent pH Probes Based on Long-Wavelength BODIPY. *J. Mater. Chem. B* **2018**, *6* (27), 4422–4426.

[97] Tang, B.; Yu, F.; Li, P.; Tong, L.; Duan, X.; Xie, T.; Wang, X. A Near-Infrared Neutral pH Fluorescent Probe for Monitoring Minor pH Changes: Imaging in Living HepG2 and HL-7702Cells. *J. Am. Chem. Soc.* **2009**, *131* (8), 3016–3023.

[98] Xia, S.; Wang, J.; Bi, J.; Wang, X.; Fang, M.; Phillips, T.; May, A.; Conner, N.; Tanasova, M.; Luo, F.-T.; Liu, H. Fluorescent Probes Based on π-Conjugation Modulation between Hemicyanine and Coumarin Moieties for Ratiometric Detection of pH Changes in Live Cells with Visible and Near- Infrared Channels. *Sens. Actuators B Chem.* **2018**, *265*, 699–708.

[99] Hammett, L. P. Some Relations between Reactions Rates and Equilibrium Constants. *Chem. Rev.* **1935**, *17* (1), 125–136.

[100] Hammett, L. P. The Effect of Structure upon the Reactions of Organic Compounds. Temperature and Solvent Influences. *J. Chem. Phys.* **1937**, *59* (1), 96–103.

[101] Krygowski, T. M.; Stępień, B. T. Sigma- and Pi-Electron Delocalization: Focus on Substituent Effects. *Chem. Rev.* **2005**, *105* (10), 3482–3512.

[102] Jaffé, H. H. A Reëxamination of the Hammett Equation. *Chem. Rev.* **1953**, *53* (2), 191–261.

[103] Taft, R. W. Linear Free Energy Relationships from Rates of Esterification and Hydrolysis of Aliphatic and Ortho-Substituted Benzoate Esters. *J. Am. Chem. Soc.* **1952**, *74* (11), 2729–2732.

[104] Taft, R. W. Polar and Steric Substituent Constants for Aliphatic and o-Benzoate Groups from Rates of Esterification and Hydrolysis of Esters. *J. Am. Chem. Soc.* **1952**, *74* (12), 3120–3128.

[105] Taft, R. W. Linear Steric Energy Relationships. *J. Am. Chem. Soc.* **1953**, *75* (18), 4538–4539.

[106] Liu, P.; Mu, X.; Zhang, X. D.; Ming, D. The Near-Infrared-II Fluorophores and Advanced Microscopy Technologies Development and Application in Bioimaging. *Bioconjug. Chem.* **2020**, *31* (2), 260–275.

[107] Schermelleh, L.; Ferrand, A.; Huser, T.; Eggeling, C.; Sauer, M.; Biehlmaier, O.; Drummen, G. P. C. Super-Resolution Microscopy Demystified. *Nat. Cell Biol.* **2019**, *21* (1), 72–84.

[109] Thiel, Z.; Rivera-Fuentes, P. Photochemically Active Dyes for Super-Resolution Microscopy. *Chimia* **2018**, *72* (11), 764–770.

[109] Shaw, P. A.; Forsyth, E.; Haseeb, F.; Yang, S.; Bradley, M.; Klausen, M. Two-Photon Absorption: An Open Door to the NIR-II Biological Window? *Front. Chem.* **2022**, *10*:921354.

[110] Kim, H. M.; Cho, B. R. Two-Photon Probes for Intracellular Free Metal Ions, Acidic Vesicles, and Lipid Rafts in Live Tissues. *Acc. Chem. Res.* **2009**, *42* (7), 863–872.

[111] Hou, J. T.; Ren, W. X.; Li, K.; Seo, J.; Sharma, A.; Yu, X. Q.; Kim, J. S. Fluorescent Bioimaging of pH: From Design to Applications. *Chem. Soc. Rev.* **2017**, *46* (8), 2076–2090.

[112] King, G. F. Venoms as a Platform for Human Drugs: Translating Toxins into Therapeutics. *Expert Opin. Biol. Ther.* **2011**, *11* (11), 1469–1484.

[113] Holford, B. M.; Daly, M.; King, G. F.; Norton, R. S. Venoms to the Rescue. *Science* **2018**, *361* (6405), 842–844.

[114] Casewell, N. R.; Wüster, W.; Vonk, F. J.; Harrison, R. A.; Fry, B. G. Complex Cocktails: The Evolutionary Novelty of Venoms. *Trends Ecol. Evol.* **2013**, *28* (4), 219–229.

[115] Oliveira, A. L.; Viegas, M. F.; da Silva, S. L.; Soares, A. M.; Ramos, M. J.; Fernandes, P. A. The Chemistry of Snake Venom and Its Medicinal Potential. *Nat. Rev. Chem.* **2022**, *6* (7), 451–469.

[116] Machkour-M'Rabet, S.; Hénaut, Y.; Winterton, P.; Rojo, R. A Case of Zootherapy with the Tarantula Brachypelma Vagans Ausserer, 1875 in Traditional Medicine of the Chol Mayan Ethnic Group in Mexico. *J. Ethnobiol. Ethnomed.* **2011**, *7* (1), 12–18.

[117] Zhang, S.; Liu, Y.; Ye, Y.; Wang, X. R.; Lin, L. T.; Xiao, L. Y.; Zhou, P.; Shi, G. X.; Liu, C. Z. Bee Venom Therapy: Potential Mechanisms and Therapeutic Applications. *Toxicon* **2018**, *148,* 64–73.

[118] Bordon, K. de C. F.; Cologna, C. T.; Fornari-Baldo, E. C.; Pinheiro-Júnior, E. L.; Cerni, F. A.; Amorim, F. G.; Anjolette, F. A. P.; Cordeiro, F. A.; Wiezel, G. A.; Cardoso, I. A.; Ferreira, I. G.; Oliveira, I. S. de; Boldrini-França, J.; Pucca, M. B.; Baldo, M. A.; Arantes, E. C. From Animal Poisons and Venoms to Medicines: Achievements, Challenges and Perspectives in Drug Discovery. *Front. Pharmacol.* **2020**, *11*: 1132.

[119] Koh, W. U. K.; Choi, S. S.; Lee, J. H.; Lee, S. H.; Lee, S. K.; Lee, Y. K.; Leem, J. G.; Song, J. G.; Shin, J. W. Perineural Pretreatment of Bee Venom Attenuated the Development of Allodynia in the Spinal Nerve Ligation Injured Neuropathic Pain Model; an Experimental Study. *BMC Complement. Altern. Med.* **2014**, *14*: 431.

[120] Vidya, V.; Ram Achar, R.; Himathi, M.U; Akshita, N.; Yogish Somayaji, T.; Kameshwar, V. H.; Byrappa, K.; Ramadas, D. Venom Peptides – A Comprehensive Translational Perspective in Pain Management. *Curr. Res. Toxicol.* **2021**, *2*, 329–340.

[121] Dardevet, L.; Rani, D.; El Aziz, T. A.; Bazin, I.; Sabatier, J. M.; Fadl, M.; Brambilla, E.; De Waard, M. Chlorotoxin: A Helpful Natural Scorpion Peptide to Diagnose Glioma and Fight Tumour Invasion. *Toxins* **2015**, *7* (4), 1079–1101.

[122] Lighting up brain tumour tissue. *Seattle Children's Hospital.* Available at: https://www.seattlechildrens.org/about/stories/lighting-up-brain-tumour-tissue/ (accessed October 24, 2022).

[123] Yamada, M.; Miller, D. M.; Lowe, M.; Rowe, C.; Wood, D.; Soyer, H. P.; Byrnes-Blake, K.; Parrish-Novak, J.; Ishak, L.; Olson, J. M.; Brandt, G.; Griffin, P.; Spelman, L.; Prow, T. W. A First-in-Human Study of BLZ-100 (Tozuleristide) Demonstrates Tolerability and Safety in Skin Cancer Patients. *Contemp. Clin. Trials Commun.* **2021**, *23*:100830.

[124] Khanyile, S.; Masamba, P.; Oyinloye, B. E.; Mbatha, L. S.; Kappo, A. P. Current Biochemical Applications and Future Prospects of Chlorotoxin in Cancer Diagnostics and Therapeutics. *Adv. Pharm. Bull.* **2019**, *9* (4), 510–520.

[125] Moreno, M.; Giralt, E. Three Valuable Peptides from Bee and Wasp Venoms for Therapeutic and Biotechnological Use: Melittin, Apamin and Mastoparan. *Toxins* **2015**, *7* (4), 1126–1150.

[126] Hirai, Y.; Yasuhara, T.; Yoshida, H.; Nakajima, T.; Fujino, M.; Kitada, C. A New Mast Cell Degranulating Peptide “Mastoparan” in the Venom of Vespula Lewisii. *Chem. Pharm. Bull.* **1979**, *27* (8), 1942–1944.

[127] Hirai, Y.; Kuwada, M.; Yasuhara., T.; Yoshida, H.; Nakajima, T. A New Mast Cell Degranulating Peptide Homologous to Mastoparan in the Venom of Japanese Hornet (Vespa Xanthoptera). *Chem. Pharm. Bull.* **1979**, *27* (8), 1945–1946.

[128] Monson de Souza, B.; Vaso Rodrigues da Silva, A.; Ferreira Resende, V. M.; Andrade Arcuri, H.; Perez dos Santos Cabrera, M.; Ruggiero Neto, J.; Palma, M. S. Characterization of Two Novel Polyfunctional Mastoparan Peptides from the Venom of the Social Wasp Polybia Paulista. *Peptides* **2009**, *30* (8), 1387–1395.

[129] Yoon, K. A.; Kim, K.; Nguyen, P.; Seo, J. B.; Park, Y. H.; Kim, K. G.; Seo, H. Y.; Koh, Y. H.; Lee, S. H. Comparative Bioactivities of Mastoparans from Social Hornets Vespa Crabro and Vespa Analis. *J. Asia. Pac. Entomol.* **2015**, *18* (4), 825–829

[130] Whiles, J. A.; Brasseur, R.; Glover, K. J.; Melacini, G.; Komives, E. A.; Vold, R. R. Orientation and Effects of Mastoparan X on Phospholipid Bicelles. *Biophys. J.* **2001**, *80* (1), 280–293.

[131] Arbuzova, A.; Schwarz, G. Pore-Forming Action of Mastoparan Peptides on Liposomes: A Quantitative Analysis. *Biochim. Biophys. Acta - Biomembr.* **1999**, *1420* (1–2), 139–152.

[132] Dos Santos Cabrera, M. P.; Alvares, D. S.; Leite, N. B.; Monson De Souza, B.; Palma, M. S.; Riske, K. A.; Ruggiero Neto, J. New Insight into the Mechanism of Action of Wasp Mastoparan Peptides: Lytic Activity and Clustering Observed with Giant Vesicles. *Langmuir* **2011**, *27* (17), 10805–10813.

[133] Matsuzaki, K.; Yoneyama, S.; Murase, O.; Miyajima, K. Transbilayer Transport of Ions and Lipids Coupled with Mastoparan X Translocation. *Biochemistry* **1996**, *35* (25), 8450–8456.

[134] Henriksen, J. R.; Andresen, T. L. Thermodynamic Profiling of Peptide Membrane Interactions by Isothermal Titration Calorimetry: A Search for Pores and Micelles. *Biophys. J.* **2011**, *101* (1), 100–109.

[135] Mellor, I. R.; Sansom, M. S. P. Ion-Channel Properties of Mastoparan, a 14-Residue Peptide from Wasp Venom, and of MP3, a 12-Residue Analogue. *Proc. R. Soc. B Biol. Sci.* **1990**, *239* (1296), 383–400.

[136] da Silva, A. M. B.; Silva-Gonçalves, L. C.; Oliveira, F. A.; Arcisio-Miranda, M. Pro-Necrotic Activity of Cationic Mastoparan Peptides in Human Glioblastoma Multiforme Cells Via Membranolytic Action. *Mol. Neurobiol.* **2018**, *55* (7), 5490–5504.

[137] de Azevedo, R. A. Figueiredo, C. R.; Ferreira, A. K.; Matsuo, A. L.; Massaoka, M. H.; Girola, N.; Auada, A. V. V; Farias, C. F.; Pasqualoto, K. F. M.; Rodrigues, C. P.; Barbuto,

J. A.; Levy, D.; Bydlowski, S. P.; Sá-Junior, P. L. De; Travassos, L. R.; Lebrun, I. Mastoparan Induces Apoptosis in B16F10-Nex2 Melanoma Cells via the Intrinsic Mitochondrial Pathway and Displays Antitumour Activity in Vivo. *Peptides* **2015**, *68*, 113–119.

[138] Higashijima, T.; Uzu, S.; Nakajima, T.; Ross, E. M. Mastoparan, a Peptide Toxin from Wasp Venom, Mimics Receptors by Activating GTP-Binding Regulatory Proteins (G Proteins). *J. Biol. Chem.* **1988**, *263* (14), 6491–6494.

[139] Higashijima, T.; Burnier, J.; Ross, E. M. Regulation of G(i) and G(o) by Mastoparan, Related Amphiphilic Peptides, and Hydrophobic Amines. Mechanism and Structural Determinants of Activity. *J. Biol. Chem.* **1990**, *265* (24), 14176–14186.

[140] Koch, G.; Haberman, B.; Mohr, C.; Just, I.; Aktories, K. Interaction of Mastoparan with the Low Molecular Mass GTP-Binding Proteins Rho/Rac. *FEBS Lett.* **1991**, *291* (2), 336–340.

[141] Lentschat, A.; Karahashi, H.; Michelsen, K. S.; Thomas, L. S.; Zhang, W.; Vogel, S. N.; Arditi, M. Mastoparan, a G Protein Agonist Peptide, Differentially Modulates TLR4- and TLR2-Mediated Signaling in Human Endothelial Cells and Murine Macrophages. *J. Immunol.* **2005**, *174* (7), 4252–4261.

[142] Hilchie, A. L.; Sharon, A. J.; Haney, E. F.; Hoskin, D. W.; Bally, M. B.; Franco, O. L.; Corcoran, J. A.; Hancock, R. E. W. Mastoparan Is a Membranolytic Anti-Cancer Peptide That Works Synergistically with Gemcitabine in a Mouse Model of Mammary Carcinoma. *Biochim. Biophys. Acta Biomembr.* **2016**, *1858* (12), 3195–3204.

[143] Sharma, G.; Modgil, A.; Zhong, T.; Sun, C.; Singh, J. Influence of Short-Chain Cell-Penetrating Peptides on Transport of Doxorubicin Encapsulating Receptor-Targeted Liposomes across Brain Endothelial Barrier. *Pharm. Res.* **2014**, *31* (5), 1194–1209.

[144] Sample, C. J.; Hudak, K. E.; Barefoot, B. E.; Koci, M. D.; Wanyonyi, M. S.; Abraham, S.; Staats, H. F.; Ramsburg, E. A. A Mastoparan-Derived Peptide Has Broad-Spectrum Antiviral Activity against Enveloped Viruses. *Peptides* **2013**, *48*, 96–105.

[145] Yibin, G.; Jiang, Z.; Hong, Z.; Gengfa, L.; Liangxi, W.; Guo, W.; Yongling, L. A Synthesized Cationic Tetradecapeptide from Hornet Venom Kills Bacteria and Neutralizes Lipopolysaccharide in Vivo and in Vitro. *Biochem. Pharmacol.* **2005**, *70* (2), 209–219.

[146] Lewis, R. J.; Garcia, M. L. Therapeutic Potential of Venom Peptides. *Nat. Rev. Drug Discov.* **2003**, *2* (10), 790–802.

[147] Anand, P.; Filipenko, P.; Huaman, J.; Lyudmer, M.; Hossain, M.; Santamaria, C.; Huang, K.; Ogunwobi, O. O.; Holford, M. Selective Inhibition of Liver Cancer Cells Using Venom Peptide. *Mar. Drugs* **2019**, *17* (10), 587–607.

[148] Dutertre, S.; Jin, A. H.; Vetter, I.; Hamilton, B.; Sunagar, K.; Lavergne, V.; Dutertre, V.; Fry, B. G.; Antunes, A.; Venter, D. J.; Alewood, P. F.; Lewis, R. J. Evolution of Separate Predation-and Defence-Evoked Venoms in Carnivorous Cone Snails. *Nat. Commun.* **2014**, *5*:3521.

[149] Tobassum, S.; Tahir, H. M.; Zahid, M. T.; Gardner, Q. A.; Ahsan, M. M. Effect of Milking Method, Diet, and Temperature on Venom Production in Scorpions. *J. Insect Sci.* **2018**, *18* (4), 1–7.

[150] Gaza, J. T.; Leyson, J. J. C.; Peña, G. T.; Nellas, R. B. pH-Dependent Conformations of an Antimicrobial Spider Venom Peptide, Cupiennin 1a, from Unbiased HREMD Simulations. *ACS Omega* **2021**, *6* (37), 24166–24175.

[151] Cornish-Bowden, A. The Origins of Enzyme Kinetics. *FEBS Lett.* **2013**, *587* (17), 2725–2730.

[152] Angelova, M. I.; Bitbol, A. F.; Seigneuret, M.; Staneva, G.; Kodama, A.; Sakuma, Y.; Kawakatsu, T.; Imai, M.; Puff, N. pH Sensing by Lipids in Membranes: The Fundamentals of pH-Driven Migration, Polarization and Deformations of Lipid Bilayer Assemblies. *Biochim. Biophys. Acta Biomembr.* **2018**, *1860* (10), 2042–2063.

[153] Nelson, D. L.; Lehninger, A. L.; Cox, M. M.; Osgood, M.; Ocorr, K. *Lehninger Principles of Biochemistry*, 7th ed.; W.H. Freeman: New York, 2017.

[154] Kato, Y.; Ozawa, S.; Miyamoto, C.; Maehata, Y.; Suzuki, A.; Maeda, T.; Baba, Y. Acidic Extracellular Microenvironment and Cancer. *Cancer Cell Int.* **2013**, *13*:89.

[155] Semenza, G. L.; Nejfelt, M. K.; Chi, S. M.; Antonarakis, S. E. Hypoxia-Inducible Nuclear Factors Bind to an Enhancer Element Located 3′ to the Human Erythropoietin Gene. *Proc. Natl. Acad. Sci. U.S.A.* **1991**, *88* (13), 5680–5684.

[156] Wang, G. L.; Jiang, B. H.; Rue, E. A.; Semenza, G. L. Hypoxia-Inducible Factor 1 Is a Basic-Helix-Loop-Helix-PAS Heterodimer Regulated by Cellular O_2 Tension. *Proc. Natl. Acad. Sci. U.S.A.* **1995**, *92* (12), 5510–5514.

[157] Maxwell, P. H.; Wiesener, M. S.; Chang, G.-W.; Clifford, S. C.; Vaux, E. C.; Cockman, M. E.; Wykoff, C. C.; Pugh, C. W.; Maher, E. R.; Ratcliffe, P. J. The Tumoursuppressor ProteinVHLtargets Hypoxia-Inducible Factors for Oxygen-Dependent Proteolysis. *Nature* **1999**, *459* (1997), 271–275.

[158] Ivan, M.; Kondo, K.; Yang, H.; Kim, W.; Valiando, J.; Ohh, M.; Salic, A.; Asara, J. M.; Lane, W. S.; Kaelin, J. HIFα Targeted for VHL-Mediated Destruction by Proline Hydroxylation: Implications for O_2 Sensing. *Science* **2001**, *292* (5516), 464–468.

[159] Jaakkola, P.; Mole, D. R.; Tian, Y. M.; Wilson, M. I.; Gielbert, J.; Gaskell, S. J.; Von Kriegsheim, A.; Hebestreit, H. F.; Mukherji, M.; Schofield, C. J.; Maxwell, P. H.; Pugh, C. W.; Ratcliffe, P. J. Targeting of HIF-α to the von Hippel-Lindau Ubiquitylation Complex by O_2-Regulated Prolyl Hydroxylation. *Science* **2001** *292* (5516), 468–472.

[160] Warburg, O.; Wind, F.; Negelein, E. The Metabolism of Tumour in the Body. *J. Gen. Physiol.* **1927**, *8* (6), 519–530.

[1610] Swietach, P.; Vaughan-Jones, R. D.; Harris, A. L. Regulation of Tumour pH and the Role of Carbonic Anhydrase 9. *Cancer Metastasis Rev.* **2007**, *26* (2), 299–310.

[162] Anderson, M.; Moshnikova, A.; Engelman, D. M.; Reshetnyak, Y. K.; Andreev, O. A. Probe for the Measurement of Cell Surface pH in Vivo and Ex Vivo. *Proc. Natl. Acad. Sci. U.S.A.* **2016**, *113* (29), 8177–8181.

[163] Ratzke, C.; Gore, J. Modifying and Reacting to the Environmental pH Drives Bacterial Interactions. *PLoS Biol* **2018**, *16* (3): e2004248.

[164] Ratzke, C.; Denk, J.; Gore, J. Ecological Suicide in Microbes. *Nat. Ecol. Evol.* **2018**, *2* (5), 867–872.

[165] Pezzulo, A. A.; Tang, X. X.; Hoegger, M. J.; Alaiwa, M. H. A.; Ramachandran, S.; Moninger, T. O.; Karp, P. H.; Wohlford-Lenane, C. L.; Haagsman, H. P.; van Eijk, M.; Bánfi, B.; Horswill, A. R.; Stoltz, D. A.; McCray Jr, P. B.; Welsh, M. J.; Zabner, J. Reduced Airway Surface pH Impairs Bacterial Killing in the Porcine Cystic Fibrosis Lung. *Nature* **2012**, *487* (7405), 109–113.

[166] Rippke, F.; Berardesca, E.; Weber, T. M. pH and Microbial Infections. *Curr. Probl. Dermatology* **2018**, *54*, 87–94.

[167] Wang, F.; Raval, Y.; Chen, H.; Tzeng, T. R. J.; Desjardins, J. D.; Anker, J. N. Development of Luminescent pH Sensor Films for Monitoring Bacterial Growth through Tissue. *Adv. Healthc. Mater.* **2014**, *3* (2), 197–204.

[168] Mania-Pramanik, J.; Kerkar, S. C.; Mehta, P. B.; Potdar, S.; Salvi, V. S. Use of Vaginal pH in Diagnosis of Infections and Its Association with Reproductive Manifestations. *J. Clin. Lab. Anal.* **2008**, *22* (5), 375–379.

[169] Liu, B.; Zhang, Q.; Zhou, F.; Ren, L.; Zhao, Y.; Yuan, X. Enhancing Membrane-Disruptive Activity via Hydrophobic Phenylalanine and Lysine Tethered to Poly(Aspartic Acid). *ACS Appl. Mater. Interfaces* **2019**, *11* (16), 14538–14547.

[170] Simonson, T.; Carlsson, J.; Case, D. A. Proton Binding to Proteins: pKa Calculations with Explicit and Implicit Solvent Models. *J. Am. Chem. Soc.* **2004**, *126* (13), 4167–4180.

[171] Di Russo, N. V.; Estrin, D. A.; Martí, M. A.; Roitberg, A. E. pH-Dependent Conformational Changes in Proteins and Their Effect on Experimental pKas: The Case of Nitrophorin 4. *PLoS Comput. Biol.* **2012**, *8* (11): e1002761.

[172] Harris, T. K.; Turner, G. J. Structural Basis of Perturbed pKa Values of Catalytic Groups in Enzyme Active Sites. *IUBMB Life* **2002**, *53* (2), 85–98.

[173] Dwyer, J. J.; Gittis, A. G.; Karp, D. A.; Lattman, E. E.; Spencer, D. S.; Stites, W. E.; García-Moreno E., B. High Apparent Dielectric Constants in the Interior of a Protein Reflect Water Penetration. *Biophys. J.* **2000**, *79* (3), 1610–1620.

[174] Yang, A. -S; Gunner, M. R.; Sampogna, R.; Sharp, K.; Honig, B. On the Calculation of pKas in Proteins. *Proteins Struct. Funct. Bioinforma.* **1993**, *15* (3), 252–265.

[175] Neira, J. L.; Rizzuti, B.; Iovanna, J. L. Determinants of the pKa Values of Ionizable Residues in an Intrinsically Disordered Protein. *Arch. Biochem. Biophys.* **2016**, *598*, 18–27.

[176] Li, W.; Nicol, F.; Szoka Jr, F. C. GALA: A Designed Synthetic pH-Responsive Amphipathic Peptide with Applications in Drug and Gene Delivery. *Adv. Drug Deliv. Rev.* **2004**, *56* (7), 967–985.

[177] Akishiba, M.; Takeuchi, T.; Kawaguchi, Y.; Sakamoto, K.; Yu, H. H.; Nakase, I.; Takatani-Nakase, T.; Madani, F.; Gräslund, A.; Futaki, S. Cytosolic Antibody Delivery by Lipid-Sensitive Endosomolytic Peptide. *Nat. Chem.* **2017**, *9* (8), 751–761.

[178] Yu, H. H.; Sakamoto, K.; Akishiba, M.; Tamemoto, N.; Hirose, H.; Nakase, I.; Imanishi, M.; Madani, F.; Gräslund, A.; Futaki, S. Conversion of Cationic Amphiphilic Lytic Peptides to Cell-Penetration Peptides. *Pept. Sci.* **2020**, *112* (1): e24144.

[179] Zhang, S. K.; Song, J. W.; Li, S. B.; Gao, H. W.; Chang, H. Y.; Jia, L. L.; Gong, F.; Tan, Y. X.; Ji, S. P. Design of pH-Sensitive Peptides from Natural Antimicrobial Peptides for Enhancing Polyethylenimine-Mediated Gene Transfection. *J. Gene Med.* **2017**, *19* (5):e2955.

[180] Andreev, O. A.; Dupuy, A. D.; Segala, M.; Sandugu, S.; Serra, D. A.; Chichester, C. O.; Engelman, D. M.; Reshetnyak, Y. K. Mechanism and Uses of a Membrane Peptide That Targets Tumours and Other Acidic Tissues in Vivo. *Proc. Natl. Acad. Sci. U.S.A.* **2007**, *104* (19), 7893–7898.

[181] Mason, A. J.; Gasnier, C.; Kichler, A.; Prévost, G.; Aunis, D.; Metz-Boutigue, M. H.; Bechinger, B. Enhanced Membrane Disruption and Antibiotic Action against Pathogenic Bacteria by Designed Histidine-Rich Peptides at Acidic pH. *Antimicrob. Agents Chemother.* **2006**, *50* (10), 3305–3311.

[182] Lam, J. K. W.; Liang, W.; Lan, Y.; Chaudhuri, P.; Chow, M. Y. T.; Witt, K.; Kudsiova, L.; Mason, A. J. Effective Endogenous Gene Silencing Mediated by pH Responsive Peptides Proceeds via Multiple Pathways. *J. Control. Release* **2012**, *158* (2), 293–303.

[183] Zhou, K.; Wang, Y.; Huang, X.; Luby-Phelps, K.; Sumer, B. D.; Gao, J. Tunable, Ultrasensitive pH-Responsive Nanoparticles Targeting Specific Endocytic Organelles in Living Cells. *Angew. Chem. Int. Ed.* **2011**, *50* (27), 6109–6114.

[184] Wang, C.; Wang, Y.; Li, Y.; Bodemann, B.; Zhao, T.; Ma, X.; Huang, G.; Hu, Z.; Deberardinis, R. J.; White, M. A.; Gao, J. A Nanobuffer Reporter Library for Fine-Scale Imaging and Perturbation of Endocytic Organelles. *Nat. Commun.* **2015**, *6*: 8524.

[185] Ma, X.; Wang, Y.; Zhao, T.; Li, Y.; Su, L. C.; Wang, Z.; Huang, G.; Sumer, B. D.; Gao, J. Ultra-pH-Sensitive Nanoprobe Library with Broad pH Tunability and Fluorescence Emissions. *J. Am. Chem. Soc.* **2014**, *136* (31), 11085–11092.

[186] Zhao, T.; Huang, G.; Li, Y.; Yang, S.; Ramezani, S.; Lin, Z.; Wang, Y.; Ma, X.; Zeng, Z.; Luo, M.; De Boer, E.; Xie, X. J.; Thibodeaux, J.; Brekken, R. A.; Sun, X.; Sumer, B. D.; Gao, J. A Transistor-like pH Nanoprobe for Tumour Detection and Image-Guided Surgery. *Nat. Biomed. Eng.* **2017**, *1*: 0006.

[187] Peeler, D. J.; Thai, S. N.; Cheng, Y.; Horner, P. J.; Sellers, D. L.; Pun, S. H. PH-Sensitive Polymer Micelles Provide Selective and Potentiated Lytic Capacity to Venom Peptides for Effective Intracellular Delivery. *Biomaterials* **2019**, *192*, 235–244.

[188] Yu, Y.; Lv, X.; Li, J.; Zhou, Q.; Cui, C.; Hosseinzadeh, P.; Mukherjee, A.; Nilges, M. J.; Wang, J.; Lu, Y. Defining the Role of Tyrosine and Rational Tuning of Oxidase Activity by Genetic Incorporation of Unnatural Tyrosine Analogs. *J. Am. Chem. Soc.* **2015**, *137* (14), 4594–4597.

[189] Wang, F.; Qin, L.; Wong, P.; Gao, J. Facile Synthesis of Tetrafluorotyrosine and Its Application in pH Triggered Membrane Lysis. *Org. Lett.* **2011**, *13* (2), 236–239.

[190] Ngambenjawong, C.; Sylvestre, M.; Gustafson, H. H.; Pineda, J. M. B.; Pun, S. H. Reversibly Switchable, pH-Dependent Peptide Ligand Binding via 3,5-Diiodotyrosine Substitutions. *ACS Chem. Biol.* **2018**, *13* (4), 995–1002.

[191] Haas, D. H.; Murphy, R. M. Design of a pH-Sensitive Pore-Forming Peptide with Improved Performance. *J. Pept. Res.* **2004**, *63* (1), 9–16.

[192] Carlsson, A. E. Dendritic Actin Filament Nucleation Causes Traveling Waves and Patches. *Phys. Rev. Lett.* **2010**, *104* (22), 4–7.

[193] Sambeth, R.; Baumgaertner, A. Autocatalytic Polymerization Generates Persistent Random Walk of Crawling Cells. *Phys. Rev. Lett.* **2001**, *86* (22), 5196–5199.

[194] 5-(and-6)-carboxy SNARF™-1. https://www.thermofisher.com/order/catalog/product/C1270 (accessed June 28th, 2023).

[195] Booth, R.; Insua, I.; Bhak, G.; Montenegro, J. Self-Assembled Micro-Fibres by Oxime Connection of Linear Peptide Amphiphiles. *Org. Biomol. Chem.* **2019**, *17* (7), 1984–1991.

[196] Hendricks, M. P.; Sato, K.; Palmer, L. C.; Stupp, S. I. Supramolecular Assembly of Peptide Amphiphiles. *Acc. Chem. Res.* **2017**, *50* (10), 2440–2448.

[197] Wester, J. R.; Lewis, J. A.; Freeman, R.; Sai, H.; Palmer, L. C.; Henrich, S. E.; Stupp, S. I. Supramolecular Exchange among Assemblies of Opposite Charge Leads to Hierarchical Structures. *J. Am. Chem. Soc.* **2020**, *142* (28), 12216–12225.

[198] Ortony, J. H.; Newcomb, C. J.; Matson, J. B.; Palmer, L. C.; Doan, P. E.; Hoffman, B. M.; Stupp, S. I. Internal Dynamics of a Supramolecular Nanofibre. *Nat. Mater.* **2014**, *13* (8), 812–816.

[199] Wolfe, L. S.; Calabrese, M. F.; Nath, A.; Blaho, D. V.; Miranker, A. D.; Xiong, Y. Protein-Induced Photophysical Changes to the Amyloid Indicator Dye Thioflavin T. *Proc. Natl. Acad. Sci.* **2010**, *107* (39), 16863–16868.

[200] Shi, Y.; Ferreira, D. S.; Banerjee, J.; Pickford, A. R.; Azevedo, H. S. Tuning the Matrix Metalloproteinase-1 Degradability of Peptide Amphiphile Nanofibres through Supramolecular Engineering. *Biomater. Sci.* **2019**, *7* (12), 5132–5142.

[201] Jain, A.; Dhiman, S.; Dhayani, A.; Vemula, P. K.; George, S. J. Chemical Fuel-Driven Living and Transient Supramolecular Polymerization. *Nat. Commun.* **2019**, *10* (1), 450–458.

[202] Leckie, J.; Hope, A.; Hughes, M.; Debnath, S.; Fleming, S.; Wark, A. W.; Ulijn, R. V.; Haw, M. D. Nanopropulsion by Biocatalytic Self-Assembly. *ACS Nano* **2014**, *8* (9), 9580–9589.

[203] Inaba, H.; Hatta, K.; Matsuura, K. Directional Propulsion of DNA Microspheres Based on Light-Induced Asymmetric Growth of Peptide Nanofibres. *ACS Appl. Bio. Mater.* **2021**, *4* (7), 5425–5434.

[204] Miller, D. Dynamic Surface Tension: Industrial Applications and Characterisation of Commercial Surfactants. *Tenside, Surfactants, Deterg.* **2005**, *42* (4), 204–209.

[205] Schroën, K.; de Ruiter, J.; Berton-Carabin, C. The Importance of Interfacial Tension in Emulsification: Connecting Scaling Relations Used in Large Scale Preparation with Microfluidic Measurement Methods. *ChemEngineering* **2020**, *4* (4), 1–22.

[206] Bai, S.; Pappas, C.; Debnath, S.; Frederix, P. W. J. M.; Leckie, J.; Fleming, S.; Ulijn, R. V. Stable Emulsions Formed by Self-Assembly of Interfacial Networks of Dipeptide Derivatives. *ACS Nano* **2014**, *8* (7), 7005–7013.

[207] Mason, A. F.; Buddingh, B. C.; Williams, D. S.; Van Hest, J. C. M. Hierarchical Self-Assembly of a Copolymer-Stabilized Coacervate Protocell. *J. Am. Chem. Soc.* **2017**, *139* (48), 17309–17312.

[208] Tang, T. Y. D.; Cecchi, D.; Fracasso, G.; Accardi, D.; Coutable-Pennarun, A.; Mansy, S. S.; Perriman, A. W.; Anderson, J. L. R.; Mann, S. Gene-Mediated Chemical Communication in Synthetic Protocell Communities. *ACS Synth. Biol.* **2018**, *7* (2), 339–346.

[209] Gruner, P.; Riechers, B.; Semin, B.; Lim, J.; Johnston, A.; Short, K.; Baret, J. C. Controlling Molecular Transport in Minimal Emulsions. *Nat. Commun.* **2016**, *7*, 10392–10400.

[210] Etienne, G.; Vian, A.; Biočanin, M.; Deplancke, B.; Amstad, E. Cross-Talk between Emulsion Drops: How Are Hydrophilic Reagents Transported across Oil Phases? *Lab Chip* **2018**, *18* (24), 3903–3912.

[211] Snarf pH Indicators. *ThermoFisher Scientific.* https://assets.thermofisher.com/TFS-Assets/LSG/manuals/mp01270.pdf (accessed October 4th, 2022).

[212] Lamiable, A.; Thevenet, P.; Rey, J.; Vavrusa, M.; Derreumaux, P.; Tuffery, P. PEP-FOLD3: Faster Denovo Structure Prediction for Linear Peptides in Solution and in Complex. *Nucleic Acids Res.* **2016**, *44* (1), W449–W454.

[213] Christiaens, B.; Symoens, S.; Vanderheyden, S.; Engelborghs, Y.; Joliot, A.; Prochiantz, A.; Vandekerckhove, J.; Rosseneu, M.; Vanloo, B. Tryptophan Fluorescence Study of the Interaction of Penetratin Peptides with Model Membranes. *Eur. J. Biochem.* **2002**, *269* (12), 2918–2926.

[214] Jobin, M. L.; Blanchet, M.; Henry, S.; Chaignepain, S.; Manigand, C.; Castano, S.; Lecomte, S.; Burlina, F.; Sagan, S.; Alves, I. D. The Role of Tryptophans on the Cellular Uptake and Membrane Interaction of Arginine-Rich Cell Penetrating Peptides. *Biochim. Biophys. Acta Biomembr*. **2015**, *1848* (2), 593–602.

[215] Liao, Y.; Zhang, S. M.; Neo, T. L.; Tam, J. P. Tryptophan-Dependent Membrane Interaction and Heteromerization with the Internal Fusion Peptide by the Membrane Proximal External Region of SARS-CoV Spike Protein. *Biochemistry* **2015**, *54* (9), 1819–1830.

[216] Perlikowska, W. Mikołajczyk, M. A Short Synthesis of Enantiomeric Phytoprostanes B1 Type I. *Synthesis* **2009**, 16, 2715–2718.

[217] Lucien, F.; Harper, K.; Pelletier, P. P.; Volkov, L.; Dubois, C. M. Simultaneous pH Measurement in Endocytic and Cytosolic Compartments in Living Cells Using Confocal Microscopy. *J. Vis. Exp.* **2014**, *86*: e51395.

[218] Oparin, A. I. *The Origin of Life*; Foreign Languages Publishing House, 1924.

[219] Ettema, T. J. G.; Lindås, A. C.; Bernander, R. An Actin-Based Cytoskeleton in Archaea. *Mol. Microbiol.* **2011**, *80* (4), 1052–1061.

Annex I: Authorizations for the reproduction of images

The journal authorizations for the use of images can be consulted in this section.

- **Authorization for Figure 1:**

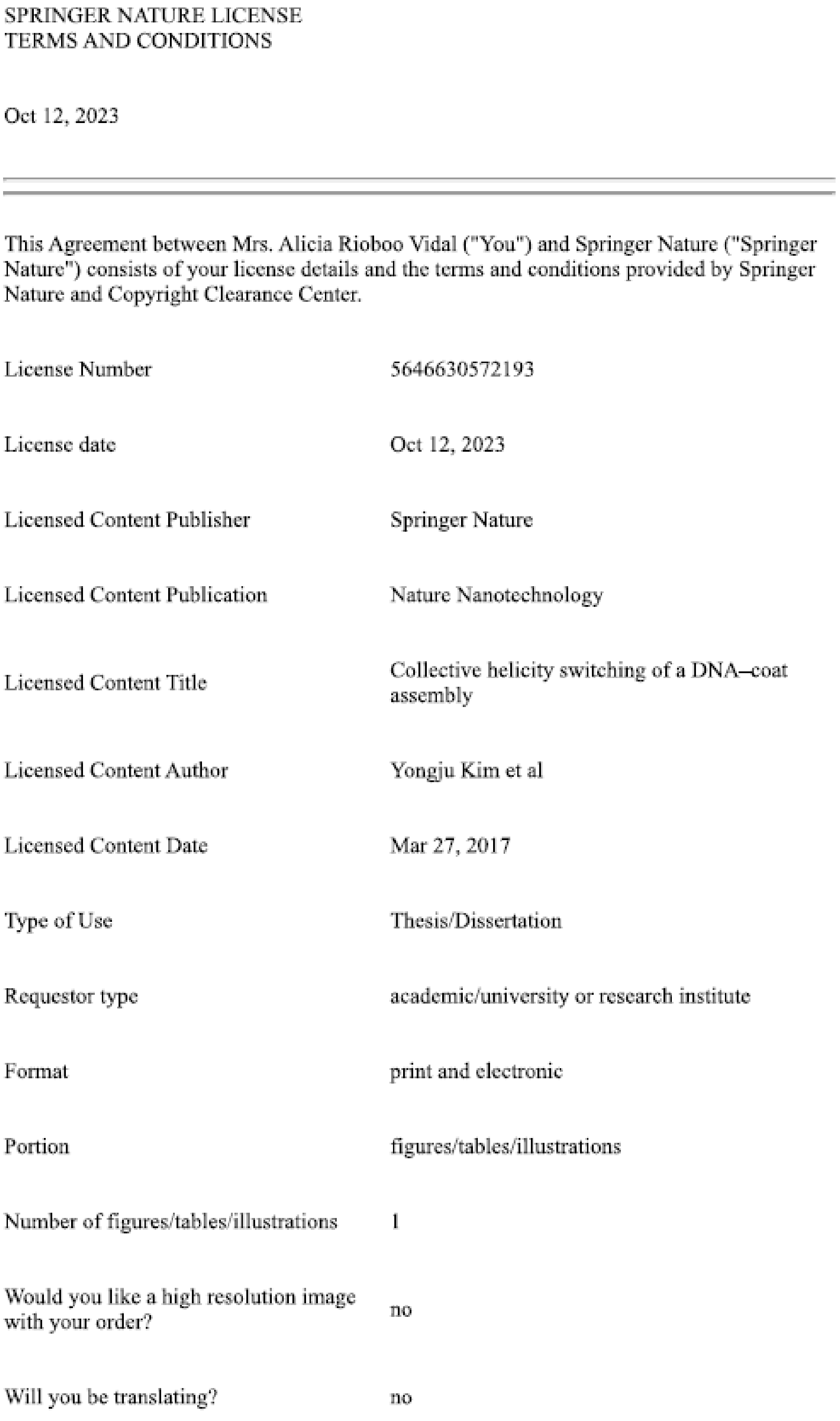

SPRINGER NATURE LICENSE
TERMS AND CONDITIONS

Oct 12, 2023

This Agreement between Mrs. Alicia Rioboo Vidal ("You") and Springer Nature ("Springer Nature") consists of your license details and the terms and conditions provided by Springer Nature and Copyright Clearance Center.

License Number	5646630572193
License date	Oct 12, 2023
Licensed Content Publisher	Springer Nature
Licensed Content Publication	Nature Nanotechnology
Licensed Content Title	Collective helicity switching of a DNA–coat assembly
Licensed Content Author	Yongju Kim et al
Licensed Content Date	Mar 27, 2017
Type of Use	Thesis/Dissertation
Requestor type	academic/university or research institute
Format	print and electronic
Portion	figures/tables/illustrations
Number of figures/tables/illustrations	1
Would you like a high resolution image with your order?	no
Will you be translating?	no

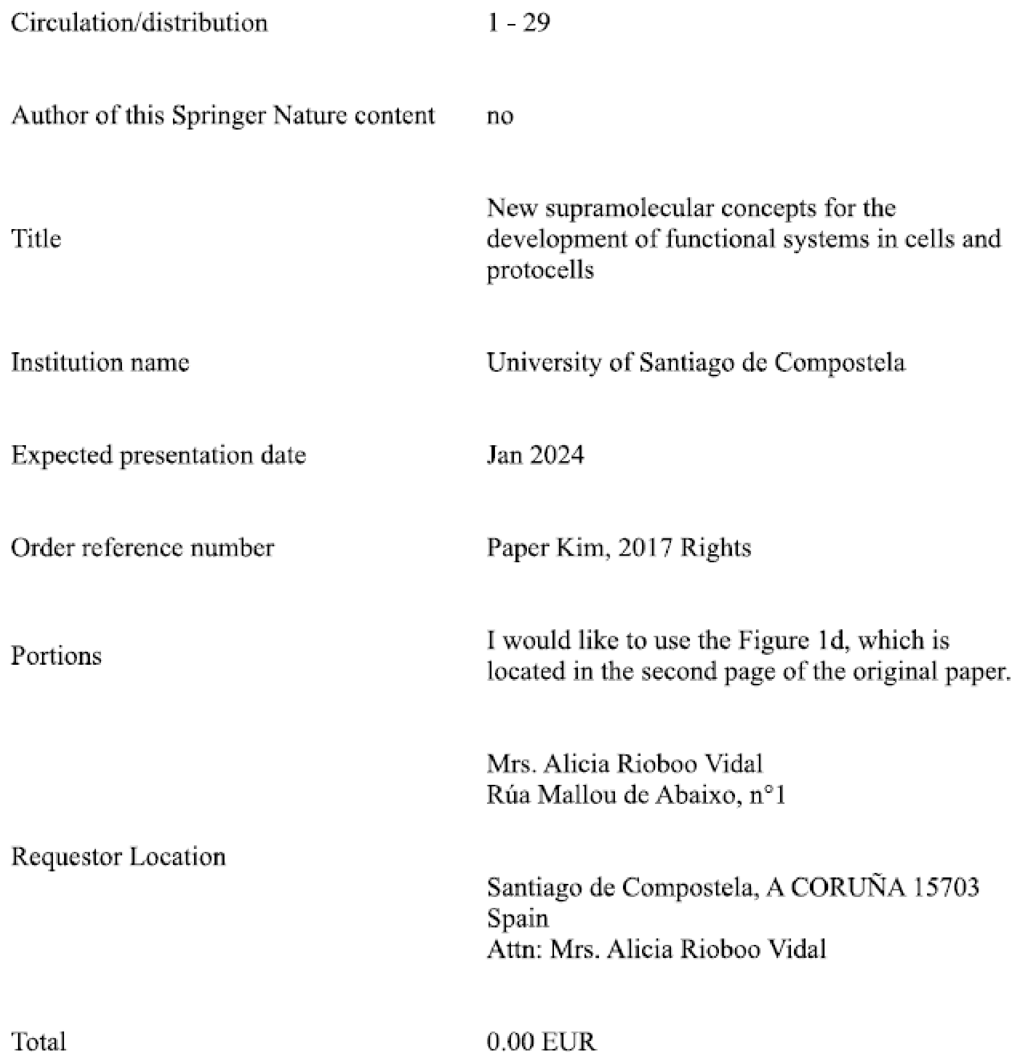

Circulation/distribution	1 - 29
Author of this Springer Nature content	no
Title	New supramolecular concepts for the development of functional systems in cells and protocells
Institution name	University of Santiago de Compostela
Expected presentation date	Jan 2024
Order reference number	Paper Kim, 2017 Rights
Portions	I would like to use the Figure 1d, which is located in the second page of the original paper.
Requestor Location	Mrs. Alicia Rioboo Vidal Rúa Mallou de Abaixo, n°1 Santiago de Compostela, A CORUÑA 15703 Spain Attn: Mrs. Alicia Rioboo Vidal
Total	0.00 EUR

- **Authorization for Figure 2:**

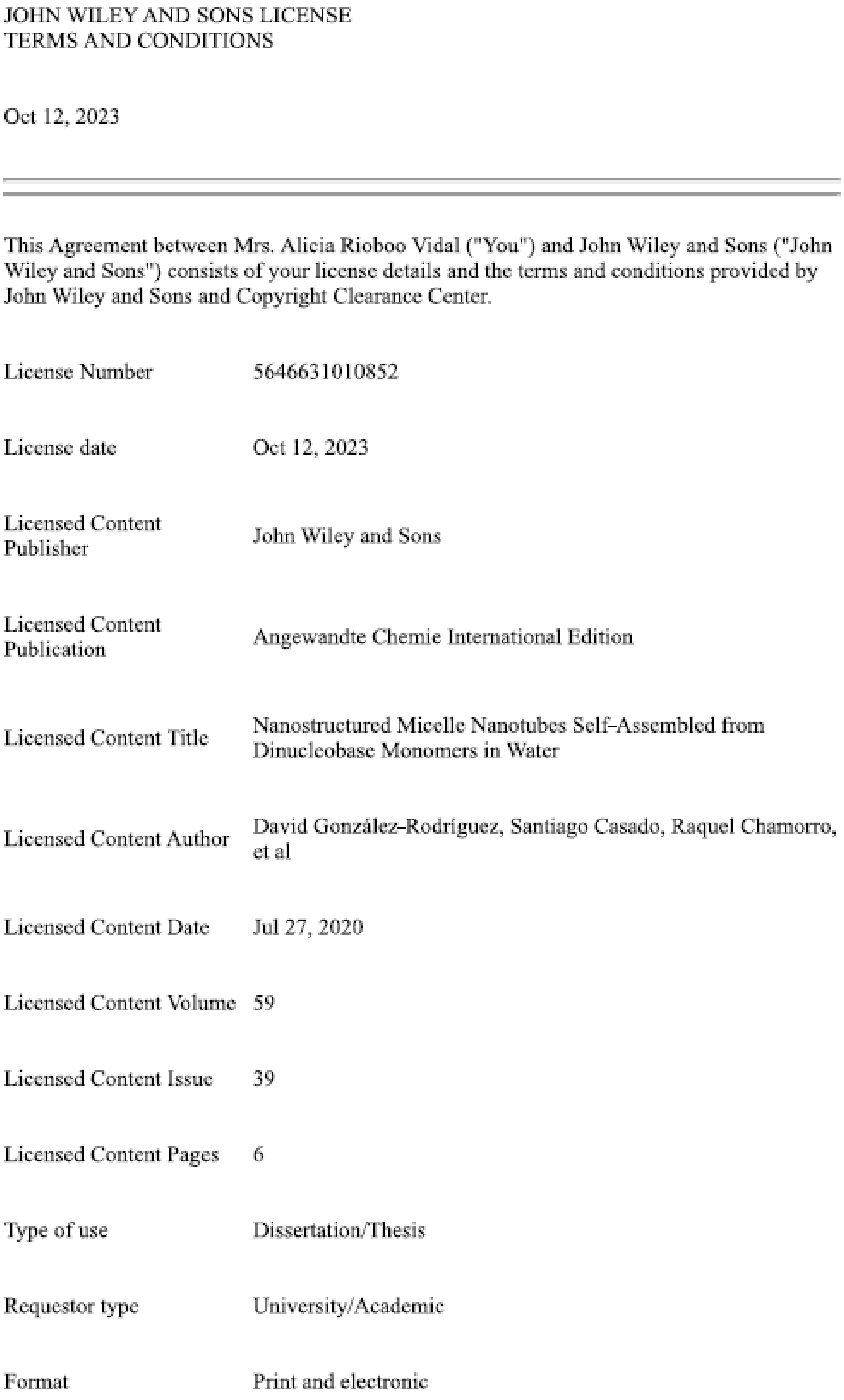

JOHN WILEY AND SONS LICENSE
TERMS AND CONDITIONS

Oct 12, 2023

This Agreement between Mrs. Alicia Rioboo Vidal ("You") and John Wiley and Sons ("John Wiley and Sons") consists of your license details and the terms and conditions provided by John Wiley and Sons and Copyright Clearance Center.

License Number	5646631010852
License date	Oct 12, 2023
Licensed Content Publisher	John Wiley and Sons
Licensed Content Publication	Angewandte Chemie International Edition
Licensed Content Title	Nanostructured Micelle Nanotubes Self-Assembled from Dinucleobase Monomers in Water
Licensed Content Author	David González-Rodríguez, Santiago Casado, Raquel Chamorro, et al
Licensed Content Date	Jul 27, 2020
Licensed Content Volume	59
Licensed Content Issue	39
Licensed Content Pages	6
Type of use	Dissertation/Thesis
Requestor type	University/Academic
Format	Print and electronic

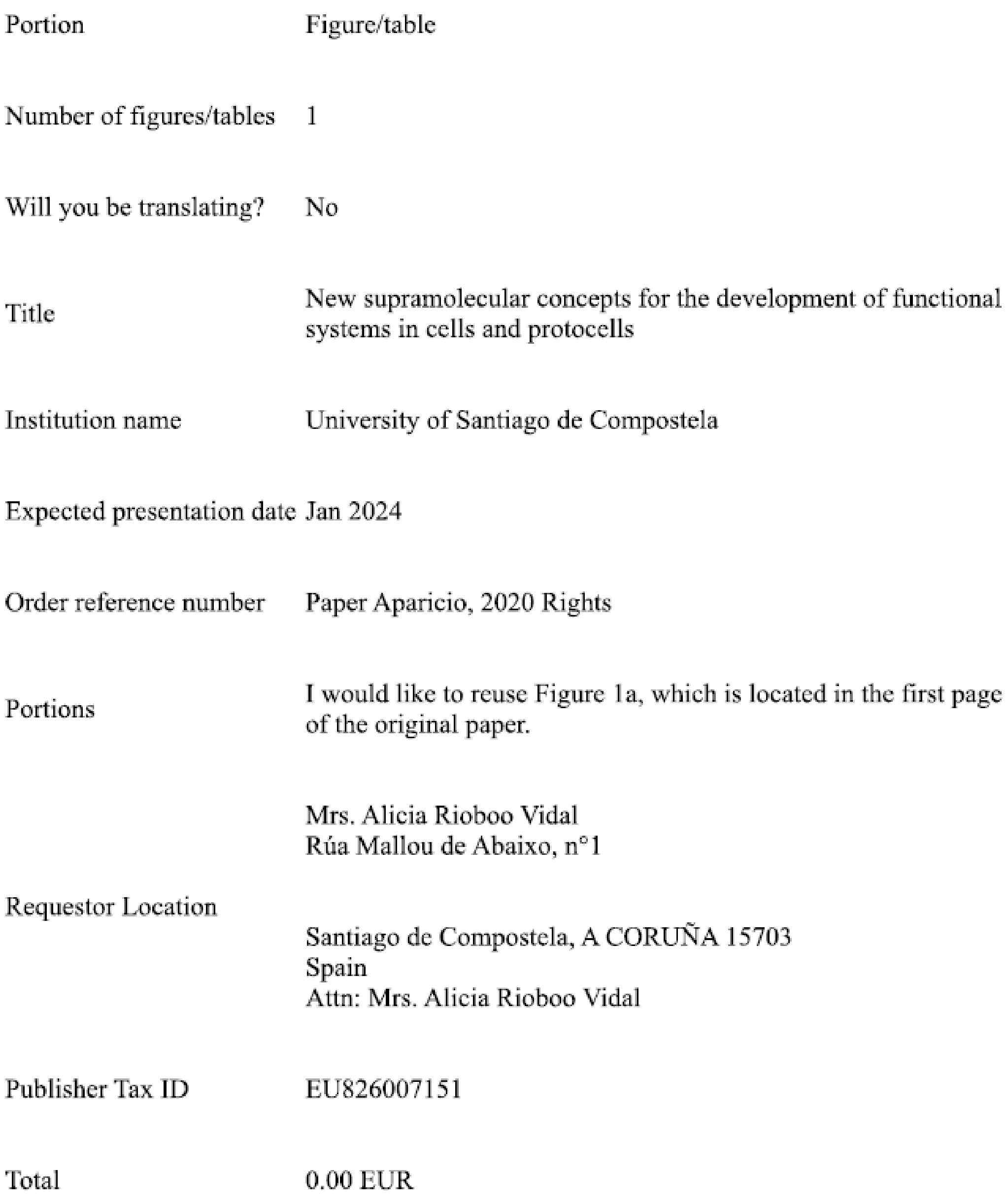

Portion	Figure/table
Number of figures/tables	1
Will you be translating?	No
Title	New supramolecular concepts for the development of functional systems in cells and protocells
Institution name	University of Santiago de Compostela
Expected presentation date	Jan 2024
Order reference number	Paper Aparicio, 2020 Rights
Portions	I would like to reuse Figure 1a, which is located in the first page of the original paper.
Requestor Location	Mrs. Alicia Rioboo Vidal Rúa Mallou de Abaixo, n°1 Santiago de Compostela, A CORUÑA 15703 Spain Attn: Mrs. Alicia Rioboo Vidal
Publisher Tax ID	EU826007151
Total	0.00 EUR

- **Authorization for Figure 5:**

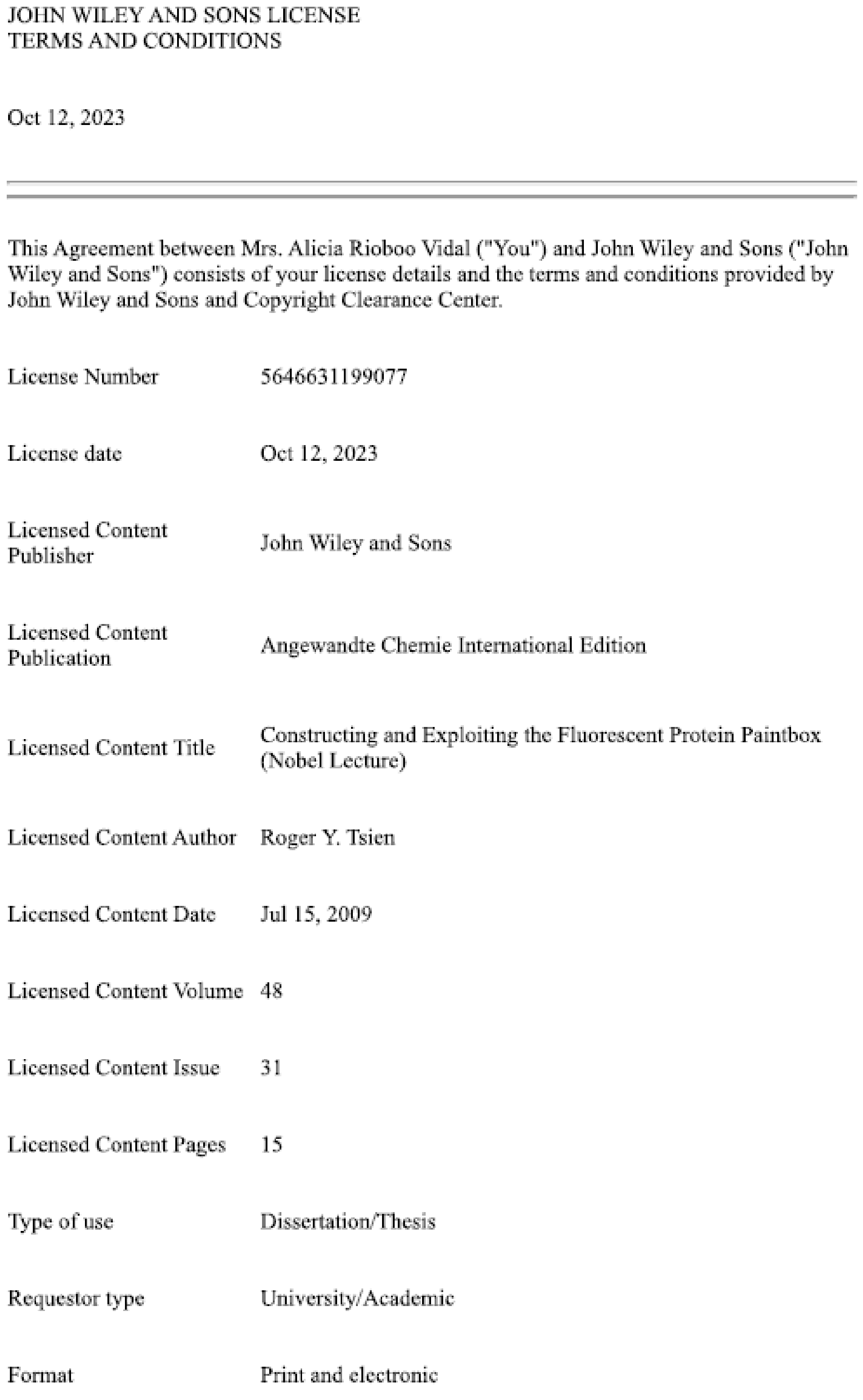

JOHN WILEY AND SONS LICENSE
TERMS AND CONDITIONS

Oct 12, 2023

This Agreement between Mrs. Alicia Rioboo Vidal ("You") and John Wiley and Sons ("John Wiley and Sons") consists of your license details and the terms and conditions provided by John Wiley and Sons and Copyright Clearance Center.

License Number	5646631199077
License date	Oct 12, 2023
Licensed Content Publisher	John Wiley and Sons
Licensed Content Publication	Angewandte Chemie International Edition
Licensed Content Title	Constructing and Exploiting the Fluorescent Protein Paintbox (Nobel Lecture)
Licensed Content Author	Roger Y. Tsien
Licensed Content Date	Jul 15, 2009
Licensed Content Volume	48
Licensed Content Issue	31
Licensed Content Pages	15
Type of use	Dissertation/Thesis
Requestor type	University/Academic
Format	Print and electronic

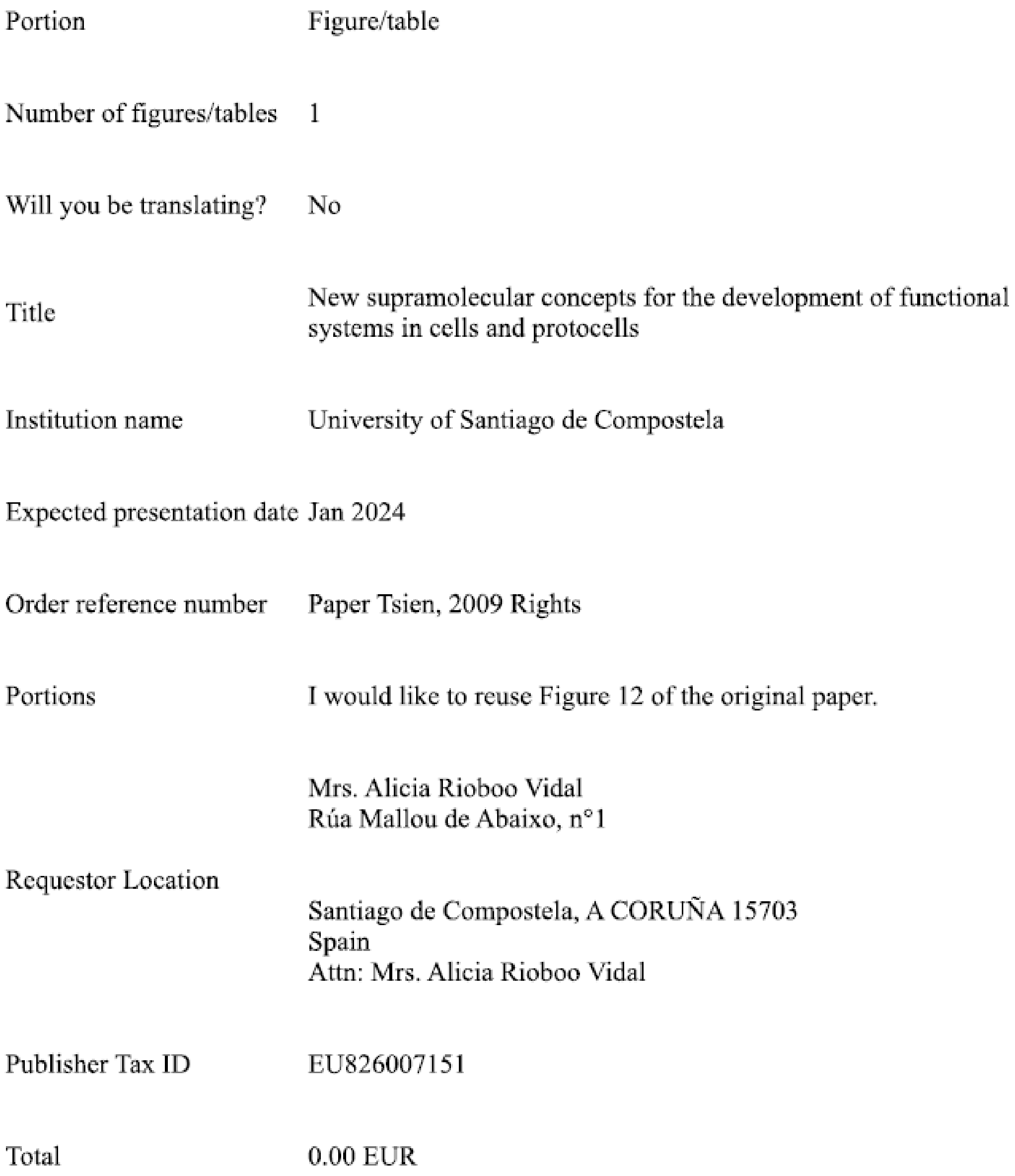

Portion	Figure/table
Number of figures/tables	1
Will you be translating?	No
Title	New supramolecular concepts for the development of functional systems in cells and protocells
Institution name	University of Santiago de Compostela
Expected presentation date	Jan 2024
Order reference number	Paper Tsien, 2009 Rights
Portions	I would like to reuse Figure 12 of the original paper.
Requestor Location	Mrs. Alicia Rioboo Vidal Rúa Mallou de Abaixo, n°1 Santiago de Compostela, A CORUÑA 15703 Spain Attn: Mrs. Alicia Rioboo Vidal
Publisher Tax ID	EU826007151
Total	0.00 EUR

- **Authorization for Figure 40:**

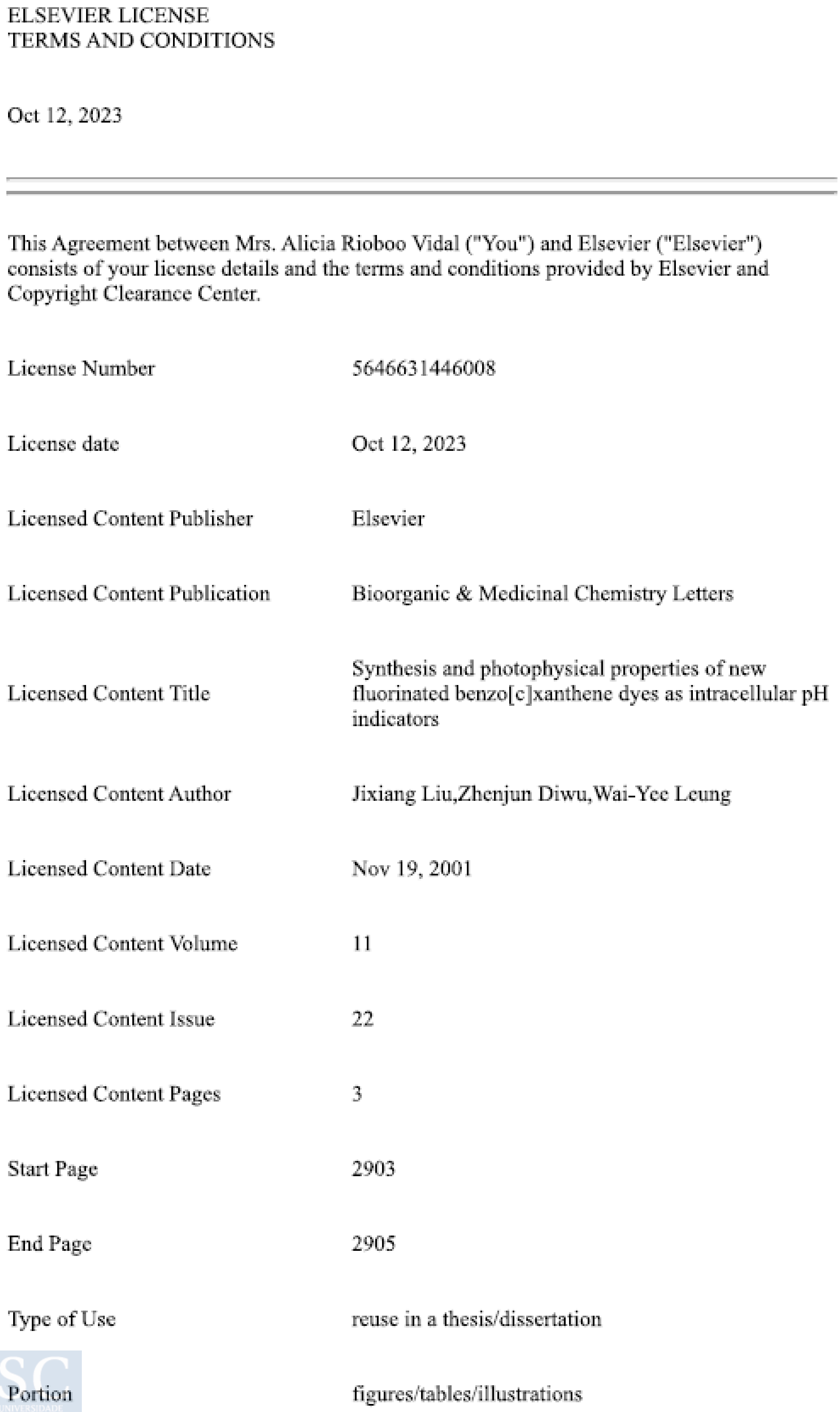

ELSEVIER LICENSE
TERMS AND CONDITIONS

Oct 12, 2023

This Agreement between Mrs. Alicia Rioboo Vidal ("You") and Elsevier ("Elsevier") consists of your license details and the terms and conditions provided by Elsevier and Copyright Clearance Center.

License Number	5646631446008
License date	Oct 12, 2023
Licensed Content Publisher	Elsevier
Licensed Content Publication	Bioorganic & Medicinal Chemistry Letters
Licensed Content Title	Synthesis and photophysical properties of new fluorinated benzo[c]xanthene dyes as intracellular pH indicators
Licensed Content Author	Jixiang Liu,Zhenjun Diwu,Wai-Yee Leung
Licensed Content Date	Nov 19, 2001
Licensed Content Volume	11
Licensed Content Issue	22
Licensed Content Pages	3
Start Page	2903
End Page	2905
Type of Use	reuse in a thesis/dissertation
Portion	figures/tables/illustrations

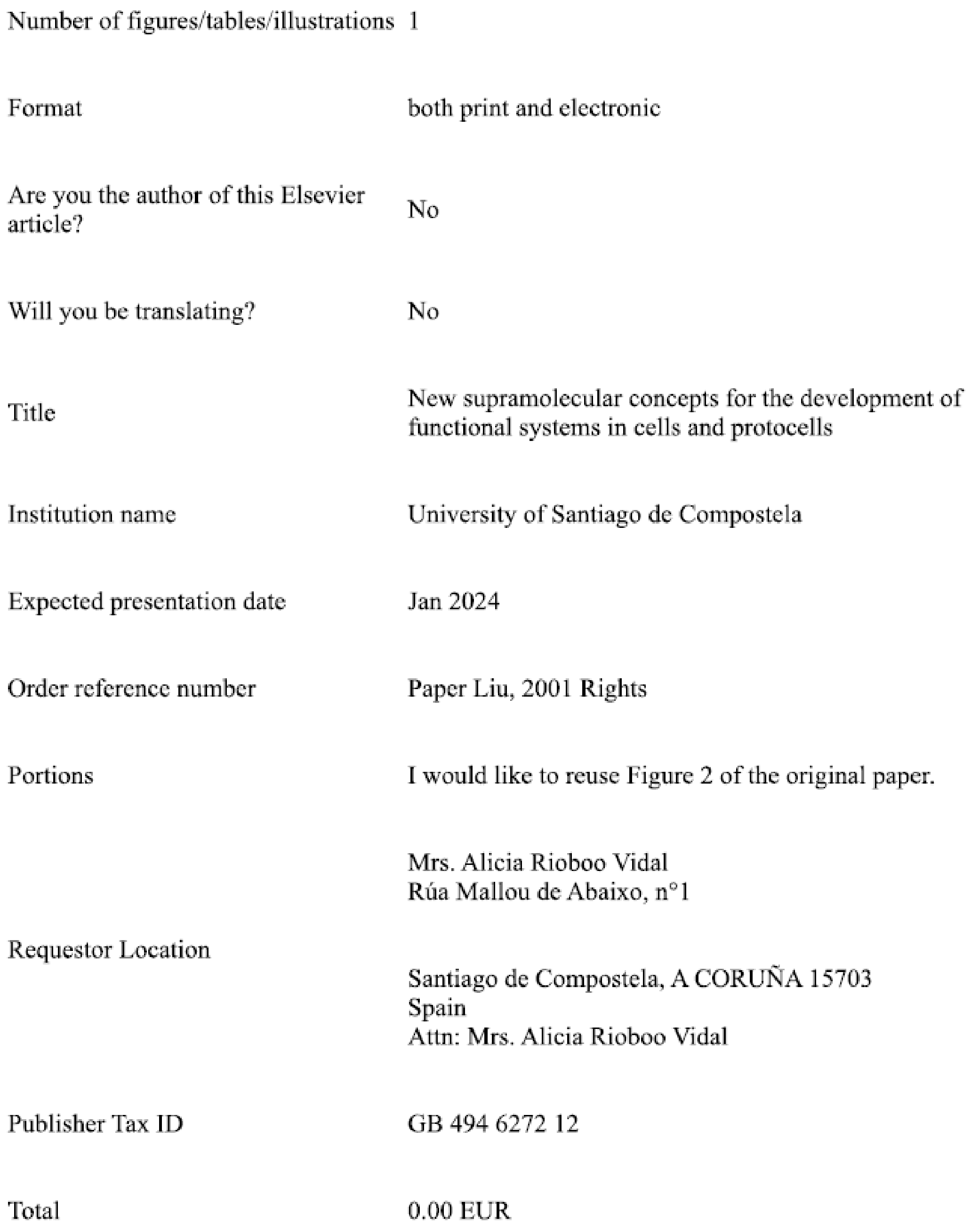

Number of figures/tables/illustrations	1
Format	both print and electronic
Are you the author of this Elsevier article?	No
Will you be translating?	No
Title	New supramolecular concepts for the development of functional systems in cells and protocells
Institution name	University of Santiago de Compostela
Expected presentation date	Jan 2024
Order reference number	Paper Liu, 2001 Rights
Portions	I would like to reuse Figure 2 of the original paper.
Requestor Location	Mrs. Alicia Rioboo Vidal Rúa Mallou de Abaixo, n°1 Santiago de Compostela, A CORUÑA 15703 Spain Attn: Mrs. Alicia Rioboo Vidal
Publisher Tax ID	GB 494 6272 12
Total	0.00 EUR

- **Authorization for Figures 13, 16, 17, 18, 19, 45 and S1. figures:**

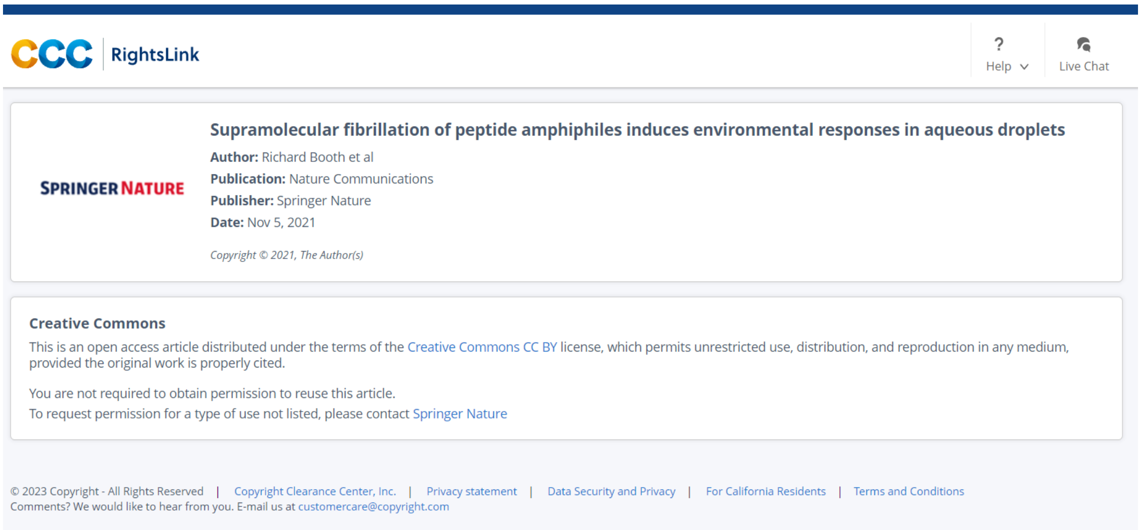

Supramolecular fibrillation of peptide amphiphiles induces environmental responses in aqueous droplets

Author: Richard Booth et al
Publication: Nature Communications
Publisher: Springer Nature
Date: Nov 5, 2021

Copyright © 2021, The Author(s)

Creative Commons

This is an open access article distributed under the terms of the Creative Commons CC BY license, which permits unrestricted use, distribution, and reproduction in any medium, provided the original work is properly cited.

You are not required to obtain permission to reuse this article.
To request permission for a type of use not listed, please contact Springer Nature

© 2023 Copyright - All Rights Reserved | Copyright Clearance Center, Inc. | Privacy statement | Data Security and Privacy | For California Residents | Terms and Conditions
Comments? We would like to hear from you. E-mail us at customercare@copyright.com


USC
UNIVERSIDADE
DE SANTIAGO
DE COMPOSTELA

Annex II: List of publications

The *Field 1: Amphiphilic self-assemblies for protocellular study* of this PhD manuscript include a paper published in:

Booth, R. [a]; Insua, I. [a]; Ahmed, S. [a]; Rioboo, A. [a]; Montenegro, J. [a]*
Supramolecular Fibrillation of Peptide Amphiphiles Induces Environmental Responses in Aqueous Droplets. *Nat. Commun.* **2021**, *12 (1)*, 6421–6428.
DOI: 10.1038/s41467-021-26681-2

[a] Centro Singular de Investigación en Química Biolóxica e Materiais Moleculares (CiQUS), Departamento de Química Orgánica, Universidade de Santiago de Compostela (USC), 15782, Spain.

Year of publication: 2021

Nature Communications Impact Score: 16.6 (2022). **Q1** in Biochemistry, Genetics and Molecular Biology; Chemistry; Physics and Astronomy.

Contribution: I have carried out chemical synthesis and characterization. I have also contributed, as all other authors, to the published article final version.

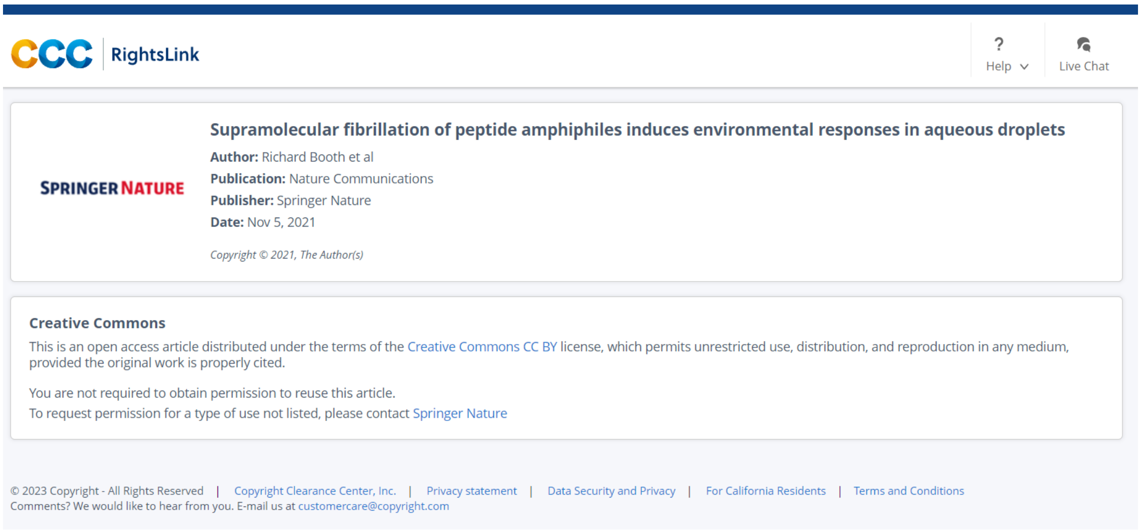

Supramolecular fibrillation of peptide amphiphiles induces environmental responses in aqueous droplets

Author: Richard Booth et al
Publication: Nature Communications
Publisher: Springer Nature
Date: Nov 5, 2021

Copyright © 2021, The Author(s)

Creative Commons

This is an open access article distributed under the terms of the Creative Commons CC BY license, which permits unrestricted use, distribution, and reproduction in any medium, provided the original work is properly cited.

You are not required to obtain permission to reuse this article.
To request permission for a type of use not listed, please contact Springer Nature

© 2023 Copyright - All Rights Reserved | Copyright Clearance Center, Inc. | Privacy statement | Data Security and Privacy | For California Residents | Terms and Conditions
Comments? We would like to hear from you. E-mail us at customercare@copyright.com


USC
UNIVERSIDADE
DE SANTIAGO
DE COMPOSTELA

USC
UNIVERSIDADE
DE SANTIAGO
DE COMPOSTELA

CAMPUS VIDA
CAMPUS DE EXCELENCIA INTERNACIONAL

In this manuscript, we have approached the development of new functional supramolecular systems from a chemical perspective and with the objective to modify or replicate cellular functions. The main driving force and link between the systems developed during this PhD work is the dynamic character of stimuli-responsiveness, which is crucial for their specific functional behaviour. The novel functional systems development focused on a protofilament cytoskeleton-mimetic system, a new ratiometric fluorescent SNARF probe with pH range sensitivity optimized and a pH sensitive antitumoral analogue of a natural venom.